Deformation and softening behaviour of commercial AlMn-alloys

Experiments and Modelling

by

Knut Sjølstad

A thesis submitted to
The Norwegian University of Science and Thechnology (NTNU)
in partial fulfilment of the requirements for the degree of

Doktor Ingeniør

Trondheim
September 2003

Acknowledgements

The work presented in this thesis has been carried out in Trondheim, at the Norwegian University of Science and Technology (NTNU), Department of Materials Technology, in the period from May 2000 to July 2003. My supervisor has been Professor Knut Marthinsen and I gratefully acknowledge his encouragement and enthusiasm in guiding me throughout this work.

I would also like to acknowledge my colleagues at NTNU who have assisted me during the work with this thesis. In particular, I would like to thank; Professor Erik Nes for his helpful discussions and for being my co-supervisor. Mr. Stian Tangen, Mr. Randulf Valle, Mr. Hans Bjerkås, Dr. Bjørn Holmedal, Dr. Shahriar Abtahi and my room-mate Mr. Øyvind Ryen are acknowledged for interesting discussions and comments. Dr. Olaf Engler has assisted me regarding recrystallisation textures and finally Dr. Jan Anders Sæter and Dr. Tanja Pettersen for their willingness in discussing my problems throughout this work.

This thesis work has been a part of a large European collaboration. The project is in short VIR[FAB] an abbreviation for Virtual Fabrication. The main objective of VIR[FAB] has been to develop "*predictive through process microstructural models for rolling and extrusion of aluminium alloys for client oriented and flexible fabrication*", which is also the full title of the project. This research was carried out as part of VIR[FAB] which is a Fifth Framework project (Contract N° G5RD-CT-1999-00132). The author would like to thank the VIR[FAB] consortium for their collaboration and support. Funding by the European Community is gratefully acknowledged. Hydro Aluminium is further acknowledged for putting some extra financial support into my thesis work.

Finally, I would like to thank my fiancé Lisbeth and our son Kasper for being patience and encouraging during my time as a PhD-student. Their support has made it easier to write this thesis.

Trondheim, September 2003

Knut Sjølstad

Contents

Abstract

A comprehensive study of the softening behaviour of two different non-heat treatable AlMn-alloys has been carried out. These alloys were a laboratory processed and an industrially processed AA3103-alloy. The primary objective of the laboratory processed alloy has been directed towards the relationship between the amount of manganese in supersaturated solid solution and the material behaviour during deformation and annealing. The focus for the industrially processed alloy was a detailed material characterisation during hot and cold rolling as well as to follow the softening behaviour of the alloy.

The cold rolled microstructures were characterised with respect to subgrain size, misorientation across the subgrain boundaries, particle break-up and global texture. As far as it concerns the cold deformed microstructure it was found that the different homogenisation treatments, resulting in different amount of Mn in supersaturation, had little effect on the deformed microstructure.

Detailed experimental work on the softening behaviour after cold deformation and the interaction between recrystallisation and precipitation, *i.e.* concurrent precipitation, has been carried out. Hardness and yield stress measurements, which defines the strength of the material, revealed that the softening behaviour was significantly slowed down in case of concurrent precipitation. It was further found that the precipitation reaction in this case occurred on the subgrain boundaries. Thus the precipitates considerably retarded the recrystallisation reaction as compared to the case when no precipitation occurred.

TTT-diagrams have been constructed on the basis of hardness and conductivity measurements. From these diagrams a characteristic temperature, T_c, for the different material conditions are identified. It was found that as the annealing was carried above this temperature the microstructure consisted of a fine grained equiaxed microstructure. Below T_c the grains become elongated in the rolling direction and the average grain size became much coarser.

With respect to recrystallisation texture, a very strong P-texture and in addition some ND-rotated cube texture was found in case of concurrent precipitation. This

strong P-texture was investigated in detail, and it can be concluded that particle stimulated nucleation of recrystallisation (PSN) plays a significant role in the nucleation of these components. It was found that these texture components had a growth advantage in the early stage of annealing and that they are most probably a result of microgrowth selection, which often are related to a nucleation effect. When precipitation did not interact with recovery and recrystallisation the recrystallisation texture was either random or consisted of a weak cube texture.

The softening behaviour of the different materials has been modelled by a physically based softening model, which involves both the recovery and recrystallisation reactions. Both for the AlMn-alloys and for an additional commercially pure Al-alloy, relatively good model predictions were obtained for the softening behaviour when recrystallisation occurred prior to precipitation. However, when the softening reactions were retarded by heavy precipitation of dispersoids the model, in its original form, was not capable to predict the softening behaviour. In this case an additional retarding drag, which reduces the total number of viable recrystallisation nuclei, was added. With the addition of this drag relatively good model predictions were also obtained in case of concurrent precipitation. However, the model was not capable to predict the softening behaviour of the industrially processed AlMn-alloy particularly well.

1. Introduction

The aluminium manufacturing industry can only keep its present competitiveness if it can provide tailored products of superior quality to its customers. Further the industry have to reach for a zero waste production throughout the processing lines. This goal can only be reached by having a fully optimised process where all processing parameters are controlled. The industry has accepted that this optimisation can only be achieved by using models that predict the influence of changes in the process upon the final product. This was the basis for the launch of the Vir[*]-projects, where the industry wanted to create physically based Through Process Models (TPM). The Vir[*]-project is subdivided into three main projects, i.e. Vir[Cast], Vir[Fab] and Vir[Form], which have the main focus on the different steps of the processing line. Vir[Cast] is concerned with casting and homogenisation, Vir[Fab] follow the homogenised material through the rolling or extrusion schedules and the subsequent backannealing (semiproducts), while Vir[Form] is focused on forming operations of the semiproducts into final products.

The present work has been funded by the Vir[Fab]-project. The industrial partners within this project are Alcan International Ltd, Corus Technology, Hydro Aluminium AS, Pechiney S.A., Raytek GmbH, Sapa Technology and VAW Aluminium AG (now Hydro Aluminium Deutschland), and the research institutes and academic partners and are Ecole des Mines Saint-Etienne, Netherlands Institute of Metals Research (NIMR), Rheinisch-Westfälische Technische Hochschule Aachen (RWTH), Swedish Institute of Metals Research (SIMR), SINTEF, University of Sheffield and Norwegian University of Science and Technology (NTNU).

The present work has been carried out as a part of the total activity within the Vir[Fab]-project and was intended as a contribution to the overall objective of the project. AlMn-alloys, which are typically used for heat exchangers and air condition units, have been investigated in this work. The main objective of the work was to study the effect of manganese in supersaturated solid solution upon annealing after cold rolling of a laboratory processed AlMn-alloy. More specifically, by different homogenisation treatments three variants of an

AA3103-alloy were achieved, these variants had different levels of Mn in supersaturated solid solution. The effects of precipitation on the softening kinetics, recrystallisation, texture and grain size have been important issues for this work. This material will in the following be called the LP 3103-alloy.

In addition to the laboratory processed material (LP 3103), a parallel detailed characterisation of an industrially homogenised and rolled AA3103-alloy has been carried out. This material is named CP 3103 in the following. In the Vir[Fab]-project the purpose of this characterisation was for validation and to provide input data for the different models within the Vir[Fab]-project. The findings from the laboratory processed material were intended to serve as a reference and a basis for the discussion of the industrially processed alloy.

Most available models for recovery and recrystallisation do not take the precipitation reaction into account and are not able to satisfactorily predict the size of the grains. The softening behaviour of the different materials has in the present work been modelled by the so-called ALSOFT-model. This model handles both recovery and recrystallisation during annealing. An attempt to improve the ALSOFT-model to be able to handle concurrent precipitation has been suggested. To validate the model predictions an “easier” alloy than the AlMn-alloys was chosen, here the Vir[Fab] AA1200-alloy has been used for this purpose.

Some of the results presented throughout the thesis have already been presented at conferences, more specifically at the 8th International Conference on Aluminium Alloys (ICAA8) and the 13th International Conference on Textures of Materials (ICOTOM13), and are published in the respective proceedings. The full references are found in Chapter 7, Sjølstad et al. (2002), Sjølstad et al. (2002b) and Tangen et al. (2002).

2. Theoretical background

2.1 Introduction

Processing of aluminium alloys normally consists of mechanical working operations designed to optimise the processing procedure, where the main objective is how the final structure of the material could be reached in the fastest and most inexpensive way. The most important material parameters are usually the yield flow stress and the ductility of the final product. A typical processing route of non-heat treatable (NHT) aluminium alloys is shown schematically in figure 2.1, where the most important steps are:

i) Heating to and holding time at homogenisation temperature.
ii) Breakdown rolling in a reversal hot rolling mill.
iii) Multistand tandem rolling with typical 2-6 stands on a row.
iv) Cooling sequence and coiling of the material, which after hot rolling has reached a typical thickness of 2.5-5 mm.
v) Cold rolling to the final thickness, including inter-annealing(s) if required.
vi) Final annealing treatment to obtain the desired ductility and strength.

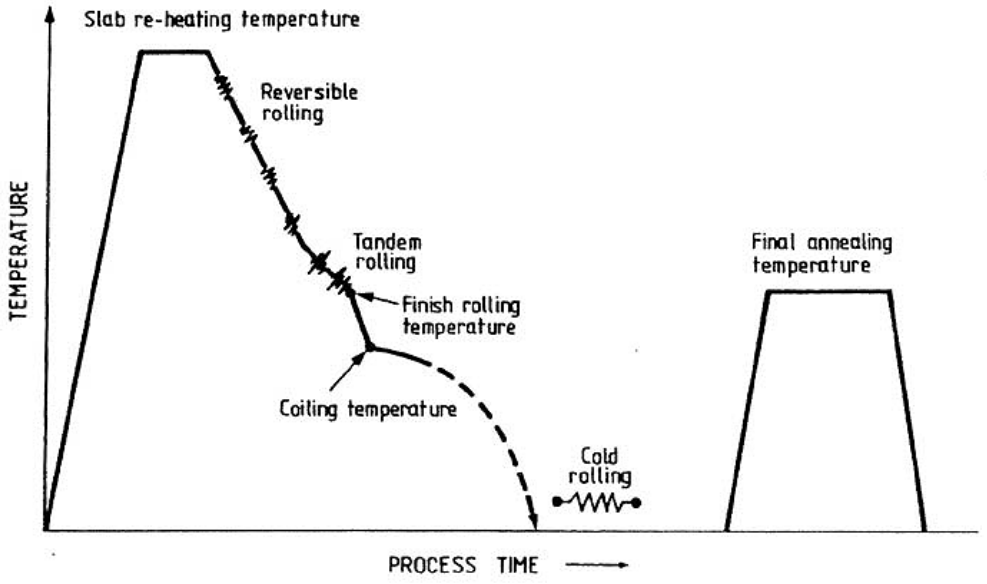

Fig.2.1: Typical rolling and annealing schedule of NHT alloys [Nes and Hutchinson (1989)].

In the following the microstructural evolution during deformation and annealing will be discussed in some detail. This chapter is divided into three main parts where the first considers the development during cold deformation. The second part concerns the microstructural evolution during annealing, here the recrystallisation process is considered in great detail. The third and final part is concerning microstructural modelling during deformation and during the subsequent annealing treatment.

2.2 Cold deformation

To be able to predict the final microstructure and texture of the material one needs to know what happen in each processing step before the final annealing treatment. By deforming a material most of the energy introduced results in heat generation, but some of the energy is also stored within the material as single dislocations and dislocation arrangements. This increases the stored energy and consequently the driving pressure for reactions like recrystallisation, precipitation and phase transformation. During deformation several microstructural phenomena occurs and the most common will be described in the following.

A typical stress-strain curve is usually divided into four stages, for illustration see Fig.2.2. Stage I is not seen when deforming a polycrystal, stage II is the elastic range where Hook's law is valid, stage III is the curved part and finally stage IV refers to the part where the stress increases linearly with strain.

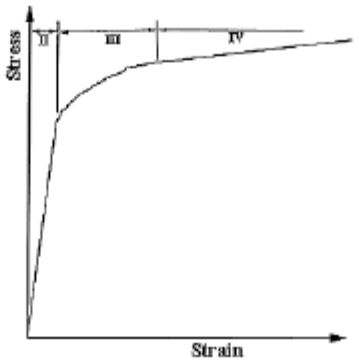

Fig.2.2: Schematic illustration of a stress-strain curve deformed at low-medium temperature. The different characteristic stages of deformation are shown.

2.2.1 Deformation heterogeneities

Slipbands/microbands represent an intrinsic slip mode, which dominates the substructure evolution at low to intermediate strains. They are crystallographic in nature and accordingly form on {111} slip planes in FCC-metals. Since these heterogeneities are associated with a small misorientation to the surrounding matrix (~1°) they are of no significance as nucleation sites for recrystallisation. In aluminium alloys with a high content of elements in solid solution the

dislocation storage capacity increases substantially, and in such alloys microbanding becomes the typical slip mode. The formation of double walled microbands is a result of destabilisation of the statistically stored dislocation within the cell boundary [Washburn and Murty (1967)].

Shear banding is an instability phenomenon that occurs when the dislocation density saturates. At this stage the material becomes unstable with respect to shear and shear banding becomes the alternative slip mode which accommodates the further straining during stage IV hardening. The strain accommodation is strongly localised, resulting in bands with large local strains, fine substructures of cells/subgrains that are extended in the band direction and large misorientations (10-40°) with respect to the surroundings [Hatherly (1978)]. The material within the heterogeneity is softer than the surrounding matrix. Shear bands are non-crystallographic and macroscopic, and are often found with an orientation relationship of 35° to the deforming plane.

Lamellar structure seems essential for the shear band formation. Further, for a band to initiate it is necessary that the plastic work required for the heterogeneous deformation is not larger than for homogeneous deformation from the start of deformation. The formation of shear bands will be largely influenced by the stacking fault energy and for aluminium, which have a rather high stacking fault energy, shear banding is less frequent and the critical rolling reduction for the onset of shear banding becomes higher. A hot rolled material will not so easily exhaust its storage capacity of dislocations due to dynamic recovery. The recovery process will also prevent the evolution of layered dislocation structures that seems to be a necessity for the formation of shear bands, and with that shear banding is suppressed.

Transition bands. During deformation of a polycrystalline material the individual crystals rotate towards stable end orientations. It might happen that single grains splits into two or more parts that take various deformation paths and rotate towards different stable and energetically equivalent end orientations. In the region between the different parts of the grains, sharp orientation gradients will bridge the neighbouring texture components. Dillamore and Katoh (1974) suggested that as transition bands develops the cube orientation should be located

in the centre of the bands. When nucleation of recrystallisation occurs within a transition band the cube might grow out of the band and into the deformed areas surrounding the transition band.

Deformation zones are gradually being built up around the hard non-deformable particles during deformation. These zones are associated with a decrease in subgrain size towards the particle surface and large orientation gradients of up to 30° are usually observed [Humphreys (1977, 1979)]. The microstructure and the size of the deformation zones are determined by the applied strain, temperature and particle size, but factors like particle shape and interphase strength have also been found to have some influence. The dislocations which accumulates at the particles are a result of the incompatibility between the plastically deforming matrix and the non-deforming particle, and the nature of the dislocation structure depends on how the resulting stresses are relieved by plastic relaxation [Ashby (1971)]. Stress relaxation at small particles and after small reductions is normally associated with the generation of prismatic loops. For larger particles (d_p>0.1 μm) the relaxation also includes local lattice rotation. Under an idealised condition of single slip on a particular slip-system the rotation axis should be a <112>-axis which is perpendicular to both the slip-plane normal and the slip-direction (Burgers vector). This has been confirmed experimentally by the work of Humphreys (1979) on moderately deformed single crystals oriented for single slip.

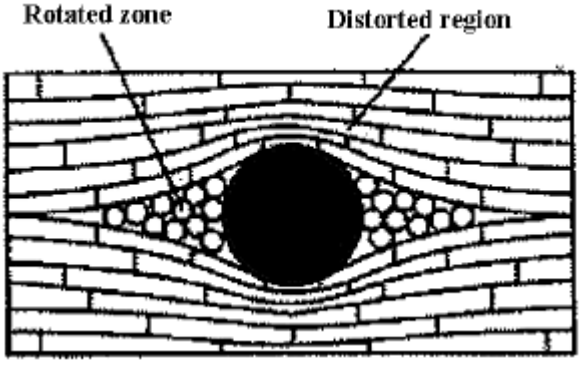

Fig.2.3: Schematic illustration of a deformation zone around a particle. After Humphreys and Hatherly (1995).

Humphreys (1977) stated that during low temperature deformation the energy stored in the deformation zone is relatively large. With respect to recrystallisation the critical step in particle stimulated nucleation of recrystallisation (PSN) during the subsequent annealing is *not* the subgrain growth within the deformation zone, but rather the growth out of the deformation zone.

Old grain boundaries are heterogeneities already present in the microstructure before deformation takes place. Like the particles the grain boundaries constitute obstacles for dislocation movement, resulting in a sharpening of the lattice rotation and a refinement of the microstructure close to the boundaries [Leffers (1981)]. Small subgrain sizes and large misorientations are associated with high stored energy and misorientation advantage, *i.e.* old grain boundaries are favoured sites for nucleation of recrystallisation by strain induced boundary migration (SIMB).

2.2.2 Global Description of the substructure development

Although the deformed microstructure have been a topic for detailed investigations for decades still much work is needed to obtain the complete understanding of the phenomena taking place. The most commonly used parameters for describing the global deformed microstructure are the dislocation density within the subgrains (r_i), the subgrain size (d) and the misorientation across subgrain boundaries (j). Further, each grain rotates towards particular orientations during the deformation.

Interior dislocation density (r_i): Quantitative information of the interior dislocation densities within the subgrains is very limited in the literature except for materials after low reductions. In these latter cases the principle of similitude is found to be obeyed, *i.e.* $d \cdot \sqrt{r_i} = \text{constant}$. For cold rolled materials it is reasonable to assume that the ratio between the number of interior dislocation and those found in the substructure will decrease with strain. This means that the principle of similitude can only be applied up to a certain deformation.

Nord-Varhaug *et al*. (2000) have measured the dislocation density and subgrain size of a variety of Al-alloys and deformation modes. After cold deformation to strains larger than 0.2 they observed that the dislocation density converged towards a saturation density, see Fig.2.4. Bardal *et al*. (1995) have measured the interior dislocation density of hot plane strain compressed (PSC) AA3004 aluminium alloy. They found that only about 10% of the stored energy were due to the interior dislocation density, the rest were due to the subgrain boundaries.

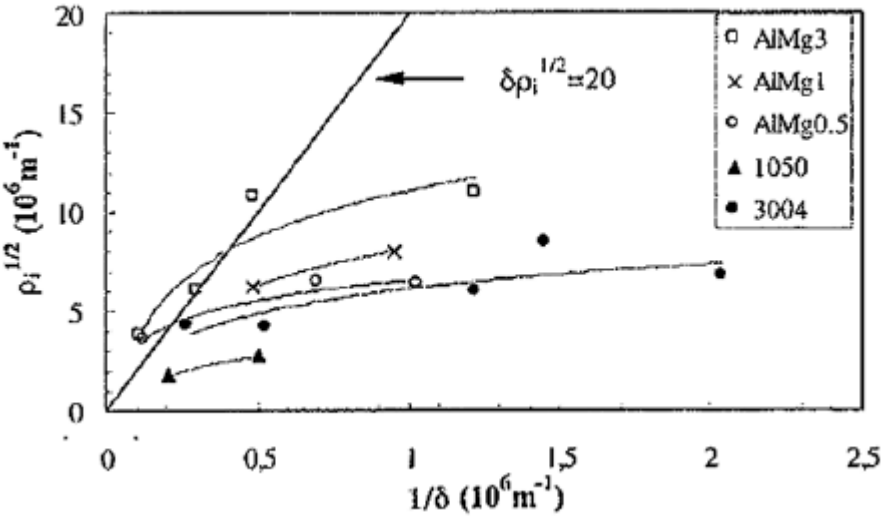

Fig.2.4: Interior dislocation density in the square ($r_i^{1/2}$) *vs.* inverse subgrain size (1/*d*) for different alloys after cold deformation [Nord-Varhaug (2000)].

Cell/subgrain size (*d*). For cubic metals there are two basic mechanisms of deformation, these are slip and twinning and the choice of mechanism is dependent on the stacking fault energy. In low stacking fault energy metals the lack of adequate cross slip results in a rather diffuse cell structure. For high stacking fault energy materials, like aluminium, a well-developed microstructure consisting of cell/subgrain is created.

At strains typically below 0.2 a uniform structure of equiaxed cells are formed. For intermediate strains, *i.e*. in stadium III of the stress-strain curve (Fig.2.2), deformation occurs by multiple slip. The homogenous distribution of dislocations becomes heterogeneous and the cell walls become sharper. The originally equiaxed cells starts to elongate in the direction of deformation and the microstructure becomes more inhomogeneous. At large strains the microstructure

once again appears uniform, where all cells have collapsed into well-defined subgrain boundaries with a given misorientation, and the microstructure consists of pancake shaped grains.

Gil Sevillano *et al.* (1980) have demonstrated that the variation of average cell/subgrain size with increasing strain seems to be common for a wide range of metals, and it is independent of the deformation mode, see Fig.2.5. Comparison of the subgrain size with the macroscopic shape change demonstrated that two regimes could be observed. At small strains the cell size decrease rapidly, indicating that the refinement of the microstructure is mainly due to the formation of new cells. This means that the newly formed dislocations are not stored in the already existing cell boundaries. At higher strains the macroscopic change is faster than the reduction in subgrain size, which is believed to be due to annihilation of cell walls. No saturation point in subgrain size was seen, and it is interesting to note that the inverse subgrain size varies linearly with increasing strain in stage IV of the stress-strain curve. The broken line in Fig 2.5 illustrates this, where the variation in subgrain size follows the relation:

$$d(e) = \frac{d_{e=1.5}}{\left(\frac{2}{3} + \frac{2}{9}e\right)} \qquad (2.1)$$

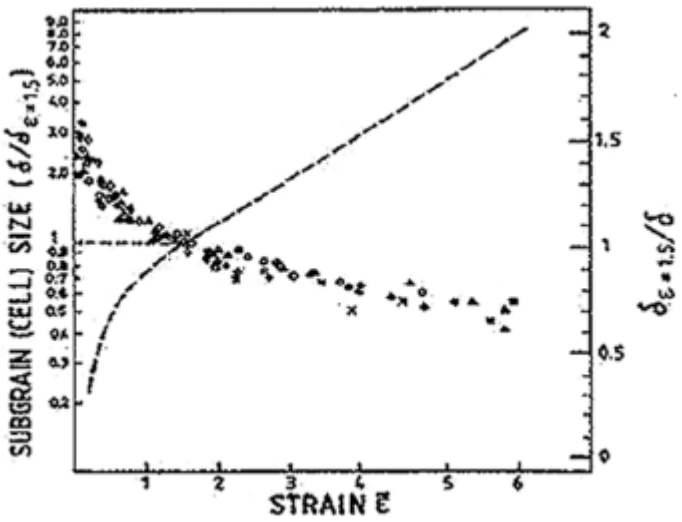

Fig.2.5: Average cell/subgrain size as a function of strain for different alloys. The size is normalised to the value observed at e=1.5 [Gil Sevillano *et al.* (1980)].

Misorientation (j). Extensive work on the misorientation across subgrain boundaries have been carried out during the last decade due to the development of the automatic electron backscatter diffraction (EBSD) technique in scanning electron microscope (SEM). Furu *et al.* (1995) compiled the available data on aluminium deformed to a variety of strains and found that the misorientation increased rapidly with strain and saturated at approximately 3° after a strain of about one, see Fig.2.6.

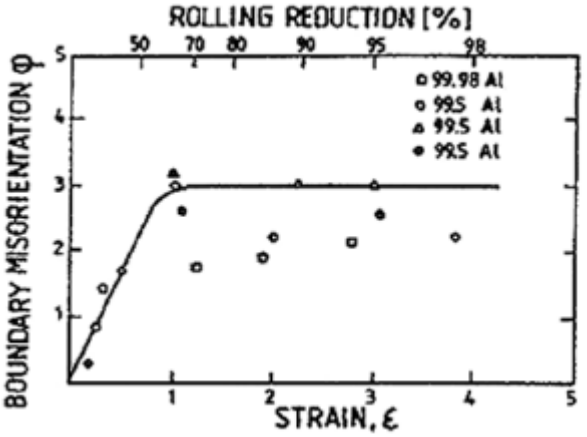

Fig.2.6: Average misorientation across subgrain boundaries as a function of rolling strain in aluminium [Furu *et al.* (1995)].

Stored energy (P_D) is introduced during deformation and is providing the driving force for recovery and recrystallisation. Almost all the stored energy is derived from the accumulation of dislocations and the essential difference between the deformed and the annealed condition lies in the dislocation content and arrangement. As a result the stored energy can be described as a function of the dislocation density in the interior of the subgrains (r_i), the subgrain size (d) and boundary energy (g_{sb}):

$$P_D = r_i \frac{Gb^2}{2} + k \frac{g_{sb}}{d} \qquad (2.2)$$

where G is the shear modulus, b is the Burgers vector and k is a geometrical constant in the order of three for an equiaxed substructure and g_{sb} is the stored energy defined by the misorientation across the subgrain boundaries.

The stored energy is calculated using the boundary energy of a tilt boundary, *i.e.* the Read Shockley relation:

$$\gamma_{sb} = \frac{Gb\theta}{4\pi(1-\nu)} \ln\left(\frac{e\theta_c}{\theta}\right) \qquad (2.3)$$

where θ is the boundary misorientation, θ_c is the critical misorientation separating between what is a high angle grain boundary and a low angle grain boundary and ν is the Poisson ratio.

2.2.3 Cold rolling textures

During plastic deformation of a polycrystal, each grain is subjected to stresses and strains as a consequence of the deformation process, and as a result the grain changes its shape and orientation. The mechanism of plastic deformation is dislocation-induced slip. This does not produce lattice rotation by itself, it is rather the accommodation of the new grain to its surroundings, which causes the change in orientation. It is well known that slip of FCC-metals occurs on the {111}<110>- slip-systems when the deformation is performed in the low to ambient temperature regime. At higher deformation temperatures Maurice and Driver (1993) clearly demonstrated that slip also occurs on other slip-systems close to the planes of maximum shear stress, *i.e.* on the {211}-planes.

Several models have been developed to simulate the texture evolution during deformation and short summaries of the most classical models by Sachs and Taylor are given below.

Sachs (1928) proposed the oldest texture model on deformed polycrystalline materials. In the original Sachs model, the stress in each grain is set equal to the macroscopic stress, and each grain deforms independently of its neighbours. The strain and change in orientation as given by geometrical restrictions are determined as for a free single crystal exposed to a stress. It is assumed that slip only takes place on those slip systems where the resolved shear stress is equal to the critical resolved shear stress, τ_{CRSS}. This model works well at very small strains, while its predictions break down when applying higher deformations

because it loses its compatibility in strain and pores forms between the different grains. The Sachs model is for this reason often called a “lower bound” model.

Taylor (1938) proposed a model, which addressed the strain during deformation and neglected the external stress. The Taylor model is based on three general assumptions: (i) Each crystallite is exposed to a strain equal to the external strain. (ii) The plastic deformation occurs by means of polyslip. (iii) The symmetric part of the strain tensor together with the law of the conservation of volume, give five linearly independent equations. The strain is then described by five independent slip systems. In the selection of the five slip systems the criterion of minimum internal work applies. The Taylor theory fulfils the requirement for compatibility in strain, but violates the criteria of stress equilibrium.

Several attempts have been made to modify these models and in order to improve the agreement between measured and calculated textures. Among these we find the Taylor Relaxed constraints models (Lath and pancake), where shear is relaxed in one plane (Lath) or in two planes for the pancake-model. The Self-Consistent models try to obtain compatibility in both strain and stress over the grain boundaries.

At time being no model is able to predict the deformation and texture evolution during deformation in a completely correct manner. The grain interaction model (GIA-model) uses a stack of grains in three directions and all possible shears are relaxed along the internal boundaries of the stack. Additional assumptions are made to accommodate for difficulties in maintaining strain compatibility inside the stack. According to a comparison of different models, done by Crumbach *et al.* (2002), the GIA-model, being continuously improved by the Aachen-group, gave the best prediction. In Fig.2.7 an experimental b-fibre plot of a 70% cold rolled AA5182 is compared with some models and here as well the GIA-model gave the best predictions (unpublished work by Crumbach).

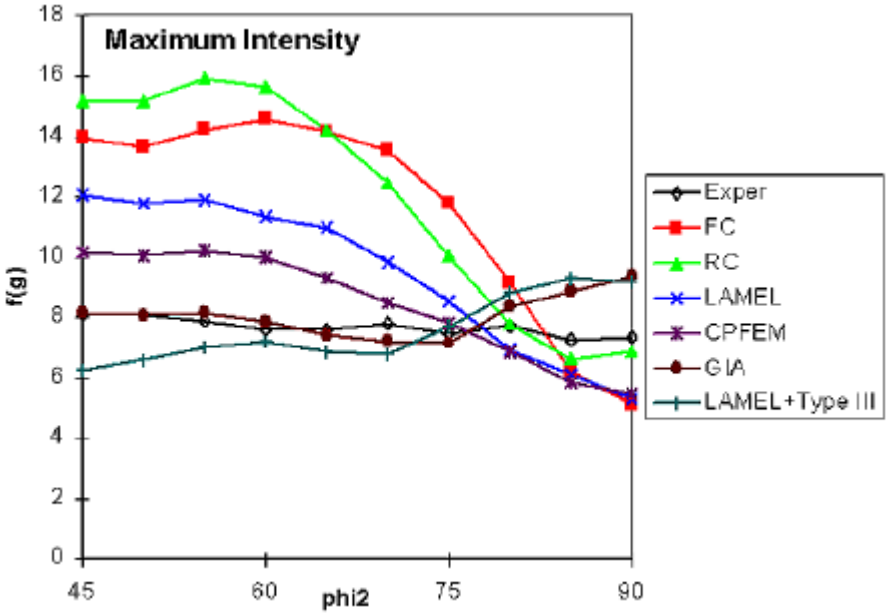

Fig.2.7: Comparison of an experimental b-fibre plot of a 70% cold rolled AA5182 with some model predictions. Courtesy of Crumbach.

Al-alloys exhibit rolling textures, which qualitatively look similar to each other. However quantitatively they differ depending on the starting texture, rolling reduction, deformation temperature and the alloy composition. Two different fibres are commonly observed for cold rolled aluminium-alloys:

- The a-fibre which runs from the Goss-orientation [{011}<100>] to the Brass-orientation (Bs) [{110}<112>]. This fibre is located in the j_2=0°-section and along the F=45° line of an ODF.
- The b-fibre starts in the Bs-orientation, passing through the S-orientation (S) [{123}<634>] and ends at the Copper-orientation (Cu) [{112}<111>].

Both fibres are described by rotations about two different <110>-axis. The a-fibre has a rotation axis parallel to normal direction (ND), and the b-fibre rotation axis has a 60° tilt from ND towards the rolling direction (RD) [Hirsch and Lücke (1988)]. At higher strains the a-fibre deteriorates to a single peak at the Bs-orientation, and the b-fibre continues to grow in strength as the reduction increases. At high reductions (>95%) peaks at certain orientations are developed as the b-fibre deteriorates. A schematic illustration of where the different orientations are localised in Euler space is shown in Fig.2.8.

Experimental results on single crystals have shown that the Bs- and Goss-orientations produce more homogeneous microstructures with lower misorientation angles compared to Cu-oriented crystals, due to their low Taylor factors and symmetrical double slip. The latter orientation develops heterogeneous microstructures with larger misorientations. A more detailed description and discussion are given in the paper Driver (1995). These observations have recently been supported by Godfrey *et al.* (2001). They investigated deformed single crystals of pure aluminium by scanning electron microscopy (SEM) and transmission electron microscopy (TEM). They found the scatter in misorientation after deformation to a strain of 1.5 to be significantly smaller for a Bs-oriented single crystal compared to S- and Cu-oriented singe crystals.

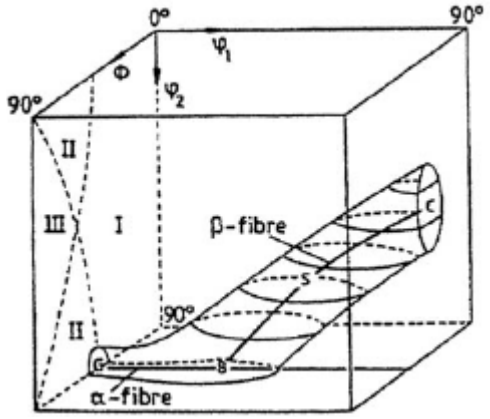

Fig.2.8: Schematic plot of a typical deformation texture in the Euler space.

2.3 Annealing behaviour of deformed material

During annealing of a deformed material several phenomena can occur, the most common are recovery, recrystallisation and precipitation. Recovery involves dislocation annihilation, rearrangement of dislocations into more stable configurations and subgrain growth. During recrystallisation new strain free grains grow into the deformed matrix, while precipitation involves formation of dispersoids that retards the other two mechanisms. More details are given in the following subchapters.

2.3.1 Precipitation

Precipitation is like other reactions controlled by the thermodynamics, where the microstructural changes are driven by the concept of free energy minimisation. In most cases the material is in a metastable condition, and for this reason it needs some activation energy before reaching a new metastable state or the final stable state.

Decomposition of a supersaturated solid solution (a) is associated with the nucleation and growth of a precipitate (b). The interface (a/b) between the precipitate and the matrix determines the further growth progress. If the interface is incoherent, *i.e.* a phase boundary separating the matrix and the particle, the growth is determined both by the diffusion of atoms into the boundary and the jump frequency across the boundary. If diffusion is fast then the growth is interface controlled, but if diffusion is slow it is diffusion controlled and the area around the precipitate will be depleted of alloying elements.

Fully coherent interfaces usually have considerably lower mobility than incoherent interfaces, and the growth of such a precipitate is determined by the normal lattice diffusion. The same situation arises regarding semicoherent interfaces provided that the misfit dislocations can climb by vacancy creation or annihilation. If the different phases have different crystal lattice structures the growth rate can even accelerate if the growth happens by the so-called ledge mechanism.

Nucleation is in almost every case occurring heterogeneously, *i.e.* at grain- or phase boundaries, dislocations, stacking faults or at clusters of vacancies. These are natural places because these sites are associated with a higher average free energy than in the metal matrix. When a nucleus forms it replaces a part of *e.g.* a boundary and this is associated with a reduction in free energy. The normal segregation of solute atoms to grain boundaries and dislocations also favours the formation of an appropriate group of atoms which constitutes a nucleus, and finally the diffusion is faster in the vicinity of these defects [Martin *et al.* (1997)].

The Zener drag is a retarding force from a dispersion of small precipitates/dispersoids exerted upon a moving boundary. As a consequence of these precipitates the processes of recovery and recrystallisation is retarded. Sometimes the density of these precipitates is so high that the softening reactions are temporary stagnated, then the restoration of the deformed microstructure occurs by extended recovery. This mechanism is also called *in-situ* recrystallisation or continuous recrystallisation, and is controlled by Ostwald ripening, *i.e.* coarsening of the dispersoids/secondary particles.

In Fig.2.9 the forces acting upon the moving boundary are shown when interacting with an obstacle, in this case a dispersoid or particle. The maximum retarding force of a particle is reached when the angle between the moving boundary and the particle is 45° and are given by:

$$F_z = prg \qquad (2.4)$$

where r is the radius of the particle and g is the interaction energy between the growing boundary and the particle. Ashby (1969) has shown that a coherent particle is twice as effective in pinning a boundary as an incoherent particle of the same size.

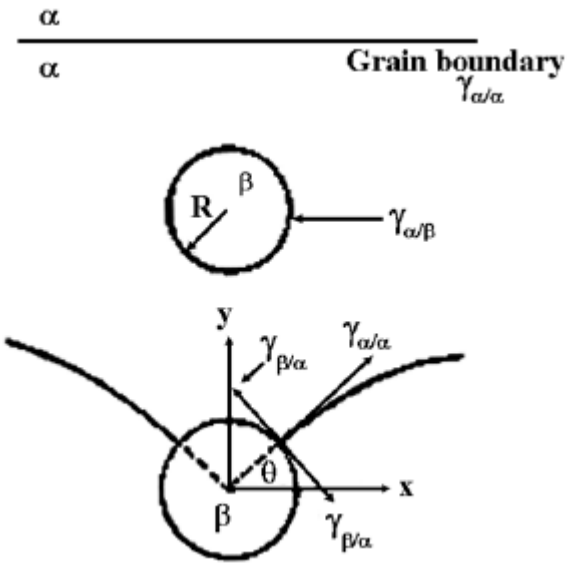

Fig.2.9: Schematically illustration of the interaction between a moving grain boundary and a spherical particle. It is seen that the assumption of equilibrium surface tension between the grain boundary and the obstacle is fulfilled.

Calculating the retarding force from a distribution of particles is a far more complicated problem. The number of particles per unit volume (N_v) of a material with a volume fraction (f_r) of randomly distributed spherical particles of a given radius (r) is given as:

$$N_v = \frac{3 f_r}{4 p r^3} \tag{2.5}$$

Assuming that the boundary is planar within a distance r on either side of the boundary the number of intersecting particles per unit area (N_s) is then:

$$N_s = 2 r N_v = \frac{3 f_r}{2 p r^2} \tag{2.6}$$

The total Zener drag can be calculated by combining this equation with the equation of the maximum force (2.4):

$$P_z = N_s \cdot F_z = \frac{3 f_r g}{2 r} \tag{2.7}$$

This latter equation (2.7) is widely used despite the non-rigorous approach to the problem. A large weakness of the original proposition is the assumption of a rigid boundary, as the calculation in fact would give a zero drag force. The particles/dispersoids are only retarding the processes if the boundary is able to bend and change its shape as it moves. Further the assumption of a random distribution is not always fulfilled. In can-stock material the pinning precipitates are often found in layers parallel to the sheet surface, and the result of this is a higher retarding force in the normal direction to these layers, and this anisotropy will be reflected in the shape of the grains or subgrains of the material.

A review of different modifications of the classical Zener theory was carried out by Nes *et al.* (1985), and they stated that all the refinements would actually give results close to Zener's estimate.

2.3.2 Effect of alloying elements

Manganese: According to Haan *et al.* (1996) as much as 1wt% of manganese can retain in solid solution after casting due to the low diffusivity of the Mn-atoms even at 600°C ($D \propto 10^{-11}$ mm^2/s). The phases forming during solidification and subsequent processing are the equilibrium phase Al_6Mn. If iron is present in the alloy Al_6(Mn,Fe)-particles are found and if the silicon-content exceeds 0.07wt% Al_{12}(Mn,Fe)Si-particles are formed. Iron has also been known to decrease the solubility of manganese, and by addition of iron the primary particles becomes more widely spaced and distributed more inhomogeneously. During homogenisation at low temperatures a high dispersion of small precipitates is formed. At high temperatures some precipitates are allowed to coarsen while other are dissolved, resulting in a widely spaced distribution of coarse particles/precipitates. In the work by Haan *et al.* (1996) on a binary AlMn alloy it was found that the precipitation rate attains its maximum at 490°C, below this temperature the growth is the limiting factor. At higher temperatures the nucleation of new precipitates is limiting the decrease of Mn in supersaturated solid solution. A work on a commercial AA3003-alloy by Li and Arnberg (2002) have demonstrated that during homogenisation the precipitation of manganese containing dispersoids starts at a temperature of 300°C and reaches a maximum precipitation rate at about 400°C.

Trømborg *et al.* (1992) have shown for two different AA3003-alloys and one AA3004-alloy that the $Al_6(Mn,Fe)$-particles formed during casting, were to some extent peritectically transformed into α-$Al_{15}(Mn,Fe)_3Si_{1-2}$ when being homogenised at 563°C and 585°C. The degree of transformation was dependent on the excess amount of Si and Fe, where the AA3003 with the lowest Fe- and highest Si contents gave most transformation compared to the other alloys.

Alexander and Greer (2002) observed no diffusion gradient of silicon over the matrix/particles interface of an Al1Mn0.5Fe0.2Si-alloy. On the basis of this observation they concluded that the lack of gradient was due to diffusion along the grain boundaries. Al-spots were formed within the particles during the phase-transformation from $Al_6(Mn,Fe)$ into α-Al(Mn,Fe)Si. According to Alexander and Greer (2002) this was due to the excess aluminium generated during the phase-transformation. These spots were usually observed in the centre of the α-particles or at the interface between the transforming $Al_6(Mn,Fe)$ and α-phase.

Hausch *et al.* (1978) have shown that alloying a binary Al1Mn-alloy with an increasing amount of Si increases the precipitation rate and retards the recrystallisation rate. This have later been supported by the work of Vörös and Kovacs (1990), who have shown by resistivity measurements that the effect of alloying a binary AlMn-alloy with both iron and silicon increases the precipitation rate and amount of precipitates compared to the binary alloy.

In several works, *e.g.* Alexander and Greer (2002) and Watanabe *et al.* (1984), it was observed that the concentration ratio of Fe/Mn decreases with increasing holding time at the homogenisation temperature. This indicates that the supersaturation of manganese in solid solution diffuses into the α-particles during the entire homogenisation treatment. Non-uniform distributions of Mn and Fe across the particles were found, where the manganese was located at the phase boundaries and the iron was found in the centre of the α-particles.

Iron: The effect of iron in solid solution of a commercially pure aluminium alloy was investigated by Furu *et al.* (1995). They performed two different homogenisation treatments to get different amounts of iron in solid solution,

these concentrations were found to be 0.01wt% and 0.02wt%. This rather small difference in iron content in solid solution had a dramatic effect on the softening response. The softening of the 0.02wt% material was shifted towards significantly longer annealing times, more specifically an order of magnitude longer times was needed to reach the same hardness as of the 0.01wt% material. At lower annealing temperatures the effect was even stronger on the recovery part of the softening. By investigating two different AlFe-alloys Ito *et al.* (1976) found the cube orientation to dominate the recrystallisation texture if a low supersaturation of iron was present prior to recrystallisation. In the opposite condition the R-oriented grains dominated the final microstructure. Constituent iron bearing particles are known to increase the rate of recrystallisation due to the formation of nuclei within the deformation zones (PSN).

Silicon has a small effect on the softening behaviour, both in supersaturated solid solution and as precipitates, but in combination with iron the effect has an influence. Silicon increases the rate of particle formation during heat-treatment, the particles become larger and thus the number of available nucleation sites for recrystallisation by PSN increases.

2.3.3 Recovery of the deformed material

Materials are often annealed after deformation in order to achieve proper formability properties for the subsequent forming processes. Softening occurs in the beginning by dislocation annihilation and subgrain growth, before recrystallisation starts to progress. Before considering recovery in more detail, it should be noted that recovery and recrystallisation are competing processes as both are driven by the stored energy. If a significant amount of recovery occurs prior to recrystallisation it might make an influence on the recrystallisation kinetics due to the lowering of stored energy. It is often difficult to make a division between recovery and the early stages of recrystallisation because recovery, by subgrain growth, plays an important role in the nucleation of recrystallisation.

Recovery results in rather small changes of the microstructure, and is usually divided into two stages, annealing out of statistically stored dislocations and a subsequent subgrain growth stage. In heavy cold worked commercial purity aluminium it is assumed that the rate of recovery is controlled by subgrain growth. The magnitude of the recovery contribution to the softening reaction, *i.e.* the flow stress, is dependent on the rate of recovery compared to the nucleation and growth rate of recrystallised grains. For aluminium a substantial proportion of the stored energy can be consumed by recovery, while for other materials like copper, recovery play no role in the softening process, see Fig.2.10. The difference in these curves is due to the difference in stacking fault energy (g_{SFE}). Climb is the rate controlling mechanism of recovery and for metals with low g_{SFE} like copper climb is difficult, while for metals with high g_{SFE} climb is much easier and extensive recovery can occur.

Dislocation migration in the early stages of annealing lowers the stored energy of the system, and this occurs by two processes, annihilation of dislocations with Burgers vector of opposite direction and rearrangement into subgrain boundaries. Both processes are achieved by climb, glide and cross-slip of dislocations. As climb requires thermal activation, this can only occur at high temperatures, a similar configuration of screw dislocations would recover by annihilation of dislocations by cross-slip. This latter process occurs at lower temperatures in materials with high γ_{SFE}. During deformation an unequal number of dislocations of opposite sign are produced, and these excess dislocations will rearrange into more stable low angle grain boundaries upon annealing. The energy of a tilt boundary increases with misorientation, but the energy per dislocation decreases with increasing misorientation, *i.e.* there is a driving force to form fewer and more misoriented boundaries. An alternative mechanism to subgrain growth is coalescence where two neighbouring subgrains rotates into the same configuration, but this is only an operating mechanism after small deformations.

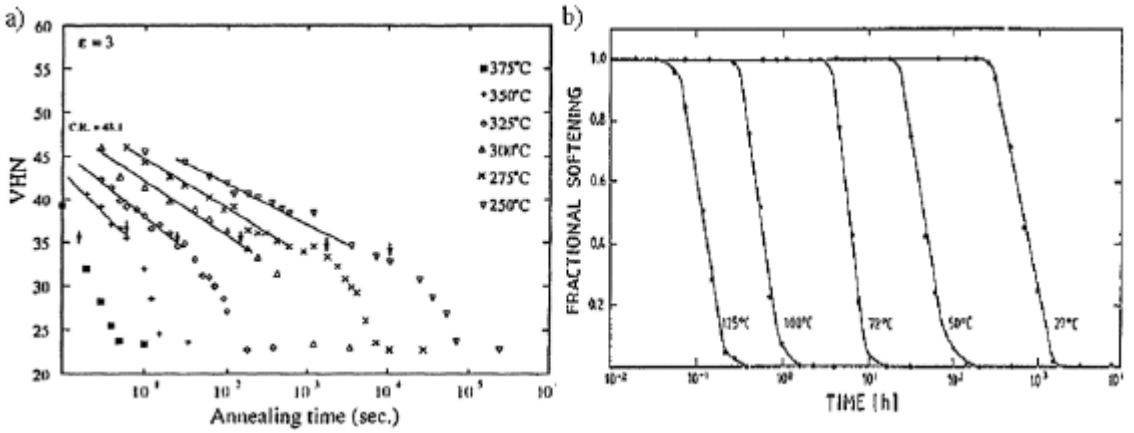

Fig.2.10: Softening behaviour of isothermally annealed a) commercial pure aluminium after a cold rolling strain of 3.0 [Furu *et al.* (1995)], and b) 99.95% pure copper after rolling strain of 3.7 [Cook and Richards (1946)].

The increase in subgrain size upon annealing has often been reported to follow the growth law in equation (2.8), where d_0^n is the subgrain size in the as deformed condition.

$$d^n = d_0^n + kt \qquad (2.8)$$

Large amounts of work have been done to determine the growth exponent (n) during the last decades. Varma *et al.* (1984, 1986, 1988) have repeatedly reported a n-value of 2, but Furu *et al.* (1995) have analysed their own results and a work by Sandstrøm *et al.* (1978) and found that a value of n=4 gives a better fit to the experimental results. A recent work by Abtahi *et al.* (2001) have determined the growth exponent of the experimental work by Ferry and Humphreys (1996) and Humphreys and Huang (2000). These works studied a deformed Al0.05Si with Goss orientation, where the subgrain growth at different temperatures was closely followed. Abtahi *et al.* (2001) found the growth exponent to vary between from 2.6 at a high annealing temperature (400°C) towards 5.5 at a low annealing temperature (250°C).

The subgrain growth may occur by two mechanisms, [i)] growth of large subgrains on expense of the smaller once in similar manner to conventional grain growth, or [ii)] subgrain coalescence, first proposed by Hu (1962), where neighbouring subgrains rotate into one subgrain by a boundary diffusion process. This latter

mechanism is only of importance after small deformations and at low annealing temperatures.

In a paper by Huang and Humphreys (2000) on a Goss oriented single crystal the mean misorientation was found to decrease slightly as the subgrains were growing at a variety of temperatures. This is the opposite observation to what Furu (1992) observed for commercial pure aluminium.

2.3.4 Recrystallisation

There has been an ongoing discussion focusing on two rival theories on the nucleation and growth of recrystallisation over more than half a century, these are the oriented nucleation theory and the oriented growth theory.

Oriented nucleation implies that the recrystallisation texture is determined by the orientations of the available nuclei. For metals and alloys with a high stacking fault energy (g_{SFE}), such as aluminium, these nuclei must be a part of the deformed microstructure. The original oriented nucleation theory was first proposed by Dehlinger (1928) and Burgers and Louwerse (1931) and later modified by Doherty (1985). The concept is based on the following: Grains with an orientation that dominates the fully recrystallised texture nucleate more frequently then grains of other orientations. Quantitatively the fraction of grains (a_{tex}) within a selected misorientation from the exact orientation, must be normalised by the fraction in a random structured material (a_{ran}). The condition for a strong oriented nucleation is that $a = a_{tex}/a_{ran} >> 1$.

The work by Dillamore and Katoh (1974) on a polycrystalline iron subjected to uniaxial compression showed that a transition band would form when rotating paths of neighbouring volumes diverges. This band would act as a favourable site for nucleation and growth of recrystallised grains, and they predicted that the cube orientation ought to be found within these bands. The supporters of the oriented growth theory have claimed that this proved that all nuclei are being present in the as deformed microstructure.

Barret (1940) did the original proposal of the **oriented growth** theory, and the idea of this theory has later been further developed by *e.g.* Lücke (1984) and Hu (1986). The oriented growth theory assumes a formation of a broad spectrum of nucleus orientations, where the nuclei with the best growth conditions with respect to the deformed microstructure will determine the recrystallisation texture. The oriented growth factor (*b*) is determined by the relative size of the given texture to the average grains. There is an oriented growth effect if $b = d_{tex}/d_{ran} >> 1$.

At present it is widely accepted that a discussion based on either of these concepts fails to interpret all the effects observed. Recrystallisation textures are therefore most probably determined by a combination of both mechanisms.

Recrystallisation kinetics is most often modelled by making use of the classical JMAK-equation [Johnson and Mehl (1939), Avrami (1939), Kolmogorov (1937)], where the fraction recrystallised is given by:

$$X_v(t) = 1 - \exp(-k \cdot t^n) \qquad (2.9)$$

where k is a constant and n is the growth- or Avrami exponent. This model, in its original form, is based on constant growth rate, isotropically growth in three dimensions and a random distribution of nucleation sites.

According to this theory, n is equal to 3 in case of site saturation nucleation kinetics, and equal to 4 if a constant nucleation rate is applied. Typically measured n-values for recrystallisation of Al-alloys is scattered around 2 [Daaland (1993)]. These lower values are probably caused by a variety of reasons, such as:

- Heterogeneous nucleation *i.e.* preferential nucleation points, such as $\Sigma 7$ boundaries and large particles that may be non-randomly distributed.
- Retardation of the growth rate due to concurrent recovery lowers the driving force for grain boundary mobility. This happens only at low annealing temperatures, at higher temperatures no or very little recovery occurs prior to recrystallisation.
- Time-dependant nucleation kinetics.

The general assumption for recrystallisation of aluminium alloys is that all the nuclei are present in the deformed state and that they are growing at a constant growth rate. In order to grow, the nuclei must be both thermodynamically stable and of a certain size. The critical radius in order for a nucleus to form a strain free grain is given by the Gibbs-Thomson relationship:

$$R > R_c = \frac{2g_{GB}}{P} \tag{2.10}$$

where g_{GB} is the specific grain boundary energy and $P=P_D-P_z$ is the stored energy given by the equations (2.2) and (2.7).

The fraction recrystallised is in case of site saturation calculated by the following equation:

$$x(t) = 1 - \exp\left(-\frac{4}{3}pN_{tot}(vt)^3\right) \tag{2.11}$$

where N_{tot} is the total number of nucleation sites and v is the growth rate of the nuclei.

The growth rate of the growing grains can then be derived from the following expression:

$$v = M(P_D - P_z) \tag{2.12}$$

where $M = \frac{M_0}{RT}\exp\left(-\frac{U_{GB}}{RT}\right)$, M_0 is a material constant, U_{GB} is the activation energy for grain boundary mobility, P_D is the driving pressure for recrystallisation and P_z is the Zener drag due to dispersoids.

Nucleation sites. Since the works by Humphreys (1977 and 1979) particle stimulated nucleation of recrystallisation (PSN) has been accepted as an important nucleation mechanism. The nucleation takes place around the largest undeformable particles due to the generation of deformation zones around these during deformation. These works concluded that the critical point was not the subgrain growth within the deformation zone, but rather the growth out of the zone. The subgrain growth within the deformation zone is very rapid due to the

large orientation gradient and the existence of small subgrains. The formation of deformation zones depends on strain rate and deformation temperature. At high temperatures or low strain rates dynamic recovery counteracts the formation of the deformation zones, and hence prevents the occurrence of PSN.

The mathematical expression of the critical particle size (h_c) for successful nucleation is given by:

$$h_c = \frac{4g_{GB}}{P_D - P_z} \tag{2.13}$$

Cube sites are very efficient nucleation sites for recrystallisation due to the subgrain size advantage in the as deformed state. Cube grains are metastable during deformation, and the cube has a 40°<111>-orientation relationship to the dominating S-orientation after deformation and these boundaries are believed to migrate faster than other high angle grain boundaries. The cube-oriented subgrains have a larger size than subgrains of other orientations. This gives the cube-oriented subgrains a growth advantage upon annealing, *i.e.* they reach an over-critical subgrain size prior to other subgrains [Vatne (1995)]. More comments regarding nucleation of the cube is given in the next chapter (2.3.5).

The final nucleation sites are high angle grain boundaries (HAGB) where strain induced boundary migration (SIMB) can take place. This happens due to differences in stored energy on each side of the grain boundary, *i.e.* because of difference in the subgrain size (d) across the boundary. This is basically what also happens for the cube nucleation.

The effect of precipitation upon annealing. If a supersaturated metal is deformed and annealed, recrystallisation will be affected by precipitation unless recrystallisation has completed before precipitation begins. Hornbogen and Köstner (1978) performed a review of these interactions in two supersaturated and deformed Al-alloys. The precipitation will as stated earlier affect both the subgrain-growth and the growth of recrystallised grains. A schematic illustration of the recrystallisation behaviour as a function of time and temperature is given in Fig.2.11. If precipitation were absent, recrystallisation would occur at times

given by the line AC. The line BD shows that the process is slowed down due to concurrent precipitation. The TTT-diagram plays an important role in the interpretation of these reactions, and these are divided into three regions.

Range I is above the solvus temperature (T_1), and no precipitation is possible in this region. In Range II precipitation occurs after recrystallisation is completed, and no retarding effects will be observed. In Range III precipitation occurs before recrystallisation, which results in a postponed start of recrystallisation. The sharp transition between Range II and Range III is only an illustration and is not true for real situations. This is because a certain period of time is required to complete recrystallisation. In the transient period both regions operates simultaneously at different sites in the material.

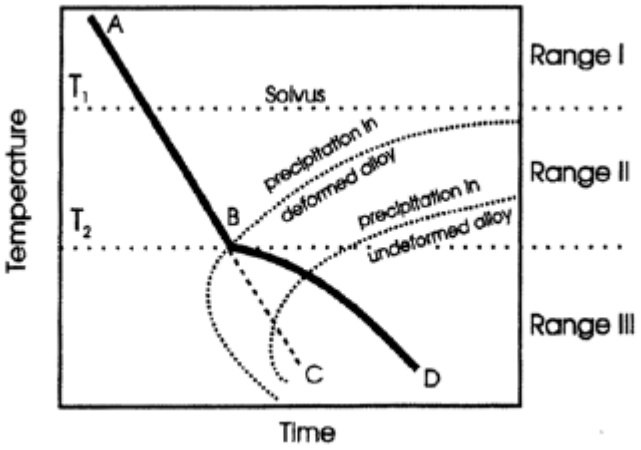

Fig.2.11: Influence of concurrent precipitation on softening kinetics [Hornbogen and Köstner (1978)].

2.3.5 Recrystallisation textures

In the following the most important recrystallisation textures found in Al-alloys subjected to plane strain compression are described. Since all the dominating recrystallisation texture components, except of the R-texture, are found in the j_2=0° section of the ODF the location of these orientations are shown in Fig.2.12.

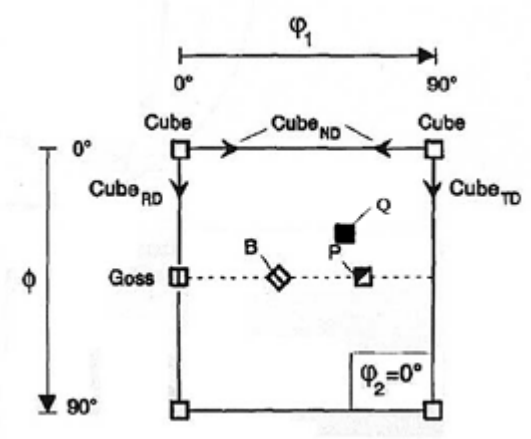

Fig.2.12: Position of different texture components of the j_2=0°-section of an ODF.

The origin of the **Cube-texture** ({001}<100>) has been a topic of debate for years. The prediction of Dillamore and Katoh (1974) suggest that crystallites of cube orientation ought to exist in the deformed state as transition bands separating volumes of major rolling texture components. TEM observations by Vandermeer and McHargue (1964) of FCC metals with medium to high g_{SFE} typically reveal that the cell/subgrain size in regions with <100>-orientations is larger than in other regions. Line-broadening measurements suggest that the <100>-regions are in a state of relatively less stress or strain than other regions. Another nucleation site is cube bands that has retained deformation. The cube orientation has a low Taylor factor, which tends to minimise the total shear strain and consequently lowering the stored dislocation density. During deformation the cube orientation, which is a metastable orientation, is assumed to rotate around the RD-direction and towards the Goss orientation. This is one of the reasons why the cube intensity of the recrystallised material is found to decrease with higher degrees of deformation, *i.e.* less cube grains from the initial state has retained deformation. Another reason is that higher deformation results in an increased stored energy for recrystallisation, which again results in an increased number of nucleating sites, especially PSN-sites. The cube texture has an approximate 40°<111>-relationship to the S-component (Σ7-boundary), and from each S-variant there is one 40°<111>-rotation that yields the cube texture. In an ODF the S-component is often observed to have a lower intensity than the other common rolling components. However due to its low symmetry compared to the Bs- and Cu-orientations, the actual volume fraction of S-oriented grains is still

usually higher than volume fraction of Bs- and Cu-oriented grains. This high volume fraction of S-orientation is part of the reason why the cube texture usually is very strong in rolled and recrystallised Al-alloys. The compromise character of the highly symmetric cube orientation, which can grow into all the four S-variants, further enhances this. The cube oriented subgrains are known to rapidly recover either dynamically during deformation or statically during the first period of annealing, due to the lack of elastic interactions between the orthogonal active slip systems. This gives rise to a considerably size advantage of the cube nuclei (Vatne 1995).

The **ND-rotated cube** ({001}<310>) has an approximate 40°<111> rotation to the Cu-orientation. Daaland *et al.* (1993b) have reported that the ND-rotated cube has a growth rate advantage in case of concurrent precipitation compared to other orientations. This was not an oriented growth effect, but rather that these grains had a shorter incubation time than other orientations, resulting in less precipitation upon these nuclei.

P-texture ({011}<122>), also termed as the ND-rotated Goss texture, has been found in cold rolled and subsequently annealed binary AlCu and in commercial 3xxx- and 5xxx-alloys with a high supersaturation of the alloying elements [Daaland and Nes (1996), Vatne *et al.* (1997), Engler *et al.* (2001)]. The P-orientation has recently been reported in other Al-alloys as well, *e.g.* AA6111, AA8006 and AA8011 [Smith *et al.* (2001), Forbord (1999) and Ryu and Lee (2002)]. This orientation has also, as the ND-rotated cube, an approximate 40°<111> rotation to one of the Cu-orientations. Engler *et al.* (1996, 2001) have reported a preferred occurrence of these components in the deformation zones around large particles causing PSN. They further suggested a preferred growth of these grains in the early stages of annealing (microgrowth selection). Ryu and Lee (2002) have supported this suggestion and they have shown, by TEM-work of an AA8011, that nucleation of the P-orientation take place in the deformation zone around the large $FeAl_3$-particles. As described in the literature [Lücke and Engler (1990)], the recrystallisation texture shifts towards P-, Q- and Goss-component in alloys developing grain scale shear bands during deformation. This occurs in alloys with high solid solution concentration and/or with fine shearable particles after large deformation.

The **Goss** orientation ({110}<001>) is usually present as a minor component in the deformation texture (*a*-fibre). The Goss orientation has a 40°<111> relationship to a *b*-fibre orientation between S and Bs (also called S/Bs). The pronounced Goss orientation in the recrystallisation texture leads to poor formability. In hot rolled and recrystallised AA3004 the Goss-texture is reported to be equal in strength compared to the cube texture [Fricke and McShane (1985)]. Hutchinson *et al.* (1989) have reported for an AA3004-alloy, that factors favouring the cube texture also seem to favour the formation of the Goss-texture, *i.e.* transition bands. Hjelen *et al.* (1988) have actually demonstrated that Goss-oriented grains may grow out of transition bands, these bands were found within the Bs-orientation. They also reported nucleation of Goss-oriented grains by strain induced boundary migration (SIBM). Grains with Goss-orientation have also been reported to nucleate from shearbands [Lücke and Engler (1990)]. Within the shearbands the Goss orientation is present as narrow transition bands, and a relatively high deformation is required to activate these bands as nucleation sites.

R-texture ({123}<634>) is frequently observed after annealing of cold rolled commercial purity Al and certain alloys. It is close to the S-deformation texture, and is therefore referred to as retained rolling texture. This appellation is correct only if the recrystallisation has occurred by extended recovery, also called continuous- or *in-situ* recrystallisation.

Q-texture ({013}<331>) is most often found in connection with the presence of the P-component. Both these orientations seem to show up in cases where inhomogeneous deformation occurs due to the presence of particles or if profuse shearband formation takes place. Nucleation of Q-grains has been reported to occur at shearbands [Lücke and Engler (1990), Engler (1996b)]. Three of the eight possible 40°<111>-rotations lead to orientations close to components along the main *b*-fibre.

2.4 Modelling

2.4.1 Modelling flow stress during deformation

Based on the parameters described in chapter 2.2.2 Nes and colleagues [Nes (1998), Marthinsen and Nes (2001), Nes *et al.* (2001) and Holmedal *et al.* (2002)] have developed a physical based model for interpretation of the evolution in flow stress during deformation, it have been named the ALFLOW-model. This model is a modified link length model. The typical outputs of the model are flow stress, dislocation density, misorientation and subgrain size. The model is based on four or three parameters dependent on where at the stress strain curve the material is operating. Stadium II and III is defined by subgrain size (d), interior dislocation density (r_i), cell wall thickness (h) and the dislocation density inside the cell walls (r_b). In stadium IV (e >0.5) the cell walls have collapsed into subgrain boundaries with a given misorientation, the structure is now defined by the misorientation (j), the subgrain size (d) and the dislocation density inside the subgrain (r_i). The transformation from a cell structure to a subgrain structure is mainly due to dipole annihilation of dislocations within the cell boundaries.

Rothers and colleagues [Rothers *et al.* (2000), Karhausen and Rothers (2002)] have recently reported an alternative approach relaying on the same microstructural descriptions, but this model will not be treated in the present work.

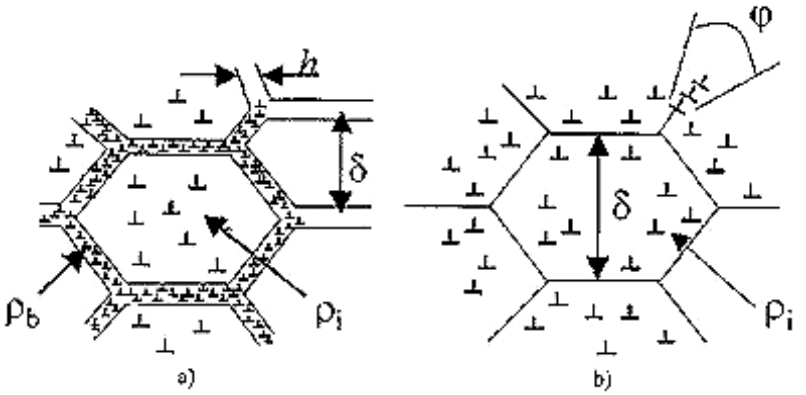

Fig.2.13: Description of the deformed microstructure after a) small deformations and b) large deformations.

2.4.2 The basics of the ALFLOW model

The model describes the critical resolved shear stress of slip within a grain as a function of the microstructure:

$$t = t_t + \hat{t}_a = t_t + t_p + a_1 Gb\sqrt{r_i} + a_2 Gb\left(\frac{1}{d} + \frac{1}{D}\right) \qquad (2.14)$$

where $\hat{t}_a$ characterises the rate and temperature independent interaction due to long range elastic stresses (athermal storage of dislocations), while t_t reflects the rate and temperature dependent interactions with short-range obstacles. t_p is the stress contribution due to undeformable particles, a_1 and a_2 are constants, G is the shear modulus, b is the Burgers vector, d is the cell/subgrain size and D is the grain size of the undeformed material. The texture is taken into account by applying an average Taylor factor (M).

In pure metals the thermal stress component (t_t) reflects the interaction between the mobile dislocations and the stored dislocations, *i.e.* cutting of a forest of trees and dragging of jogs. In alloys with a significant amount of the alloying atoms in solution this component is controlled by the thermal activation of the solute atoms away from climbing jogs on screw dislocations. The migration rate of both these cases can be described as:

$$v = l_a B_t \nu_D \exp\left(-\frac{U_t}{kT}\right) 2\sinh\left(\frac{t_t V_t}{kT}\right) \qquad (2.15)$$

where l_a is the activation length, B_t is a constant, ν_D is the Debye frequency, U_t is the activation energy, k is the Boltzsmann's constant, T is temperature and V_t is the activation volume. The reader is referred to the paper by Marthinsen and Nes (2001) on how these parameters are determined in the different cases of pure metals and alloys.

The thermal stress component (t_t) is obtained by combining this equation with the Orowan equation $\left(\dot{g} = r_m bv\right)$, where r_m is the density of mobile dislocations.

The model treats the microstructure evolution during plastic deformation in stage IV of the stress-strain curve in terms of three parameters, namely the subgrain size, dislocation density within the subgrains and the misorientation across the subgrain boundaries. These parameters are described by:

$$\frac{dd}{dg} = \frac{dd^{+}}{dg} + \frac{dd^{-}}{dg} \tag{2.16}$$

$$\frac{dr_i}{dg} = \frac{dr_i^{+}}{dg} + \frac{dr_i^{-}}{dg} \tag{2.17}$$

$$\frac{dj}{dg} = \begin{cases} \dfrac{d\tilde{j}}{dg} & for\ j > j_{St.III} \\ Max\left(\dfrac{d\tilde{j}}{dg}.0\right) & for\ j \le j_{St.III} \end{cases} \tag{2.18}$$

Once again the reader is referred to the work by Marthinsen and Nes (2001) for more details about how each mathematical term are handled in the model. Here only a brief description of each term will be given. Equation (2.16) and (2.17), which describes the evolution of subgrain size and dislocation density with applied strain. They consist of two terms, where the first is treating the athermal storage of dislocations within the microstructure and the second is handling the recovery reaction or spontaneously annihilation of dislocation with opposite Burgers vectors. For small strains where the principle of similitude applies no annihilation of dislocations occurs. At higher strains the recovery term starts to make influence on the flow curve. The equation for the misorientation evolution (2.18) follows the experimental results found by Furu *et al*. (1995) with a saturation point at approximately 3°, as was shown in a previous chapter.

The outputs of the ALFLOW-model can directly be imported as input for the ALSOFT-model, which calculates the softening behaviour of the material during the subsequent annealing treatment.

2.4.3 Modelling back-annealing (ALSOFT)

In the following the basic equations for a softening model will be discussed, the model have been called the ALSOFT-model, and is as the ALFLOW-model being continuously improved by the group at NTNU in Trondheim. This model is a combined recovery and recrystallisation model. For references to the model confer Vatne *et al*. (1996) and Sæter *et al*. (1998). The model has the flow stress, recrystallised grain size and fraction recrystallised as the main outputs, while the average misorientation, average subgrain size, interior dislocation density, strain, temperature, chemistry and a mathematical description of the particle size distribution are the main inputs for the model. The flow stress is given as:

$$s_y = s_{y,0} + (1 - X_{rex}) \cdot MG_0 b \left(a_1 \sqrt{r_i} + \frac{a_2}{d} \right) \qquad (2.19)$$

where $s_{y,0}$ is the flow stress of the undeformed material, X_{rex} is the fraction recrystallised, G_0 is the shear modulus at room temperature and a_1 and a_2 are material constants.

The stored energy of the system after deformation is given by equation (2.2). As discussed in detail in chapter 2.3.3, the recovery process occurs throughout the softening period. The evolution of interior dislocation density is given by:

$$\frac{dr_i}{dt} = -2B_r n_D b r_i^{3/2} \exp\left(-\frac{U_a}{RT} \right) \sinh\left(\sqrt{r_i} \frac{A_r G b^4}{kT} \right) \qquad (2.20)$$

where B_r is a material constant, U_a is the activation energy, $A_r = w_r c_{ss}^{-2/3}$ *i.e.* dependent of the concentration of elements in solid solution, the other variables have already been defined earlier.

The evolution of subgrain growth follows:

$$\frac{dd}{dt} = 2B_d n_D b \exp\left(-\frac{U_a}{RT} \right) \sinh\left(\frac{1}{d} \frac{A_d G b^4}{kT} \right) \qquad (2.21)$$

where B_d is a material constant and $A_d = w_d c_{ss}^{-2/3}$.

On the basis of equations (2.20) and (2.21) the total dislocation density is calculated:

$$r_{tot} = r_i + \frac{kj}{bd} \tag{2.22}$$

From these basic equations the subgrain growth and decrease in dislocation density has been calculated. In Fig.2.14 examples of good fit for the subgrain growth model has been found for two different commercial purity aluminium alloys.

The kinetics of recrystallisation is described by the JMAK-theory assuming site saturation. The mobility of the migrating grain boundaries, growth rate, fraction recrystallised and recrystallised grain size are described by equations (2.23)-(2.26):

$$M = \frac{M_0}{c_{ss} RT} \exp\left(-\frac{U_{GB}}{RT}\right) \tag{2.23}$$

$$v = M(P_D - P_z) \tag{2.24}$$

$$X_{rex} = 1 - \exp\left(-\frac{4}{3} p N_{tot} (vt)^3\right) \tag{2.25}$$

$$D_{rex} = \left(\frac{1}{N_{tot}}\right)^{1/3} \tag{2.26}$$

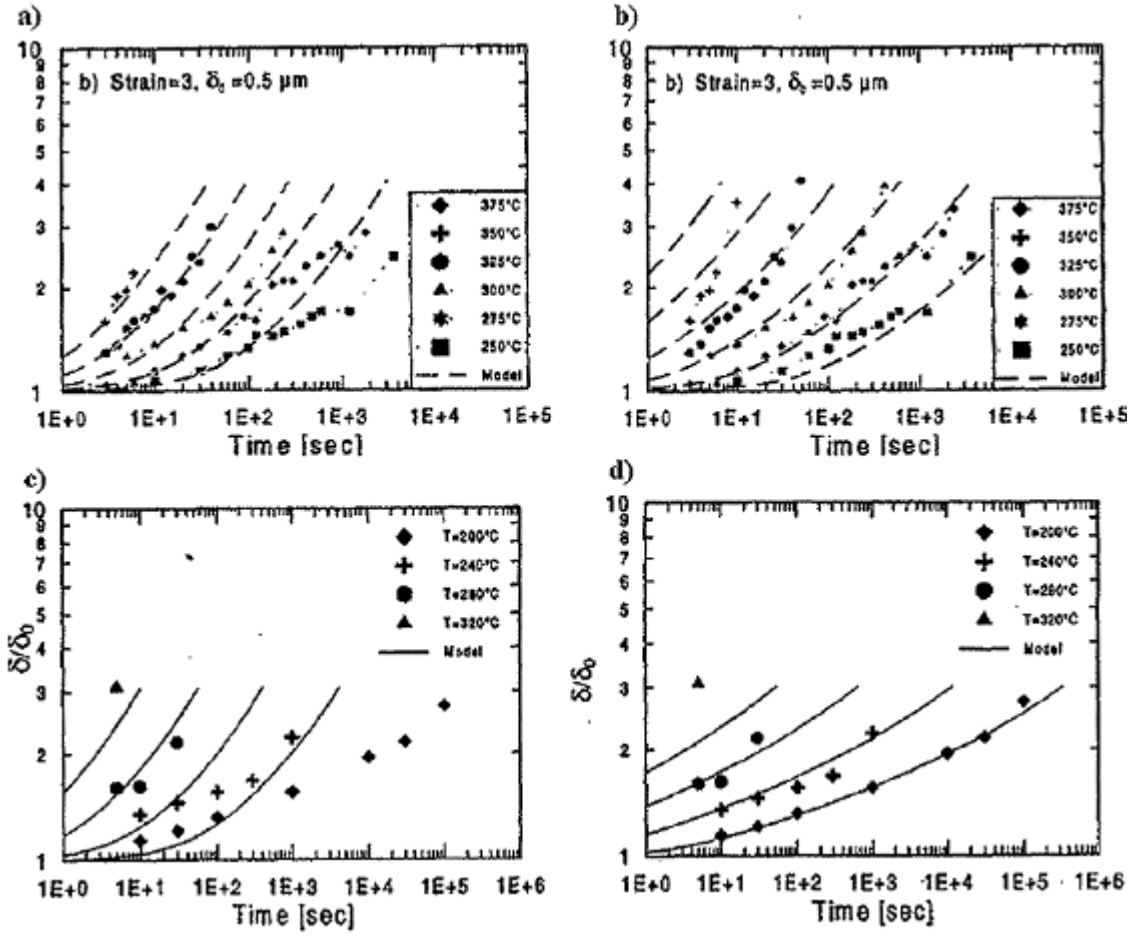

Fig.2.14: Modelling of subgrain growth. The normalised subgrain size is plotted *vs.* annealing time. a-b) AA1050-alloy [Furu *et al.* (1995)], c-d) AA1070-alloy [Sæter (1997)]. a) and c) are modelled by a simple climb mechanism, b) and d) are modelled by solute pinning mechanism.

The total number of PSN-sites (2.29) is given by combining the description of the particle size distribution (2.27) and the critical particle size (2.28), which in most cases can be represented by the following relations:

$$F(h) = H \cdot \exp(-Lh) \tag{2.27}$$

$$h_c = \frac{4g_{SB}}{P_D - P_z} \tag{2.28}$$

$$N_{PSN} = C_{PSN} N_0 \exp(-Lh_c) \tag{2.29}$$

where g_{SB} is the Read Shockley as given in equation (2.3), C_{PSN} is a tuning parameter giving the effectiveness of each over-critical particle and $N_0 = H/L$.

Number of Grain Boundary nucleation sites:

$$N_{GB} = \frac{C_{GB} d \ S_{GB}}{D_0} \left(\exp(e) + \exp(-e) + 1\right) \qquad (2.30)$$

where C_{GB} is a tuning parameter, D_0 is the grain size in the undeformed state.

Vatne (1995) has found that the subgrain size distribution of deformed aluminium is given by a *G*-distribution, where $a = d_c/d$ and $d_c = h_c$ as given by equation (2.28):

$$S_{GB} = \frac{1}{d^3} \exp(-5a) \left[1 + 5a + \frac{(5a)^2}{2!} + \frac{(5a)^3}{3!} + \frac{(5a)^4}{4!} \right] \qquad (2.31)$$

3. Experimental techniques

3.1 Material selection and processing

The present work has focussed on a selection of alloys produced and processed in various ways. The main focuses have been on a commercial pure alloy (AA1200) and two different AA3103-alloys, as defined in the introduction. The chemical compositions are given in Table 3.1.

Table 3.1: Chemical composition of the invested alloys.

Alloy	wt% Fe	wt% Si	wt% Mn	wt% Mg	wt% Cu	wt% Al
AA1200	0.52	0.13				Balance
CP 3103	0.49	0.06	1.03	0.009	0.003	Balance
LP 3103	0.57	0.12	1.0	0.015	0.012	Balance

Homogenisation of LP 3103: The LP 3103-alloy was received in the *as cast* condition, and this material was cut into three rolling slabs and homogenised differently to achieve different amount of manganese in supersaturated solid solution. The homogenisation was carried out in an air circulation furnace using a heating-rate of 100°C/h and with the following procedure:

- *Condition A* was heated to 610°C and held for 14 h before water quenching.
- *Condition B* was heated to and held at 610°C for 14 h, then slowly cooled to 550°C with a cooling rate of -20°C/h and held at this temperature for 16 h and finally water quenched.
- *Condition C* was heated to and held at 610°C for 14 h, slowly cooled to 550°C and held for 16 h, slowly cooled to 500°C and held for 24 h, and finally slowly cooled to 450°C and held for 32 h before water quenching.

Rolled materials: The LP 3103-alloy has been received in the *as cast* condition (DC-cast) from Hydro Aluminium Karmøy. This material has been homogenised as given above before being laboratory cold rolled at NTNU. The other AA3103-alloy and the AA1200-alloy have been industrially homogenised and rolled in the plants of the producers. The producers of these alloys have been Alcan (AA1200) and VAW now Hydro Aluminium Deutschland GmbH (CP 3103).

3.2 Cold deformation

The laboratory cold rolling of the AA3103-alloys have been done with the use of heavily lubricated rolls and maximum roll velocity in order to obtain a microstructure similar to industrial processed materials. Benum (1995) has shown that this treatment minimises the shear zone in the surface region of the sheet. The reduction per pass has been maximised to ensure a homogeneous through thickness deformation, to ensure this equation (3.1) should be fulfilled.

$$\left(\frac{h_b}{4R_r a_r}\right)^{1/2}(2-a_r)<1 \qquad (3.1)$$

where a_r= 1- (h_a/h_b), and h_a and h_b refers to the sheet thickness after and before each rolling pass, respectively. R_r is the radius of the rolls. Due to the limited force of the mill it has previously been found that it is difficult to obtain homogenous deformation due to the relatively small radius of the rolls for sheet thickness larger than 15 mm (Furu 1992).

The rolling slabs, cut from DC-cast billets, have been rotated 180° about the normal axis to simulate the cold rolling process, and the temperature of the sheets was kept below 40°C. The rolling reductions were 39%, 78% and 95%, *i.e.* strains of 0.5, 1.5 and 3.0, respectively.

3.3 Annealing experiments

3.3.1 Isothermal annealing

Isothermal annealing experiments of the cold rolled materials were carried out by direct immersion into salt-baths or fluidised oxide beds. After placing the specimens into the bath/bed they were stirred according to the procedure by Furu *et al.* (1995), this was done in order to minimise the heating time and was especially important for short annealing times and for thick specimens. The specimens were annealed for different holding times followed by quenching into water.

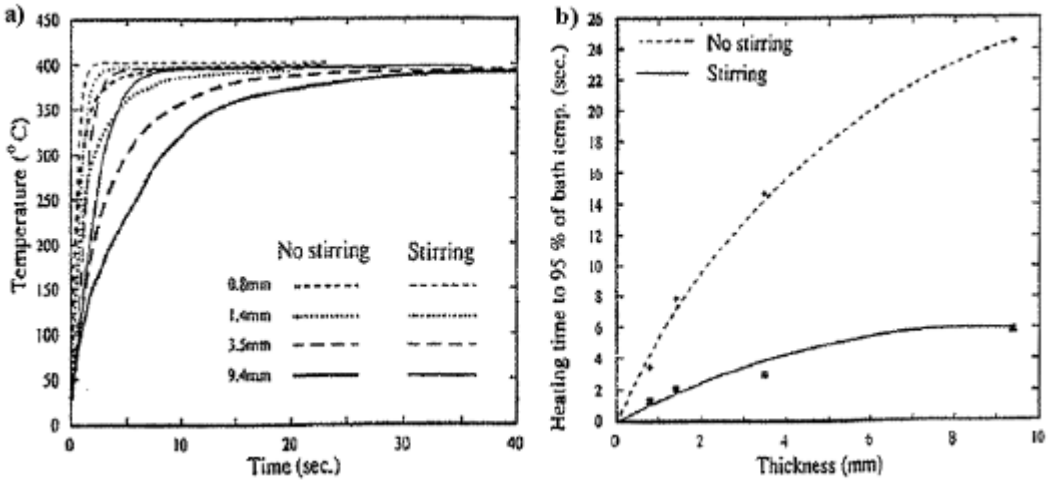

Fig.3.1: Effect of stirring of a) the heating rate to 400°C for different sample thicknesses and b) the time to 95% of salt-bath temperature vs. thickness [Furu *et al.* (1995)].

3.4 Hardness and conductivity measurements

3.4.1 Hardness measurements

Measuring hardness is a very effective and cheap way to follow the softening reaction. A Vickers hardness instrument with a load of 1 kg, loading speed of 100 μm/s and 15 seconds holding time was used in the presented investigations. An average of minimum three hardness indentations on each of the rolled surfaces was measured to follow the softening behaviour.

3.4.2 Conductivity measurements

High purity aluminium has an electrical conductivity of approximately 37.6 MS/m at room temperature [Kutner *et al.* (1976)]. The presence of alloying elements in solid solution will, through their distortion of the atomic lattice, decrease the conductivity of the material. The literature review by Lok (2001) gives a more detailed description of solute effects. On the other hand, if the alloying elements are in the form of semicoherent or incoherent precipitates they have a much weaker effect on the conductivity. This means that measurements of the electrical conductivity are a suitable way to obtain information about the elements in solid solution and the occurrence of precipitation reactions during annealing. Various elements in solid solution will influence the conductivity to different degrees. By neglecting the temperature dependent term in the Matthiessens rule, the relationship between electrical conductivity and the solid solution content in wt% for the alloys investigated here is given according to Altenpohl (1965) as:

$$\frac{1}{k} = 0.0267 + 0.036Mn + 0.032Fe + 0.0068Si \qquad (3.2)$$

where k is the electrical conductivity [MS/m].

In the presented work the electrical conductivity was measured with a Sigmatest D2.068. The measurements were performed by mounting the contact probe on a clean, planar sample surface, after grinded on a SiC paper with a surface finish of 1200 Mesh. The presented conductivity values in the results are averages of 6 measurements on each sample. The conductivity was measured on the RD-TD-plane. The minimum dimensions of the specimens were larger than 10 mm in diameter and 0.5 mm in thickness. With this experimental set-up an accuracy of ±0.05 MS/m was usually achieved. It is however, important to emphasise that these measurements only give an estimate of the total solid solution content, and it is impossible to separate the contributions from each of the various alloying elements.

3.5 Tensile testing

3.5.1 Flow stress measurements

Many material parameters can be measured by a simple tensile test, *e.g.* yield flow stress, ultimate tensile strength, strain at fracture, E-modulus, anisotropy etc. In the presented work the tensile specimens are only taken out parallel to the rolling direction. A MTS 880 universal tensile testing machine was used for the tensile testing. The width and the gauge length of tensile specimens were ~12.5 mm and 50 mm, respectively. The machine was operated in stroke control with a constant stroke speed of 2 mm/min, which gives a strain rate of $4.2\text{-}6.7 \cdot 10^{-4}$ s^{-1}. The difference was due to different initial geometry of the tensile specimens. All specimens were strained until fracture occurred.

The yield flow stress was determined by adding a straight line with a slope of 70 GPa from the strain of 0.02, and the yield stress is where this line cuts the stress strain curve. An average of two stress strain curves was used to determine the parameters of the material. In case of large deviations more than two curves were used in the evaluation.

3.5.2 Determination of flow stress from hardness measurements

Monitoring the softening reaction by tensile testing is a time consuming method. However, by establishing empirical relations between the flow stress and the hardness test values, it is possible to convert the hardness to a flow stress value. By this a much more effective way to determine the softening reaction for a wide range of conditions is achieved.

The flow stress is measured in uniaxial loading, while the stress-state during hardness testing is multiaxial. As a consequence of this the mathematical transformation is not a straightforward task, but simple empirical relationships have been found and it has been observed that this follows:

$$s_{0.2} = C \cdot VHN - 10 \cdot C \qquad (3.3)$$

where C is a constant usually varying between 2.5 and 4, see for instance Milman *et al*. (1993) and Sæter (1997).

3.6 Microstructural investigations

3.6.1 Optical microscopy

A Leica light optical microscopy has been used to investigate different material conditions. In the presented work the microscope has been used to determine grain sizes (D_{rex}) and fraction recrystallised (X_v) at different stages of annealing by using polarised light. The light optical microscope has a low resolution compared to other techniques like SEM and TEM, but provides a large field of view.

Specimen preparation was carried out by grinding on SiC-paper to a grid size of 2400 Mesh, followed by an electrolytical polishing at 20 volts for 23 seconds in a solution of 7.8% perchloric acid, 10% butylglycol, 12% distilled water and balance ethanol (A2-reagent). Finally the samples were anodised in 5% HBF_4 aqueous solution (Barkers reagent) at 20 volts for 120 seconds to reveal the microstructure.

Grain size measurements were done using the line intercept method. The measurements were performed both in the rolling direction (RD) and the normal direction (ND) and more than 300 grains were taken into account for each sample in polarised light.

A counting analysis has been performed to measure the fraction recrystallised (X_v). A grid of 121 (11x11) gridpoints in the sight of view was added to the light microscope. Each gridpoint falling into a recrystallised grain was counted and for each sample at least 800 points were taken into account. The grid spacing relative to the scale of the structure was the most critical item in determining the efficiency of the analysis. For a fraction recrystallised less than 0.5, the spacing was chosen in such way that the average number of points falling in any one recrystallised colony did not exceed unity. This means a typical magnification between 100x and 500x was used, depending on the grain size and degree of deformation.

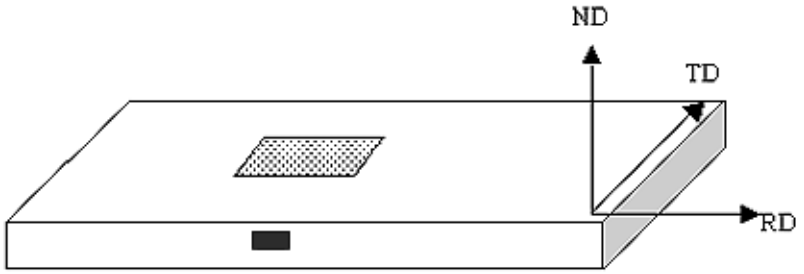

Fig.3.2: Schematic illustration of the rolled sheet with given directions. The dark area is the plane where EBSD, particle analysis and fraction recrystallised were measured. The grey area is where conductivity, hardness and global textures were measured.

3.6.2 Scanning electron microscopy

In addition to giving a better resolution than the light optical microscope, the scanning electron microscopy (SEM) can provide information about the chemical composition and orientation of crystals in the sample. In the presented work SEM was used primarily to determine the size distribution of recrystallised grains and second phase particles, to measure subgrain sizes and misorientations across subgrain boundaries and finally for measuring texture of the different material conditions. In addition to the conventional SEM (JEOL JSM-840) a Field Emission SEM (Hitachi S-4300SE) has been used. The FEG-SEM has been used to investigate dispersoids and deformation zones around coarse particles during the early stages of annealing. According Humphreys *et al*. (1999) an FEG-SEM has 2-3 times better resolution than the conventional SEM, but the resolution is still not as good as in transmission electron microscopy (TEM).

Particle characterisation: The objective of the particles in an AA3xxx alloy is to control the grain structure. Large particles, typically larger than 1 μm, are acting as nucleation sites for PSN, while small precipitates/dispersoids are stalling the recrystallisation process due to the Zener drag [Humphreys and Hatherly (1995)], details are found in chapter 2.3.1. The primary particles in 3xxx-alloys are often in the size range from about 0.5 *m*m to about 10 *m*m. With these particle sizes the light optical microscopy has too course resolution. To use TEM is too time consuming to get the wanted statistics even though the accuracy is better than in SEM. The SEM has high enough resolution and is relatively rapid, thus SEM is the best alternative for this type of analysis.

Specimen preparation was carried out by grinding to 2400 Mesh on SiC-paper. This was followed by an intermediate polishing on a 3 μm hard polishing cloth followed by a short polishing sequence for less than one minute on a soft polishing cloth with 1 μm diamond paste and finally a 3-5 minutes treatment with a 10% OPS-solution. The feature scans were carried out on the conventional SEM in the back-scattered mode at a magnification of 1000x, and the saved pictures were analysed with the KS-300 software. The parameters measured were the aspect ratio and the area of each particle. A minimum of 1000 particles was taken into account for each measured condition, and 0.2 μm was set as the limit for the smallest particle size analysed.

To transpose the measured 2D-distribution into a 3D-distribution a Johnson-Saltykov method modified to correct for non zero information depth has been applied [Ekström *et al.* (1998)]. The basis of this transformation is that all particles are assumed to belong to different classes with given sizes, these classes scales with the logarithm of the equivalent diameter, $d_k = 10^{0.1k}$. For a planar cut through the microstructure with spherical particles, it is known that the particles will be cut at different cross-sections. On average the found radius will be lower than the true value, it is easy to show that the true value of the particle radius follows equation (3.4). Further it have been considered that the beam penetrates some distance down into the microstructure, for this reason the dividing value in equation (3.4) has been modified, *i.e.* being closer to unity.

$$r_{true} = \frac{r_{measured}}{\sqrt{2/3}} \qquad (3.4)$$

To get images of the dispersoids an FEG-SEM have been used. The preparation of the samples for this analysis was as above, but in addition 40-60 seconds of electropolishing at -30°C was applied. This treatment was performed in order to remove the deformed surface layer due to the mechanically preparation. Here several different magnifications have been used to show different microstructural effects.

The EBSD-technique: The principles of the Electron Back-Scattering Diffraction method (EBSD) are as follows. As the electrons of the incident beam hit the tilted specimen, some of them undergoes elastic scattering with the atoms in the specimen, a certain fraction of these electrons will become diffracted according to Bragg's law. Some of these back-scattered and diffracted electrons hit a phosphor screen, which results in a Kikuchi- or EBSD-pattern, and this pattern gives the atomic planes of the crystal at that position. A camera registers the pattern displayed on the monitor. An example of a Kikuchi pattern can be seen in Fig.3.3. Before being presented on the monitor, the background is subtracted and the image is processed to give the best visual impression. To provide a high density of detected back-scattered electrons, the sample is tilted 70°. The following parameters have been used to get as good results as possible: acceleration voltage of 20 kV, beam current of $1 \cdot 10^{-9}$–$6 \cdot 10^{-8}$ A and a working distance of 21-23 mm (conventional SEM). A review by Humphreys (2001) is a strongly recommended paper for all users of the EBSD-technique. In this paper the limitations of the technique are discussed and how the postprocessing should be done to get reliable results.

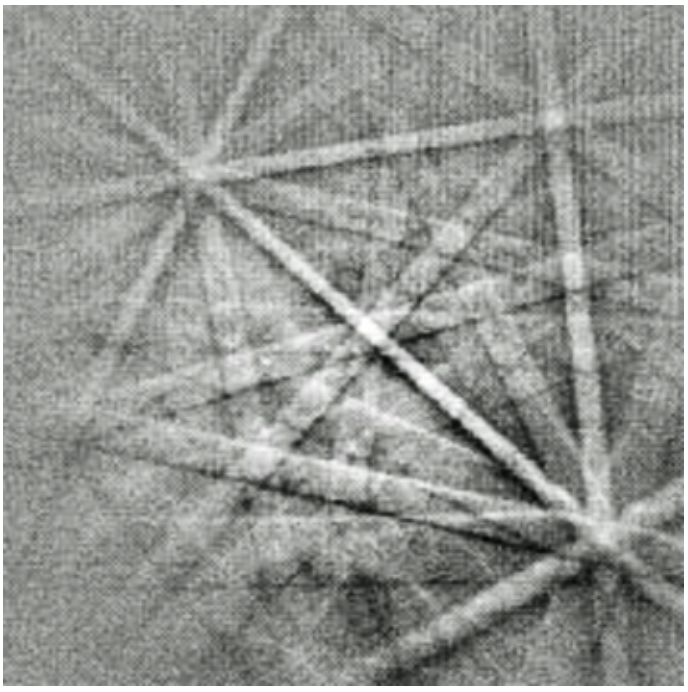

Fig.3.3: An example of a monitored Kikuchi-pattern.

The orientation of a specific grain or subgrain can be obtained from the EBSD-patterns by indexing the displayed patterns. When running the indexing in an automated mode, the EBSD-pattern is detected automatically from the recorded image on the monitor, and a software package is calculating the orientation of each individual pattern, before the beam is moved to measure the orientation of the next point. Thousands of orientations can be collected in this manner, and a orientations map (OIM-map) of the specimen is obtained. The orientation map includes information on crystal orientation and grain boundary character.

Specimen preparation was carried out by grinding to a grid size of 2400 Mesh, followed by an electrolytical polishing at 20 volts for 23 seconds in the A2-reagent. The reagent temperature was held in the range 15-17°C. The specimens investigated in the FEG-SEM were after the 2400 grinding polished down to 1 μm, followed by polishing with 10% OPS for 3-5 minutes before the final electrolytical polishing of the specimens was carried out. The solution used for this treatment was a 70% methanol (CH_4OH) and 30% nitric acid (HNO_3). The temperature of the solution was held between -30°C and -38°C. This was done by pouring liquid nitrogen into the solution. The electrolytical polishing was carried out with a voltage of 12 V for 30-80 seconds.

The Channel 5.0-software, developed by HKL Technology, has been used to analyse the EBSD-patterns as well as for postprocessing of the data. EBSD has been used in order to measure grain and subgrain sizes, misorientation and texture evolution. Grain sizes of a fully recrystallised material are determined both by the area of each individual grain and by the line intercept method. Here an angle of 5° has been used to define individual grains, this rather low angle was used to separate different grains of strongly textured specimens. Subgrain sizes have been calculated from measured areas where the subgrains are defined by being surrounded of a boundary with a misorientation between 1.5° and 15°. Misorientation across subgrain boundaries was calculated for all neighbouring pixels with a misorientation angle between 1.5° and 15°. The problem of both the subgrain size measurements and the misorientation is that some of the low angle boundaries that are below 1.5° are lost. Local texture measurements were used in order to investigate of some specific texture components.

3.7 Global texture measurements

Texture is defined as an orientation distribution of the material crystallites. It is usually presented as pole figures, which are stereographic projections showing the distribution of particular sets of crystal planes of the individual crystallites. Pole figures have the weakness of only describing texture in two dimensions, and for this reason it has become more convenient to represent the texture as an orientation distribution function (ODF). The ODF presents texture in three dimensions, illustrating the continuous nature of the crystal orientations.

In order to describe the orientation of a crystallite in a polycrystalline material, it is necessary to define a global co-ordinate system of the material. In the case of rolling it is common to use the rolling direction (RD), transverse direction (TD) and normal direction (ND) as the global system, also called K_a. Secondly each crystallite has its own co-ordinate system, which is fixed with respect to the crystal axis (K_b), in case of cubic crystal symmetry it is convenient to use the edges of the unit cell. The orientation of the crystallite can then be defined by the rotation (g), which transfers K_a into K_b. This rotation can be specified in several ways, in the present investigations only Euler angles (f_1, F, f_2) in the Bunge convention were used [Bunge (1982)].

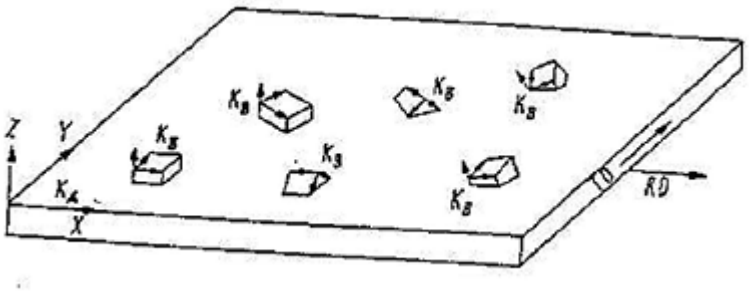

Fig.3.4: The Euler orientation of a crystallite is defined by the rotation of the global co-ordinate system K_a into the co-ordinate system of the crystallite K_b.

Each crystallite represents an orientation (g) and the texture of the material is the totality of all these orientations. The definition of the texture is then given by a continuous orientation distribution function, which represents the volume fraction of the orientation g:

$$f(g) = f(j_1, \Phi, j_2) = \frac{dV(g)/V}{dg} \qquad (3.5)$$

where V is the total specimen volume and dV(g) is the sum of all volume elements of the sample which possess the orientation g within the element of orientation dg (from g to g+dg). This function is calculated from measured polefigures, as it is impossible to measure in physical space.

Diffraction takes place according to the well-known Bragg's law:

$$2d\sin(q) = nl \qquad (3.6)$$

which states that for an incoming X-ray beam with a wave length l and inclination angle q, reflection only takes place from planes of interplanar distance d that fulfil the equation (3.6). For cubic crystals:

$$d = \frac{a}{\sqrt{h^2 + k^2 + l^2}} \qquad (3.7)$$

where a is the lattice constant and {hkl} are the Miller indices of the corresponding plane.

Since the wavelength is constant during a measurement, the above equations give a unique relationship between the angle of the incoming beam and the reflective plane. A pole figure for a given plane is measured by selecting the angle (q) in accordance with Bragg's law and keeping it constant throughout the measurement. The distribution of the plane normals of the wanted {hkl} plane was recorded by rotation and tilting of the specimen. To calculate an ODF at least four polefigures are needed, the four incomplete polefigures measured in the present study were the (111)-, (200)-, (220)- and the (311)-polefigures. The ODFs were calculated by the series expansion method (22 steps in the expansion) and ghost corrected by the positivity method described by Lücke *et al.* (1981).

A Siemens D5000 X-ray diffractometer equipped with a Hüber Eulerian cradle was used to measure the global textures in the presented work. Preparation was carried out by mechanical grinding to 2400 Mesh, before etching for 10 minutes in a 15% NaOH-solution followed by a quick cleaning in water before the specimen finally was held in a 25% HNO_3 solution for 20 seconds to stop the electrochemical reaction. The MTM-FHM software developed by van Houtte (1994) was used to calculate the global ODFs and for further postprocessing.

4. Experimental results

The main objective of this work has been to investigate the final annealing behaviour of a laboratory processed alloy AA3103 (LP 3103) and two commercially processed aluminium alloys, more specifically AA1200 and AA3103 (CP 3103). For the lab-rolled material the effect of manganese in supersaturated solid solution has been investigated in great detail. To avoid confusion, each alloy has a sub-chapter where the results are presented chronologically from start of processing to the final annealing treatment.

4.1 Laboratory processed AA3103-alloy

4.1.1 As cast microstructure

The material was DC-cast into a billet with a diameter of 217 mm and several meters in length at Hydro Aluminium Karmøy. From this billet a piece was received in the *as cast* condition. The *as cast* material was investigated with respect to particles and elements in solid solution.

The particle structure of the *as cast* material is presented in Fig.4.1a). From this figure it is seen that the particles were, as expected, formed on the dendrite arms due to segregation of alloying elements during solidification. The shape of the particles was found to be closely spaced plates. Additionally, some dispersoids were observed as a result of the cooling sequence, but the density was low and with an inhomogeneous distribution. The high cooling rates achieved during DC-casting resulted in a large supersaturation of elements in solid solution. Conductivity measurements and calculations by the use of Matthiessens rule, equation (3.2) gave an estimation of the amount of manganese in solid solution. Estimations of Fe and Si in solid solution after casting have been calculated by the ALSTRUC-model. The calculated value of the *as cast* material based on conductivity measurements is given in Table 4.1. The area fraction of particles based on images obtained in SEM is also included in the table.

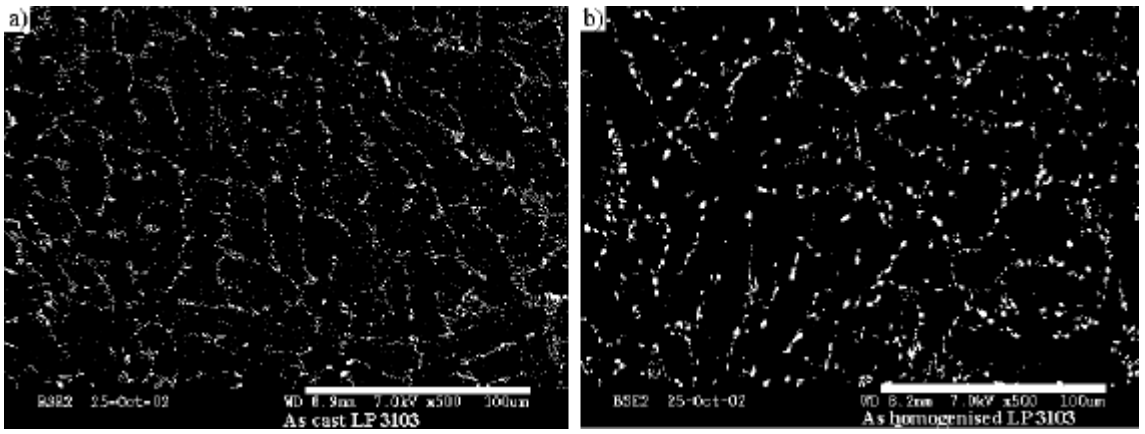

Fig.4.1: Particle structure of the a) as cast and b) homogenised LP 3103-material.

Table 4.1: Area-fraction of particles and amount of Mn in solid solution (corrected for Fe and Si in solid solution) based on conductivity measurements at different stages of homogenisation.

Condition	Area fraction	Conductivity [MS/m]	Mn in ss [wt%]
As cast	0.018	17.7	0.80
After heating to 610°C	0.024	20.3	0.59
Homogenisation A	0.045	22.0	0.50
Homogenisation B	0.046	23.6	0.42
Homogenisation C	0.048	26.3	0.31

4.1.2 Homogenised microstructure

In the following experiments the effects of supersaturated manganese in solid solution have been the topic of interest. By using different homogenisation treatments it is relatively easy to control the amount of manganese in solid solution. During homogenisation at a constant temperature the conductivity usually saturates after typically 12-14 hours at the given temperature, thus by choosing the correct annealing treatment it is relatively easy do achieve the desired supersaturation of manganese.

Three slabs were taken out of the *as cast* billet, where the outer 20 mm was avoided due to segregation effects in this region. These slabs were then given different homogenisation treatments in an air circulation furnace, as described in Chapter 3.1. The observed changes in microstructure after complete

homogenisation comprised spheroidisation and growth of the constitutive particles and a reduction of the elements in solid solution. A SEM-image of a typical particle structure of the homogenised material is given in Fig.4.1b), here the spheroidisation of the original plate like particles of the *as cast* structure is shown. Only small differences in structure were observed for the different homogenisation treatments. Very few dispersoids were found in the homogenised materials, indicating that the dispersoids formed during casting and re-heating during homogenisation have dissolved. As seen in Table 4.1 the area-fraction of particles, calculated from BS-images (back-scatter) monitored by SEM, was found to increase with longer homogenisation times.

The original grain sizes of the *as cast* and homogenised materials were measured by means of EBSD-mapping with a step size of 3 μm. The grain diameters were calculated from the measured area of each grain, assuming that all grains are circular. It was found that all conditions had a large scatter in diameter ranging from a few microns to more than three hundred microns. In Table 4.2 the grain diameter of the different conditions are given after removing all “grains” of size less than 4 pixels. These “grains” were omitted because they were believed to be wrongly indexed pixels (noise) or indexed coarse constitutive particles. The relatively small differences in grain size of the homogenised materials were attributed to differences in grain size of the originally *as cast* material, which had variations through the thickness of the billet. From these small differences no or very little grain growth is assumed to have occurred during homogenisation.

Table 4.2 Grain diameters of the *as cast* and homogenised materials.

Condition	As cast	Hom. A	Hom. B	Hom. C
Diameter [μm]	83.1	74.4	84.0	72.3

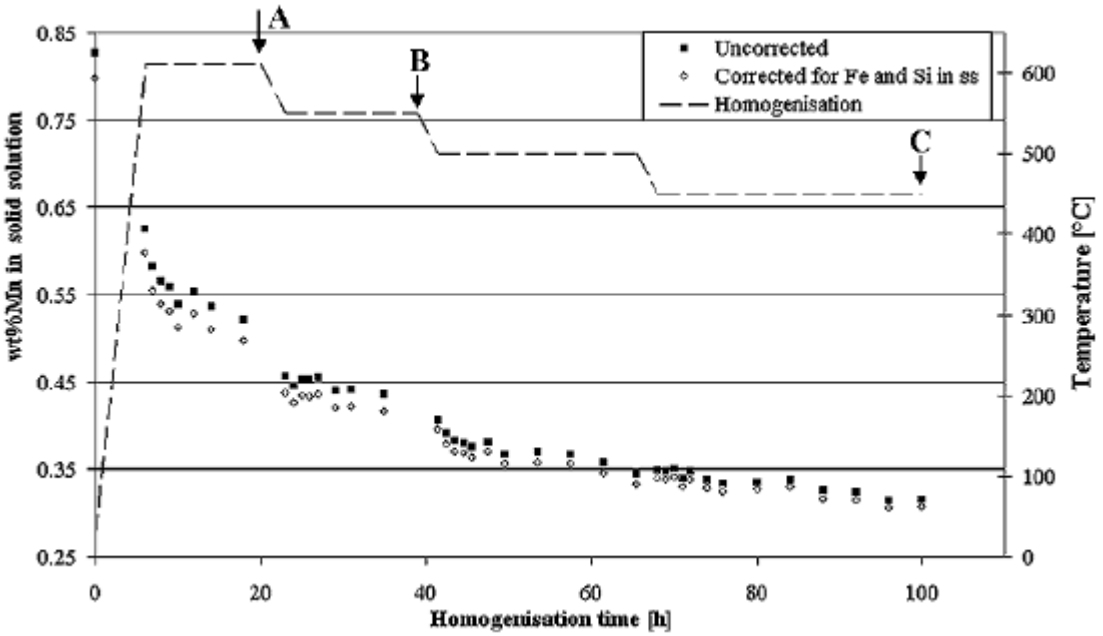

Fig.4.2: Evolution of manganese in solid solution during the different homogenisation treatments. Calculations were done both by assuming only Mn in solution (uncorrected), and by taking the assumed changes in concentration of Fe and Si in solid solution into account. The broken line is the homogenisation temperature *vs.* time, scale to the right. The arrows indicate the quenching point of the different homogenisation treatments.

In Fig.4.2 the calculated amounts of manganese in solid solution during homogenisation are shown. The absolute values are given in Appendix 1. It is seen that the largest drop in conductivity is found during the first hours of annealing at a given temperature, then for long times at that temperature the conductivity almost saturates as it reaches the equilibrium. After this saturation the temperature is reduced for the B- and C-condition, giving other saturation levels making it possible to achieve material conditions with different levels of manganese in solid solution. The final amounts of manganese in solid solution of the different homogenisation treatments are given in Table 4.1. These latter values are corrected for iron and silicon in solid solution, which have been estimated by using the solidification and homogenisation model ALSTRUC [Dons (2002)].

A phase transformation was observed for the material homogenised at a final temperature of 550°C and 450°C, *i.e.* homogenisation B and C, respectively. An example of this phase transformation is given in Fig.4.3 as an Al_6(Mn,Fe)-particles (grey) is partly transformed into α-Al(Mn,Fe)Si (white). For the

homogenised A-material, where the temperature was held at 610°C before quenching, no phase transformation was observed. This phase transformation was far from completed at any of the other homogenisation treatments, probably due to limited excess silicon. Only some particles were found to be in a partly transformed condition at both temperatures.

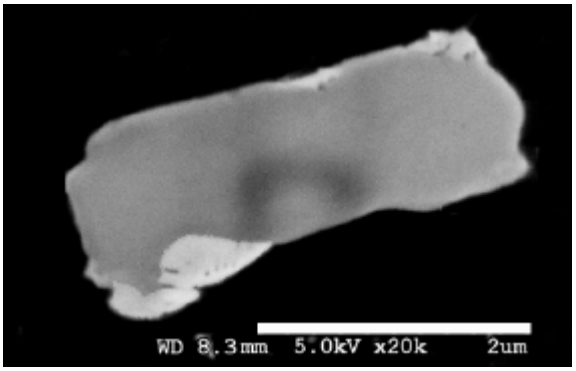

Fig.4.3: Phase transformation during homogenisation.

4.1.3 Cold rolling

The homogenised materials were subsequently cold rolled to different reductions, more specifically to reductions of ~39%, ~78% and ~95%, corresponding to true strains (e) of 0.5, 1.5 and 3.0, respectively. The rolling was carried out on a laboratory mill. The rolls had a low diameter, thus several passes were necessary to achieve the desired reductions. In the following the materials will be named by a letter and a number, referring to the homogenisation treatment and applied strain, respectively.

In the following the results of the evolution in subgrain size, misorientation, texture evolution and particle fragmentation will be presented. All these parameters have a large influence on the subsequent annealing behaviour, with respect to the recovery and recrystallisation reactions.

Substructure evolution: The microstructure of the deformed materials was recorded by EBSD-mapping. As an example in Fig.4.4 a) and b) OIM-maps from the A-material rolled to strains of 1.5 and 3.0 are shown, respectively. In these figures it is seen that as the degree of deformation increases the subgrain size

decreases and the original grains become more elongated in the rolling direction. From these and other OIM-maps average misorientation and subgrain size were calculated, and the values are given in Table 4.3. The misorientation represents an average of all boundaries between 1.5° and 15°. The subgrain sizes in the rolling- and normal directions were calculated by the linear intercept method. From the table it is seen that the average misorientation increases slightly with increasing deformation, while the average subgrain sizes decrease significantly.

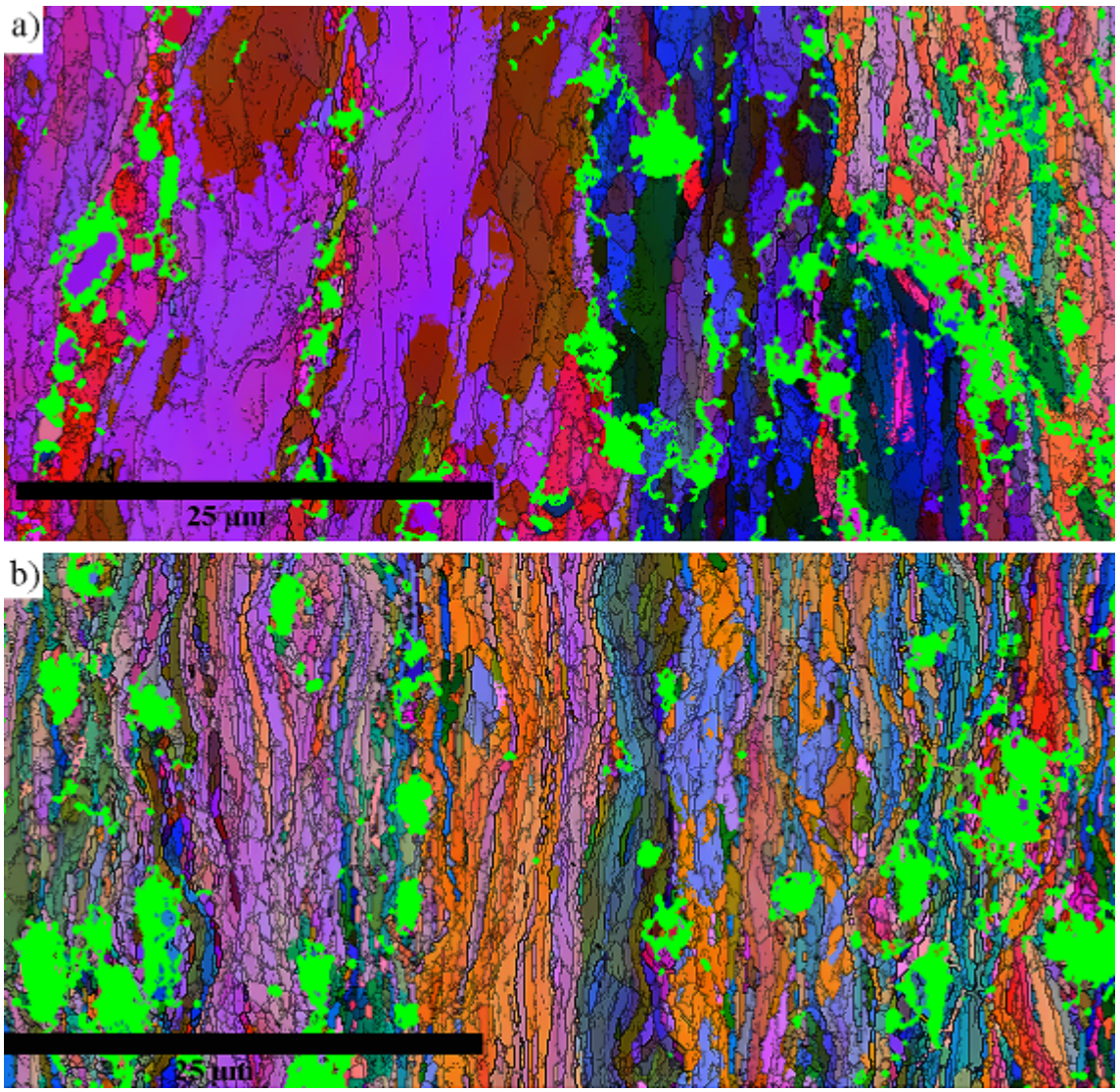

Fig.4.4: OIM-maps of the A-material cold rolling to strains of a) 1.5 and b) 3.0. Thin lines indicate low angle grain boundaries ($1.5 < j < 15$), whereas thick lines have a high angle character. Lime green areas are unindexed areas, most probably primary particles.

The effect of different amounts of manganese in solid solution only resulted in minor changes, but it is seen that the A-materials had slightly lower misorientations and subgrain sizes than the B- and C-materials. These values are important during the subsequent annealing treatment since they determine the stored energy of the material conditions, *i.e.* the driving force for recrystallisation. From this it follows that the stored energy for processes such as recrystallisation is somewhat higher for A-condition than the B- and C-conditions, which are almost similar with respect to misorientation and subgrain size.

Table 4.3: Average misorientation and subgrain sizes of the deformed materials.

Homogen-isation	Strain e	Misorientation [°]	Subgrain size RD [μm]	Subgrain size ND [μm]
A	1.5	4.0	0.82	0.53
	3.0	4.2	0.59	0.38
B	1.5	4.1	0.84	0.54
	3.0	4.3	0.66	0.43
C	1.5	4.1	0.89	0.60
	3.0	4.3	0.66	0.42

Texture evolution: The global cold rolling textures of the different reductions of the differently homogenised materials were measured by X-ray diffraction. As expected, the intensity along the b-fibre increased with increasing strain as illustrated for the A-condition in Fig.4.5 a) to c). The deformation textures of the other homogenised materials were both quantitatively and qualitatively similar to that of the A-material. This indicates that the amount of manganese in solid solution had little effect on the evolution of the deformation texture, as seen in Fig.4.5d). In this figure the skeleton plots along the b-fibre of the deformed A- and C-conditions are presented, and the only difference for the two material conditions seems to be that the A-condition form slightly stronger deformation textures.

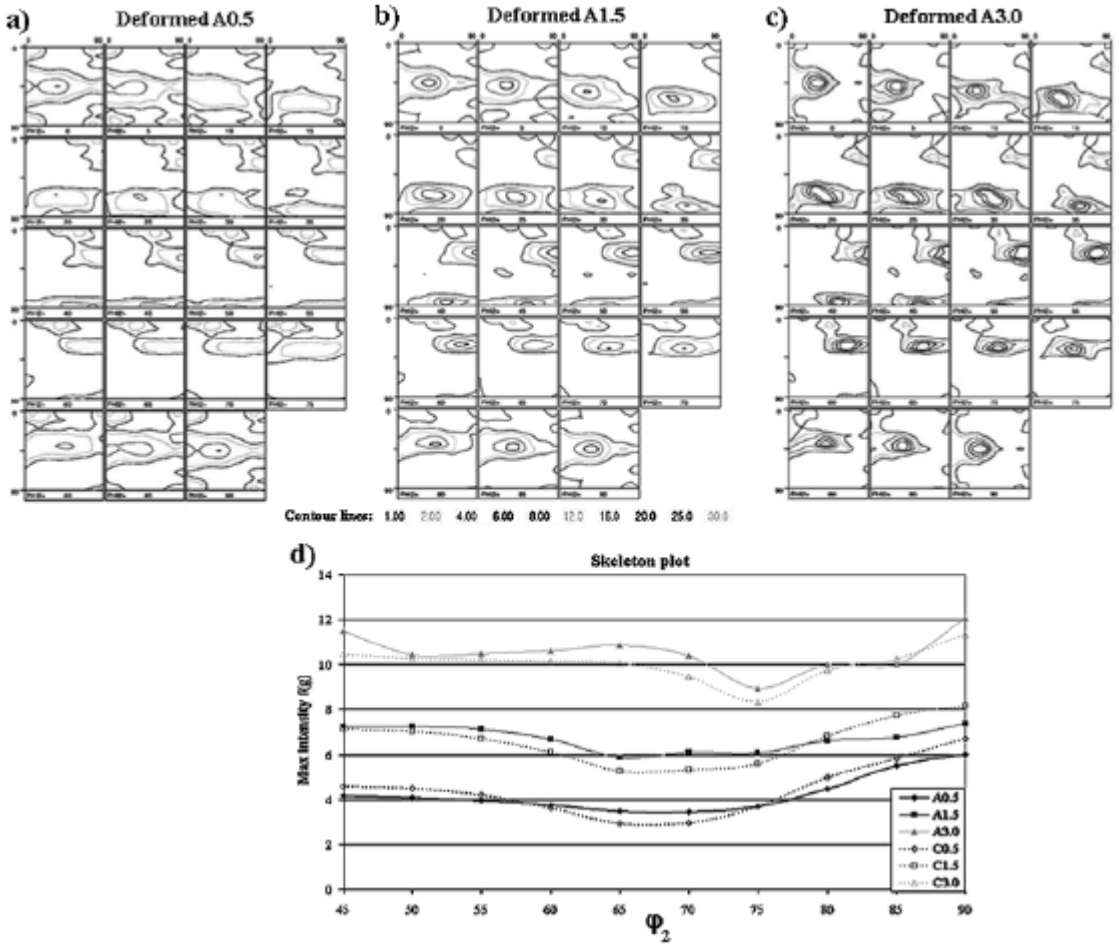

Fig.4.5: Deformation textures of the A-homogenised material after a true strain of a) 0.5, b) 1.5 and c) 3.0. In d) the *b*-fibre skeleton plots of the deformed A- and C-conditions are shown.

In Fig.4.6a) an OIM-map of the microstructure of A3.0 is given and in Fig.4.6b) the corresponding map of cube-oriented grains is presented. The red areas represent the cube orientation including all orientations within 15° of the exact cube orientation, and it is seen that only a very small fraction of the microstructure are cube oriented. These cube-oriented subgrains are possible nucleation sites for cube orientated grains during the subsequent annealing treatment. From this map it is reasonable to assume that very few nucleation sites for the cube orientation are available from cube bands that have survived deformation. Hence if a strong cube texture is found after annealing, this must be due to other nucleation mechanisms, *e.g.* transition bands.

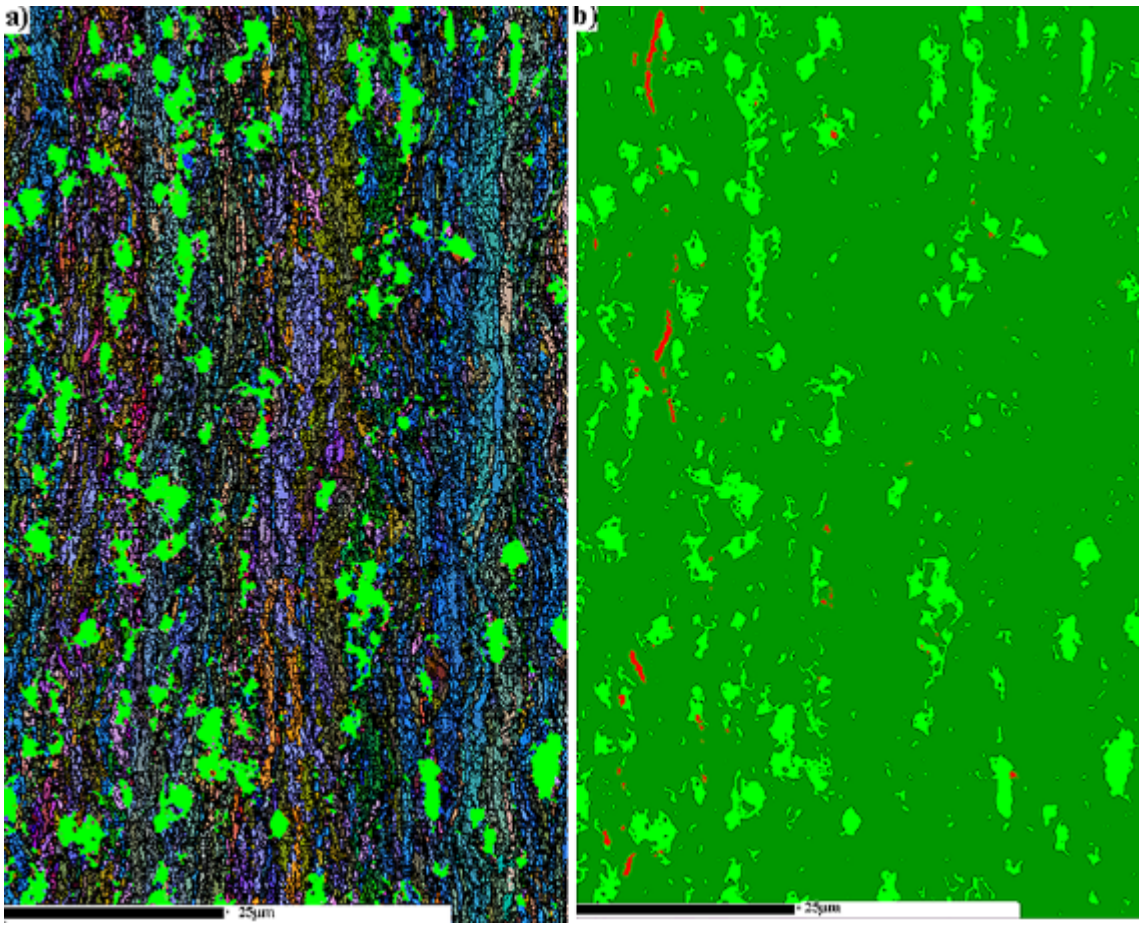

Fig.4.6: a) EBSD-map of the cold rolled material deformed to a strain of 3.0 (A3.0). Lime green areas are unindexed areas, most probably primary particles. In b) the cube-oriented grains of a) is shown. Red areas are within 15° of the exact cube orientation, green areas are other orientations. A very small fraction of the microstructure are cube oriented, *i.e.* there are few potential nucleation sites for cube oriented grains during the subsequent annealing.

The volume fraction of the most common deformation texture components for all material conditions are given in Table 4.4. These fractions were calculated using spherical volumes with radius of 16.5° in Euler space around the exact orientation. From this table it is seen that the volume fractions of cube and Goss seem insensitive to the amount of deformation. For the Bs-orientation the volume fraction increases slightly with increasing strain, and for the S- and Cu-orientations the increase in volume fraction is significant.

Table 4.4: Volume fraction of the most important deformation textures of the deformed LP 3103-materials using spherical volumes with a radius of 16.5°.

Material	Cube	Goss	Brass (Bs)	S	Copper (Cu)
Homogenisation A, ε=0.5	0.04	0.07	0.14	0.23	0.12
Homogenisation A, ε=1.5	0.04	0.06	0.15	0.29	0.16
Homogenisation A, ε=3.0	0.04	0.06	0.16	0.33	0.19
Homogenisation B, ε=0.5	0.04	0.06	0.14	0.24	0.13
Homogenisation B, ε=1.5	0.04	0.06	0.14	0.26	0.14
Homogenisation B, ε=3.0	0.04	0.06	0.16	0.33	0.19
Homogenisation C, ε=0.5	0.04	0.07	0.15	0.26	0.14
Homogenisation C, ε=1.5	0.04	0.07	0.16	0.29	0.16
Homogenisation C, ε=3.0	0.04	0.06	0.17	0.34	0.20

Particle break-up during cold rolling: The particle size distributions of the deformed materials were measured with the use of SEM in back-scatter mode. In Fig.4.7 the effect of particle break-up of the deformed B-homogenised material conditions are shown. From this figure it is seen that there are no *large* differences in the distributions of the homogenised and deformed conditions, although indication of some break-up seems to be present. The effect of break-up is best seen for the largest particles, *i.e.* for those particles larger than ~2.5 μm. For the smaller particles the break-up is not seen due to the large numbers of these in combination with the logarithmic scale on this axis. Little break-up was observed when increasing the deformation from a strain of 1.5 to 3.0. This indicates that most of the fragmentation occurred at lower reductions. Before deformation the particles do not have any preferred orientation with respect to the rolling slab, it can thus be assumed that particle break-up occurred before the particles were aligned into the rolling direction, *i.e.* after relatively small cold rolling reductions.

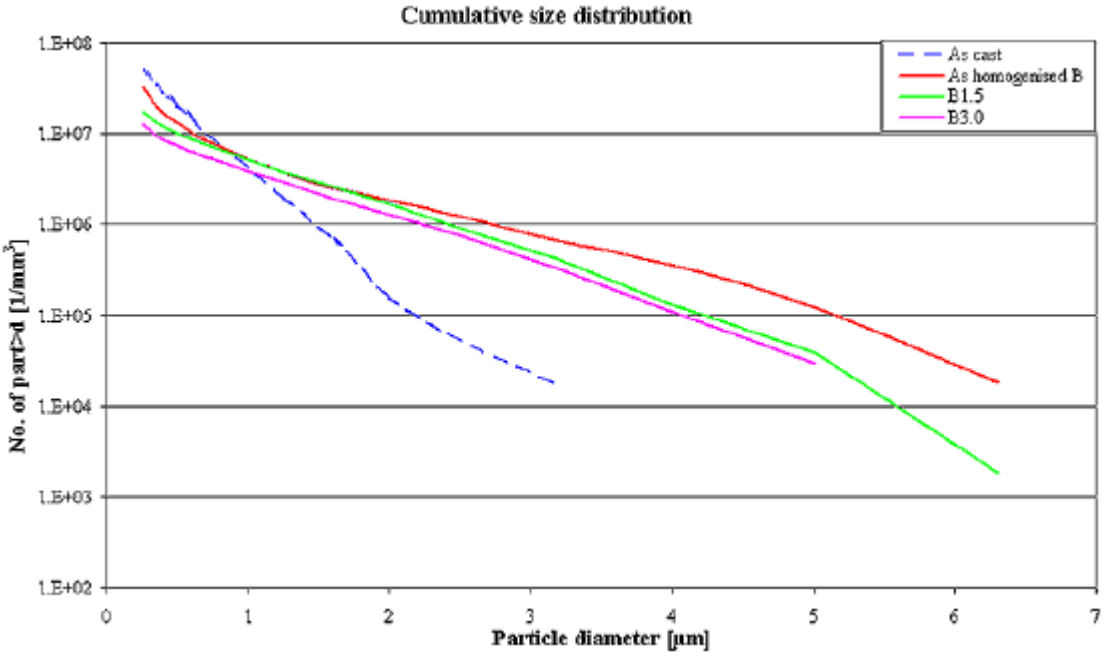

Fig.4.7: Particle distributions of the deformed B-homogenised materials where a tendency of particle break-up during cold rolling were observed. Similar trends were as well seen for the A- and C-material conditions.

4.1.4 Isothermal annealing

In the following the materials will be named by a letter and a number as explained earlier and in addition sometimes also a temperature is included. This temperature refers to the isothermal annealing temperature. A general partition between low and high temperature annealing has also been made, whereas low temperature annealing refers to annealing at 350°C and below, while the high temperature annealing was carried out at 400°C and 500°C.

The cold rolled materials were isothermally annealed in salt baths (flash annealed), in the temperature range 250-500°C and time ranging from a few seconds up to 10^6 seconds (~11 ½ days). At the lowest annealing temperature of 250°C none of the investigated material conditions recrystallised within 11½ days, while at 500°C all material conditions recrystallised within 10 seconds. At the other temperatures large differences in softening behaviour were found dependent on both reduction and supersaturation of manganese in solid solution.

The softening reaction was measured by means of Vickers hardness testing and the precipitation reaction was monitored by conductivity measurements. In Fig.4.8 the softening and precipitation curves of the materials deformed to a strain of 3.0 are shown, the results after strains of 0.5 and 1.5 are given in Appendix 2. Precipitation has an effect on the softening, but this effect is small compared to the total drop in hardness during annealing. For the annealing sequence at 250°C of the A-condition, black line in Fig.4.8a), it is seen that the hardness has increased somewhat after 3000 seconds compared to the as deformed material. This is probably due to the precipitation reactions taking place during annealing, as clusters of solute atom precipitate.

The conductivity was measured for annealing times beyond the fully recrystallised condition and a large increase in conductivity was observed. This indicates that the supersaturation either precipitates homogeneously within the recrystallised grains and/or by growth of the already formed dispersoids by diffusion of solute atoms towards the dispersoids, which results in growth of these dispersoids.

In Fig.4.8a-c) it is clearly demonstrated that the amount of manganese in supersaturated solid solution has a large influence on the softening reactions. With increasing amount of alloying elements in solid solution (C→A) the softening was slowed down and in some cases almost completely stopped at the lower annealing temperatures. When comparing the softening curves with the conductivity measurements for the lower annealing temperatures, it is seen that when softening is retarded the conductivity increased. This increase in conductivity indicates that precipitation of dispersoids occur concurrent to recovery and recrystallisation. For the A- and B-materials, Fig.4.8a-b), annealed at low temperatures it is seen that once the recrystallisation process is the dominating softening process the conductivity increased significantly, suggesting that the main precipitation event occurred on the moving boundaries.

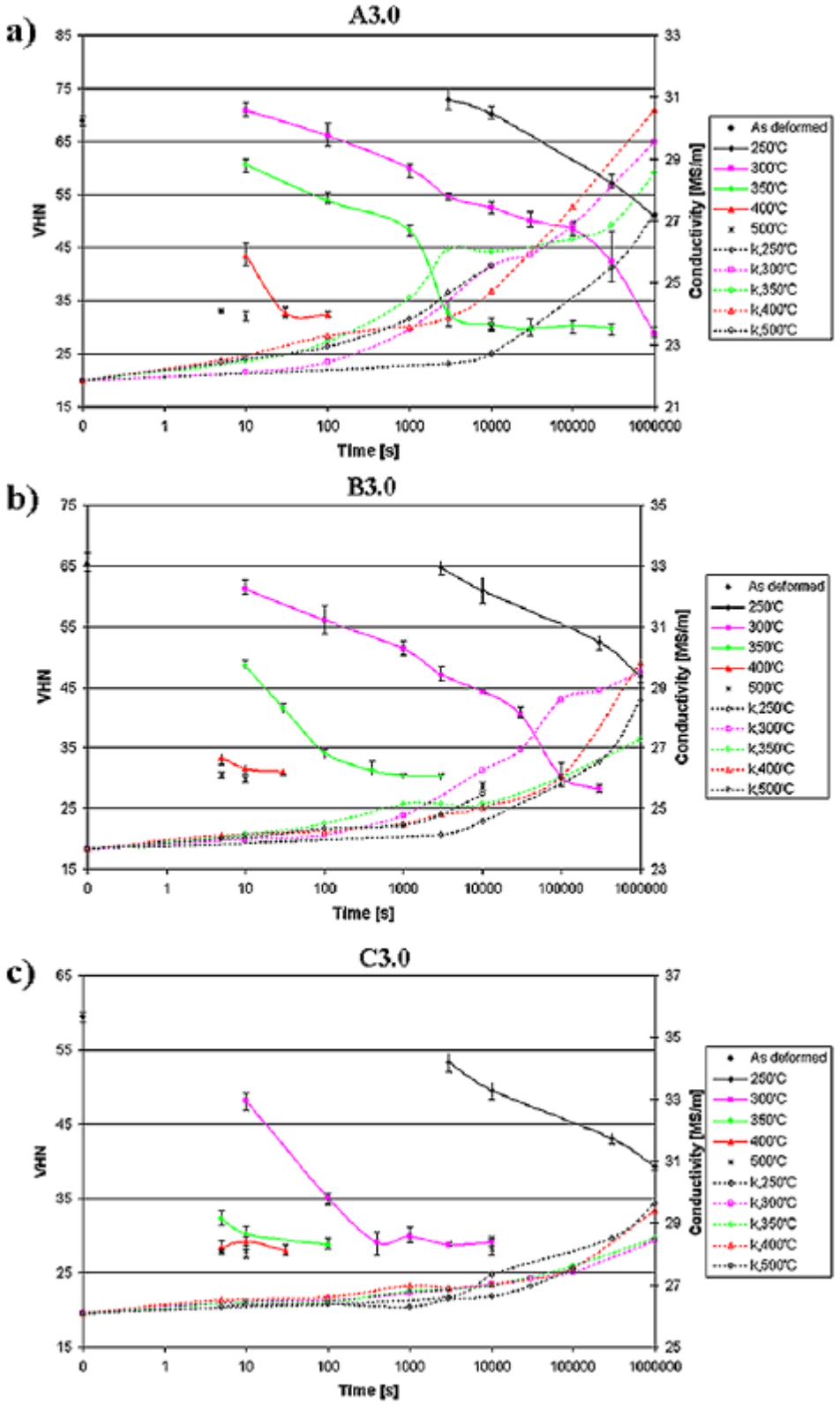

Fig.4.8: Softening and precipitation curves during annealing of the homogenised materials deformed to a true strain of 3.0.

For the A-material annealed at low temperatures it was observed that the conductivity increased rapidly as recovery and recrystallisation progressed. For these conditions some interesting observations were made with respect to recrystallisation texture, grain size and precipitation. In the following the main focus will be on the A3.0-material annealed at 350°C. At this temperature recrystallisation and precipitation occurred after relatively short annealing times, making it possible to study these processes in detail. During annealing of the A3.0-350°C material it was found that recrystallisation started in the centre of the sheet, the same observation was also made for the A3.0-300°C-material. For this reason conductivity and hardness were measured in the centre as well as on the surface of the sheet through the annealing sequence of A3.0-350°C. These measurements obviously confirmed the above observations, the drop in hardness due to recrystallisation was first observed in the centre of the material. The results of the hardness and conductivity measurements are shown in Fig.4.9. It is seen that the conductivity increased as recrystallisation progressed, *i.e.* first in the centre. This indicates that precipitation is promoted by mobile grain boundaries.

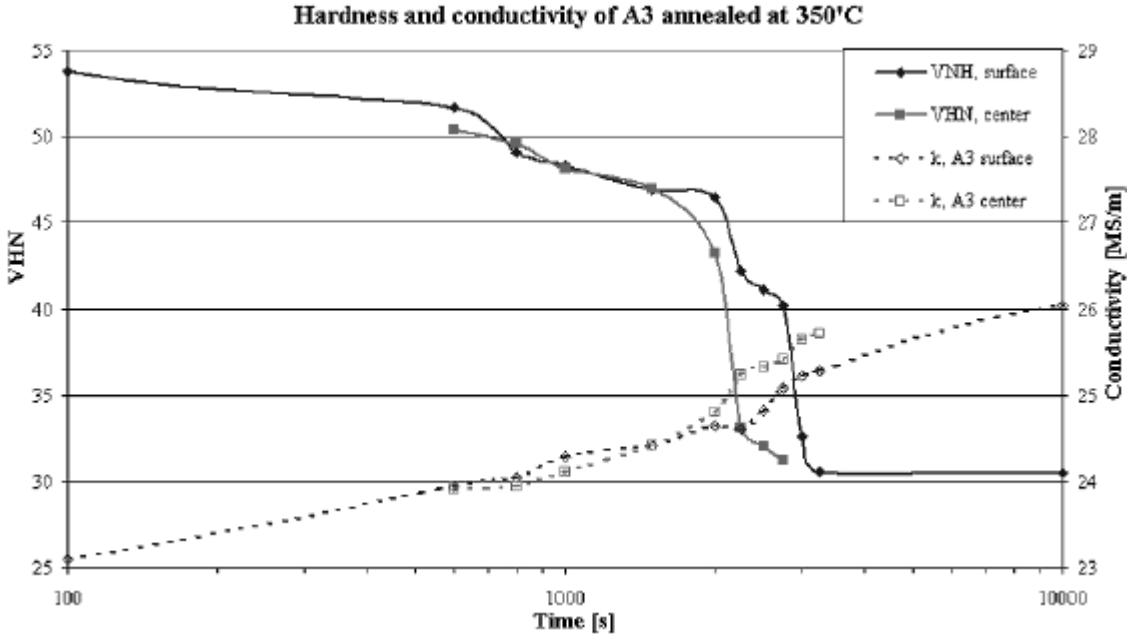

Fig.4.9: Hardness and conductivity curves of A3.0 annealed at 350°C in the centre and at the surface of the sheet.

TTT-diagram: How the precipitation and softening reactions interacts with each other in determining overall transformation kinetics can be illustrated by so-called TTT-diagrams, where the T's corresponds to temperature, time and transformation. The precipitates are effective in retarding the mobility of the migrating grain boundaries during recovery and recrystallisation. The result of concurrent precipitation is not only slower softening kinetics, but also fewer active nucleation sites and thus a coarser recrystallised grain size.

Based on the hardness and conductivity measurements (Fig.4.8 and Appendix 2) it was possible to construct TTT-diagrams, which predict when recrystallisation occurs prior to precipitation and when the softening reaction is slowed down by concurrent precipitation. The construction of the TTT-diagrams was done in the following way:

- It was assumed that recrystallisation start after a 25% drop in hardness from the as-deformed state. Time to 25% softening and time to complete recrystallisation were found from the softening curves.
- An increase in conductivity of 2.5% from the as deformed state was decided as the starting point of precipitation. Other percentages were also tested, but at this percentage (2.5%) the TTT-diagram actually predicted the "true microstructure" very well, *i.e.* whether the precipitation has an effect on the recrystallisation process or not.

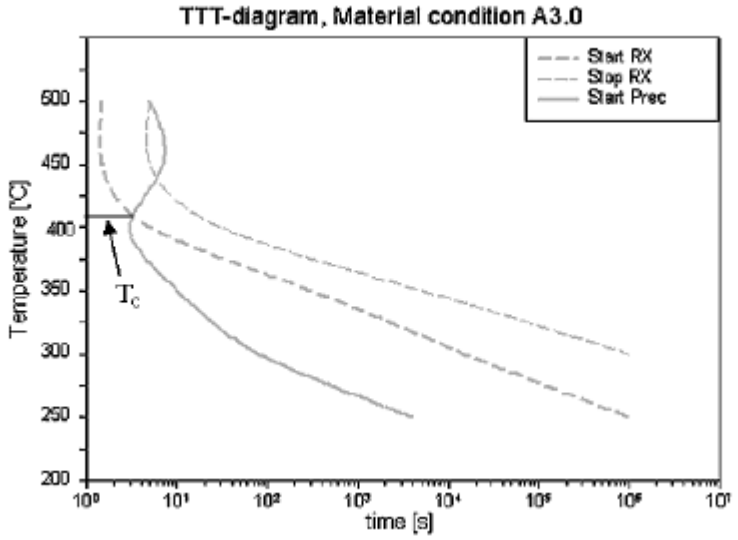

Fig.4.10: TTT-diagram of the A-material deformed to a strain of 3.0.

In Fig.4.10 the TTT-diagram of the A3.0-material is given. The full line indicates start of precipitation, while the broken lines indicate start and end of recrystallisation, respectively. In this figure a characteristic temperature, T_c, is indicated, *i.e.* a characteristic temperature where the precipitation curve crosses the curve indicating start of recrystallisation. Above this temperature recrystallisation is being less affected by concurrent precipitation, while at temperatures below T_c heavy precipitation retards recrystallisation effectively.

In Fig.4.11a-c) the TTT-diagrams of the different conditions are presented. Here the effect of strain is seen, *i.e.* with increasing strain both reactions of recrystallisation and precipitation are promoted. In Fig.4.12 the information given by the TTT-diagrams with respect to concurrent precipitation has been summarised. In this figure T_c has been plotted *vs.* amount of manganese in solid solution for the three respective strains.

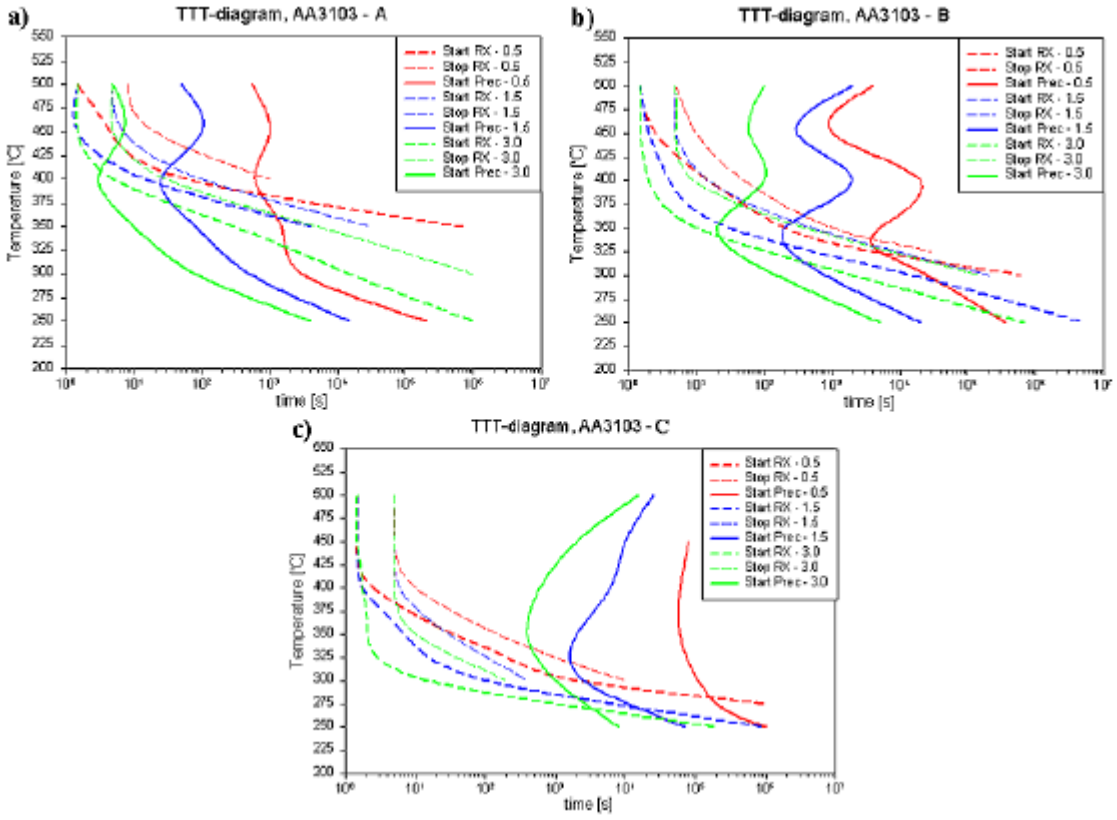

Fig.4.11: TTT-diagrams of the LP 3103-materials after different reductions.

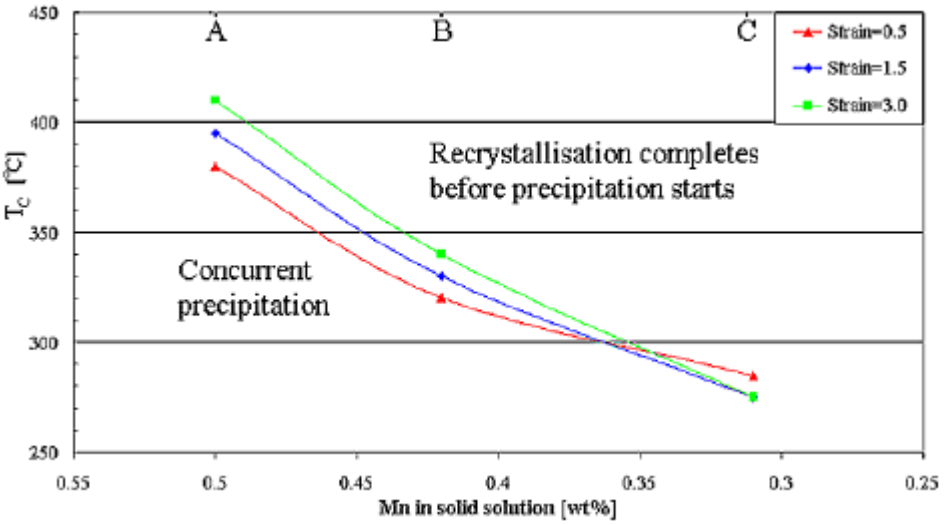

Fig.4.12: T_c *vs.* amount of Mn in solid solution, indicating when concurrent precipitation occurs.

From the TTT-diagram of the A-material, Fig.4.11a), it is seen that recrystallisation at temperatures above 450°C occurred without concurrent precipitation after cold rolling to a strain of 3.0. For the other two reductions, recrystallisation was unaffected by precipitation when the annealing was carried out above ~425°C. The precipitation nose for the A-material is found at 400°C. For the B-material, Fig.4.11b), the precipitation nose is found at 350°C, and above this temperature recrystallisation of B0.5 and B1.5 occurred without concurrent precipitation. After a strain of 3.0 the characterisitc temperature is ~375°C. Finally for the C-material, Fig.4.11c), no distinct sharp nose as for the two other material conditions was found. The nose of the C-material is found around 325°C-350°C.

4.1.5 Softening kinetics

Investigations of the softening kinetics were based on the well-known JMAK theory. To find the growth- or Avrami exponent $\log[\ln(1-X)^{-1}]$ is plotted *vs.* log time, and the slope of the curve gives the Avrami-exponent. Here X is the fraction recrystallised at the different stages of annealing, the value of X was determined by a counting procedure in a light optical microscope. Two material conditions were chosen for the following investigation, *i.e.* one was affected by precipitation, while the other condition was unaffected by precipitation during

softening. To represent these different conditions the samples A3.0-350°C and C3.0-300°C materials were chosen. The growth exponents of these conditions were expected to differ, since precipitation is expected to slow down the softening reactions. To check for dependencies of strain the materials A0.5 annealed at 400°C and C0.5 annealed at 350°C were also investigated. Both these material conditions should be unaffected by any precipitation reactions. The calculated growth exponents were found from Fig.4.13 and these values are given in Table 4.5. However, it is further seen that the lines are not completely straight. It is seen that the n-value is larger for the A3.0-condition than for the other conditions. According to theory this should have been the other way around due to the precipitation reaction taking place concurrent to recrystallisation for the A3.0-condition. Thus, the general assumption of site saturation is probably not valid in case of concurrent precipitation. In case of concurrent precipitation the postulation of such an investigation is maybe not fulfilled. *i.e.* heterogeneous nucleation, time-dependant nucleation or much recovery prior to recrystallisation might have occurred, which makes an influence on the kinetics.

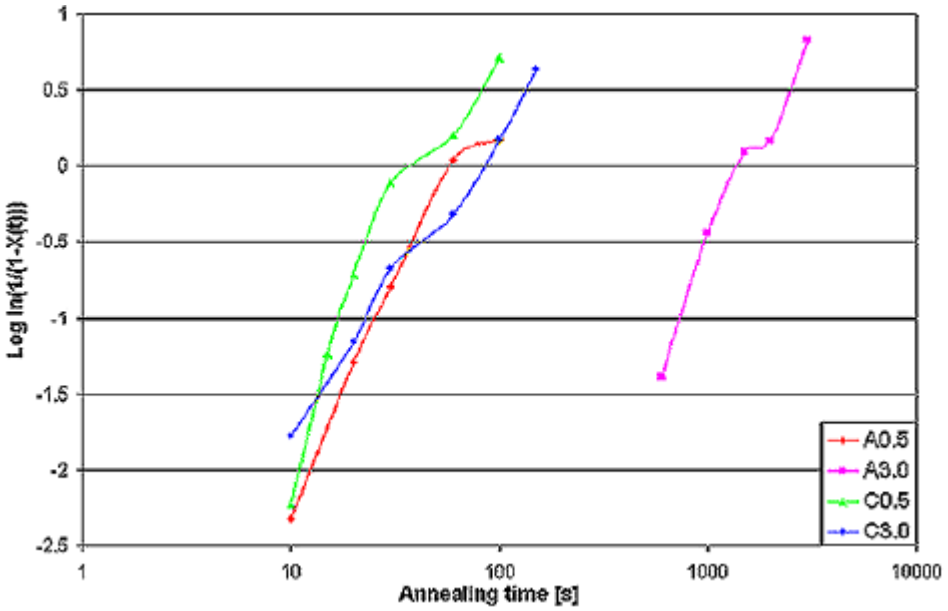

Fig.4.13: Avrami plots of A0.5-400°C, A3.0-350°C, C0.5-350°C and C3.0-300°C.

Table 4.5: Growth exponent of some material conditions during recrystallisation.

Material condition	A0.5(400°C)	A3.0(350°C)	C0.5(350°C)	C3.0(300°C)
Growth exponent	2.4	3.2	2.4	2.1

4.1.6 Recrystallised grain size

The average recrystallised grain sizes were measured from OIM-maps, using the linear intercept method in the rolling direction. More than 300 grains were taken into account for the analysis. The recrystallised grain size varied significantly, depending on whether concurrent precipitation occurred or not. The average grain size was found to be about 10 μm when the annealing temperature was above T_c in the TTT-diagrams, given in Fig.4.12, while in the opposite case, *i.e.* when concurrent precipitation occurred, the recrystallised grains became very coarse ranging up to several hundred microns in the rolling direction.

The average recrystallised grain size of the different conditions are given in Table 4.6, but it is strongly emphasised that there is a large scatter in the distributions as seen in Appendix 3. By comparing this table with the softening behaviour in Fig.4.8 and Appendix 2 it is observed that when the conductivity increases considerable prior to complete recrystallisation the grain size become coarse. Surprisingly, the grain size of the B1.5-300°C material is smaller than for B3.0-300°C. However by comparing the variations in conductivity for the two materials a larger increase is found for B3.0, indicating that more precipitation occurs for this condition and thus consequently fewer nuclei are activated.

It is further seen that after an applied strain of 0.5 the average grain size for all supersaturations and annealing temperatures are almost constant of about 20 μm. This observation is probably due to the low deformation. It is probable that the reduction is so low that PSN is not important. This is due to fact that too small deformation zones are built up around the particles after a strain of 0.5, and no other important heterogeneities for nucleation of recrystallisation are generated either, as e.g. transition bands due to grain splitting. For those conditions that managed to completely recrystallise within the limited annealing time no large increase in conductivity was observed. This is in accordance with a constant grain size of 20 μm for the conditions deformed to a strain of 0.5, *i.e.* the precipitates are not pinning certain nucleation sites which would have resulted in an increased grain size due to fewer nuclei.

Table 4.6: Average grain size of the recrystallised materials, measured from OIM-maps using the linear intercept method in the rolling direction.

Condition	Recrystallised grain size in RD [μm]			
	T=300°C	T=350°C	T=400°C	T=500°C
A 0.5	---	---	19.0	20.5
B 0.5	---	22.3	21.1	18.5
C 0.5	26.2	21.1	21.6	22.0
A 1.5	---	---	10.8	10.1
B 1.5	34.8	9.0	8.8	11.0
C 1.5	9.6	9.8	11.8	12.7
A 3.0	237.3	62.0	9.9	8.8
B 3.0	60.6	7.5	9.7	10.9
C 3.0	7.4	7.9	9.5	10.8

In Fig.4.14 two types of recrystallised grain size distributions of the A3.0-material annealed at 350°C are shown. The first is the actual distribution, while the other is normalised with respect to the average grain size, this was done to get an impression on how large area each class covers of the microstructure. The logarithmic scale size distribution is also included in Fig.4.14 to check for log-normality of the grain size distributions, which is a feature commonly observed for recrystallised aluminium alloys. The distributions of the differently homogenised material conditions deformed to a strain of 3.0 and annealed at various temperatures are given in Appendix 3.

In Fig.4.15 OIM-micrographs of the recrystallised A3.0-material annealed at different temperatures are seen, and the effect of precipitation is clearly seen. At low temperatures the grains are large and elongated in the rolling direction, while at higher annealing temperatures the grains are more equiaxed with a much smaller grain size than for low temperatures.

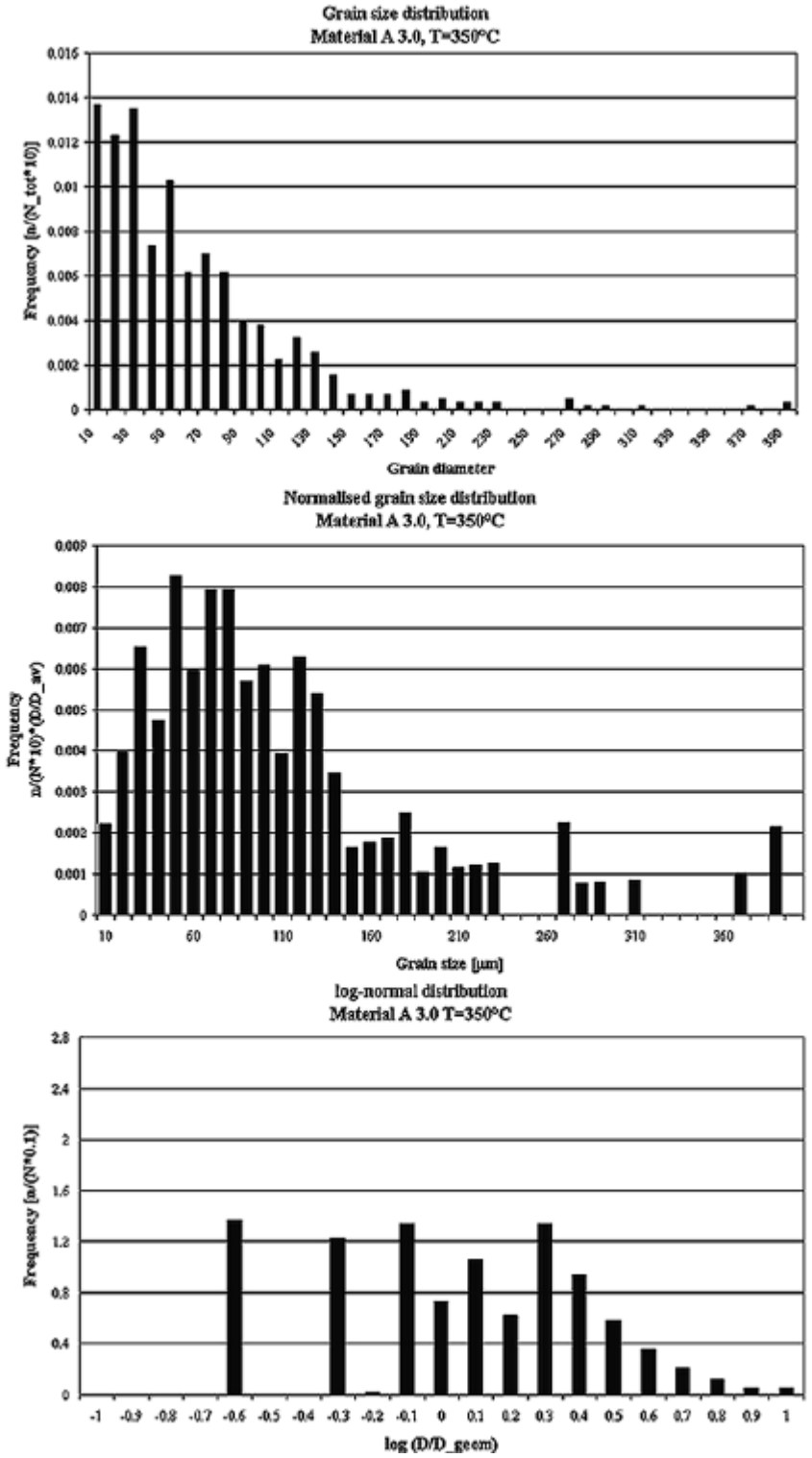

Fig.4.14: Grain size distributions of A3.0 annealed at 350°C.

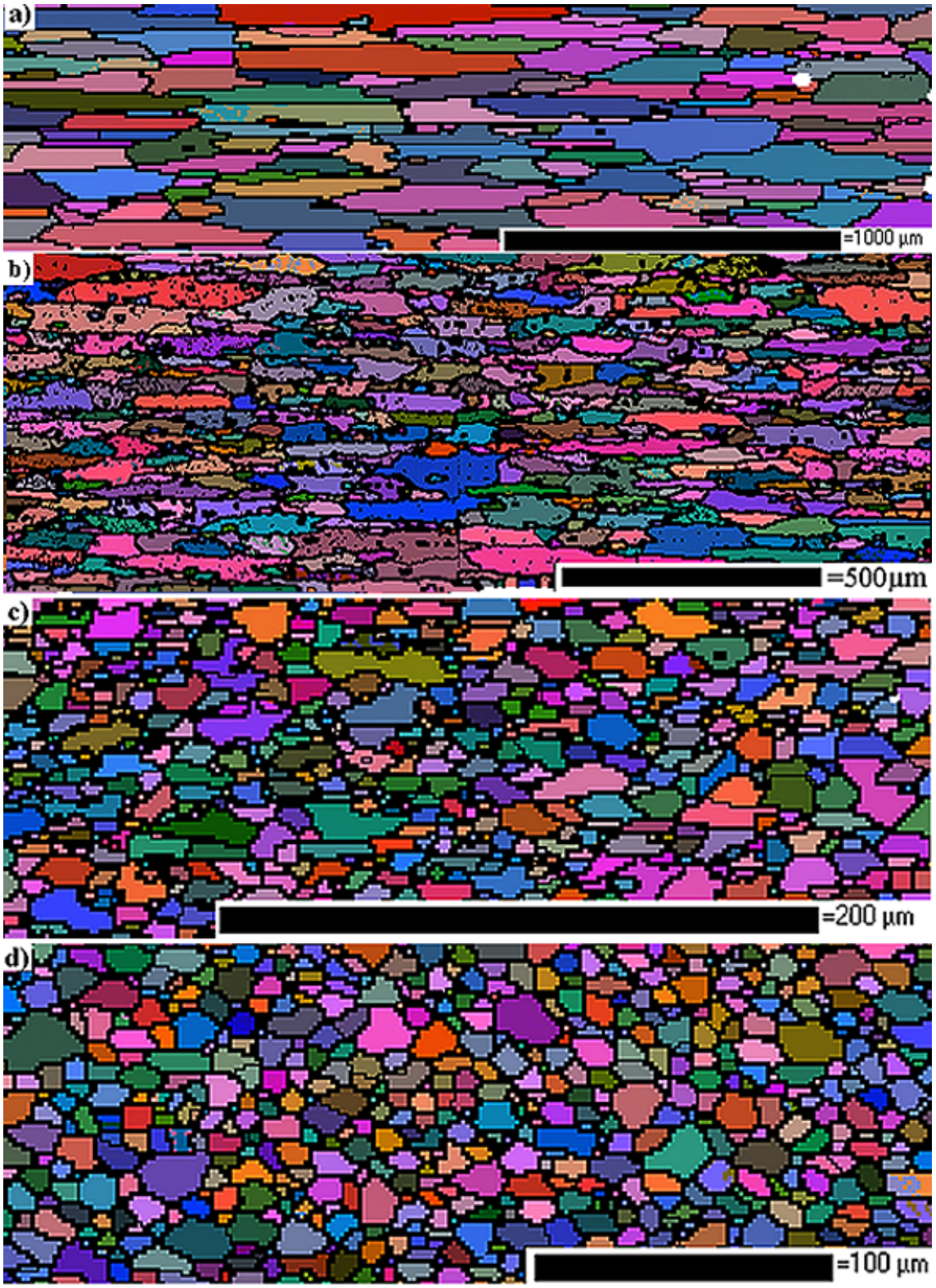

Fig.4.15: Micrographs of the recrystallised A3.0-material annealed at a) 300°C, b) 350°C, c) 400°C and d) 500°C. Note the differences in the scaling bar.

4.1.7 Recrystallisation textures

During isothermal annealing of a deformed supersaturated condition the chosen annealing temperature is very important on the final recrystallisation texture, as well as on the recrystallised grain size as seen in the previous chapter. By choosing a high annealing temperature concurrent precipitation can be avoided as seen in the TTT-diagrams in Fig.4.11. By reducing the forces that retards recrystallisation, the recrystallisation texture could appear differently as compared to what was found when precipitation occur concurrent to recovery and recrystallisation. The effect of PSN, resulting in a more random texture, is known to be more important as the temperature increase.

Like the grain size, the recrystallisation texture was also strongly affected by selecting recrystallisation temperatures above the characteristic temperature of the TTT-diagrams. The effect of recrystallisation temperature for the different combinations of homogenisation variants and rolling reductions are shown in the ODFs in Fig.4.16 and Fig.4.17. The fully recrystallised materials annealed at 400°C and 500°C had qualitatively similar recrystallisation textures, and for this reason only the ODFs of T=500°C are shown in these figures. For the coarse grained conditions several texture measurements have been averaged to present the global texture. After annealing the materials deformed to a strain of 0.5 the final recrystallisation textures were close to random for all combinations of amounts of manganese in solid solution and annealing temperature. From the ODFs it is seen that a strain of 3.0 was required to produce recrystallisation textures with some strength.

By comparing the softening and conductivity curves with the final recrystallisation textures it is seen that in the case of concurrent precipitation, *i.e.* below T_c, the recrystallisation texture is dominated by the P- and ND-rotated cube textures. In the opposite case a relatively weak cube texture is observed. The cube texture strengthens with decreasing amount of manganese in solid solution and with increasing annealing temperature. Fig.2.12 illustrates where the different texture components are found in the φ_2=0°-section of the ODF.

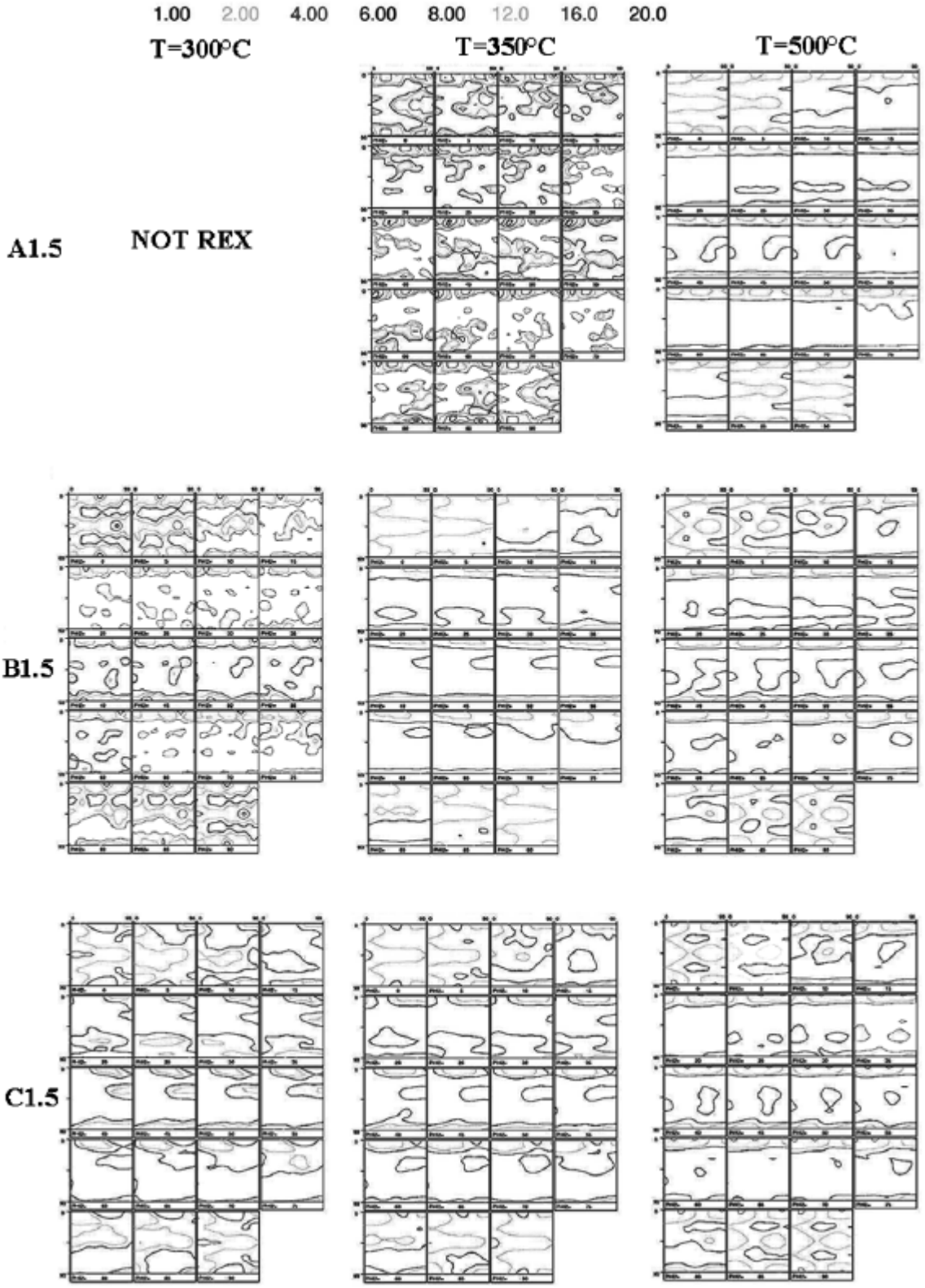

Fig.4.16: Recrystallisation textures of the LP 3103-materials after cold rolling to a true strain of 1.5 and subsequently annealing.

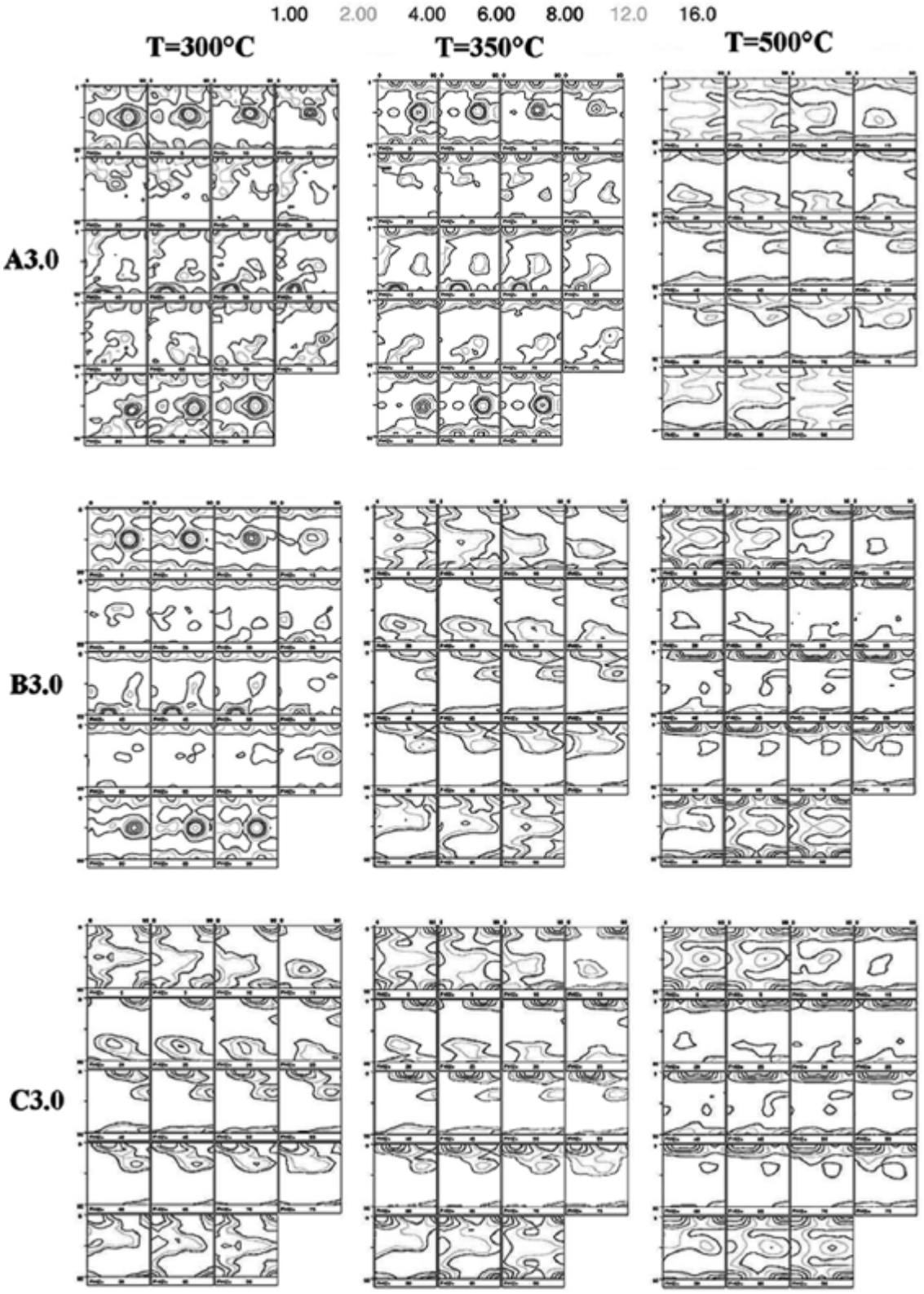

Fig.4.17: Recrystallisation textures of the LP 3103-materials after cold rolling to a true strain of 3.0 and subsequently annealing.

In Fig.4.18 the intensities of the dominating texture components taken from the ODFs are plotted *vs.* annealing temperature. These material conditions have been deformed to a strain of 3.0 before the subsequent annealing at the various temperatures. In Fig.4.18 it is seen that the P- and ND- rotated cube orientations follows the same tendencies, while the exact cube texture increases in strength with increasing temperature and saturates at 8 times random for the C3.0-material condition. The cube orientation also reaches an intensity of 8x random for the B3.0-500°C material. It is further seen that when concurrent precipitation takes place the P- and ND-rotated cube orientations dominates the recrystallisation texture. These material conditions are A3.0-300°C, A3.0-350°C and B3.0-300°C and in addition A1.5-350°C and B1.5-300°C. Under these conditions the P-orientation is always found to be the strongest component.

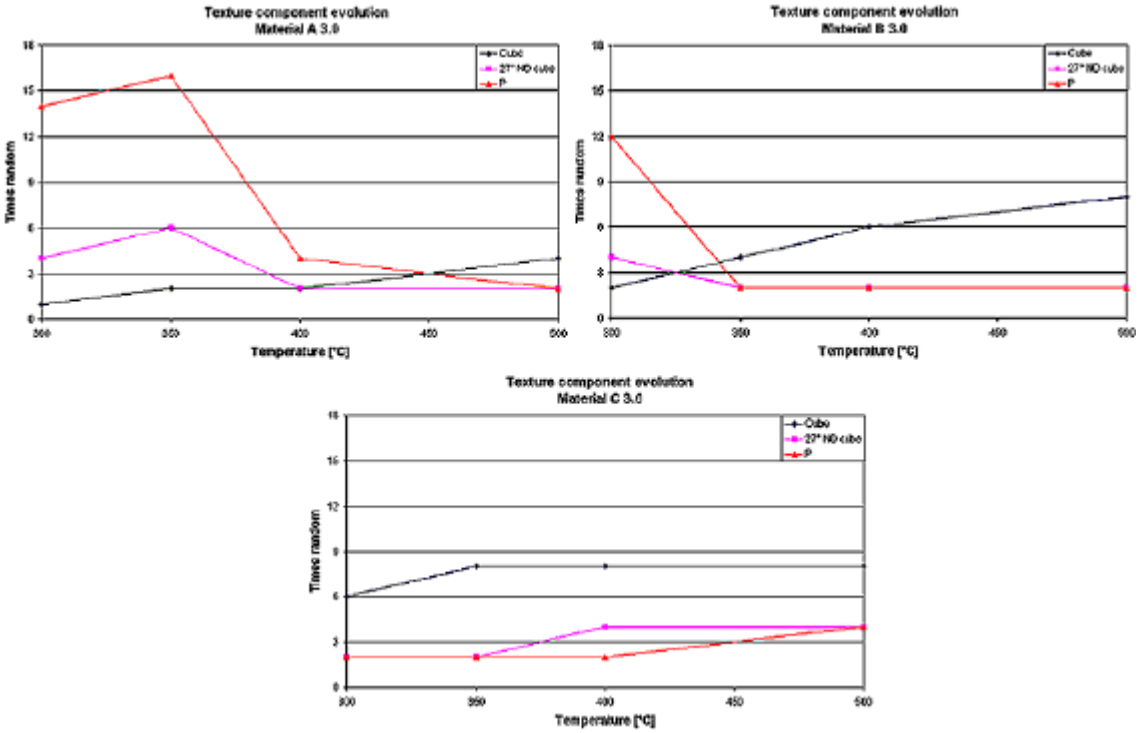

Fig.4.18: Contour line intensity of the recrystallised LP 3103-alloy deformed to a strain of 3.0, the figures are based on the intensity of the respective ODFs.

4.1.8 Texture evolution of A3.0 annealed at 350°C

The global textures of the A3.0-material annealed for different times at 350°C were measured by X-ray diffraction. Since the final recrystallisation texture was dominated by the P- and ND-rotated cube textures, as seen in Fig.4.17, only the φ_2=0° section is shown in Fig.4.19. A very abrupt change in texture was observed once the texture changed from a typical deformation type to the final recrystallisation texture. The texture sharpened at the later stages of annealing, as the α- and *b*-deformation texture fibres disappeared.

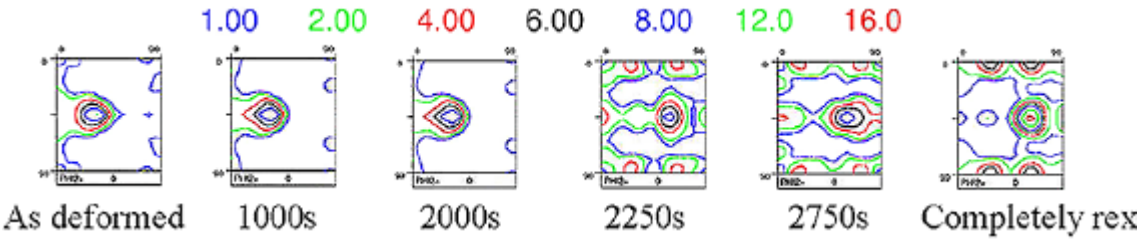

Fig.4.19: Evolution of global texture of A3.0 annealed for different times at 350°C measured by X-ray diffraction.

4.1.9 Growth rate experiments of A3.0 annealed at 350°C

In case of concurrent precipitation, *i.e.* an observation of a large increase in conductivity prior to and during recovery and recrystallisation, the growth rate of the randomly oriented grains have been compared to those with P- and ND-rotated cube orientations. For this examination OIM-mapping of the A3.0-material annealed for different times at 350°C were carried out. All grains within 15° of the given orientations were counted for belonging to the ideal orientation. More than hundred grains of each orientation were taken into account for the growth rate investigations. From the calculated growth rates given in Fig.4.20a), *i.e.* the slope of the curves, it is seen that the P- and ND rotated cube textures have their growth advantages in the early stages of annealing, more specifically during the first thousand seconds of annealing. At the later stages, all grains seem to grow with an almost constant growth rate. This indicates that it is the nucleation event and the early stages of growth of these nuclei that determines the final recrystallisation texture of this material.

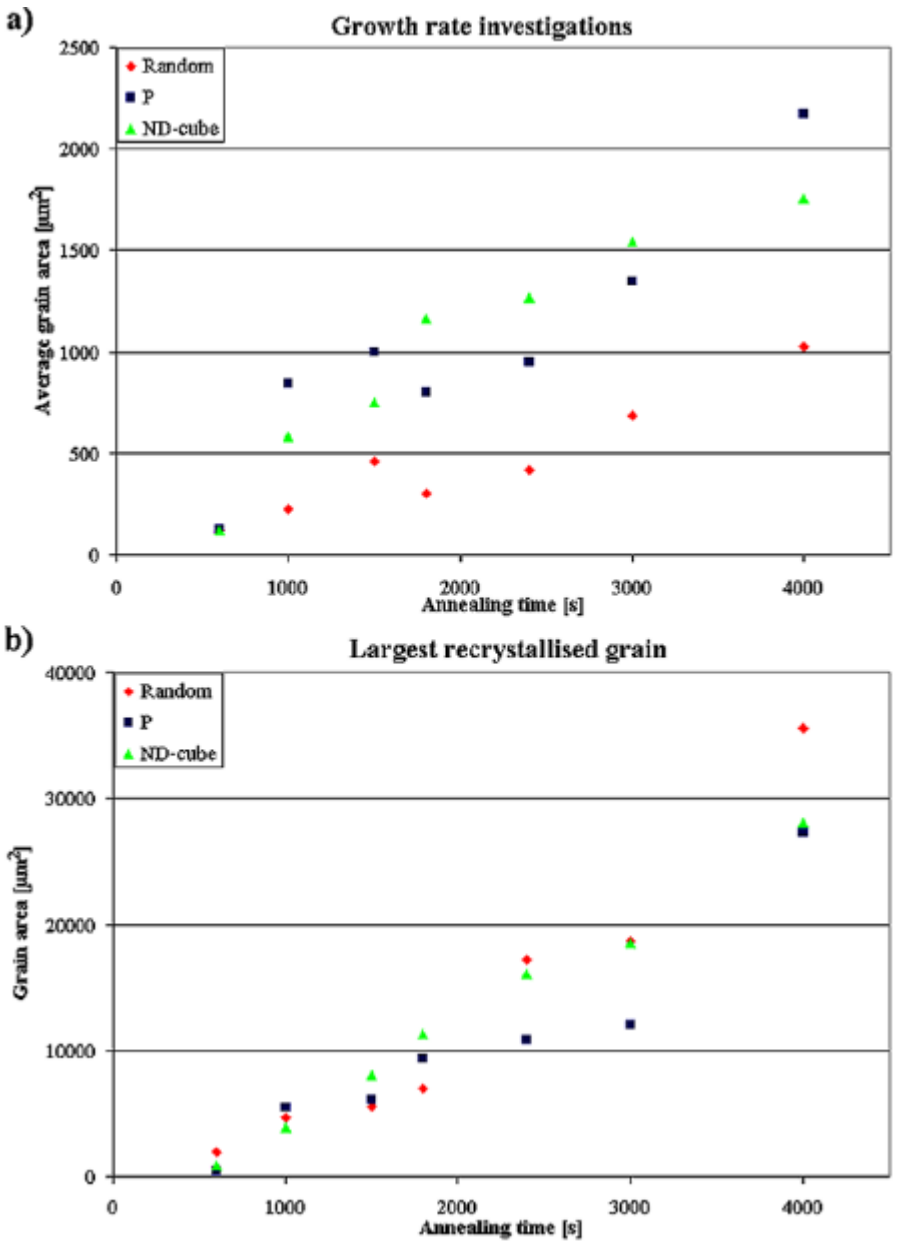

Fig.4.20: Based on OIM-maps of A3.0-350°C an investigation of the P, ND rotated cube and randomly oriented grains as function of annealing time has been carried out. In a) the growth rate is seen as the slope of the average grain size evolutions, while in b) the size of the largest grains of the different orientations are plotted.

By following the largest grain in the distribution upon annealing no significant difference of the various conditions could be detected, Fig.4.20b). This indicates that no growth selection is taking place during annealing of the present alloy. It thus seems more likely that it is a nucleation effect that gives the P- and ND-rotated cube their advantage in the early stage of annealing.

4.1.10 Nucleation of the P- and ND-rotated cube orientations

The dominating recrystallisation texture components, *i.e.* the P- and ND-rotated cube orientations, of the A3.0 material condition annealed for 10 minutes at 350°C was investigated in an FEG-SEM with the EBSD technique. All grains within 15° of the exact orientations were taken as the ideal orientation. From the investigations presented in Chapter 4.1.9, it is seen that some nucleation was detected in the conventional SEM and that the nucleated recrystallised grains had grown to a size of about 10 μm. At the same time, the grains are so small that in some cases it is possible to suggest where the grains have nucleated. For such small grain sizes it is more convenient to use the FEG-SEM which has better spatial resolution.

From the growth rate experiments it was found that only one out of five grains belonged to either the P-orientation or the ND-rotated cube orientation. The other grains contribute to the random scatter in the ODFs.

In Fig.4.21 some examples of recrystallised grains of P- and ND-rotated cube orientations are shown (right). These grains are positioned close to areas were indexing was impossible. These unindexed areas are most probably primary particles, which are unindexed due to a different crystallographic structure than the aluminium matrix. From these maps it is reasonable to suggest that PSN play a role in the nucleation event of the P- and ND-rotated cube orientations. The OIM-maps to the left are the microstructure where all grains are included. It is seen that also grains of other orientations than of P- and ND-rotated cube orientations have been nucleated.

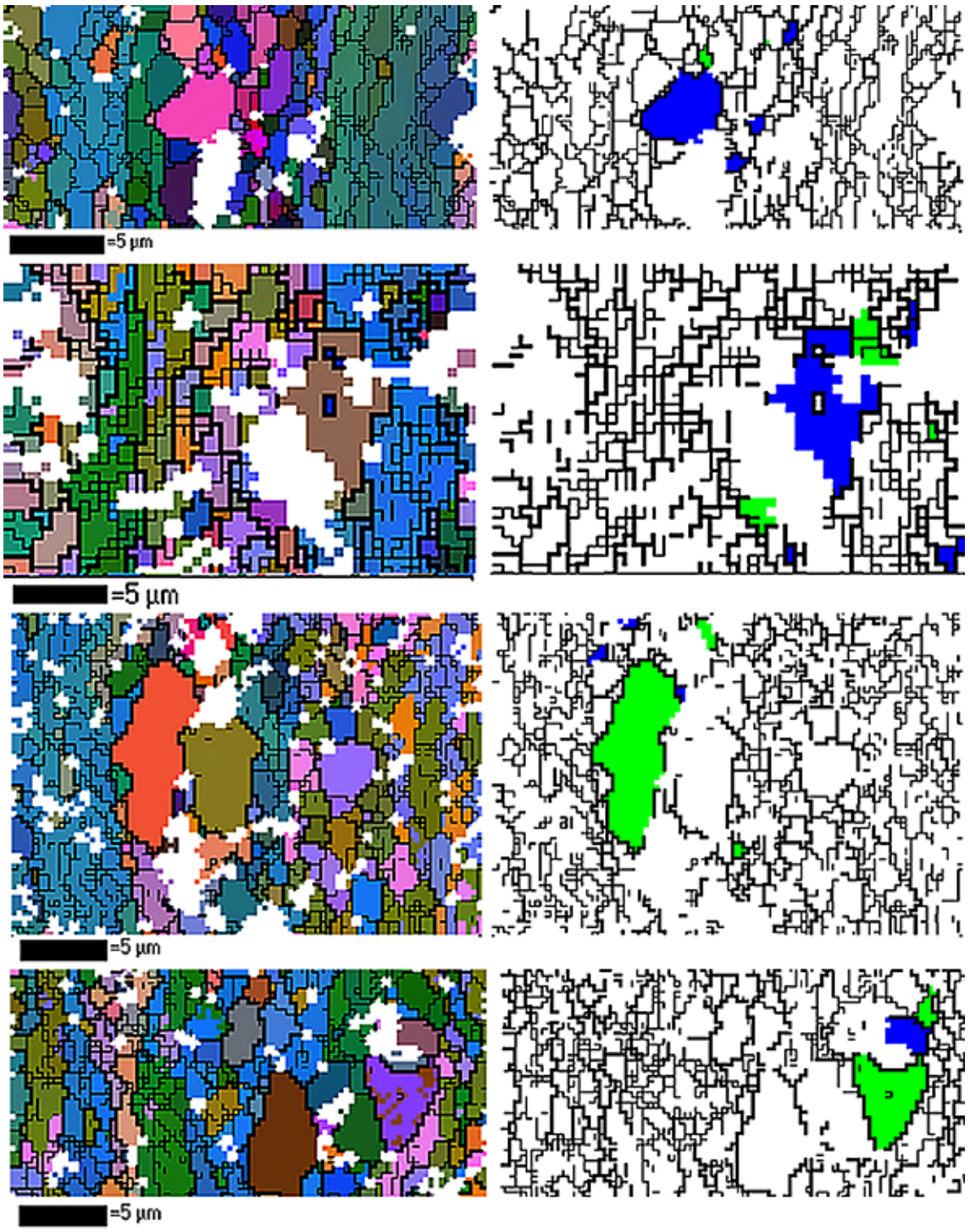

Fig.4.21: Nucleation of P and ND-rotated cube grains, mapped by the EBSD-technique. The images to the left are the mapped areas of the microstructure. The images to the right show the P and ND-rotated cube grains, which are coloured by blue and green, respectively. The grain boundaries are also added to the micrographs, thin lines represents low angle grain boundaries ($1.5° < j < 15°$), while thick lines represent high angle grain boundaries (>15°).

4.1.11 Precipitation of A3.0 upon annealing at 350°C

The A3.0-material annealed at 350°C was investigated in detail with respect to the number of dispersoids per area as a function of annealing time. Counting of dispersoids at different stages of annealing was carried out manually on micrographs taken at magnifications between 5.000-20.000x. In Fig.4.22 the microstructural evolution of A3.0 annealed at 350°C is shown. These micrographs were obtained at two different magnifications, this was done in order to visualise both the microstructural evolution on a "global" scale and the formation and evolution of the precipitates in more detail. From the high magnification micrographs it is seen that most of the precipitates formed within the first minute of annealing. It is also seen that precipitation occurred on the grain boundaries, which are accompanied with higher stored energy. At these heterogeneities it is easier for precipitation to occur, and the solute atoms have a higher diffusivity in these areas. Upon further annealing the subgrains where found to change from being elongated in the rolling direction to a more equiaxed configuration. From Fig.4.22 c) and d) it is seen that nucleation of strain free grains has occurred by particle stimulated nucleation of recrystallisation (PSN), but it should be noted that nucleation from other sites was also observed or possibly that the grains have nucleated at a particle below the investigated surface.

Further, a closer examination of the materials A3.0 annealed at 300°C and 400°C, and C3.0 annealed at 300°C were performed. According to the conductivity curves, Fig.4.8, lots of dispersoid should be found for A3.0-300°C and only a few for the other conditions. The result of precipitation of A3.0 annealed at 300°C and 400°C are shown in Fig.4.23. It is seen that for the lowest temperature lots of dispersoids were formed, and they grow upon annealing. At high temperature (400°C) some dispersoids were formed during annealing. The dispersoid density is seen to be lower as compared to the materials annealed at a lower temperature. For the C3.0-material annealed at 300°C hardly any dispersoids were detected even in the fully recrystallised material.

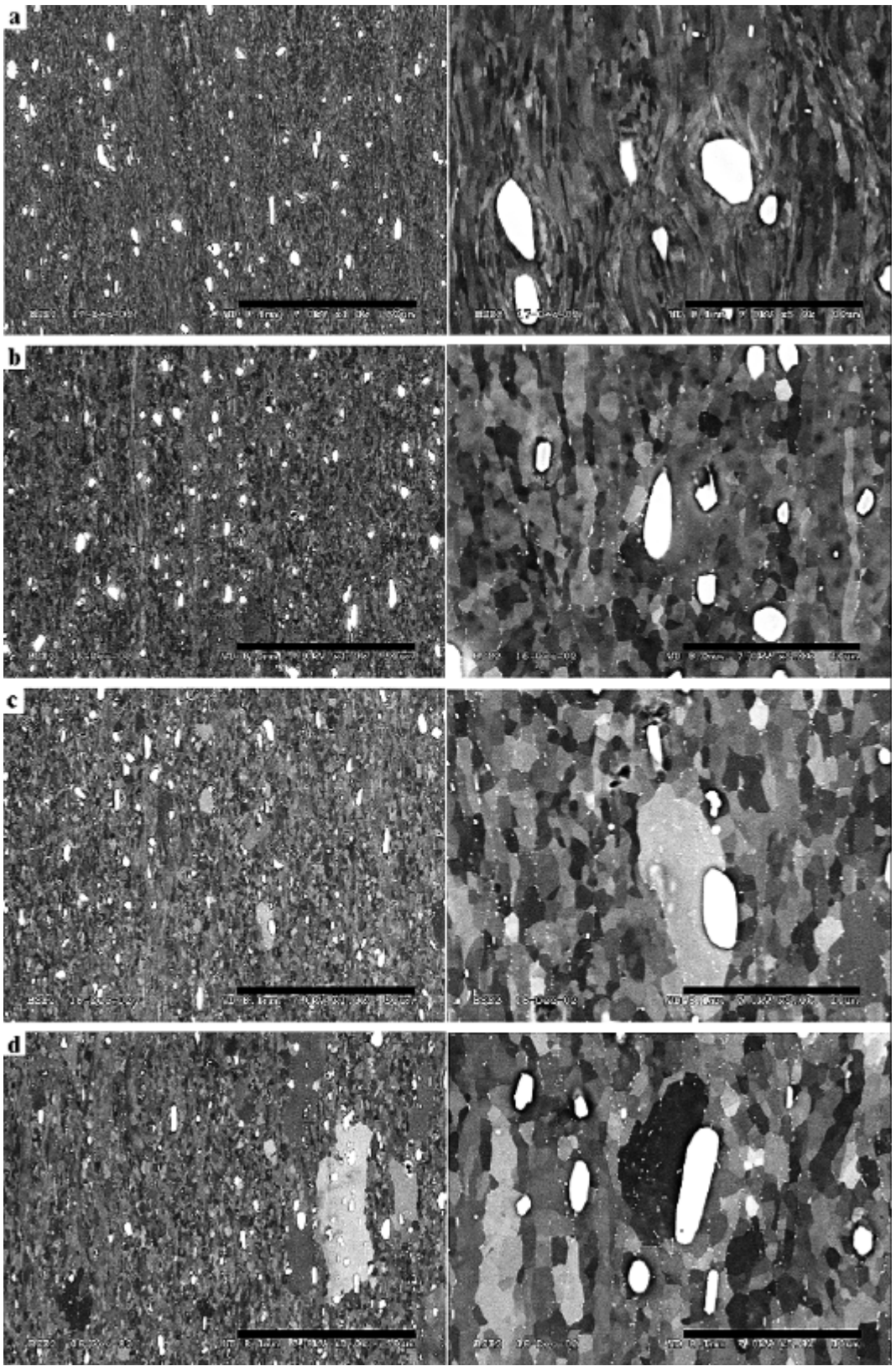

Fig.4.22: Continued next page.

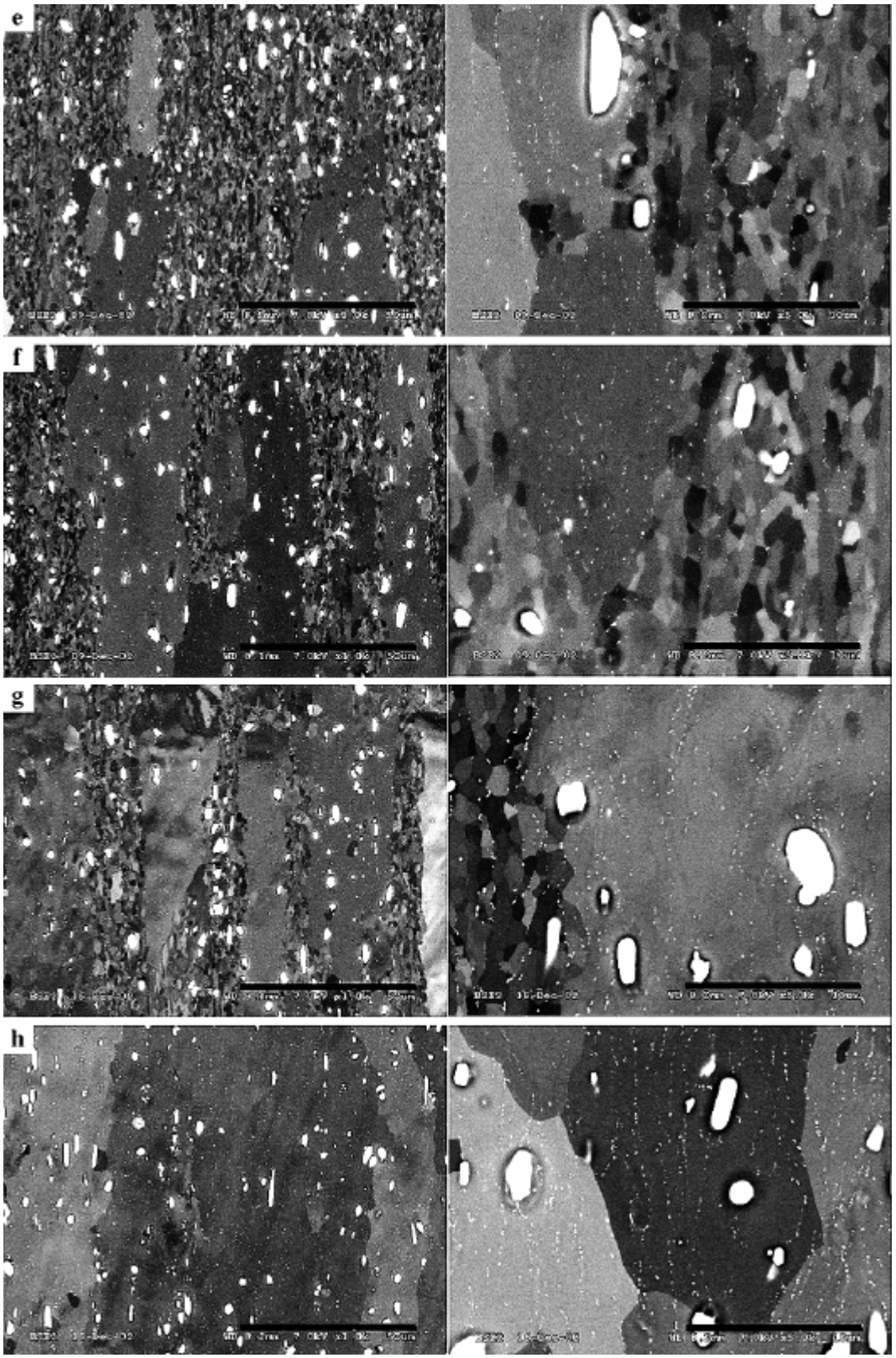

Fig.4.22: Micrographs of A3.0, a) as deformed, b-h) annealed at 350°C for, b) 1 min, c) 10 min, d) 20 min, e) 30 min, f) 40 min, g) 50 min and h) 60 min.

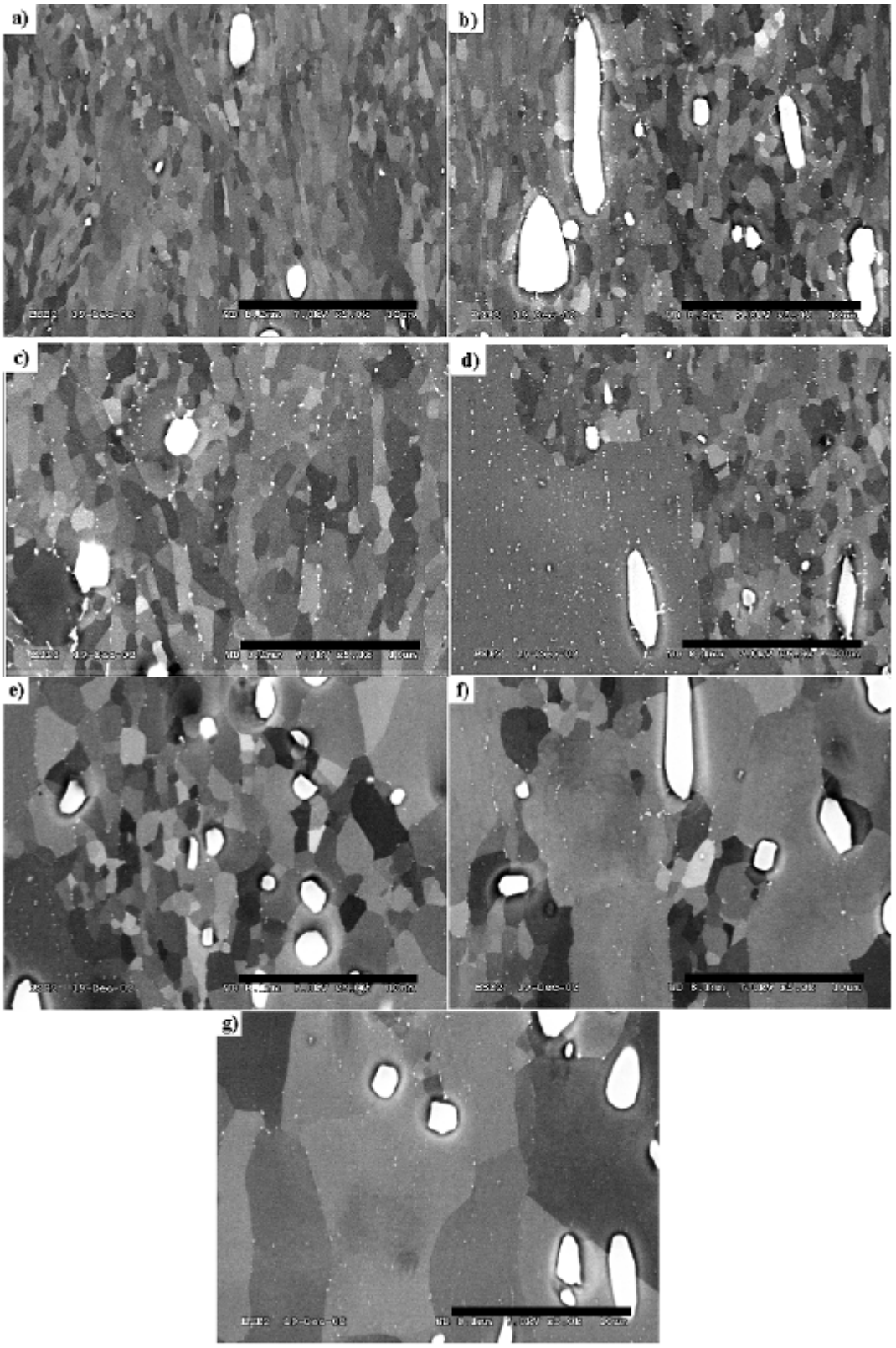

Fig.4.23: Micrographs of A3.0-material annealed at 300°C for a) 1.000 s, b) 30.000 s, c) 100.000 s and d) 300.000 s, and 400°C for e) 30 s, f) 100 s and g) 300 s.

In Fig.4.24 the evolution in dispersoid density of the A3.0-350°C condition *vs.* annealing time is presented. From this figure it is seen that the dispersoids were formed during the first minute of annealing, as was observed in the micrographs of the microstructure in Fig.4.22. The number of dispersoids was then almost constant throughout the annealing, except for the final stage where an increase was observed. Also included in the figure is the evolution in electrical conductivity and the fraction recrystallised measured by light optical microscopy. It should be noted, however, that the conductivity and dispersoid density was not measured on the same samples as where the fraction recrystallised was measured.

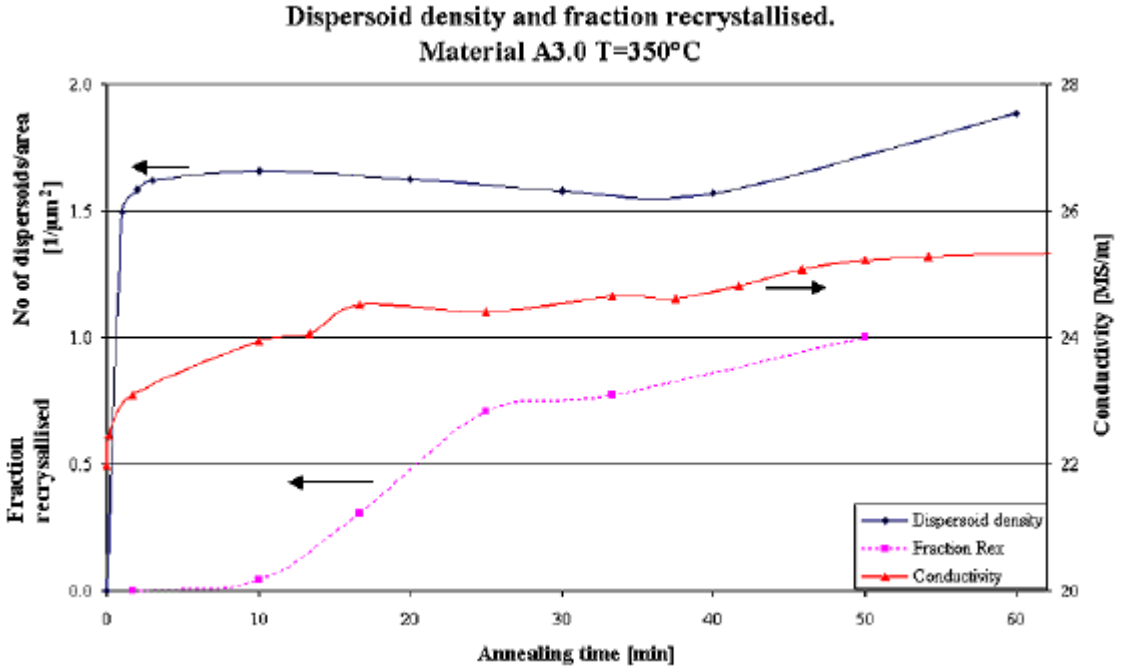

Fig.4.24: Evolution of dispersoid density during annealing at 350°C of the A3.0-material. The evolution of electrical conductivity and the fraction recrystallised as found by a point counting procedure in light optical microscope are also included in the figure.

4.1.12 Dispersoids after long annealing times at 400°C

After long annealing times at a high annealing temperature the conductivity of the three conditions deformed to a strain of 3.0 increased. This increase occurred in the fully recrystallised material, which indicates precipitation or growth of the already existing dispersoids. The objective of this investigation was to check for differences in density, size and morphology of the three materials.

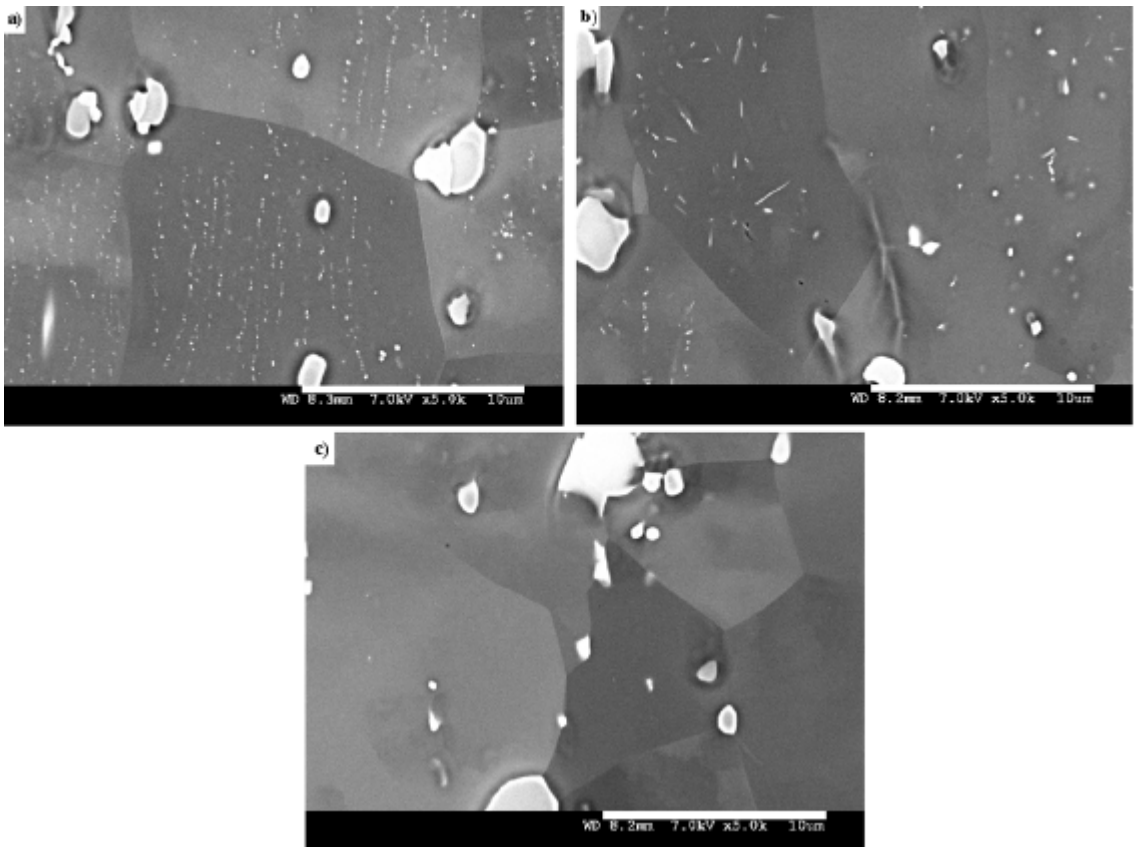

Fig.4.25: Micrographs after annealing at 400°C for 11 ½ days for the conditions a) A3.0, b) B3.0 and c) C3.0.

In Fig.4.25 micrographs of the materials deformed to a strain of 3.0 and annealed at 400°C for 11 ½ days are shown. It is seen that the morphology is quite different for the different material conditions, as expected from the conductivity curves. The increase in conductivity for the A-material was large and increased throughout the annealing. In Fig.4.25a) the dispersoids are seen to be narrowly spaced and they lie in strings, *i.e*. the nucleation has presumably occurred on the original deformation bands. In Fig.4.23e-f), where the precipitation reaction was investigated in the course of the recrystallisation reaction, the dispersoid density is certainly not as high as in Fig.4.25a). This means that some clustering and decoration of the subboundaries happened at the early stage of annealing, but the precipitates were probably too small to be observed after the time investigated in 4.23e-f). In Fig.4.25a) the precipitates have coarsened and resulted in a structure as shown in the figure. With regard to the dispersoids it is seen that close to the grain boundaries and primary particles few dispersoids are observed. This observation is most probably due to coarsening of the larger constituent particles

(Ostwald ripening), *i.e.* the small precipitates are dissolved and the solute atoms migrates towards the large particles, for more details see *e.g.* Martin *et al.* (1997). It is as well known that diffusion of solute atoms occurs easier in the vicinity of a high angle grain boundary, thus these areas become depleted before areas which require longer diffusion distances.

The B-material has a differently dispersoid morphology, as seen in Fig.4.25b). Here the shape of the dispersoids is found as a combination of rod like and spherical precipitates, while for the A-material only spherical dispersoids were found. The dispersoids are also significantly larger and have a lower density than for the A-material, this is obviously because of a lower supersaturation of solute atoms that might precipitate during annealing.

For the C-material only a few dispersoids were found, and they have grown quite large after this long annealing treatment, see Fig.4.25c). The increase in conductivity is not very large either, so it was not surprising that a low dispersoid density was actually observed. The increase in conductivity can be ascribed to the growth of these few dispersoids and to the diffusion of atoms in supersaturated solid solution to the primary particles. From the micrograph it seems most likely that the dispersoids have nucleated at the high angle grain boundaries of the recrystallised material.

4.2 Industrially processed AA3103-alloy

This alloy was produced by Hydro Aluminium Deutschland, former VAW, in order to perform a through process experimental investigation as a part of the Vir[Fab]-project. For simplicity the name of the alloy has been called CP 3103 (commercially processed) to avoid confusion with the LP 3103-material (laboratory processed) investigated in the Chapter 4.1.

Basically two aspects have been investigated for this alloy. Firstly the softening kinetics of the cold rolled material has been followed in detail. Secondly some microstructural investigations of the material exiting the breakdown mill and the tandem mill, respectively, *i.e.* through the hot rolling schedule, have been carried out.

The homogenisation and rolling was carried out at the rolling mill in Norf. The processing route has been a standard one:

- The first step was DC casting into a rolling slab with a dimension of 600 mm x 1700 mm (thickness x width) and with a length of 4.5 m.
- Before rolling the material was heated and homogenised at a temperature between 520°C-600°C and held for more than five hours, followed by a slow cooling sequence to about 450°C.
- The material then entered the breakdown mill. The breakdown mill is a reversal mill where the material was rolled down to a thickness of 30 mm. The first reduction was low, about 5%, then the amount of deformation increased with a final reduction of 30-40% after 15-18 passes. The material after breakdown rolling will in the following be named transfer slab or transfer-gauge material.
- The material was subsequently hot rolled in a multi-stand finishing mill with an exit temperature above 300°C and a thickness of 4.2 mm. The material was coiled after rolling, and will in the following be named as re-rolled material.
- After cooling to room temperature the material was cold rolled to a final thickness of 1.2 mm and finally coiled. It should be noted that the industrial cold rolling may involve temperatures up to 100-150°C, yet these temperatures are still being termed as cold.

4.2.1 As cast material

The particle structure of the *as cast* material was not surprisingly similar to the LP 3103-alloy. Micrographs of the particle structure are given in Fig.4.26, while the cumulative size distribution of particles is given in Fig.4.34. It can be seen from the high magnification picture that no dispersoids were present in the *as cast* structure.

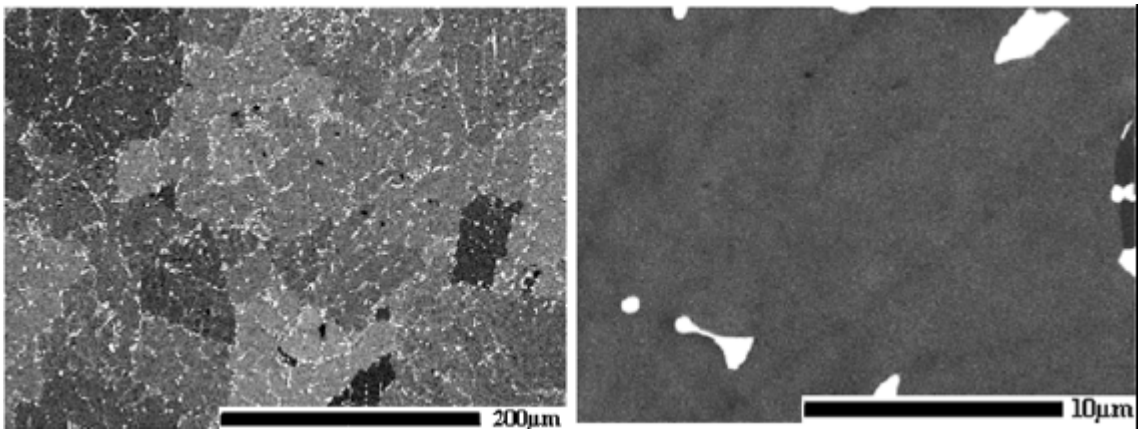

Fig.4.26: Particle structure of the *as cast* CP 3103-alloy.

Due to high cooling rates during DC-casting a high supersaturation of alloying elements are obtained in supersaturated solid solution. Based on electrical conductivity measurements the amount of manganese was calculated by the Matthiessens rule, the result of the calculations through the processing route are given in Table 4.7. The producer of the materials has also estimated the amounts of manganese in solid solution through the processing line [Löchte (2001)]. These latter amounts were calculated from rest-resistivity measurements at 4.2 K. By comparing the estimations of the two different methods it is seen that no large differences were found except for the re-rolled and cold rolled materials. If the estimations calculated by the Matthiessens rule have been corrected for Fe and Si in solid solution a better agreement would probably have been achieved. However, accurate estimates of these values are however impossible to obtain.

Table 4.7: Amount of manganese in solid solution (assuming only a supersaturation of Mn) after the different processing steps. The amounts were calculated from electrical conductivity measurements at room temperature (RT) and from rest-resistivity at 4.2 K.

Condition	**Conductivity at RT [MS/m]**	**wt%Mn in ss based on the Matthiessens rule**	**wt%Mn in ss based on rest-resistivity at 4.2 K***
As cast	18.3	0.78	0.77
Homogenised	21.3	0.56	0.51
Transfer slab	23.8	0.43	0.42
Re-rolled	24.2	0.41	0.36
Cold rolled	23.6	0.44	0.34

* Measured and calculated by the producer of the alloy [Löchte (2001)].

4.2.2 Transfer-gauge material

The transfer-gauge material, *i.e.* after breakdown rolling, was in a fully recrystallised condition as seen from the EBSD-map in Fig.4.27. Also included in this figure is the recrystallisation texture in the centre of the slab measured by X-ray diffraction (XRD). The recrystallised texture was dominated by the cube orientation, and the intensity of the cube was found to be ~16x random. The texture close to the surface has also been measured, but only minor differences were found as compared to the texture in the centre of the slab.

From the particle distribution (Fig.4.34) it is seen that the number of particles are higher than for the *as cast* material, but it should be kept in mind that before rolling the material was homogenised for several hours at a temperature above the rolling temperature. During this preheating period the particles spheroidise and grow due to grain boundary diffusion of manganese. It is further expected that the particles continue to grow during the cooling sequence before reaching the rolling temperature. However, as the material is rolled the particles are expected to break up somewhat.

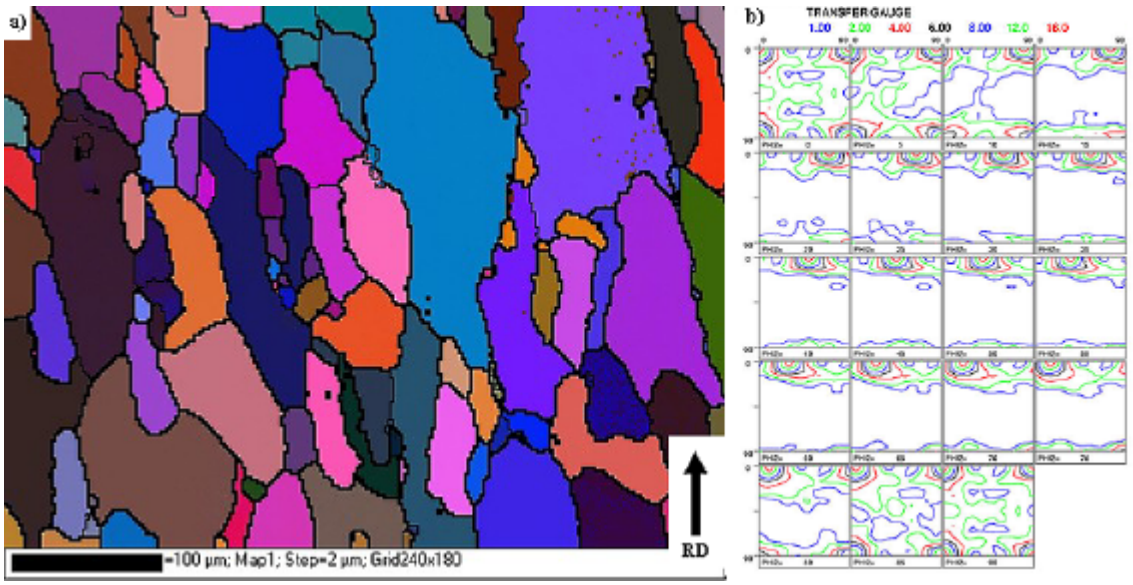

Fig.4.27: a) OIM-map of the transfer-gauge material showing large scatter in grain sizes and that the grains are elongated in the rolling direction. b) An ODF showing global texture measured by XRD.

4.2.3 Re-rolled material

In the centre of the re-rolled material the microstructure consisted of a combination of recrystallised grains which were layered in bands separated by deformation bands, Fig.4.28a). Within the deformation bands some small recrystallised grains are also observed, they are assumed to have nucleated at the later stage of the cooling sequence after tandem rolling or been pinned by a high suspension of small precipitates. As for the transfer gauge material the scatter in grain size was large and the recrystallised grains were elongated in the rolling direction. The ODF of the centre section show a combination of the cube texture and the orientations along the *b*-fibre with a minor peak for the brass orientation, Fig.4.28b-c).

According to the Matthiessens rule, based on the conductivity measurements, about 0.41wt% manganese is expected to be in solid solution after the multi-stand tandem rolling, Table 4.7. The calculation of manganese in solid solution from conductivity measurements gave only a minor decrease compared to the transfer-gauge material, while rest-resistivity measurements gave a decrease of 15%.

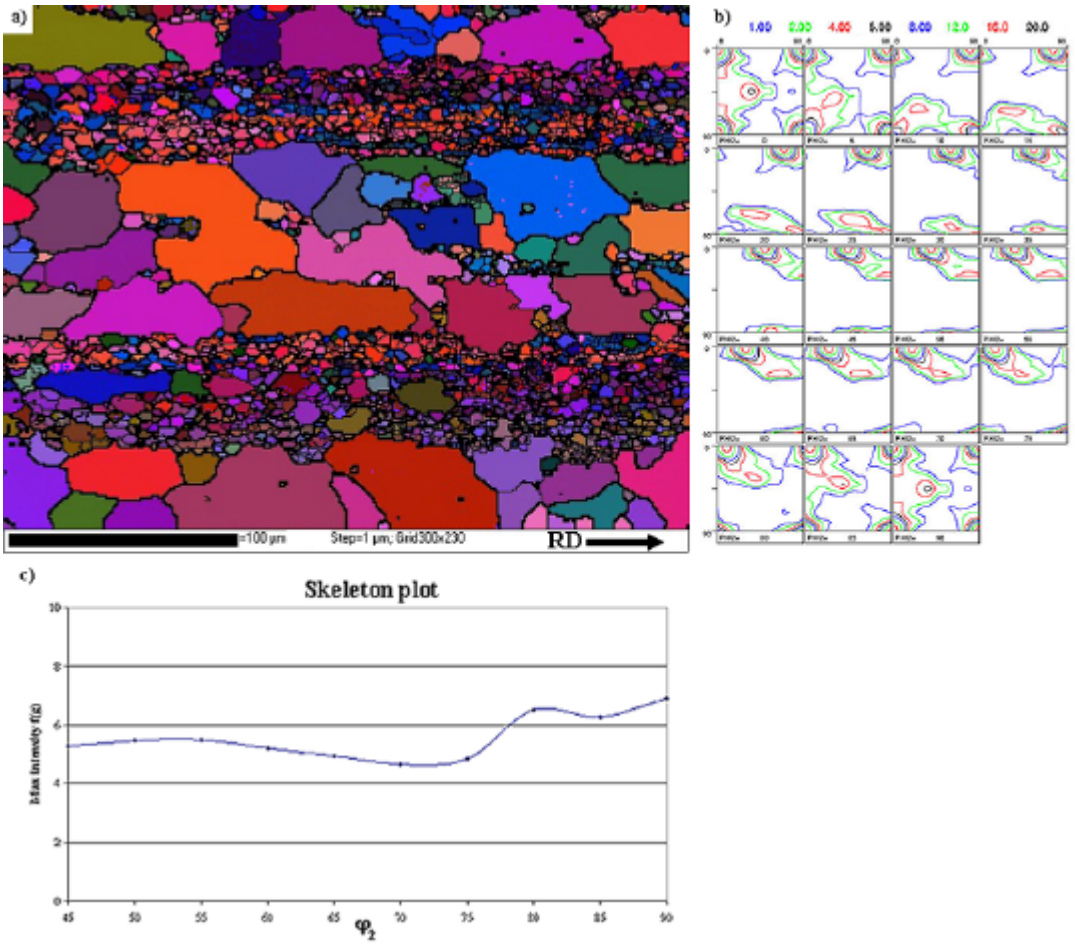

Fig.4.28: a) EBSD-map in the centre of the re-rolled material, which show a combination of recrystallised grains and a deformation banded structure. b) Show the global texture of the material as measured by XRD, while c) show the skeleton plot of the *b*-fibre.

The surface of the material was found to be in a fully recrystallised condition, which is in contrast to the centre region that was partly recrystallised. The texture of this area was measured by XRD and the ODF is given in Fig.4.29. This surface texture was dominated by a strong cube component with an intensity of about 30x random, which is significantly stronger than for the centre section that had an intensity of ~16x random.

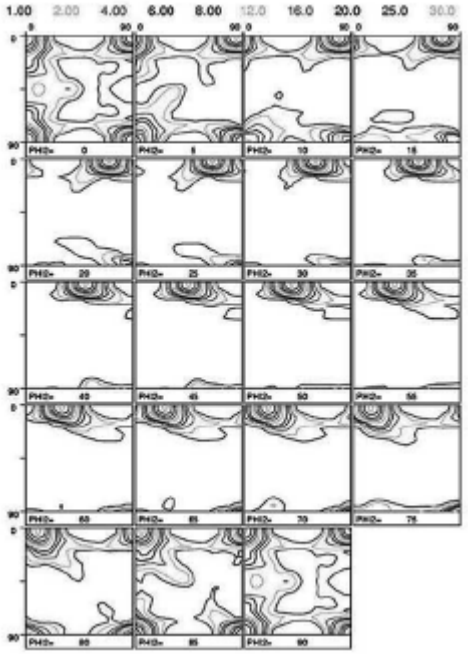

Fig.4.29: ODF illustrating the global texture in the surface of the re-rolled material, measured by XRD.

From the particle size distribution in Fig.4.34 it is seen that the number of large particles has decreased significantly, and the largest particle was found to have a diameter of approximately 8 μm compared to 12.5 μm for the transfer-gauge material. Further, it is seen that the re-rolled material contained somewhat more particles in the 1-4 μm range, which is probably a result of the break-up of the coarser particles during this rolling sequence.

The misorientations of the re-rolled substructure have been measured from EBSD-maps and the average misorientation was determined to be just below an angle of 7°. It should be noted that a broad peak was found for the distribution going from a misorientation of 3° to 11°, when all misorientations between 1.5° and 15° were taken into account. The wide peak with a relatively high average misorientation indicates that some subgrain growth has occurred after deformation. This was as expected totally different for the cold rolled condition, the results of this condition are given in Chapter 4.2.4, where most of the low angle grain boundaries had misorientations between 1.5° and 6°.

In order to fully recrystallise the re-rolled material annealing in salt bath at 390°C was carried out and a micrograph of the fully recrystallised structure is given in Fig.4.30. The material did not recrystallise as rapidly as expected, it took about 20 hours to achieve a fully recrystallised condition. This indicates that heavy precipitation of dispersoids has occurred during hot rolling and/or during the cooling sequence after tandem rolling. Some but no large differences in texture were detected in the fully recrystallised ODF, except of the vanishing of the *b*-fibre components, as compared to the originally ODF of the re-rolled material. The changes were a sharpening of the cube orientation from ~16x random to ~30x random and the appearance of the P-texture with an intensity of ~4x random. Because such a long annealing time was needed to fully recrystallise the material and no new texture components were observed, it is reasonable to assume that only the already existing recrystallised grains of the re-rolled condition were able to grow on the expense of the banded features. This explains the coarse grains in the centre of the fully recrystallised material and also the strengthening of the cube texture, as seen in Fig.4.30. The intensity of the cube orientation in the fully recrystallised condition was found to be as strong as at the surface before this additional annealing treatment.

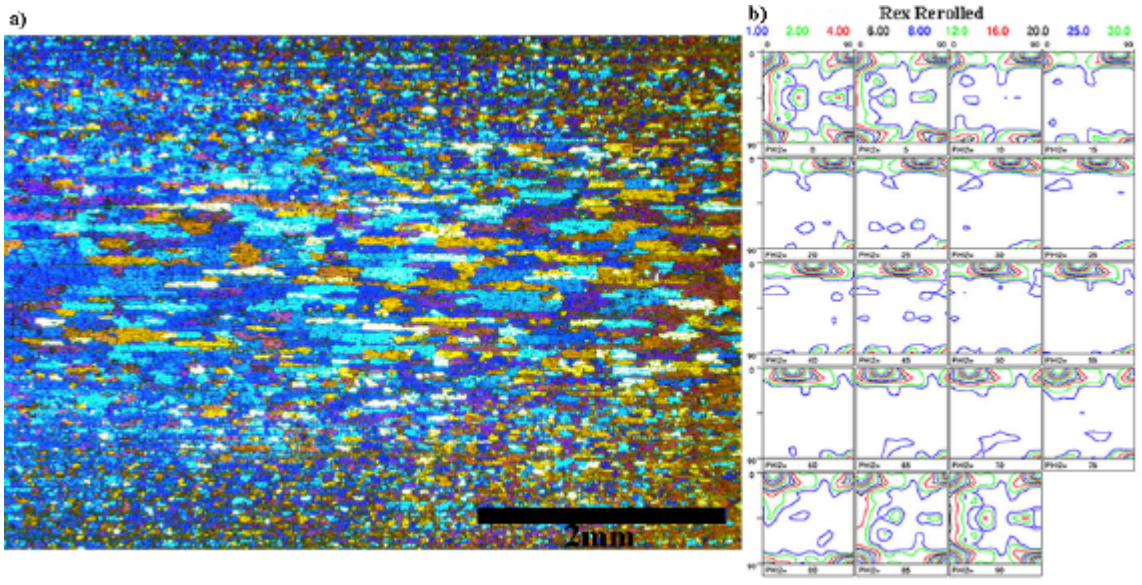

Fig.4.30: a) Micrograph showing through thickness variations of the fully recrystallised re-rolled material. The material had to be annealed for 20 hours at 390°C to reach a fully recrystallised condition. b) Global texture of the fully recrystallised centre layer, measured by XRD.

4.2.4 Cold rolled material

Total applied strain after cold rolling was calculated to be 1.25, *i.e.* a rolling reduction of 71%. Since the re-rolled material was in a partly recrystallised condition prior to cold rolling, as seen in Fig.4.28a), the totally stored energy for processes like recovery and recrystallisation may be slightly higher.

In order to investigate different models, *i.e.* work hardening and texture models, ability to predict the microstructural behaviour after different rolling reductions, without retuning, another cold rolled condition was produced. This was given an additional 50% reduction after the first cold rolling, this material will be termed W50 in the following. The total cold rolling reduction of W50 was 86% or e=2.0. Once again it must be kept in mind that the re-rolled material was partly recrystallised. In the following the different cold rolled materials will be termed W0 and W50. If nothing else is written then the results refer to the W0-material. Only results from the annealing sequence of the W50-material will be presented in this work, while the W0-material has been investigated more in detail.

In Table 4.7 it is seen that the cold rolled material still contained a fairly high amount of manganese in solid solution. This supersaturation of manganese will act as obstacles against recovery and recrystallisation during the subsequent annealing treatment.

An OIM-map of the cold rolled structure is illustrated in Fig.4.31a). From this and other maps (not shown here) the average subgrain size in the normal and rolling directions were found to be 0.45 μm and 0.71 μm, respectively. These values were found by using the linear intercept method. All subgrains with a size equal to the step size (0.1 μm) were ignored in the estimation. Moreover the arithmetic mean for the misorientation was calculated to be 4.2°, where the measurement was based on all low angle grain boundaries having misorientations between 1.5° and 15°. In Fig.4.31b) a map of the cube oriented grains within the same area as in a) is given, here all orientations within 15° of the exact cube are coloured red. Several cube bands are seen, and the retained fraction of cube from this map was found to be 4.1%. These bands may act as possible nucleation sites for the cube orientation during the subsequent annealing treatment (Vatne 1995).

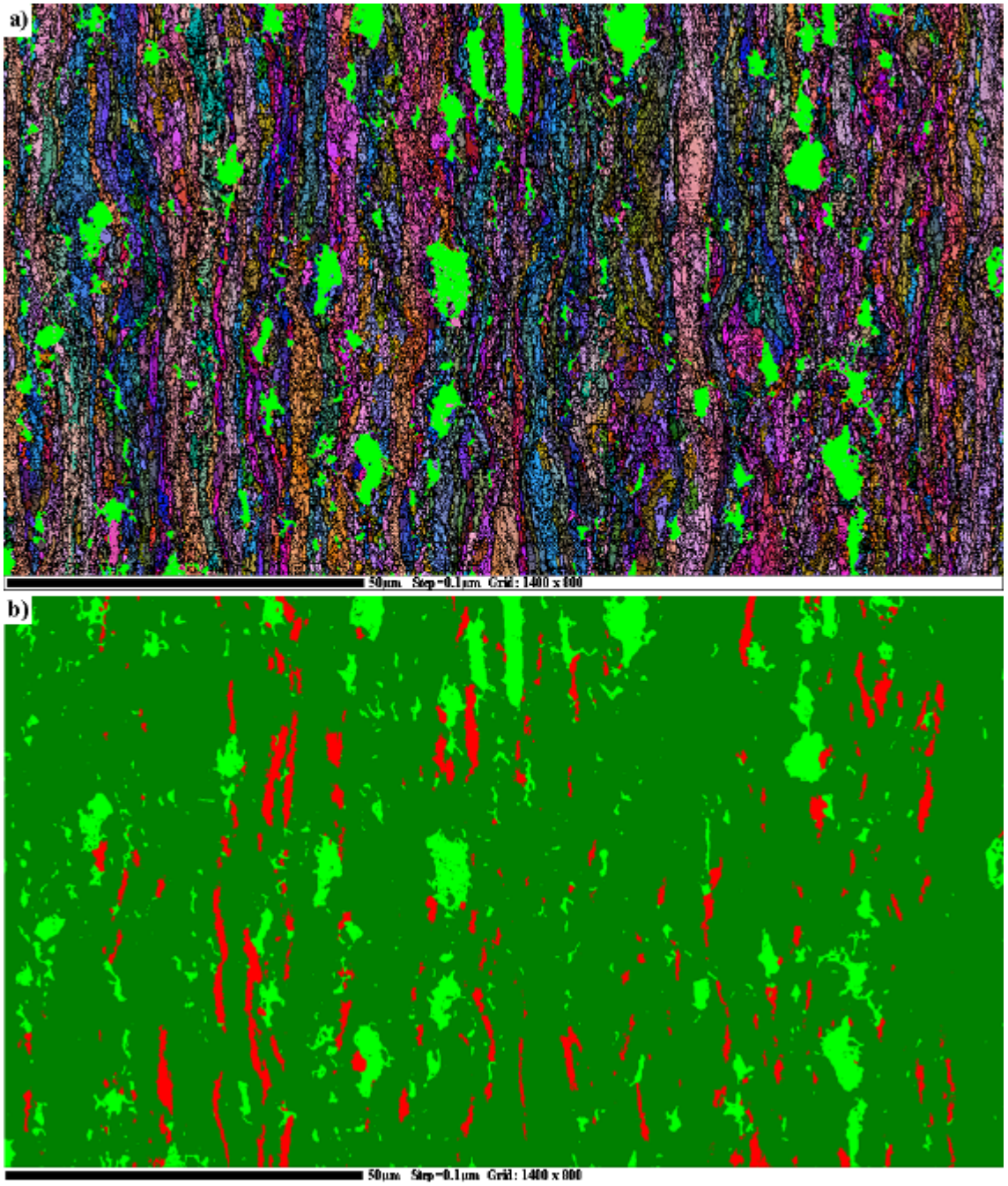

Fig.4.31: a) OIM-map of the cold rolled structure of the CP 3103-alloy. b) Cube texture map of a). Red areas are within 15° of the exact cube orientation, green areas are grains of other orientations and lime green areas are unindexed areas, assumed to be constituent particles.

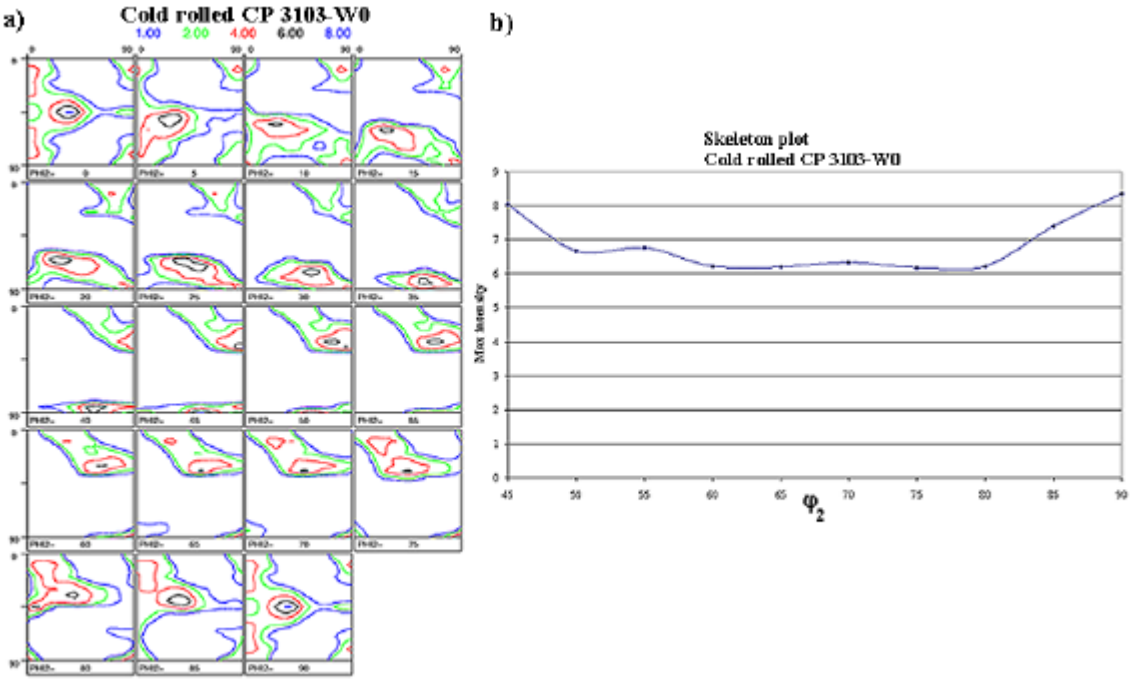

Fig.4.32: a) Global texture of the cold rolled sheet, measured by XRD. The texture consists of the typical *b*-fibre components and RD-rotated cube. b) Skeleton plot of the *b*-fibre, showing peaks at the Cu- (45°) and Bs- (90°) orientations.

The global texture of the cold rolled sheet and a skeleton plot of the *b*-fibre are shown in Fig.4.32. It is seen that the deformation texture consists of a combination of the *b*-deformation fibre and some RD-rotated cube. This latter texture component was expected since the starting texture, *i.e.* the texture of the re-rolled material, was a combination of the cube-orientation and orientation along the *b*-fibre. As the cube-oriented grains are deformed, they are known to rotate out of their orientation and towards the Goss-orientation, *i.e.* a RD-rotation. From the *b*-fibre plot it is seen that all orientations along the fibre sharpened, however the Cu-orientation and those close to this has sharpened the most as compared to the re-rolled material.

Images of the microstructure through the processing line are presented in Fig.4.33, and it is seen that the morphology of the dispersoids is a combination of thin plates and spheroids. It is seen, as found by EBSD-mapping, that the transfer-gauge material was fully recrystallised, while the re-rolled material was partly recrystallised. It is further seen that the thin plate-like dispersoids are already rotated into the rolling direction after exiting the breakdown mill.

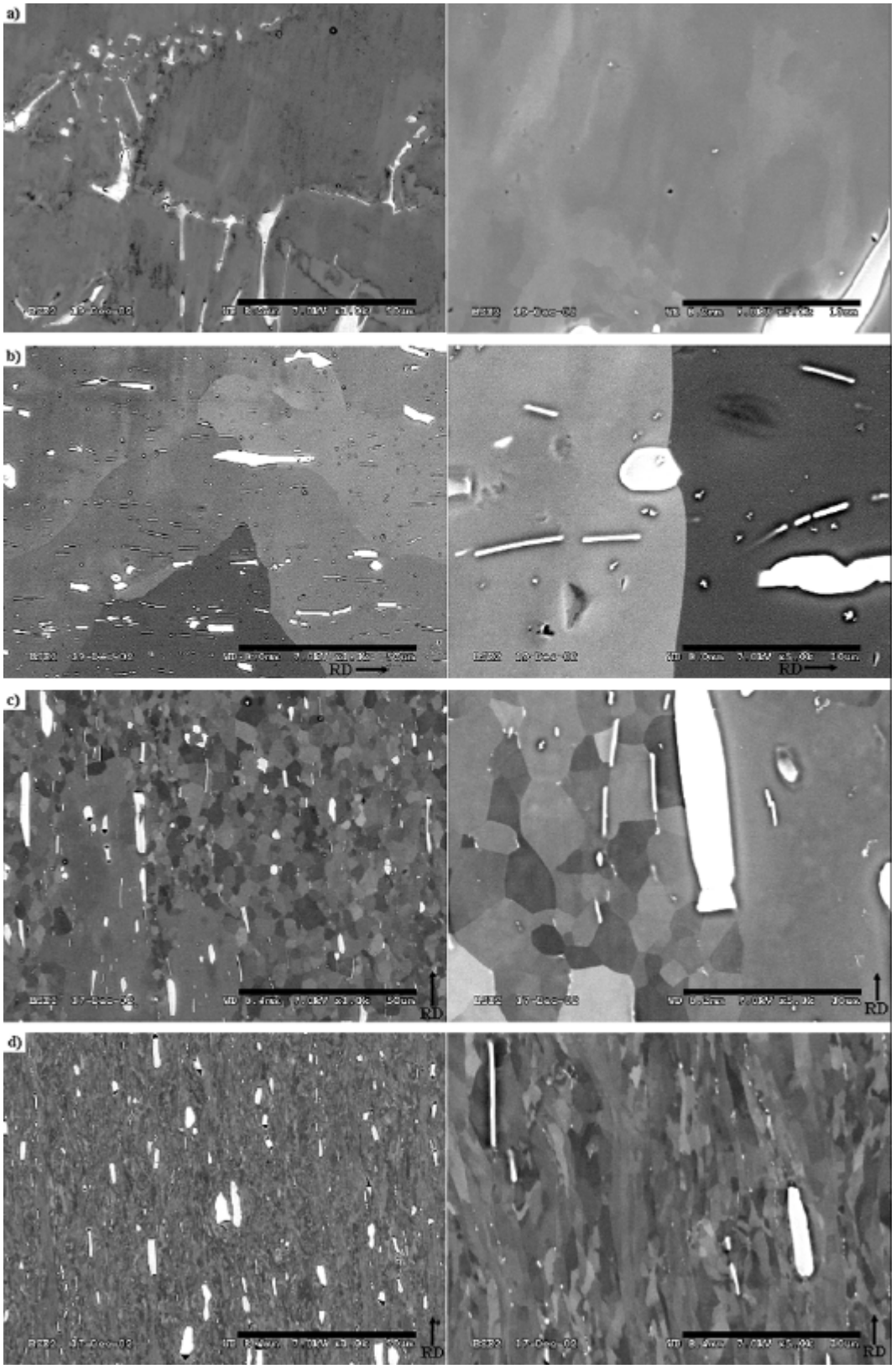

Fig.4.33: Images of the microstructure through the processing line a) as cast, b) transfer-gauge, c) re-rolled and d) cold rolled. The rolling direction (RD) is indicated by arrows.

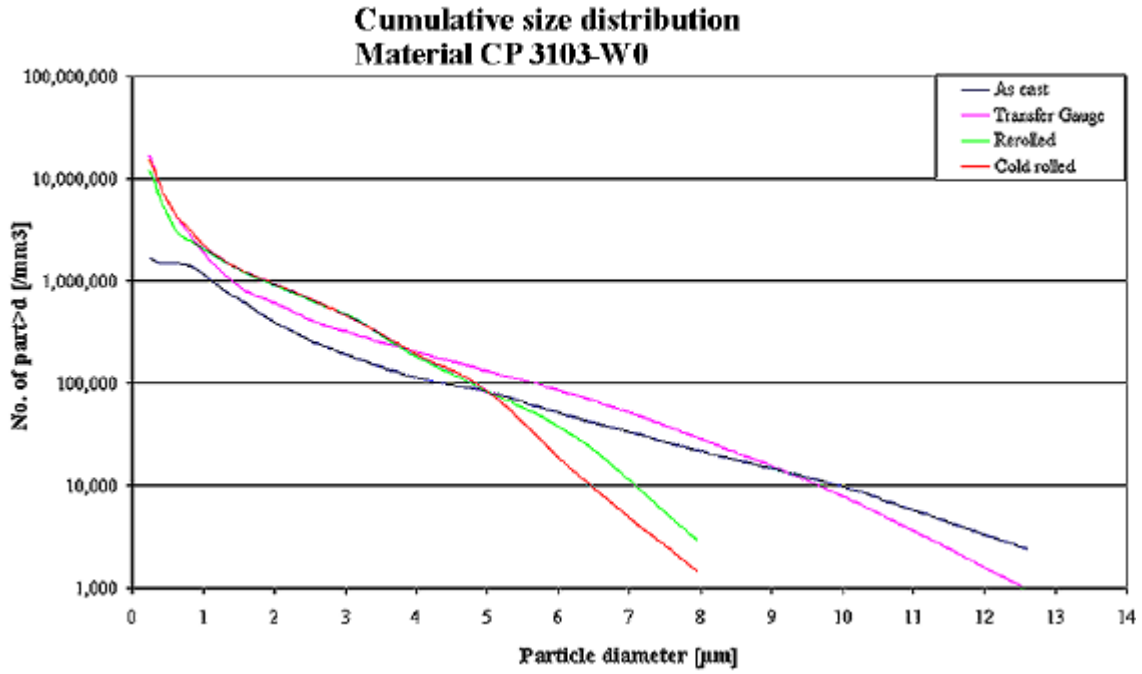

Fig.4.34: Cumulative particle size distributions of the *as cast* and deformed materials through the processing line. A SEM in BS-mode was used to measure particle sizes, where the measured area of each particle has been recalculated into a circle. A modified Johnson-Saltykov method has been used to transform the 2D-distribution into a 3D-distribution. A clear tendency of break-up of the largest particles is observed.

Regarding the cumulative particle size distribution, Fig.4.34, the largest particles were found to have broken up even more during cold rolling than they were in the re-rolled condition. The number of particles less than 5 μm were however found to be almost equal to that in the re-rolled material, as seen in Fig.4.34. Comments regarding the other distributions are given in the chapters for the different material conditions. To summarise the different distributions it is seen that the largest particles in particular tend to break up as the material is deformed, this observation is independent on whether deformation was carried out at elevated temperatures or by cold deformation. The number of intermediate sized particles increase somewhat, while the number of small particles does not change much with respect to relative differences. Hagstöm (2001) did as well measure the particle size distributions of the different material conditions of the CP 3103-alloy, and his results were almost completely the same as to the distributions given in Fig.4.34.

4.2.5 Annealed material

The cold rolled material was isothermally annealed in salt baths at five different temperatures, *i.e.* at 280°C, 290°C, 300°C, 325°C and 350°C, to reach a fully recrystallised condition. Tensile testing and conductivity measurements were carried out in order to follow the softening and precipitation behaviour at these temperatures, and the results of these measurements are plotted in Fig.4.35. From this figure it is seen that the material annealed at 280°C did not recrystallise within the maximum time, while the flow stress of the material annealed at 290°C for 11½ days indicate that this condition has just become fully recrystallised. An OIM-map of this material after annealing at 290°C, however, revealed that it was not fully recrystallised. Images of the microstructure after annealing for 11½ days at 280°C and 290°C are given in Fig.4.36. In Appendix 4 the yield stress, ultimate tensile strength, strain at fracture and conductivity values of the cold rolled and annealed material conditions are presented.

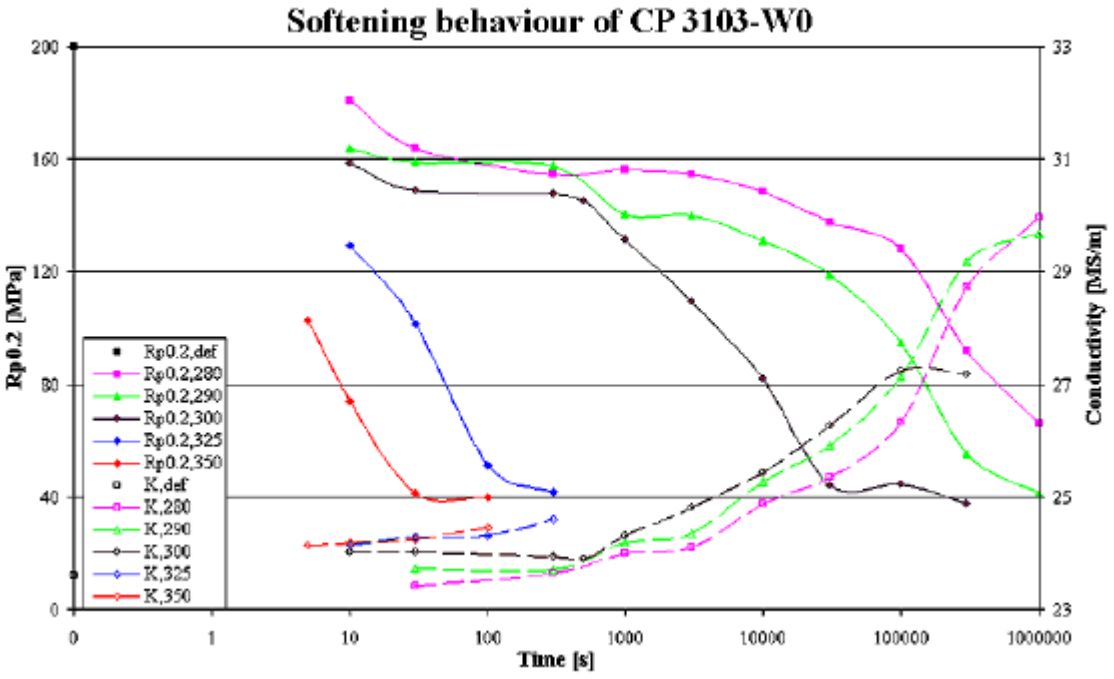

Fig.4.35: Softening and precipitation behaviour of the cold rolled CP 3103 followed by tensile tests and conductivity measurements, respectively.

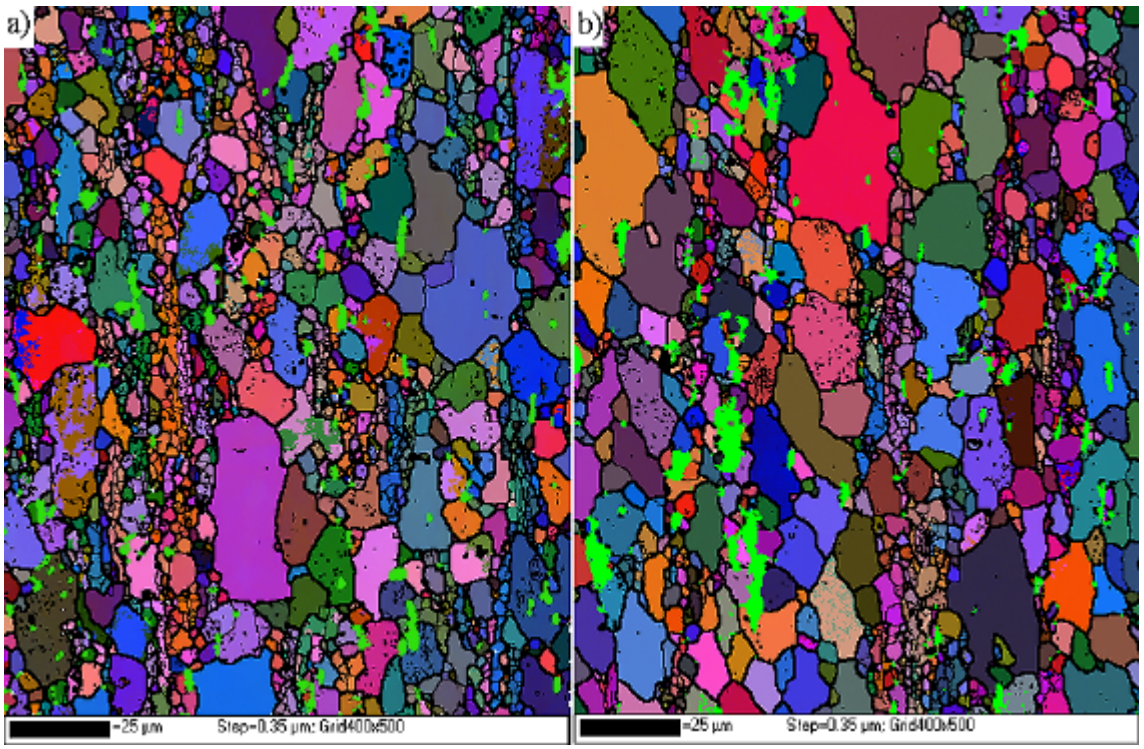

Fig.4.36: OIM-maps of the CP 3103-alloy annealed 11½ days at a) 280°C and b) 290°C.

In Table 4.8 the recrystallised grain sizes of the annealed materials measured by the linear intercept method (LIM) are presented. The average grain size of the material annealed at 290°C are obviously too low since a partly recrystallised microstructure was found by inspecting OIM-maps of this condition, Fig.4.36b). The HKL-software predicted that about 10% of the material was in an unrecrystallised condition. The result of these substructured areas is an overestimation of small grains, *i.e.* to many small grains are taken into account in the LIM-analysis. If these grains have been excluded, a similar or somewhat larger average grain size, as given for the 300°C-annealing, would probably have been observed.

Table 4.8: Average grain diameter of the recrystallised materials measured by LIM.

Annealing temperature	280°C	290°C	300°C	325°C	350°C
Average diameter [μm]	Not rex	11.02 ~90%Rex	13.73	10.31	10.35

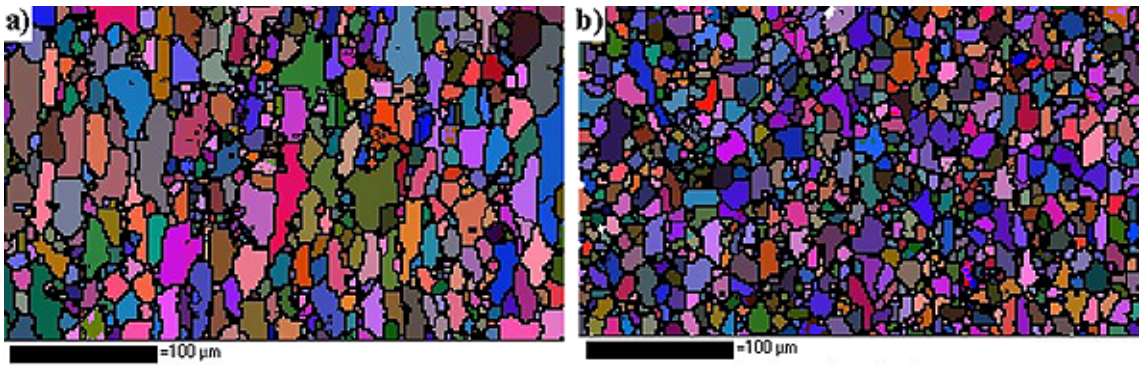

Fig.4.37: OIM-maps of CP 3103-alloy annealed at a) 300°C and b) 350°C.

In Fig.4.37 the dependency of annealing temperature on the grain size and shape of the grains is illustrated. At a temperature of 300°C as well as below this temperature, the recrystallised grains were larger, more elongated in the rolling direction and they were more serrated than at higher annealing temperatures. It is further seen that there exists a lot of small equiaxed grains at both temperatures. Some of these grains are so-called island grains, which are assumed to have nucleated by PSN [Chan and Humphreys (1984)]. These grains are partly the reason why the average grain size in Table 4.8 at low temperatures is only slightly larger than the grain size values at higher temperatures. For higher annealing temperatures, in this particular case at 350°C, the grains were more equiaxed and not as large as for lower annealing temperatures, Fig.4.37b). The grain size distributions of these material conditions are given in Appendix 5.

In Fig.4.38 a TTT-diagram of the CP 3103-alloy has been constructed to illustrate possible effects of precipitation at the investigated temperatures. The construction was similar to that for the LP 3103-alloy, but in the present case changes in yield stress has been used instead of hardness. A drop of 25% in yield stress is assumed to be start of recrystallisation and a 2.5% increase in conductivity is taken as start of precipitation. In this figure it is clearly demonstrated that recrystallisation is affected by precipitation at all investigated temperatures, however the effect is most pronounced at temperatures below 315°C. This is also clearly demonstrated in the OIM-maps in Fig.4.37 of the recrystallised materials at 300°C and 350°C, where the grains were smaller and more equiaxed at the highest annealing temperature.

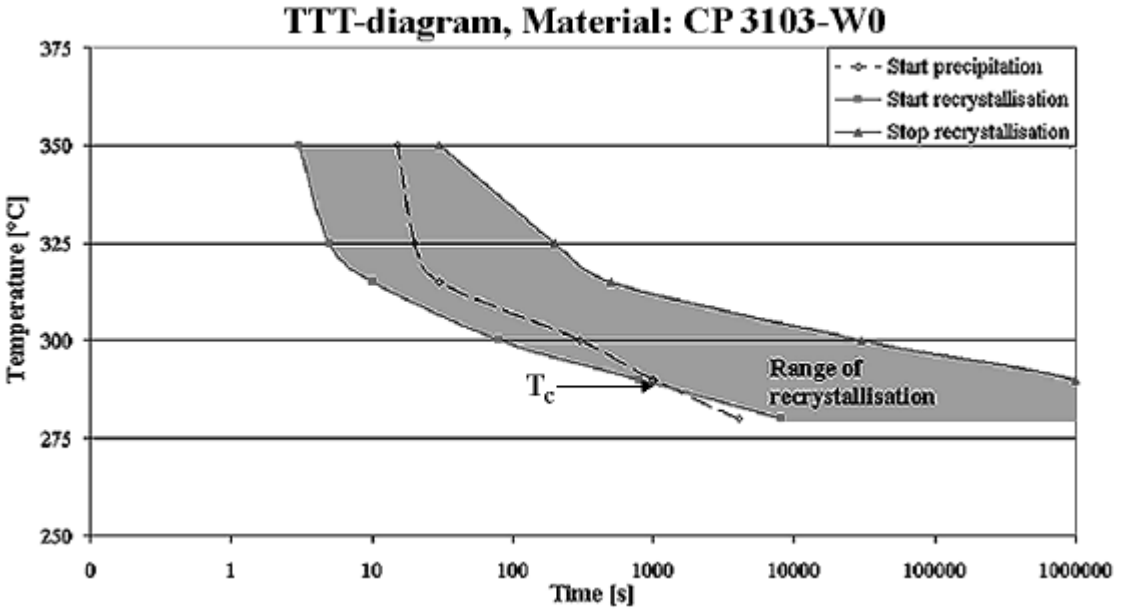

Fig.4.38: TTT-diagram of the CP 3103-alloy. Constructed on the basis of yield stress and conductivity measurements.

The characteristic temperature, T_c, as defined by the crossing of the precipitation start curve and the recrystallisation start curve is found at a temperature close to 290°C. The characteristic temperature is somewhat higher than was found for the C-homogenised LP 3103-alloy. However, the precipitation nose is not as sharp for this material as it was for the LP 3103-material conditions.

The hardness of the tensile samples was measured to check for a correlation between hardness and yield strength. This correlation is useful in order to be able to use hardness measurements of the LP 3103-alloy for modelling activities. The results of the modelling activities are given in the discussion. It was found that the relationship between yield stress and Vickers hardness of the CP 3103-material was reasonably well described by the following equation:

$$s_y \cong 4.8 \cdot VHN - 100 \qquad (4.1)$$

A plot of VHN *vs*. yield stress is presented in Appendix 6.

4.2.6 Annealing of sample W50

The results of annealing treatment of the cold rolled W50-material are given in Fig.4.39. This condition was isothermally annealed at temperatures of 290°C,

300°C and 310°C for holding times up to 11½ days. As for conductivity it is seen that this material behave similar to the W0-material. For the softening behaviour on the other hand no distinct recrystallisation knee was observed, as for the W0-material. This kind of constant decrease in flow stress has often been attributed to continuous or *in-situ* recrystallisation. The as deformed flow stresses of the two material conditions (W0 and W50) were similar. Ekström (2002) has reported a value of 206 MPa for the cold rolled W50-material, while for W0 he found a value similar to what was presented in Fig.4.35 (200 MPa). The reason why no change in yield stress was observed is thus probably due to uncertainties in the determination of the flow stress.

The yield stress, ultimate tensile strength, strain at fracture and conductivity values of the cold rolled and annealed material conditions are presented in Appendix 4.

By investigating OIM-maps of the W50-material it was found that the material annealed at 290°C for 11½ days was not fully recrystallised. About 15% of the microstructure were still in an untransformed condition even after this long annealing time. For the other two temperatures a fully recrystallised condition was found within the maximum annealing time.

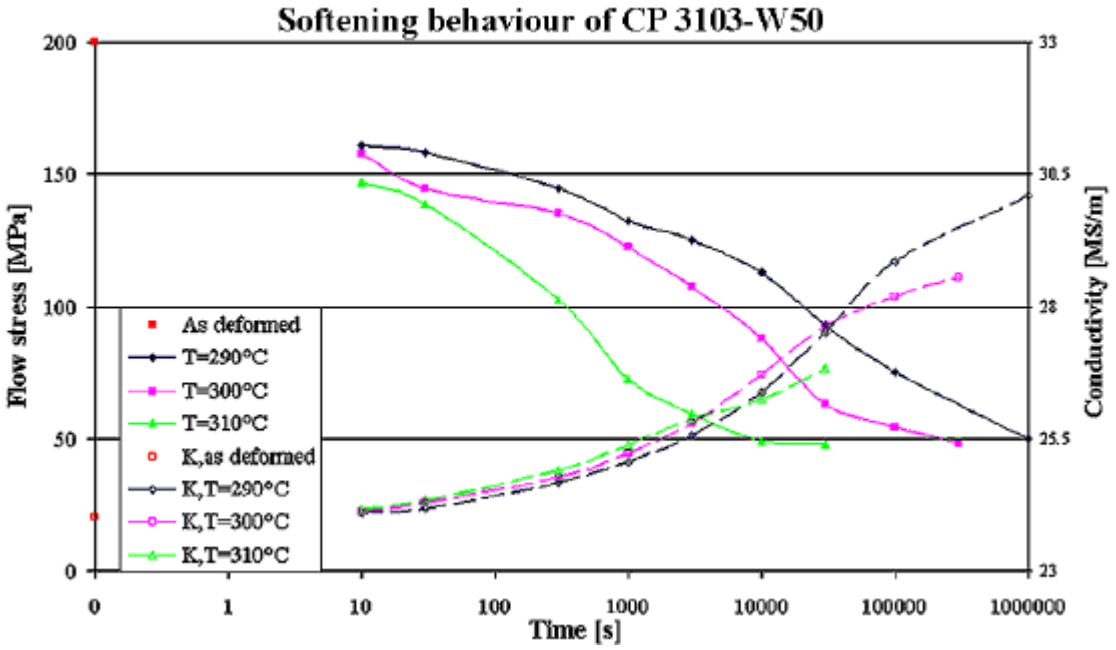

Fig.4.39: Softening and conductivity curves of the AA3103 W50-material.

4.2.7 Recrystallisation textures of CP 3103

The recrystallisation textures are presented as ODF, which have been calculated from large EBSD-maps. In Fig.4.40 the recrystallisation textures after annealing at 300°C, 325°C and 350°C are presented. It is seen that with increasing temperature the intensity of the cube texture strengthens, the cube texture intensity is found to increase from ~4x random after annealing at 300°C to ~8x random at 350°C. The cube textured grains, which are believed to have nucleated from cube-bands that have survived deformation, Fig.4.31b), seem to be less efficiently nucleated at low temperatures compared to high temperature annealing. For all temperatures orientations along the *b*-fibre are observed, these orientations are believed to have nucleated by strain induced boundary migration.

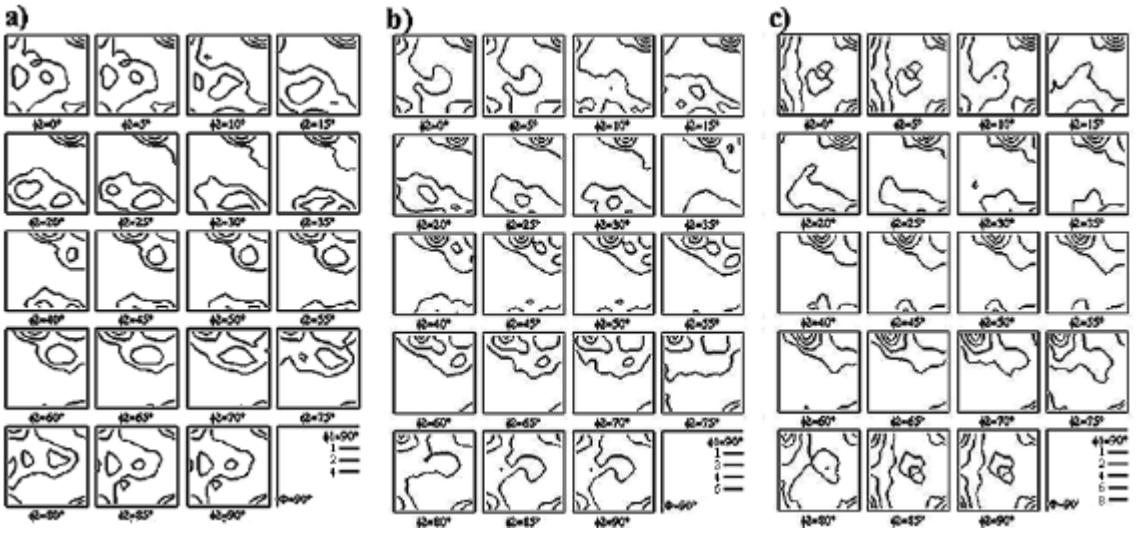

Fig.4.40: Recrystallisation textures of CP 3103 annealed at a) 300°C, b) 325°C and c) 350°C. The ODFs are calculated from large EBSD-maps.

The textures of the W50-material annealed at 290°C, 300°C and 310°C are given in Fig.4.41. The most reasonable answer to why the orientations along the *b*-fibre appears with such high intensities in the ODF for the material annealed at 290°C, is probably due to *in-situ* recrystallisation in combination with the fact that only ~85% of the microstructure was recrystallised. For the other temperatures the ODFs were dominated by weak cube textures in combination with some *b*-fibre orientations and the P-texture. The intensity of the cube texture was found to increase with raising temperatures as for the W0-condition.

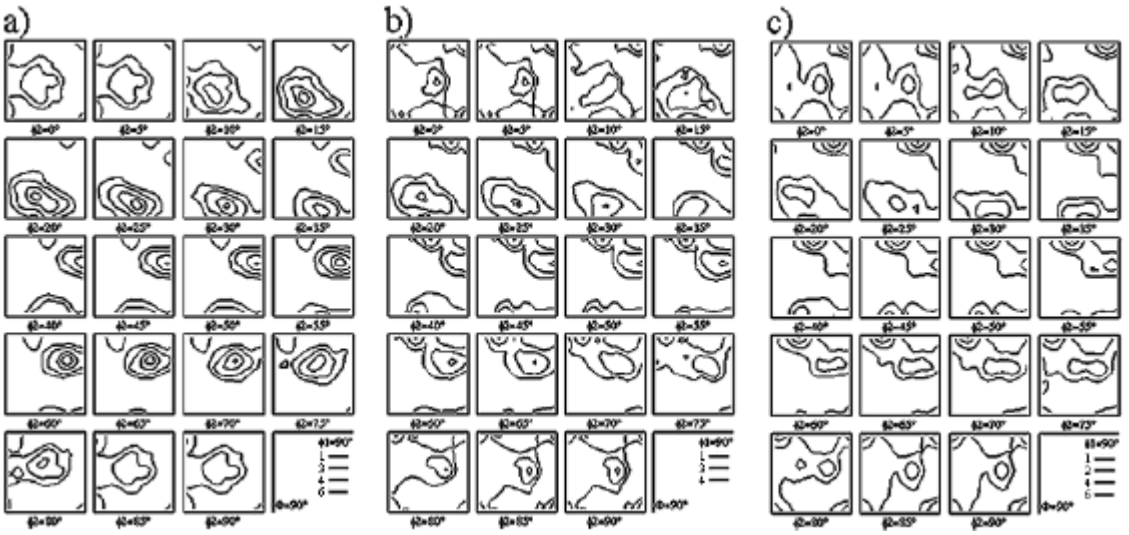

Fig.4.41: Recrystallisation texture of CP 3103 (W50) after annealing at a) 290°C, b) 300°C and c) 310°C. The ODFs were calculated from EBSD-maps.

4.2.8 Laboratory cold rolling and annealing

To investigate the effect of alloying elements, the different material conditions through the processing line, *i.e.* the homogenised, transfer gauge and re-rolled materials, were all cold rolled to the same strains as the LP 3103 alloy, *i.e.* to strains of 1.5 and 3.0. The re-rolled material was not cold rolled to more than a strain of 1.5, because after a strain of 3.0 the thickness would be too thin to be investigated by X-ray diffraction (XRD). For similar cold rolling reductions, the re-rolled and cold rolled materials should behave similar during annealing, this is why only the re-rolled material was investigated here. The deformed materials were subsequently annealed in salt baths at temperatures of 300°C, 350°C and 500°C.

In Fig.4.42 and Fig.4.43 the ODFs of the fully recrystallised materials measured by XRD are shown. The recrystallisation textures after an applied strain of 1.5 were weak for the as homogenised (AH) and the transfer-gauge (TG) materials, while for the re-rolled (RR) material it was dominated by the cube orientation.

After an applied strain of 3.0 the recrystallisation texture of the as homogenised material had a peak at the P-orientation after being annealed at 300°C. Annealing at 350°C resulted in a recrystallisation texture dominated by the b-deformation fibre. The as homogenised material was investigated by EBSD-mapping where a fully recrystallised condition was confirmed. This indicates that *in-situ* recrystallisation has occurred at this temperature. The reason why this latter mechanism was not dominating at 300°C is probably due to more effective precipitation at 350°C where the precipitation nose is believed to be found. The recrystallisation texture after annealing at 500°C was a combination of P- and the exact cube orientations, with the cube being strongest. For the transfer-gauge material a weak P-texture was found for annealing at 300°C. At higher annealing temperatures a strong cube texture was totally dominating.

With this setup it was further possible to study the effect of an initial texture prior to cold rolling. The transfer-gauge and re-rolled materials had strong cube textures before cold rolling, while the LP 3103-materials had random starting textures. The following comparisons could be made: the transfer-gauge material *vs*. the B-homogenised material and the re-rolled material *vs*. the C-homogenised material. The homogenised CP 3103-material might be compared to the A-homogenised material, but obviously neither of these had a texture of significance before deformation. These comparisons will be further commented in the discussion.

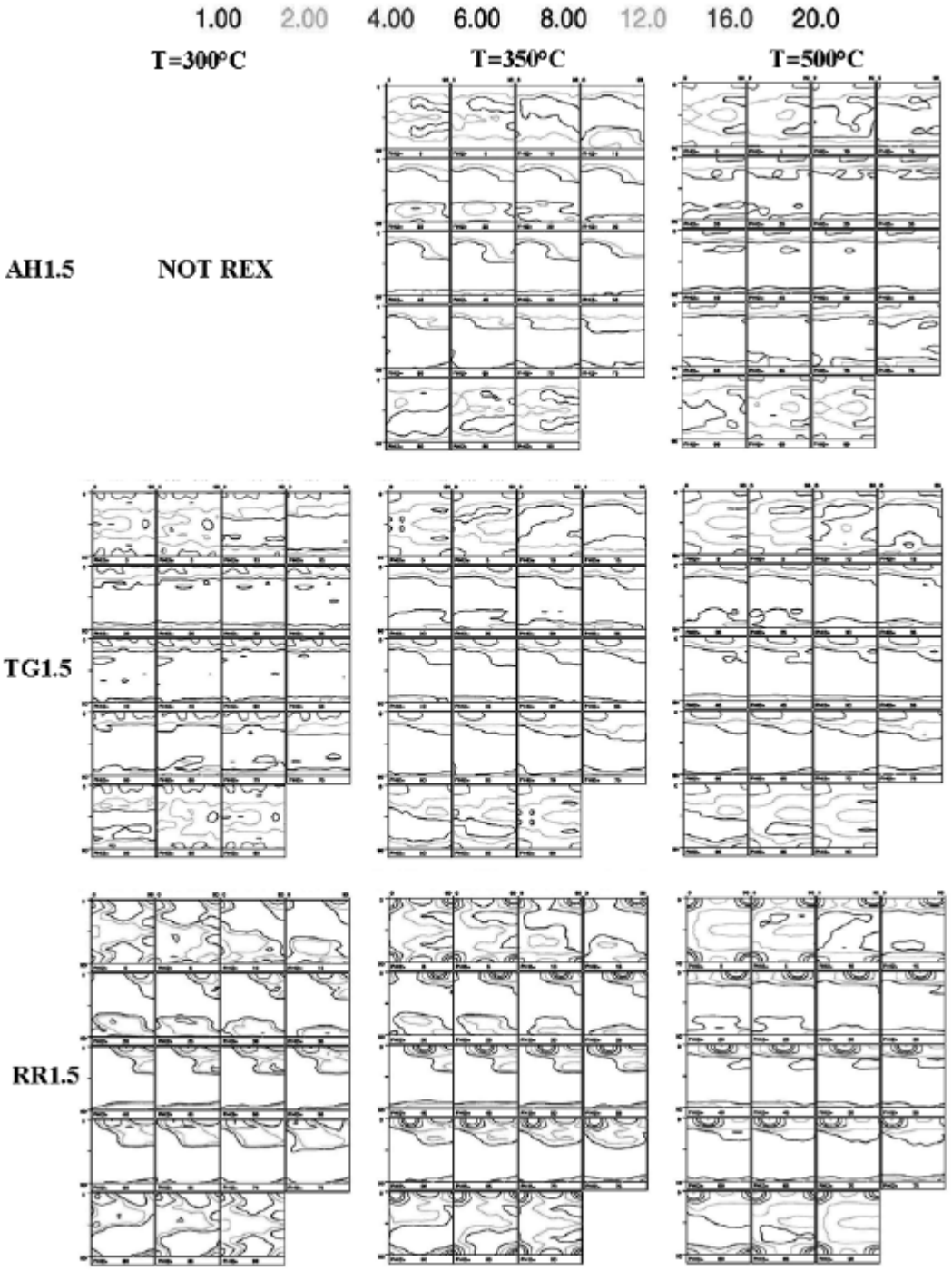

Fig.4.42: Recrystallisation textures of the CP 3103-materials after cold rolling to a strain of 1.5. AH= As homogenised, TG= Transfer-gauge and RR= Re-rolled.

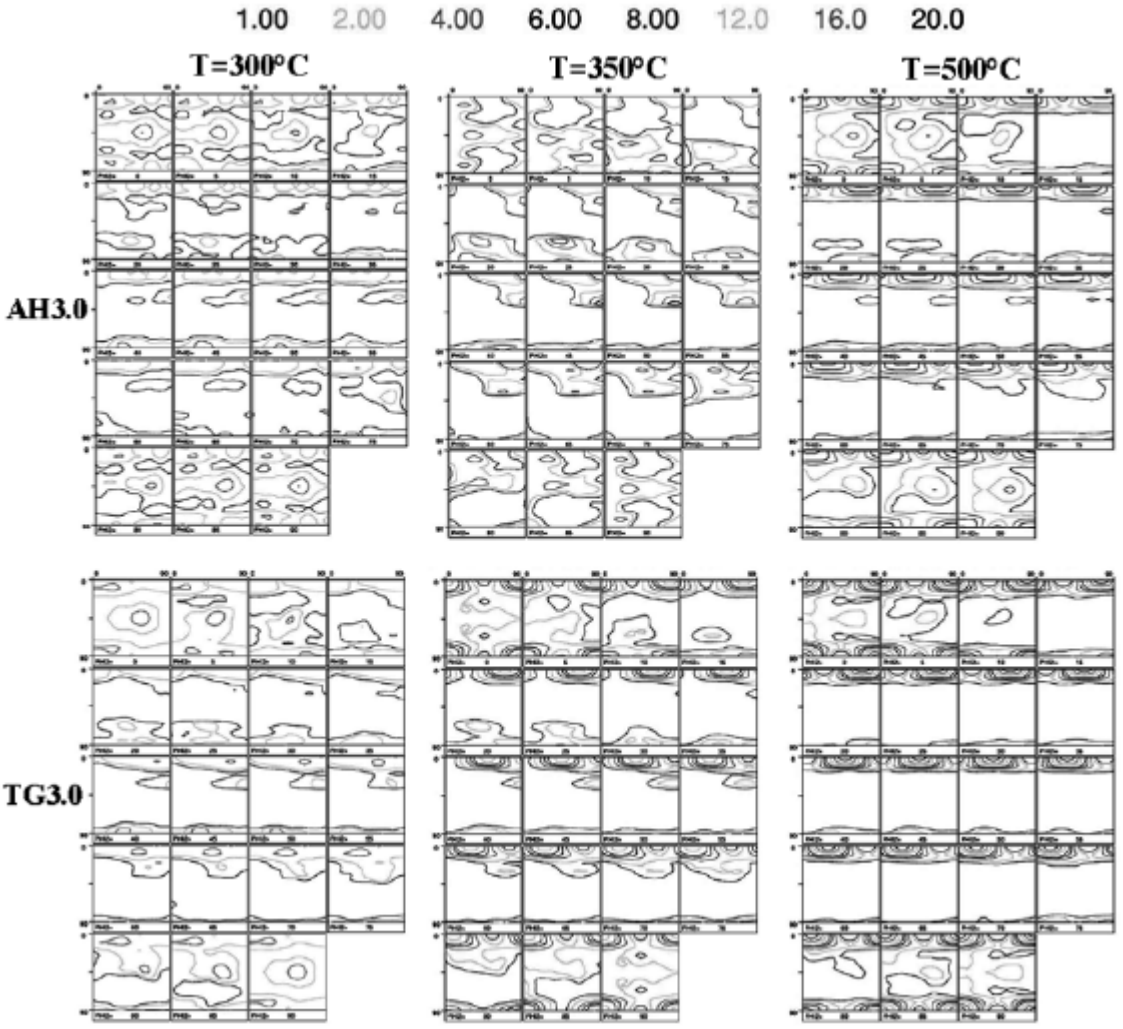

Fig.4.43: Recrystallisation textures of the CP 3103-materials after cold rolling to a strain of 3.0. AH= As homogenised and TG= Transfer-gauge.

4.3 Characterisation of AA1200

The AA1200-alloy was cast and deformed by Alcan International LTD in Banbury. The rolling was carried out in a standard way with a hot rolling schedule followed by a cold rolling sequence. The thickness after hot rolling was 2.8 mm and after cold rolling 0.6 mm, *i.e.* the applied cold rolling reduction was 75% or a true strain of approximately 1.5.

The producer has done some material characterisation and a short summary is given below, for more details the reader is referred to a Vir[Fab]-report by Hamerton (2000).

The transfer slab consisted of coarse grains and was predominantly recrystallised. Small variations in grain size between different positions through the slab thickness and in the width were detected. The particles were clustered into stringers aligned in the rolling direction.

The re-rolled material was fully recrystallised with a non-uniform grain size distribution. The grain size appeared to be finer towards the mid-thickness. No differences in grain size were observed in the width. The particles were more uniformly distributed than in the transfer slab.

The cold rolled sheet exhibited a typical cold deformed grain structure through thickness and the particles tended to be finer toward the surfaces. The yield stress in the rolling direction was determined to be 134 MPa, with an ultimate tensile strength of 149 MPa and a total elongation at fracture of 3.8%.

The present author has only investigated the cold rolled and subsequently annealed materials. These investigations were basically done to obtain a reference system for modelling of the softening reactions.

4.3.1 Characterisation of the cold rolled material

The starting material was in a soft condition after exiting the hot rolling mill and the texture was totally dominated by the cube orientation. After cold rolling the texture changed into a combination of RD-rotated cube and the *b*-deformation fibre, but the intensities were fairly low, as seen in Fig.4.44.

The cold rolled microstructure was investigated by FEG-SEM using the EBSD-technique. Relatively large maps were recorded and from these maps the average misorientation and subgrain size were calculated. The average misorientation was found to be 4.0° after removing all misorientations less than 1.5° and the high angle grain boundaries (>15°). The subgrain size was measured by the linear intercept method, the average subgrain size in the rolling direction (RD) and normal direction (ND) were found to be 0.98 μm and 0.64 μm, respectively.

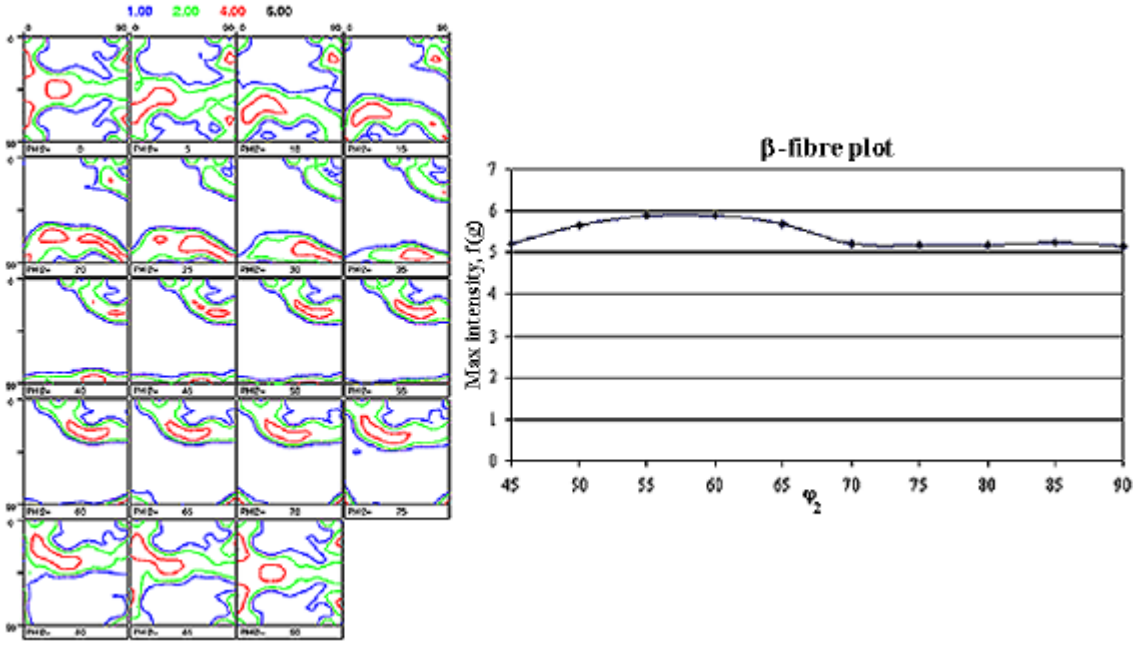

Fig.4.44: Deformation texture in the centre of the AA1200-alloy after a cold rolling reduction of ~75%, presented as a) ODF and b) skeleton plot. The texture was measured by XRD.

An OIM-map is shown in Fig.4.45a), and it consists of typical deformation bands. Large differences in the thickness of the deformation bands are seen, some are only a couple of subgrains thick while others are about 20 μm thick.

This can be explained by the difference in original grain size prior to cold rolling and by the fact that some orientations undergoes more plastic deformation than others due to differences in the Schmid factor. To check for potential nucleation sites for the cube orientation, the corresponding map of cube oriented grains is given in Fig.4.45b) and it is seen that some of the originally cube oriented grains have survived deformation.

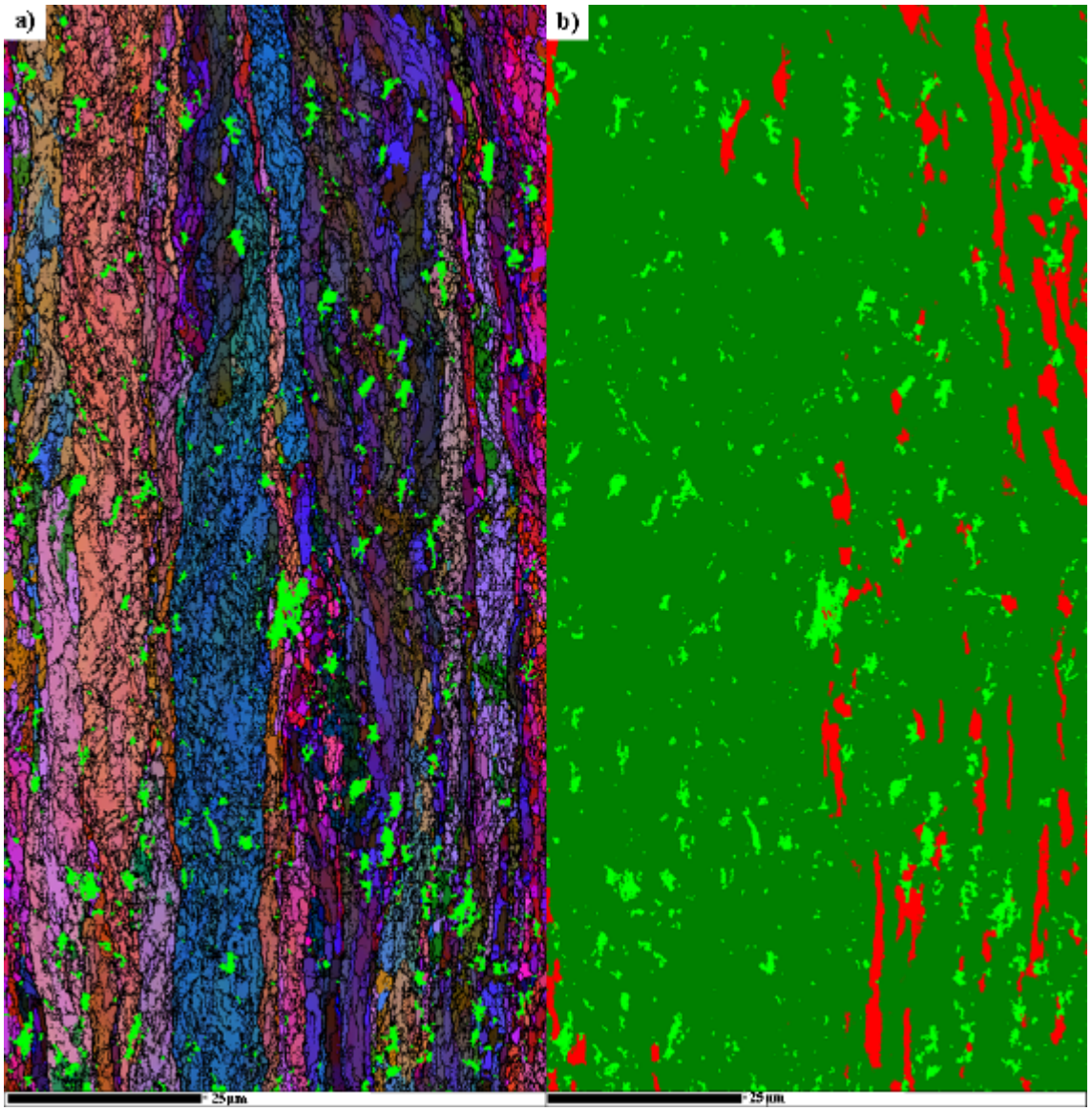

Fig.4.45: a) OIM-map of the cold rolled AA1200 alloy, and b) a corresponding map of cube oriented grains, where all grains within 15° of the exact cube orientation are given in red colour. Lime green areas are unindexed, most probably course primary particles, green areas are grains of other orientations.

4.3.2 Isothermal annealing of AA1200

The softening reactions of the cold rolled AA1200-alloy were monitored by means of tensile testing. Some typical material parameters obtained by tensile testing and conductivity measurements of the alloy annealed at different temperatures are presented in Appendix 4. The annealing treatments were carried out in fluidised bed furnaces set at temperatures of 240°C, 260°C and 280°C, respectively. In Fig.4.46 the yield stress and conductivity are plotted *vs.* annealing time. It is seen that a rather small increase in annealing temperature has a large influence on the time needed to reach a fully recrystallised condition. A difference of about 10% in flow stress of the deformed material compared to what Hamerton (2000) has reported was found in the present investigations. This is most probably due to room temperature softening, because the alloy was stored for almost two years before the present investigations were carried out. Regarding conductivity it is seen that there is only a very small increase in conductivity from the as deformed condition to the fully recrystallised condition at all temperatures. This change can be attributed to disappearance of subgrain boundaries, *i.e.* obstacles against current flow. Due to the relatively low annealing temperatures it must be kept in mind that diffusion of the alloying elements is limited, because of a low diffusivity at these temperatures.

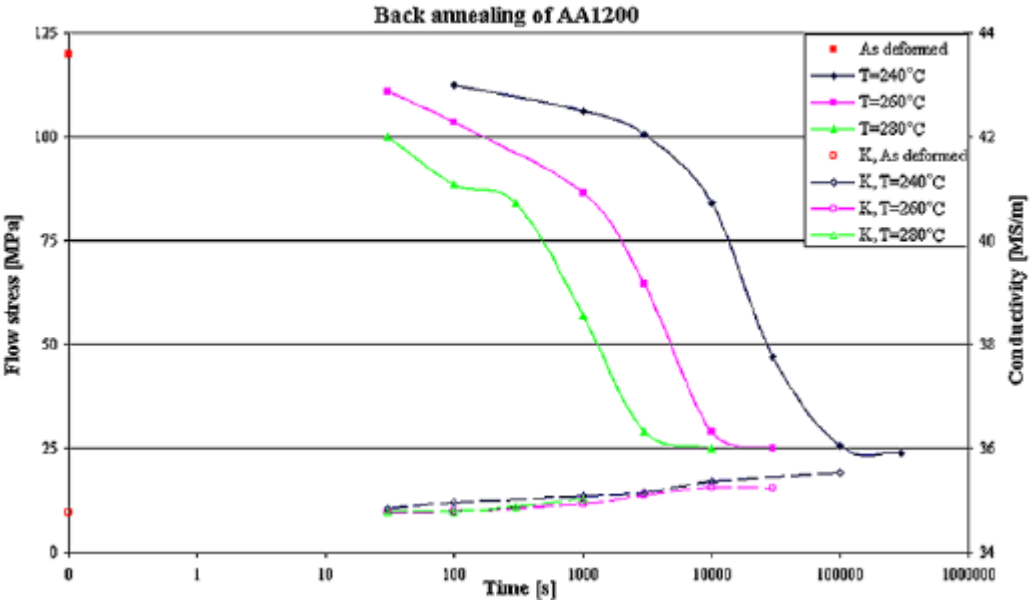

Fig.4.46: Softening curves of the AA1200-alloy isothermally annealed at temperatures of 240°C, 260°C and 280°C. The changes in conductivity upon annealing are included.

4.3.3 Recrystallisation textures of AA1200

The fully recrystallised materials after annealing at 240°C, 260°C and 280°C were investigated with respect to recrystallisation texture. The EBSD-technique was used to measure the recrystallisation textures. In Fig.4.47 the deformation texture is illustrated in a) and the recrystallisation textures are presented in b-d). In the given temperature range it was observed that the annealing temperature had little influence on the final recrystallisation texture. The only observed difference was that with increasing temperature the maximum intensity of the cube orientation decreased slightly, and the cube became more rotated in the RD-direction. Small differences in deformation texture were observed when comparing the texture measured by X-ray diffraction with the texture found from large maps measured by EBSD. This fact indicates that the EBSD-technique could be sufficient for texture analysis if carried out in a correct manner.

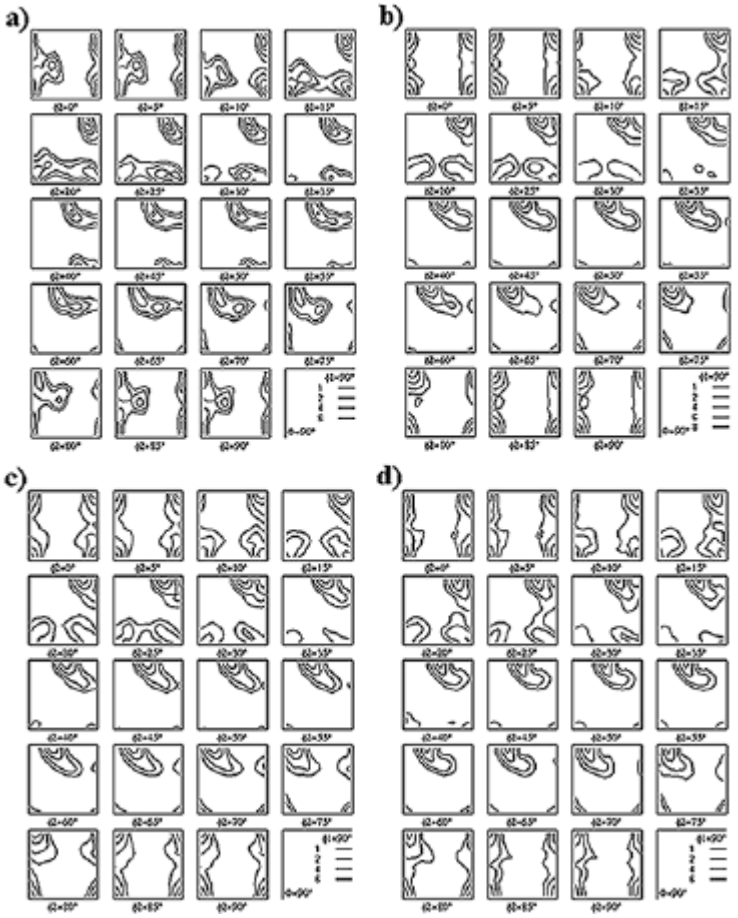

Fig.4.47: a) Deformation texture, and b-d) recrystallisation textures after annealing at 240°C, 260°C and 280°C, respectively. Calculated from several large OIM-maps.

5. Discussion

5.1 Introduction

The main objective of this work has been to study the effect of manganese in supersaturation on the annealing behaviour after cold rolling of two different commercial AlMn-alloys. These materials were a laboratory processed AA3103, cast by Hydro Aluminium Karmøy, and an industrially processed variant produced by Hydro Aluminium Deutschland (former VAW). The microstructural evolution of the two different AA3103-alloys (LP and CP) have been characterised in detail with focus on texture, hardness/yield stress and supersaturation of alloying elements. An AA1200-alloy, produced by Alcan Int. LTD, has also been investigated, although less detailed than the AA3103-alloys. This latter alloy was included in the material-matrix as a base alloy, mainly for modelling purposes.

The main focus of the discussion is on the texture evolution and in particular on the formation of the P- and ND-rotated cube orientations, Chapter 5.5. These orientations were found when precipitation occurred concurrent to recovery and recrystallisation. Little work has been published on the formation of these orientations, and none has reported the same intensities as obtained in the present investigations. In the following the results obtained in the present work will be discussed in view of previous observations of these texture components. Finally some ideas related to how the nucleation process takes place will be presented as an attempt to explain the appearance of these texture components in supersaturated alloys subjected to an annealing treatment after cold rolling.

Modelling of the softening behaviour of the three different alloys by a physically based model have been carried out. At the launch of this work none of the existing softening models were able to handle concurrent precipitation. In this discussion a suggestion of how to include the effect of concurrent precipitation will be presented. This results in good model prediction for the LP 3103-alloy, but the CP 3103-alloy was not well predicted by this approach.

5.2 Microstructural evolution during deformation

Although only a minor part of the experimental work was carried out on the deformed microstructure, it is useful to start the discussion here. As is widely known, the driving force for reactions like recovery, recrystallisation and precipitation is highly dependent on the deformed microstructure.

5.2.1 Substructure evolution of the cold rolled materials

Misorientation: In Table 4.3 where the average misorientation across the subgrain boundaries are given. The misorientation was found to increase slightly when increasing the strain from 1.5 to 3.0 for the LP 3103-alloy. Even though an increase of ~0.1-0.2° was found for all three conditions, the increase is too low to categorically say that there is an increase in misorientation with increasing deformation. A difference in misorientation was also observed for the differently homogenised LP 3103 conditions, *i.e.* the average misorientation became larger as the amount of Mn in solid solution decreased, but the increase was low here as well.

It was further found that the three investigated alloys had approximately the same misorientation when being deformed to a strain of ~1.5. From several large OIM-maps of the different alloys the average misorientation was found to be 4.0° for the AA1200-alloy, 4.1° for the LP 3103-alloy and 4.2° for the CP 3103-alloy. These differences in misorientation indicate that AlMn-alloys produce somewhat more misoriented subgrains, but the difference is not large compared to commercial pure Al-alloys.

Subgrain size: The variations in subgrain size versus degree of deformation measured for the LP 3103-alloy are compared with earlier measurements. The present values were determined by EBSD-mapping, and the absolute subgrain size values of the LP 3103-alloy are given in Table 4.3. In Fig.5.1 the normalised subgrain size after a strain of 3.0 is compared to previous works and it is seen that the investigated alloy follow a similar trend to what has been described earlier [Gil Sevillano *et al.* (1980)].

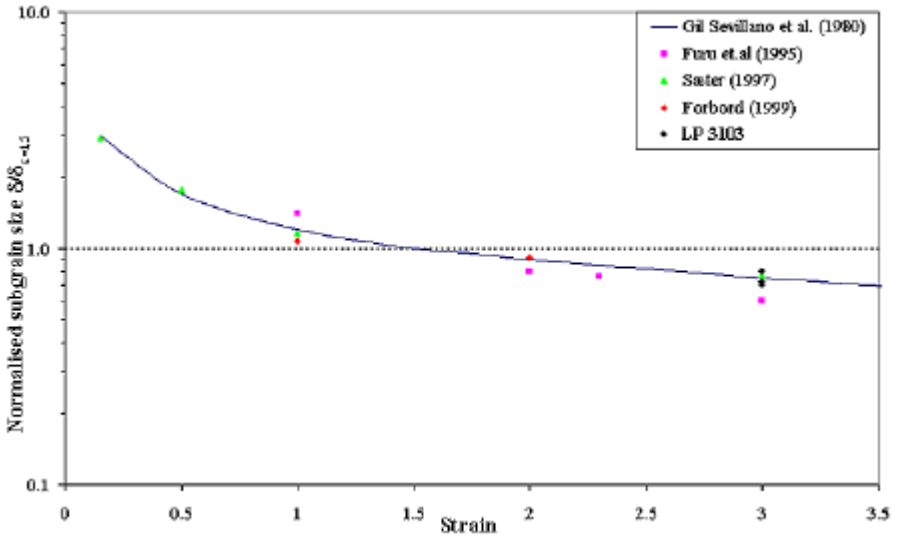

Fig.5.1: Normalised subgrain size of the LP 3103-alloy in the rolling direction compared to previous works.

For the differently homogenised LP 3103-conditions deformed to the same reduction the differences in subgrain size were as for the misorientation small. With decreasing amount of Mn in solid solution the subgrain size became larger. The subgrain sizes of the deformed C-conditions were about 10% larger than the subgrain sizes of the deformed A-conditions.

The subgrain size varied quite significantly when the three investigated alloys deformed to approximately the same strain where compared. As for misorientation, the stored energy associated with the subgrain size, given in equation (2.2), was highest for the CP 3103-material. For this material the subgrain size was 0.45 μm x 0.71 μm, while for the AA1200-alloy, which corresponds to having the lowest stored energy, the average subgrain size was 0.64 μm x 0.98 μm.

5.2.2 Effect of elements in solid solution

From the Vickers hardness measurements of the deformed LP 3103-alloy, summarised in Table 5.1, it is seen that the amount of manganese in solid solution has a large influence on hardness. Low supersaturation results in a softer material than for a condition with high supersaturation of alloying elements. Hinesley and Morris (1970) observed the same trends when measuring the yield

stress of an AA3003-alloy, after cold rolling of the alloy to different reductions. This latter alloy was pre-treated differently to achieve different amounts of manganese in solid solution, although estimations of these variations were not given in the paper. The only difference in their observations compared with the LP 3103-alloy was that they found the difference in yield stress to decrease with increasing deformation, while for the LP 3103-alloy no consistent trend for the change in hardness with increasing reduction was observed.

Table 5.1: Vickers hardness of the deformed LP 3103-alloy. The estimated amounts of Mn in solid solution are given in parenthesis.

Homogenisation	e=0.5	e=1.5	e=3.0
A (0.50wt% Mn)	53.7	59.3	69.0
B (0.42wt% Mn)	50.2	56.5	65.3
C (0.31wt% Mn)	45.2	53.1	59.4

5.2.3 Grain fragmentation

In Table 5.2 the grain fragmentation of the investigated alloys has been summarised, and for all alloys an effect of formation of new high angle grain boundaries has been observed, except for the LP 3103-alloy deformed to a strain of 1.5. The grain break-up factor is given by:

$$\frac{D_{calculated}}{D_{measured}} = \frac{D_0 / \exp(e)}{D_{measured}} \qquad (5.1)$$

where D_0 is the original grain size and e is the strain.

Table 5.2: Observations of grain fragmentation subjected to cold rolling.

Alloy	$D_{0,ND}$ [μm]	Measured band thickness ND [μm]	Predicted band thickness ND [μm]	Grain break-up
AA1200, e~1.5	70	3.9	15.6	4.0
CP 3103, e~1.5	30	2.3	8.6	3.7
LP 3103, e=1.5	80	15.1	17.9	1.2
LP 3103, e=3	80	1.9	4.0	2.1

It should be noted that the starting material of the CP 3103-alloy was in a partly recrystallised condition. As seen in Fig.4.28 the microstructure was layered in bands of recrystallised grains and several recovered deformation bands. This observation leads to the conclusion that less fragmentation has occurred than what is given in Table 5.2. Thus it can be stated that a lower break-up factor is expected if the material had been fully recrystallised before deformation of the CP 3103-material. The original grain sizes of the other alloys were relatively large, and thus grain fragmentation is expected for these alloys.

According to several works [Hughes (1995), Sæter (1997), Forbord (1999)] the most important aspect to whether grain fragmentation occurs is the original grain size. For an initial grain size of typically less than 40 μm little break-up is reported. Hughes (1995) related these observations to the assumption of more homogeneous deformation when the original grain size is small. If break-up is not observed another possible explanation of why this is not happening is the initial texture of the material, because subdivision of grains is very orientation dependent. At medium to high strains the stored energy can be heterogeneous, leading to the formation of deformation induced boundaries [Doherty *et al.* (1997)]. Starting deformation with a stable initial texture, less fragmentation would result compared to an unstable or a randomly textured material. In contrast to the above works, Engler *et al.* (1996) investigated break-up of originally cube-oriented grains that had an initial grain size of 40 μm after cold rolling of an Al1.3Mn-alloy. They found the grain break-up factor to be scattered around 2-4, which indicate that cube textured materials are subjected to break-up even if the grain size is small.

5.2.4 Particle break-up

When comparing the particle distributions of the *as cast* LP- and CP 3103-alloys some differences are observed. The particle structure of the CP 3103-material consists of more large particles than the LP 3103-alloy, this difference is most probably due to differences in the casting conditions of the two alloys. For billet casting the dendrite arm spacing is usually much smaller than for materials cast into rolling slabs. This fact results in more segregation for the latter materials and, thus coarser particles in this case.

Upon deformation of the homogenised LP 3103-alloy to a strain of 1.5 some particle break-up occurred, Fig.4.7, but hardly any break-up was observed when increasing the strain from 1.5 to 3.0. This lack of break-up indicates that the particles are most sensitive to break-up during the first cold rolling passes, *i.e.* before the particles are aligned in the rolling direction.

The trend of particle break-up of the CP 3103-alloy is that the coarsest primary particles break up at all stages of deformation, as seen in Fig.4.34. This observation is similar to observations by Daaland (1993). During hot deformation of an Al1Mn1Mg-alloy it was observed that the particles tended to break up quite significantly. The break-up was larger in the surface of the slab than in the centre during the first deformation passes and the particle distribution was more uniform for the final hot-rolling gauge than after the first passes. The hot rolling mainly resulted in break-up of the coarsest constitutive particles, which is similar to the observations for the CP 3103-alloy. Daaland (1993) did not investigate the cold rolled condition, but for the present investigations of the CP 3103-alloy the largest particles tended to break up as well for the cold rolling sequence, but not as much as during hot rolling.

5.2.5 Deformation texture

A comparison of the b-fibre for the three investigated alloys, all deformed to approximately the same strain of 1.5 is given in Fig.5.2. In this figure it is seen that the trends in variation along the b-fibre for the two AA3103-alloys are similar, but with different intensities. The AA1200-alloy evolved differently from the two other alloys, where the orientations along j_2=45-65° sharpen more than those being oriented close to the Bs-orientation (j_2=90°).

The deformation texture of the LP 3103-alloy evolved as expected, Fig.4.5, starting with a random texture followed by a gradually build up of the a- and b-fibres as strain increased. The intensity of the a-fibre saturated after a low reduction if the Bs-orientation is assumed belonging to the b-fibre.

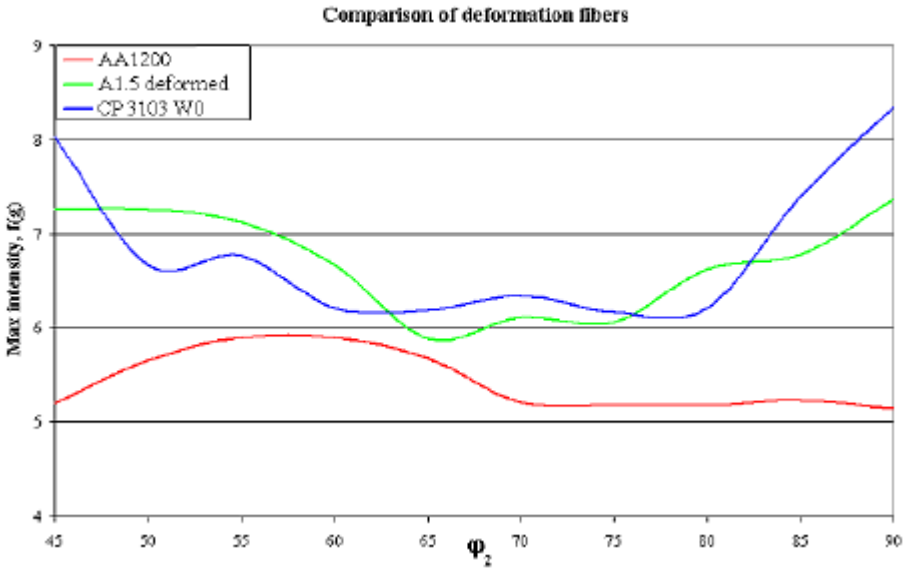

Fig.5.2: Comparison of the *b*-fibre plots of the three investigated alloys.

The deformation textures of the B- and C-conditions were almost similar to those of the A-conditions. This similarity is seen in the *b*-fibre plots, Fig.4.5d), where the *b*-fibres of the A- and C-material conditions are included. This observation indicates that the amount of manganese in supersaturated solid solution has little influence on the texture formation. The only observed difference is that the texture tends to sharpen somewhat as the amount of supersaturation increases.

In Table 4.4 the changes in volume fraction of various texture component for the different conditions shows that the amount of manganese in solid solution had no effect on the evolution of the deformation texture. From these results it is seen that the only components which sharpened upon deformation beyond e=0.5 were the S- and Cu-orientations. However, comparing this with the *b*-fibre plot in Fig.4.5d) it is seen that the strength, f(g), of the Bs-orientation has doubled going from a strain of 0.5 to a strain of 3.0. This observation exemplifies the problem of reliability of calculated volume fractions, and especially when the volume fractions are calculated from large volumes. This is further supported by comparing the OIM-map of grains being cube-oriented (Fig.4.6b), where less than 1% of the microstructure were oriented within 15° of the exact cube, to the calculated volume fraction of cube from the ODF found to be 4.3%. To conclude, one must be cautious if volume fractions, calculated from an ODF, are used as input for modelling activities.

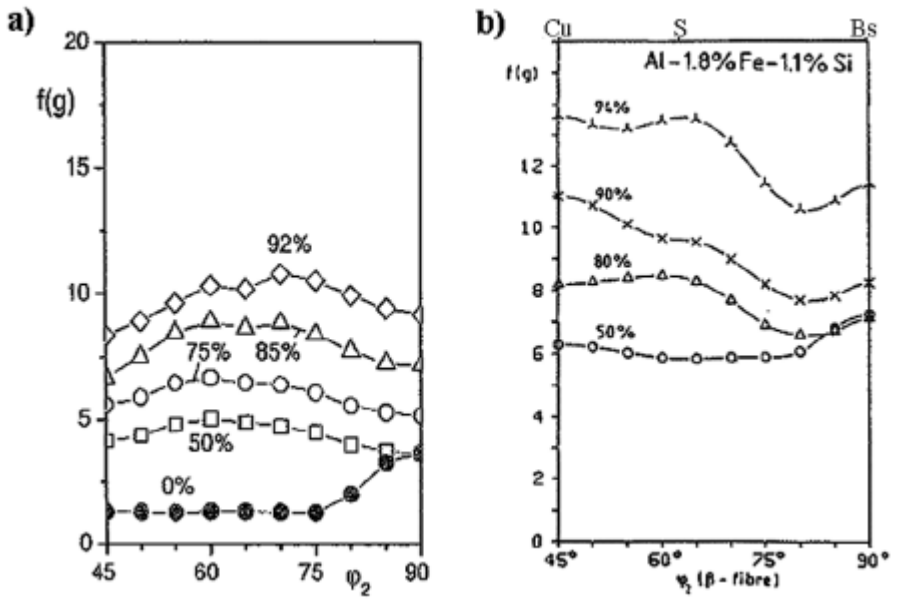

Fig.5.3: Evolution of the *b*-fibre with increasing strain of a) an AA3104-alloy [Engler (2002)] and b) an AlFeSi-alloy [Lücke and Engler (1990)].

The deformation textures of the CP 3103- and the AA1200-alloys both consisted of RD-rotated cube and the *b*-fibre as seen in Fig.4.32b) and Fig.4.44, respectively. Some differences are observed when comparing the *b*-fibre plots of the industrially processed materials. The AA1200-alloy has a wide peak about j_2=55°-60° (~S). This peak is located in the same range as observed for an 80% deformed AlFeSi-alloy [Lücke and Engler (1990)] as seen in Fig.5.3b). However, no distinct minimum was located near the Bs-orientation as observed for the AlFeSi-alloy.

The CP 3103-alloy has peak intensities for the Cu- and Bs-orientations and no distinct minima, these peaks were significantly sharper than for the LP 3103-alloy. Possible reasons for this are [1)] different deformation temperature, [2)] different initial texture and [3)] different chemical composition. Even though this latter difference was small it might have had an effect on the texture formation.

As seen in the above figures (Fig.5.3), the effect of alloying elements and deformation has a large influence on the evolution and shape of the *b*-fibre. In this figure the changes in the strength of the *b*-fibre with increasing deformation for two rather different alloys are seen. Similarities are seen when comparing

these alloys to the b-fibre plots for the investigated alloys within this work. However, the overall conclusion is that the alloying elements play an important role in the texture formation and evolution upon deformation. Engler (2002) has presented the b-fibre evolution of an AA3104-alloy and Lücke and Engler (1990) have investigated an Al1.8Fe1.1Si-alloy deformed to different cold rolling reductions. These papers have shown that the grain rotation acts differently when being cold rolled, as seen in the b-fibre-plots of Fig.5.3. For the AA3104-alloy a wide peak for j_2=60-80° is found at all deformations, while minimum intensities are located at the Cu- and Bs-orientation. For the AlFeSi-alloy the orientations along j_2=45-60° evolved first, while a minimum is found close to the Bs-orientation. With increasing strain the S- and Cu-orientations sharpens more then orientations close to the Bs-orientation. Neither of these observations is similar to what is observed for the LP 3103-alloy which have been given different reductions. For the LP 3103-alloy all orientations along the b-fibre grow gradually, with small peaks for the Cu- and Bs-orientations, Fig.4.5d).

Both of the industrially processed alloys had another pronounced texture component in the ODFs. This component was the RD-rotated cube orientation, which was rotated 20-30° about the F-axis. The RD-rotated cube texture is a natural consequence of the strong initial cube texture prior to cold rolling of these materials. It is known that the cube texture is a metastable orientation during hot deformation [Hirsch (1990), Samajdar and Doherty (1995), Vatne (1995)], while it is unstable in case of cold deformation to large strains [Akef (1992), Maurice and Driver (1993)].

5.3 Recovery

5.3.1 Texture evolution during recovery

The texture evolution during the first stages of annealing of the A3.0-350°C material was investigated. The material behaviour is important with respect to the texture formation, *i.e.* orientations that form Σ7-boundaries with respect to common orientations found in the recrystallisation texture can strengthen. This sharpening is exactly what is seen in Fig.5.4, where the texture evolution during the first 10 minutes of annealing is shown in form of *b*-fibre plots. It is seen that it is in particular the Cu- and S-orientations that tend to sharpen upon annealing. These orientations have a 40°<111>-relationship to the P- and ND-rotated cube and to the exact cube orientations, respectively. For an AlMgMn-alloy (AA5083) investigated by Engler *et al.* (1994), the *b*-fibre intensity increased 20% during the first period of annealing. Further this increase was found to be independent of initial texture. This texture strengthening was related to the rearrangement of the dislocations into more stable configurations (subgrains) and to the subsequent subgrain growth. These mechanisms lead to less spread of the orientations within the deformation bands and thus a texture sharpening.

The sharpening of the *b*-fibre is larger for the A3.0-350°C material condition than what Engler *et al.* (1994) have reported for the AlMgMn-alloy. A possible reason for this could be the differences in mechanisms that contribute mostly to the sharpening, *i.e.* for the AA5083-alloy a higher interior dislocation density is expected to be found compared to the LP 3103-alloy. On the other hand more subgrain growth is expected to occur for the AlMn-alloy than for the AlMgMn-alloy. After longer annealing times, *i.e.* after 600 seconds at temperature, the *b*-fibre intensity gradually weakened due to the fact that recrystallisation has started, as confirmed by the back-scattered images in Fig.4.22.

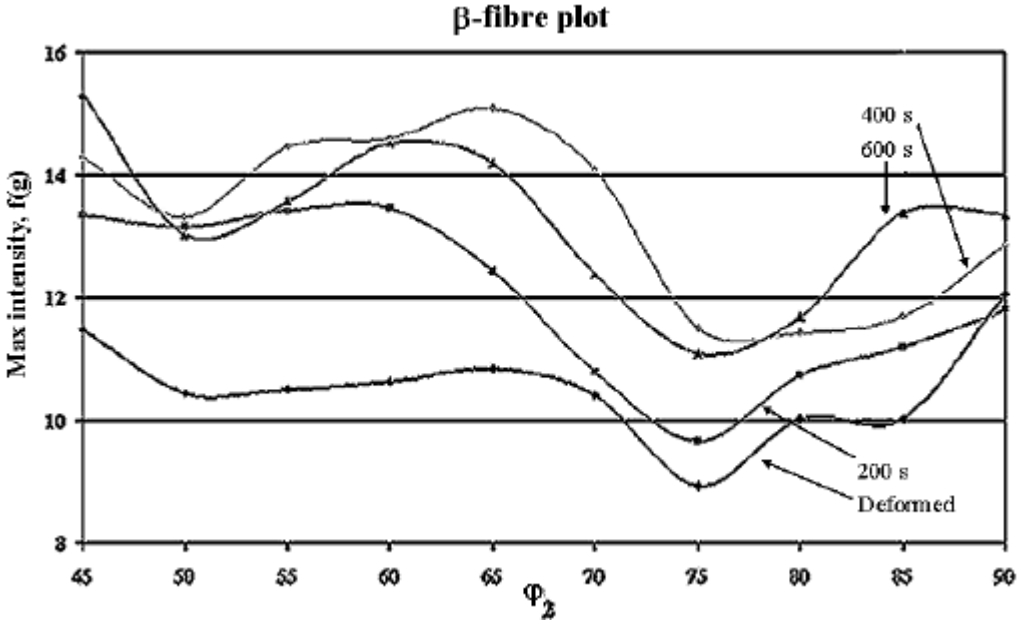

Fig.5.4: *b*-fibre evolution during the first annealing stages of A3.0-350°C.

5.3.2 Precipitation during recovery and recrystallisation

The hardness of A1.5 and A3.0 annealed at 250°C and 300°C was found to increase at the early stages of annealing. This observation is similar to what Sæter (1997) found for a deformed AlMn-alloy, which was annealed at low temperatures. He investigated this effect in more detail, using TEM, and found indications of cluster formation of solute atoms. The effect of cluster formation on hardness became less significant with increasing temperature due to an increased recovery rate. Thus the increase in hardness due to precipitation was impossible to measure at higher temperatures. The initial increase in hardness has not been subjected to any investigation in the present study, but it is reasonable to assume that the increase in hardness is due to cluster formation of solute atoms for the present investigations as well. This assumption is supported by a TEM investigation by Hagström (2003) on the CP 3103-alloy in the cold rolled condition. Here indications of some cluster formation was found in the cold rolled condition and upon annealing these clusters precipitated.

Already in the early stages of the isothermal annealing sequence precipitation occurred for some conditions of the LP 3103-alloy, as seen by the increase in conductivity in Fig.4.8 and Appendix 2. Especially the A-material was subjected

to heavy precipitation, but some precipitation also occurred for the B-material at lower annealing temperatures. The C-material was virtually unaffected by precipitation prior to recrystallisation, but for long annealing times an increase in conductivity was seen to occur in the fully recrystallised microstructure. For this latter material condition it is seen in Fig.4.25 that the precipitation and growth of a few precipitates has mainly occurred at the high angle grain boundaries, which are closely spaced due to the fine recrystallised grain size of approximately 10 μm.

In Fig.4.22b) for the A-homogenised material it is seen that lots of dispersoids have formed after only one minute of annealing. The annealing temperature was 350°C and at this temperature manganese atoms are known to migrate slowly. This observation indicates that matrix diffusion is not the dominating mechanism in the nucleation process at this temperature. Hence, the solute atoms must either migrate through the grain boundaries and nucleate at these, or the clusters formed during deformation precipitates upon the subsequent annealing.

Chen *et al.* (2003) investigated a supersaturated hot rolled AA3003-alloy with respect to precipitation. The material was in a fully recrystallised condition after a hot rolling sequence. The alloy was first given a solution heat-treatment at 630°C, then they produced two material conditions prior to an isothermal annealing treatment. These conditions were a fully recrystallised hot rolled material and a material that has been given a subsequent cold rolling reduction of 50% after the solution treatment. For the undeformed material precipitation occurred at the high angle grain boundaries after short annealing times, while at the later stage precipitation also occurred in the grain interior. For the deformed material fine precipitates were almost uniformly distributed already at the early stage of annealing, which points to a formation of precipitates on the substructure prior to recrystallisation. The fraction of precipitates was calculated according to the equation:

$$x = \frac{k_t - k_0}{k_\infty - k_0} \qquad (5.2)$$

where k_t is the conductivity at annealing time t, k_0 is the conductivity prior to annealing and k_∞ is the saturation conductivity of a fully precipitated sample.

It was assumed that the precipitation could be described by an Avrami-equation:

$$x = 1 - \exp\left(-kt^n\right) \qquad (5.3)$$

By combining equations 5.2 and 5.3 Chen *et al.* (2003) reported a good fit between the predicted evolution and the experimentally measured evolution in conductivity. A good fit was found both for the deformed and undeformed materials. When applying a cold rolling reduction a decrease in n-value (equation 5.2) and an increase in k-value compared to the undeformed condition were found to give the best fit to the measured values.

This approach was used to describe precipitation of the LP 3103-alloy of the deformed and subsequently annealed A- and C-conditions. To achieve the best fit for the A-material with increasing deformation a decrease in the n-value and a minor increase in the k-value had to be used, which is similar to the observations of Chen *et al.* (2003). For the C-material, on the other hand, a n-value that increased with strain and a k-value close to constant had to be used. In Fig.5.5 modelling for A1.5, A3.0, C1.5 and C3.0-materials giving the best fit are shown.

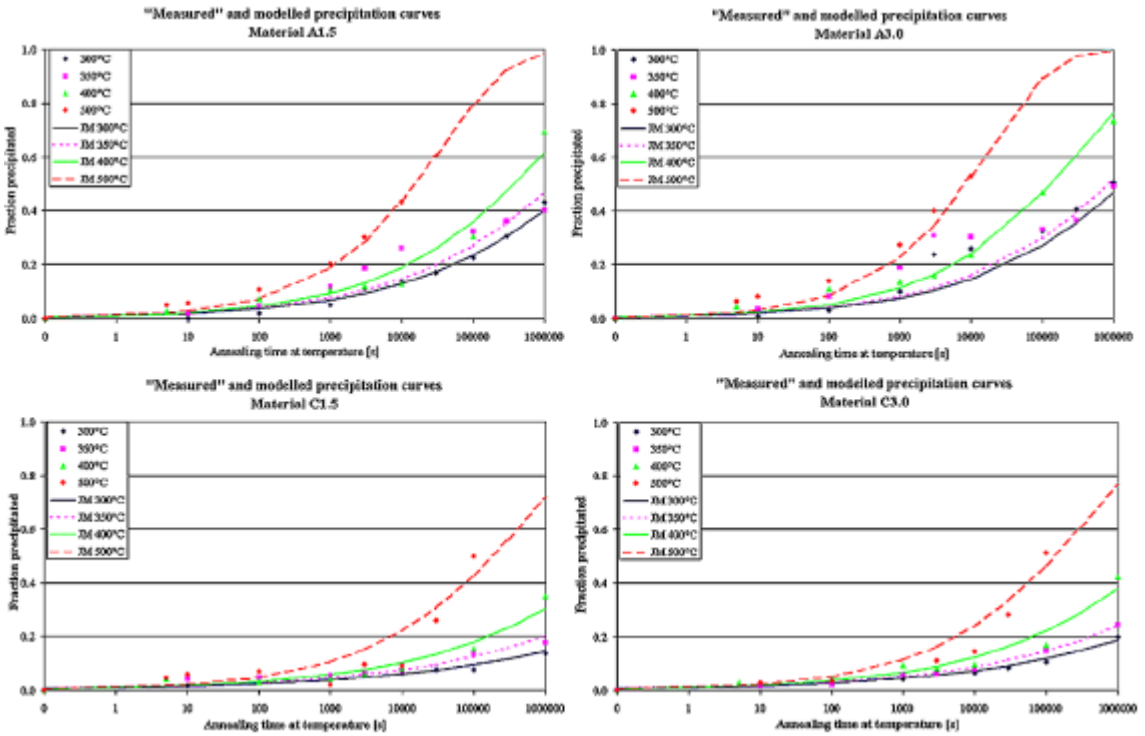

Fig.5.5: The measured conductivity was calculated to fraction precipitated according to equation 5.2. By tuning equation 5.3 good fits to the experimental points were found.

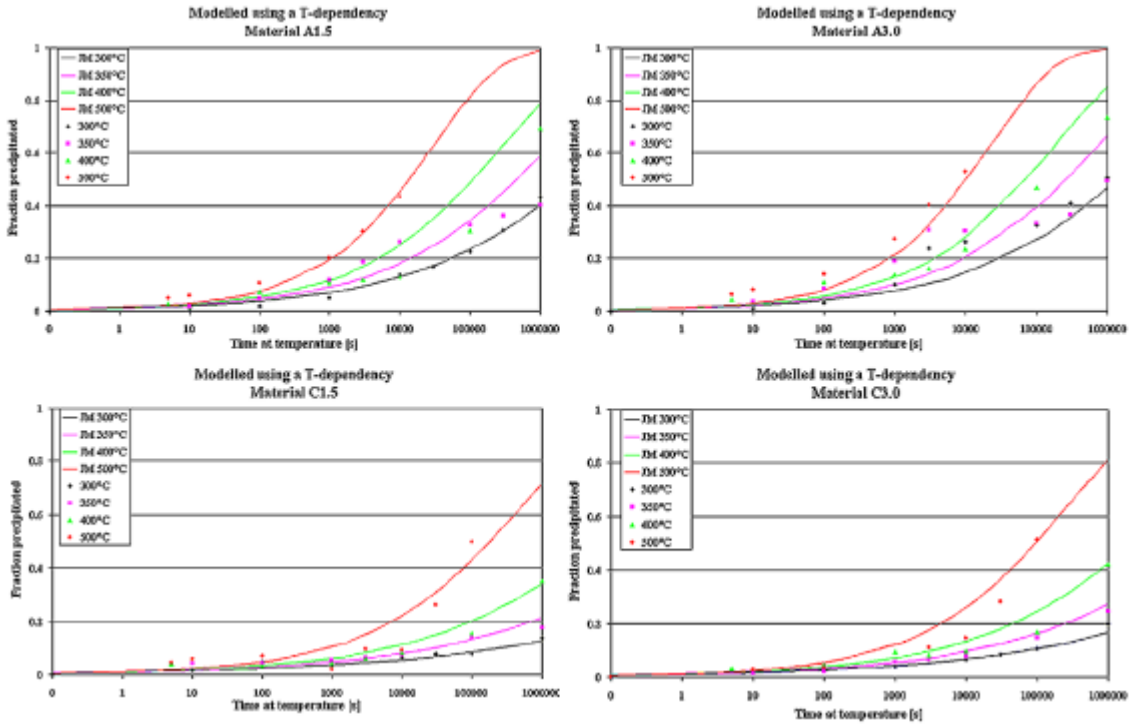

Fig.5.6: Calculated and measured evolution of fraction precipitated with time at temperature. The calculated evolution is based on a classical JMAK approach, where k is kept constant and n is given as f(T), formulated as given in equation (5.4).

To check for temperature dependency the k-value was kept constant while the n-value was changed. A reasonably good expression for the change in n-value with increasing time was found, and this empirical temperature dependency is given as:

$$n = n_{T,tuning} + 8 \cdot 10^{-4} \left(T - T_{tuning} \right) \qquad (5.4)$$

where $n_{T,tuning}$ is the n-value found at a given temperature (T_{tuning}). The constant value is the average increase in n-value for all investigated curves with increasing temperature. In Fig.5.6 the results of this modelling approach is shown.

It was impossible to model the A-material annealed at 350°C given reductions of 78% and 95%, and the A3.0-300°C material was neither well predicted by this modelling approach. The reason for this is probably the fact that the fraction precipitated (conductivity) increased rapidly during recrystallisation of these materials, see Fig.4.8 and Appendix 2.

This change is very complex and in an attempt to explain this increase in conductivity two mechanisms are suggested: [i)] nucleation events on the moving boundaries as recrystallisation progresses, or [ii)] removal of solute atoms from the matrix to the already existing dispersoids.

The first idea, [i)] nucleation events on the moving boundaries as recrystallisation progresses, is a classical approach for concurrent precipitation. Westengen and Ryum (1978) have shown that precipitation occurs easier on a moving boundary than on a stationary boundary. The idea is that the precipitates are formed on the moving boundary. Thus the boundary is pinned ($P_D<P_z$), but is later unlocked from the precipitates as they have coarsened, locally this results in $P_D>P_z$. If this mechanism takes place a higher density of dispersoids would be expected on the boundaries, somewhat lower behind the boundary due to the coarsening and the lowest density is expected to be found in the untransformed areas.

The presented experimental observations do not seem to support such behaviour for the LP 3103-alloy. The evolution in dispersoid density, Fig.4.24, indicates a nearly constant density throughout annealing, while the theory suggests that the density should increase during recrystallisation. Even if some precipitation is assumed to occur prior to recrystallisation this idea does not seem to apply for the present alloy. In such situation one would expect an increase in dispersoid density throughout annealing and the high angle grain boundaries (HAGBs) should have been decorated by precipitates in the partly recrystallised condition, which was not the case of the present study.

Support for the latter idea [(ii)], removal of solute atoms from the matrix to the already existing dispersoids, is found in Fig.4.24. In this figure the evolution in dispersoid density is seen to be nearly constant after the first couple of minutes of annealing at 350°C, *i.e.* little or no formation of new dispersoids as annealing progressed. For these short times of a few minutes the dispersoids nucleate and grow to become visible in the electron microscope. In Fig.4.22 the microstructural evolution of the A3.0-350°C material condition is shown, and these micrographs clearly demonstrated that lots of dispersoids have formed, while no recrystallised grains are observed after one minute of annealing.

A more detailed picture of this idea is presented in the following and it refers to the sketch in Fig.5.7, still concerning the A3.0-350°C material condition. During the first minute(s) the interior dislocations are annealed out and some subgrain growth occurs. Further, the dispersoids are nucleated on the substructure and grow quite rapidly by diffusion of Mn-atoms along the high angle grain boundaries and subgrain boundaries. The areas around the dispersoids become depleted of alloying elements, *i.e.* of Mn-atoms as the dispersoids grow. During this first period of annealing the dispersoids (presumably $Al_{12}Mn$-phase) do obviously not need many Mn-atoms to grow, and thereby the increase in conductivity is not that large. However, it is seen in the linear time plot of the change in conductivity, Fig.4.24, that it is during these first minutes of annealing that the conductivity increases the most. After this short incubation time the microstructure is well defined consisting of subgrains, dispersoids, solute atoms of Mn and primary particles. The particles will be ignored in the following discussion.

At a later stage of annealing some subgrains reach a critical size for nucleation and become recrystallised grains, Fig.5.7a). These growing grains are exposed to several forces acting upon them. The driving force for further growth is the removal of the substructure, while the dispersoids pin the boundary and the solute atoms reduce the migration rate. The HAGBs are efficient diffusion paths for the solute atoms, thus the solute atoms migrate towards the dispersoids. After the removal of the solute atoms at and close to the boundary, the boundary bow out, but it is still pinned by the dispersoids, Fig.5.7b-c). The removal of solute atoms leads to an increase in the size of the dispersoids. This increase has not been measured experimentally, but it is the presenting author's opinion that this has happened. Such a growth is certainly the case for the A3.0-300°C material as seen in Fig.4.23a-d), even though no dispersoid counting was carried out for this particular condition.

Finally the curvature is so large that the HAGB can advance before being pinned again. Obviously some manganese will remain in supersaturated solid solution after the HAGB has swept the area, but this fact has been ignored in the figure. A support for this latter assumption is seen in the conductivity measurements for

e.g. A3.0-350°C, where the conductivity increases even after long annealing times of the fully recrystallised material.

The reason why this mechanism does not occur at higher temperatures is that the migration rate of the HAGBs is so high that the solute atoms are not able to migrate along the boundary towards the dispersoids before the HAGB has moved passed the dispersoids.

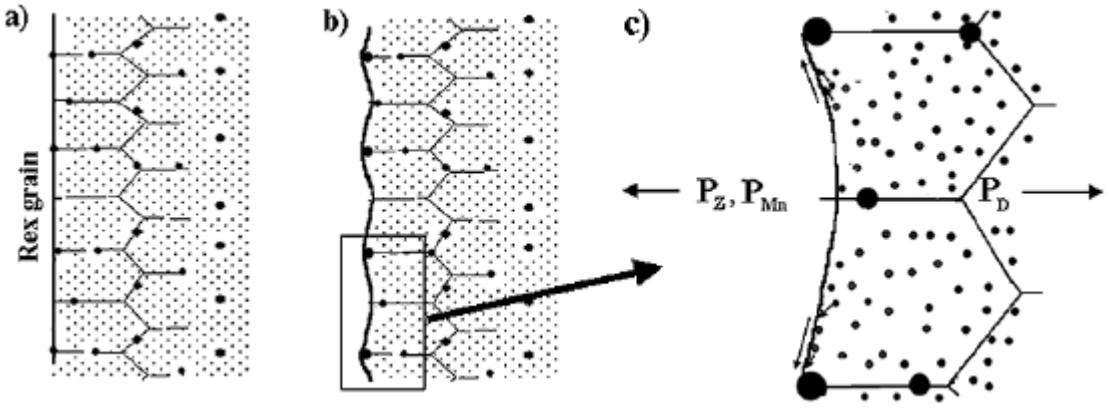

Fig.5.7: Sketch of how the Mn-atoms in solid solution are removed from the matrix. In the figure the small dots represents solute Mn-atoms, big dots are dispersoids and the fully drawn lines are grain boundaries. The dispersoids are formed at the early stages of annealing, *i.e.* prior to recrystallisation. In a) a recrystallised grain boundary is seen as a straight line. In b) this grain boundary bows out due to removal of the substructure, but is pinned by the dispersoids and solute atoms. As the solute atoms come in contact with the HAGB they migrate along this boundary towards the dispersoids, as indicated in c). The consequence of this mechanism is that the dispersoids grow.

A presupposition for this idea is that the retarding force is periodically reduced as the nearby solute atoms migrate towards the dispersoids and the high angle grain boundaries enabling unpinning from the dispersoids. However, a closer analysis of this process indicates that this is not the case, given that the dispersoid density is constant throughout the entire annealing treatment as seen in Fig.4.24. If the dispersoids grows in combination with a constant density, an increased Zener drag would be the result.

This increase in retarding force is seen from the equation defining Zener drag:

$$P_z = \frac{3}{2}\gamma_{GB}\frac{f}{r} = \frac{3}{2}\gamma_{GB}\frac{N \times \frac{4}{3}\pi r^3}{r} \quad \Rightarrow \quad P_z \propto r^2 \qquad (5.5)$$

where γ_{GB} is the interaction energy, f is the volume fraction of dispersoids, N is the number of dispersoids with a given radius r.

Since both mechanisms for different reasons are inconsistent with what is observed experimentally a modification of the second mechanism is suggested. This modified mechanism assumes that the driving pressure for recrystallisation at all times is larger than the retarding force due to the dispersoids (Zener drag). As seen from the change in conductivity of the A3.0-350°C material on the linear time-scale, Fig.4.24, the largest increase is observed during the first minutes of annealing, *i.e.* when precipitation occurs. The increase in conductivity during recrystallisation is in this modified mechanism assumed to be due to the growth of the existing dispersoids as the grain boundary interacts with the precipitates. As the high angle grain boundaries migrate through the deformed structure, solute atoms are connected to the boundaries. This connection of solute atoms occurs because it is associated with a reduction in the stored energy of the system.

At low annealing temperatures the boundary moves so slowly that some of the solute atoms which are connected to the boundary and positioned close to the dispersoids as the boundary passes the precipitates are added to the precipitate. Locally this results in a slightly increased Zener drag, as indicated by equation (5.5), but the driving force is still believed to be larger than the retarding force. As the driving force is reduced somewhat during this interaction the migration rate decreases, but the boundary is still able to break away from these obstacles and move further. Since some of the solute atoms are added to the precipitates this would result in a gradual increase in conductivity as seen in Fig.4.24.

This phenomenon occurs at low temperatures (T<350°C for the A-homogenised material) where the migration rate of the boundaries is relatively slow. At higher temperatures (T>400°C) the migration rate is so high that the solute atoms close

to the boundary are not able to follow the moving boundaries for long distances. They are left behind the moving boundary still being in solid solution, as clusters of solute atoms that nucleates at the later stages or as very small dispersoids that were not observable in a FEG-SEM. In Fig.4.23e-f) following the recrystallisation reaction at 400°C-annealing some dispersoids are seen. However, it seems that these dispersoids have nucleated on the subgrain boundaries rather than on the migrating high angle grain boundary. This behaviour is similar to the behaviour at lower annealing temperatures. In Fig.4.25 where the material has been annealed for a very long time at 400°C a high dispersoid density is observed. It seems that these dispersoids have nucleated in the regions of the originally deformed subgrains, thus it is most likely that the high angle grain boundary leaves behind clusters of solute atoms as it passes a subgrain boundary. These clusters thus cause nucleation at the later stages of annealing.

The solid atoms do not directly pin the grain boundaries, *i.e.* does not make an influence on whether the grain boundary migrates or not, they rather affect the rate of migration. As the density of atoms on the grain boundary increases the migration rate is reduced. This effect has previously been shown by Dimitrov *et al.* (1978) for cold rolled aluminium with additions of Cu and Mg.

5.3.3 Precipitation effects predicted by TTT-diagrams

As discussed in the experimental part, TTT-diagrams for the different variants of the LP 3103-alloy (Fig.4.11) have been constructed from hardness and conductivity measurements. The TTT-diagrams indicate that two precipitation reactions occur in the LP 3103-alloy. According to Chen *et al.* (2003) the high temperature precipitation (T>500°C) of an undeformed microstructure is a direct formation of Al_6Mn-dispersoids. At lower annealing temperatures the metastable $Al_{12}Mn$-phase forms first, followed by a solid state transformation into the stable Al_6Mn-phase. However, when a substructure is present prior to annealing, as for the LP 3103-alloy in the present work, a direct formation of Al_6Mn-dispersoids starts at a lower temperature. Yang *et al.* (1999) found that Al_6Mn-dispersoids formed most frequently when investigating an Al1.3Mn-alloy. $Al_{12}Mn$-dispersoids were only occasionally observed.

The chemistry of the dispersoids was not examined in the present work but it is assumed that the same phases as found by Chen *et al.* (2003) were formed. According to the TTT-diagram of Chen *et al.* (2003) this takes place at temperatures above 450°C after a rolling reduction of 50%. For the LP 3103-alloy the precipitation nose was not found to shift towards lower temperatures as the deformation increased.

In the TTT-diagrams for the LP 3103-alloy it is seen that the formation of metastable $Al_{12}Mn$-phase is shifted downwards as the amount of Mn in solid solution decreases. The explanation of this shift in temperature of when precipitation starts is associated to the phase-diagram as can readily be seen in the illustration in Fig.5.8. A decreasing amount of manganese in solid solution results in a shift towards the pure Al-side of the phase-diagram, and as a consequence the nucleation of dispersoids starts at a lower temperature.

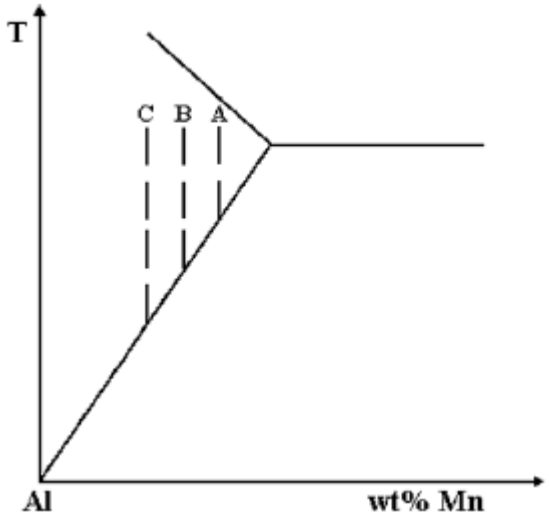

Fig.5.8: Effect of supersaturation of Mn on the precipitation behaviour. The sketch illustrates why precipitation starts at a higher temperature for the A-condition than for the B- and C-conditions.

5.4 Recrystallisation

5.4.1 Effect of chemistry

There were relatively small differences in the chemical composition of the two investigated AA3103-alloys. The overall compositions are given in Table 3.1, but the main differences were that the LP 3103-alloy had higher contents of iron and silicon. The latter difference is known to result in different particle composition [Haan *et al*. (1996)], where the constitutive particles of the LP 3103-alloy should be a combination of Al_6(Mn,Fe) and α-Al(Mn,Fe)Si, while for the CP 3103-alloy only Al_6(Mn,Fe) is expected to be found.

To compare the effect of alloying composition with respect to the recrystallisation behaviour, the TTT-diagrams have been compared. However, before comparing the TTT-diagrams a decision has to be made on which of the LP 3103-conditions that should be compared to the cold rolled CP 3103-material. With respect to the conductivity measurements the B-condition should be chosen. Also the variation in conductivity of the CP 3103-material upon annealing (Fig.4.35) was more similar to the B1.5-material than to the C1.5-material (Appendix 2). The softening behaviour was also more similar when comparing the W50-material, Fig.4.39, with the B-homogenised LP 3103-material deformed to a strain of 3.0 (Fig.4.8). Hence the B-condition deformed to a strain of 1.5 should be compared to the CP 3103-alloy.

Comparing the TTT-diagram for the CP 3103-material, Fig.4.38, with the one given for the LP 3103-alloy in Fig.4.11, containing approximately similar supersaturation of Mn, it is seen that the precipitation nose is shifted toward significantly shorter annealing times for the CP 3103-alloy

The recrystallisation texture of the CP 3103-alloy (Fig.4.40) sharpened as the effect of precipitation on recrystallisation became less significant. This observation is in contrast to what has been observed previously, where the recrystallisation textures have been found to strengthen and to be dominated by the cube texture in case of concurrent precipitation [Benum and Nes (1997), Sæter *et al*. (1997), Vatne *et al*. (1997)].

5.4.2 Effect of precipitation of dispersoids on the final grain structure

As seen for the A-condition of the LP 3103-material deformed to a strain of 3.0 and subsequently annealed at temperatures above and below the characteristic temperature, T_C, as defined on page 68, the grain size became different, Fig.5.9. TTT-diagrams are, as seen for the A-condition, effective in predicting the effect of precipitation on the recrystallised grain size. Below T_C the grain size became coarse while above T_c a very fine-grained material was obtained.

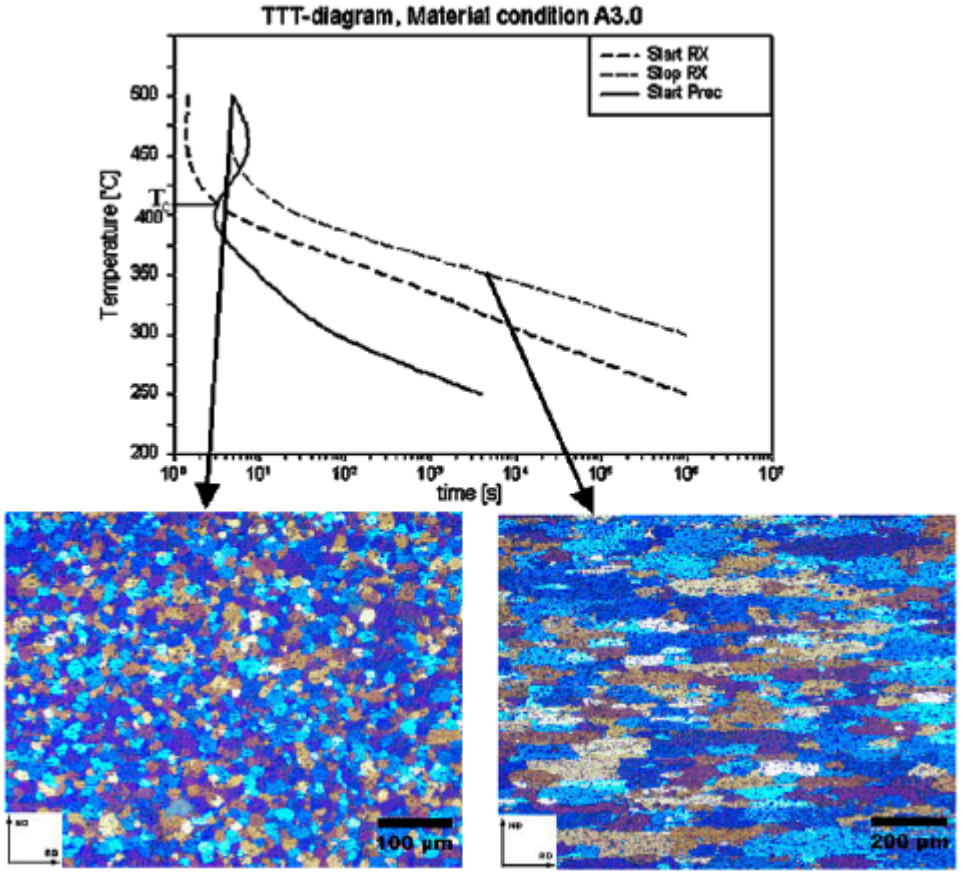

Fig.5.9: Effect of temperature on the final grain size with respect to the TTT-diagram of the A-homogenised LP 3103-material.

For those materials where precipitation occurred concurrent to recovery and recrystallisation, *i.e.* A3.0-300°C, A3.0-350°C and B3.0-300°C, recrystallisation was found to start in the centre of the sheets. Similar observations have been found by Furrer and Hausch (1979) in an AlMn-alloy and by Oscarsson *et al.* (1992) in an AA3003-alloy. They found the grain structure to become coarse

when long annealing treatments were needed to complete recrystallisation of these alloys. The same effect was observed for the LP 3103-alloy of the presented investigations.

Elements in solid solution and precipitation of dispersoids have for decades been known to retard the recrystallisation process. Hornbogen and Köstner (1978) have schematically shown that recrystallisation is slowed down if precipitation occurs prior or concurrent to recrystallisation. Nes and Slevolden (1979) showed for two commercial pure aluminium alloys and an AA3xxx-series aluminium alloy that recrystallisation was significantly slowed down if concurrent precipitation occurred, and in such a case the grains size became coarse. The same observations have also been found in the present investigation of the LP 3103-alloy. By comparing the TTT-diagrams it is seen that once recrystallisation is influenced by precipitation the grain size became coarser. Furthermore, a significantly longer annealing time was required to recrystallise the material in case of concurrent precipitation than for a condition without precipitation.

In case of concurrent precipitation of the two 3103-alloys the grains boundaries of the fully recrystallised condition became more serrated than when the annealing was carried out above T_c. This observation is in accordance with observations by Hansen and Bay (1981), who showed micrographs of serrated grain boundaries when recrystallisation was retarded by a dispersion of small particles.

5.4.3 Grain size distributions of the AA3103-alloys

The cumulative particle size distribution of the deformed CP 3103-alloy was coarser than that of the LP 3103-alloy. Upon annealing more nuclei are thus produced in the vicinity of the supercritical particles for the CP 3103-alloy. Hence, a smaller recrystallised grain size was found for this alloy in case of concurrent precipitation than of the LP 3103-alloy given approximately the same rolling reduction.

From the recrystallised grain size distributions of the LP 3103-alloy deformed to a strain of 3.0 and of the CP 3103-alloy, Appendix 3 and 5, it is seen that most of

the conditions show log-normal distributions. For the CP 3103-alloy it is seen that at the lowest annealing temperature (300°C) the grains become somewhat larger than for an annealing temperature of 350°C. This increase in grain size is in accordance with what Furrer and Hausch (1979) observed for an Al1Mn-alloy. They found the local scatter in grain size to disappear at 360°C, *i.e.* the grain size distribution became more narrow and homogeneous below this temperature. Comparing this observation to the distributions of the LP 3103-materials, it is noted that this shift seems rather to depend on the amount of manganese in solid solution prior to recrystallisation than on the annealing temperature. This shift is illustrated in Fig.5.10. The shift is found somewhere between 350°C and 400°C for the A-condition, between 300°C and 350°C for the B-condition and is not observed for the C-condition. In Fig.5.10 this temperature is assumed to be found just above 250°C, this assumption seems reasonable since the material did not recrystallise within 10^6 seconds at this temperature, while the material recrystallised relatively rapid at 300°C. Furrer and Hausch (1979) estimated an amount of 0.45 wt% manganese in solid solution prior to annealing, *i.e.* in accordance with the dependency in amount of Mn in solid solution. The shift in distribution for the CP 3103-alloy is probably found somewhere between 280°C to 300°C. The solid line in Fig.5.10 follows:

$$T_{scatter} = 650 * [Mn] + 40 \qquad (5.6)$$

where [Mn] is the amount of manganese in solid solution.

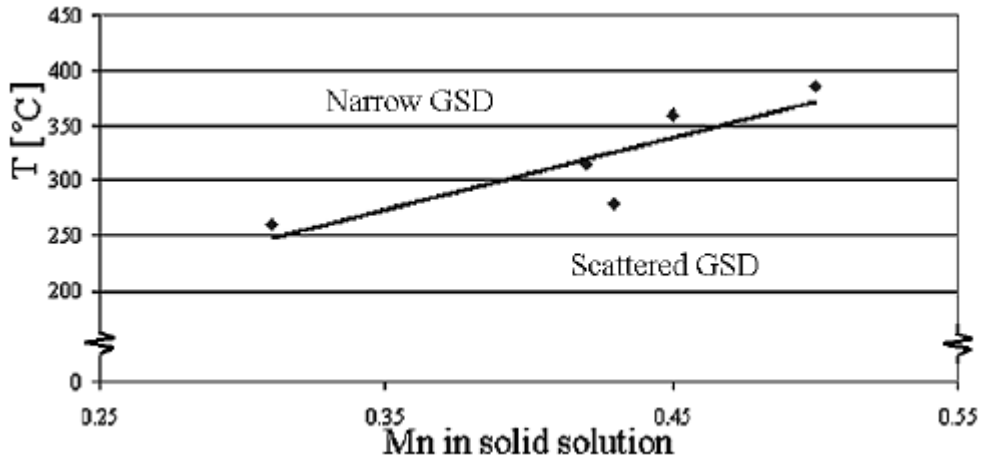

Fig.5.10: Dependency of when the grain size distributions (GSD) become more scattered *vs.* amount of Mn in solid solution.

5.5 Recrystallisation texture

5.5.1 On the origin of the P-texture

In the following the origin of the P-texture will be discussed in the view of previous work reported in the literature regarding recrystallisation texture and PSN-nucleation. These papers will be discussed and commented in relation to the observations of the present work. Finally, a summary of these papers is given and this summary is used to in order to describe the most likely reason of why a strong P-texture in combination with the ND-rotated cube texture was observed in the investigated LP 3103-alloy in case of concurrent precipitation.

In a resent work by Liu and Morris (2003) a continuos cast AA3015-alloy was investigated with respect to recrystallisation texture. The alloy was deformed to reductions of 70%, 80% and 90% and subsequently annealed at 350°C, 450°C and 550°C for 30 minutes. At the lowest annealing temperature recrystallisation was not completed for any of the deformed materials. They found the P- and ND-rotated cube orientations to dominate the recrystallisation texture for the other materials. The P-texture was found to increase in strength with increasing deformation, but decreased in strength with increasing temperature. The observations of the ND-rotated cube were opposite to that of the P-texture, *i.e.* it became stronger at higher temperature and weaker with larger reductions. For the present work, considering the LP 3103-alloy, the recrystallisation texture at such high annealing temperatures was dominated by the exact cube orientation, see Fig.4.18 for contour line plots of the materials deformed to a strain of 3.0. At low annealing temperatures for the A-material the P- and ND-rotated cube were observed, and both these orientations increased in strength with increasing deformation. For increasing temperature the orientations had a peak at 350°C, being slightly stronger at 300°C, before “disappearing” at higher temperatures. Liu and Morris (2003) related the P-orientation to a fibre, where the Bs-oriented deformation bands were transformed to P-orientation during recrystallisation. They had no explanation of the appearance of the rotated cube. In Fig.4.21 partly recrystallised OIM-maps of the A3.0-350°C condition are shown. From these maps it is reasonable to suggest that the actual orientations nucleated in the vicinity of primary particles, *i.e.* by PSN. This latter observation is in accordance with previous observations by Engler and co-workers [Engler *et al.* (1996),

Engler (1996b)] and Ryu and Lee (2002), who have done TEM investigations and found P-oriented grains to grow out of deformation zones surrounding coarse primary particles. The idea suggested by Liu and Morris (2003) of a fibre going from the Bs- to P-orientation does not seem to be a reasonable explanation of the P-texture formation, at least not for the present investigation.

The rivalry theories of oriented growth and oriented nucleation has a long tradition in texture research. The special 40°<111> orientation relationship is fundamental in the first theory, but this relationship is also used in order to explain recrystallisation texture by the oriented nucleation theory. Such boundaries are thought of as faster growing boundaries during recrystallisation. In particular the orientation relationship between the S- and the cube-orientations has been investigated in detail to explain the appearance of the cube orientation after deformation and subsequent annealing. However, other orientations are sometimes also found in the recrystallisation texture, which have this 40°<111> orientation relationship to some of the main deformation components. Among these both the P- and the ND-rotated cube orientations have a 40°<111> rotation relationship to the Cu-orientation. In Fig.4.20 of the LP 3103 A3.0-350°C-condition where the growth rate of different components was investigated, no growth effect beyond an initial growth advantage was observed. The observation of a strong P- and ND-rotated cube texture can be explained in terms of oriented nucleation or a microgrowth selection giving these orientations a nucleation advantage. In the fully recrystallised condition this results in a majority of grains with these orientations. This observation can not be an oriented growth effect, because in such a case the given orientations should continuously become larger than the grains of random orientation.

Vatne *et al*. (1997) have found the presence of the P-texture of a supersaturated AA3103-alloy after large reductions (e >3.0). At lower reductions the cube texture was the dominating orientation after recrystallisation, and the cube texture was found to strengthen in case of concurrent precipitation. The alloy had a strong initial cube texture due to hot rolling prior to the cold rolling, it is thus reasonable to assume that the retained cube-bands were active nucleation sites for recrystallisation during the subsequent annealing. The cube-oriented subgrains were found to have a larger size than subgrains of other orientations. Upon

annealing these cube-oriented subgrains reached an over-critical size faster than the subgrains of other orientations, and thus the recrystallisation texture became dominated by the cube texture. Sæter *et al.* (1997) and Benum and Nes (1997) have also experimentally shown an increasing intensity of the cube orientation in the recrystallisation texture in case of concurrent precipitation.

The reason why the P-texture only appeared after large reductions in the work by Vatne *et al.* (1997) was probably because the number of cube-bands that have survived deformation decreased with increasing strain. At such high strains (e >3.0) only very few cube-grains have survived deformation, such that PSN play the most important role in the nucleation of recrystallised grains. In case of the present LP 3103-alloy a random initial texture was present prior to cold rolling. This results in very few retained cube bands after deformation (Fig.4.6b), and thus other nucleation sites become active, *e.g.* PSN resulting in the P- and ND-rotated cube orientations. A possible explanation why the P-texture, assumed to be nucleated by PSN, is strong for the LP 3103-material with high supersaturation of manganese is that during homogenisation regions close to the primary particles becomes depleted of solute atoms. Upon the subsequent annealing after deformation less precipitation occurs in these regions than in the matrix, hence recrystallisation occurs easier here due to less retarding forces in the vicinity of the particles. The precipitation reaction during annealing strengthens the P-texture due to more effective pinning of the other nucleation sites.

Engler *et al.* (1997) applied a certain counting procedure of to quantify the number of successful PSN-nucleated grains in an Al1.3Mn-alloy. They found a pronounced occurrence of the ND-rotated cube when the grains had nucleated in a Cu- or S-oriented matrix. For nucleation in the Bs-oriented matrix a more random texture was found. They did not find the P-orientation, but assumed that this was due to the relatively low degree of reduction (82%).

Burger *et al.* (1997) investigated the effect of Mg-additions to an AlMn-alloy with respect to recrystallisation texture after hot and subsequent cold rolling. The materials were pre-treated differently to achieve different dispersoid distributions. The recrystallisation annealing was carried out at a high

temperature (550°C), and for the AlMn-alloy they found the P-texture (termed RX-texture in the actual paper) to become stronger as the dispersoid density increased. In addition to the P-texture a strong ND-rotated cube texture was observed. The grains with cube orientation became less rotated as the dispersoid density decreased, *i.e.* the grains were oriented closer to the exact cube orientation. The effect of Mg-additions was a decrease in intensity of the rotated cube and the absence of the P-orientation after pre-annealing only at 480°C. The P-texture once again appeared when the preannealing treatment was changed to a solution treatment, followed by slow cooling to 480°C and held at this temperature for 12 hours. This treatment led to a more widely spaced distribution of coarse dispersoids. For all conditions the ND-rotated cube texture was stronger than the P-texture. This observation is opposite to the observations of the present LP 3103-alloy, but is similar to the observations of an AlMnMg-alloy by Daaland and Nes (1996).

Recently Liu (2003) has reported the appearance of the P-texture in combination with a cube texture being slightly rotated in the ND-direction of an industrially processed AA3103-alloy. This alloy was produced by hot and cold rolling. The texture after hot rolling was a combination of the cube texture and the orientations running along the b-fibre. During batch annealing the amount of manganese in solid solution decreased from approximately 0.38 wt% to 0.19 wt%. No images of the precipitates were given in the report, but it is reasonable to assume that a high density of small dispersoids was present in the as annealed material. No explanation of the appearance of the P-texture was given in this report. It is reasonable however based on the results presented in Chapter 4.1 to assume that precipitation of dispersoids played a major role in the formation of the P-texture also for this material.

Morris and Duggan (1978) investigated a cold rolled Al1.8Mn-alloy. They reported a rapid build-up of depleted zones around the original grain boundaries after annealing at 320°C for 30 minutes. The size of these zones was measured to approximately 1 μm. This depletion occurred prior to recrystallisation and thus these areas became effective nucleation sites for recrystallisation due to less retarding forces from solute atoms and dispersoids. They found that enhanced diffusion of solute atoms along the grain boundaries rather than bulk diffusion

was responsible for the rapid depletion of the solute Mn-atoms. Nucleation of recrystallisation was totally dominated by PSN, but only particles located at the original grain boundaries were successful in nucleating recrystallised grains. This reaction took place by dissolution of dispersoids near the particles, resulting in unpinning of the subboundaries. The process continued until a subgrain had grown sufficiently large and thus became a recrystallised grain. Careful investigations of the A3.0-350°C-material annealed for more than 10 minutes revealed that the dispersoid density around some of the coarse particles was slightly lower than in the matrix, and an example of this effect is seen in Fig.5.11.

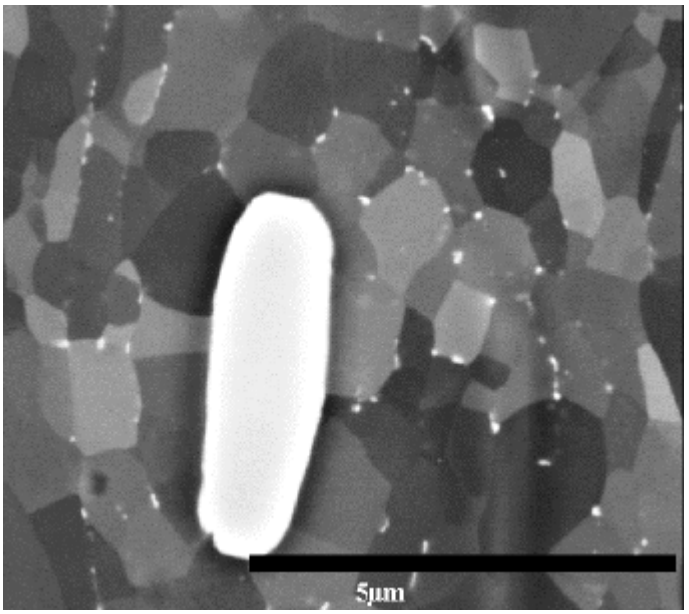

Fig.5.11: Precipitation effect close to a primary particle of A3.0-350°C annealed for 10 minutes.

Weiland (2000) investigated an AlMnMg-alloy after plane strain deformation (T_{def}=500°C) with respect to nucleation mechanisms. With respect to PSN he stated that, after casting and homogenisation the areas adjacent to the particles become depleted of alloying elements. Thus the subgrain size and grain boundary mobility are increased compared to that in the supersaturated matrix. For AlMn-alloys a lower dispersoid density formed in these areas during homogenisation. Locally this effect further increases the subgrain size, and the grain boundary mobility increases even more due to the reduced Zener drag. No completely

depleted zone was found adjacent to the iron bearing primary particles, but a lower dispersoid density was found around these particles. Even though this was observed for hot deformed materials, Weiland (2000) suggested that these observations could be utilised for cold deformed structures as well.

Engler and Yang (1995) investigated the effect of precipitation of an Al1.3Mn-alloy upon annealing at low temperature by TEM. They found a higher dispersoid density in Cu-, S- and Goss oriented grains than in Bs-oriented grains. The reason for this was attributed to the fact that Bs-oriented grains deform more homogeneous, *i.e*. lower misorientations within these grains than of grains with other orientations. This observation can possibly explain the heterogeneous nucleation of dispersoids for the A-homogenised LP 3103-alloy, Fig.4.22-23.

In single crystals the build up of the deformation zones has been described by <112>-rotations of the matrix [Russell and Ashby (1970)]. Under polyslip conditions a random orientation distribution has been reported, *i.e.* defined <112>-rotations cannot result since more slip-systems are active simultaneously [Bleck and Bunge (1981), Oscarsson (1991)]. In contrast, work published by Humphreys and co-workers (1990), (1994) and by Kong *et al*. (1991) have shown that even under polyslip condition the rotations in the deformation zones can be related to the operating slip-system in a similar manner to what have been found for single crystals. By such rotations the P- and ND-rotated cube orientations can be found within the deformation zone if the particle lie in a Cu-oriented matrix. It should however be noted that relatively large amount of deformation is required to generate these orientations within the deformation zones. For this reason these texture components are not found after low reductions.

During deformation very high dislocation densities build up close to the particles. These deformation zones are able to rapidly recover in the early stages of annealing and finally one or more subgrains consume the complete deformation zone. If the condition is right recrystallisation can occur by further growth of these subgrains, *i.e*. the decisive step for nucleation of a recrystallised grain is the growth out of the deformation zone rather than the subgrain growth within the zone [Humphreys (1977)]. In Fig.5.12 a result of the classical work on PSN by

Humphreys (1977) of an AlSi-alloy deformed by cold rolling is shown. It was found that the particles had to be larger than 2 μm to produce large enough deformation zones during rolling. Upon the subsequent annealing these areas will act as efficient nucleation sites. Based on this work it has become common to say that all particles larger than 1 μm could result in PSN if the processing conditions are right, *i.e.* cold deformation and relatively low annealing temperature.

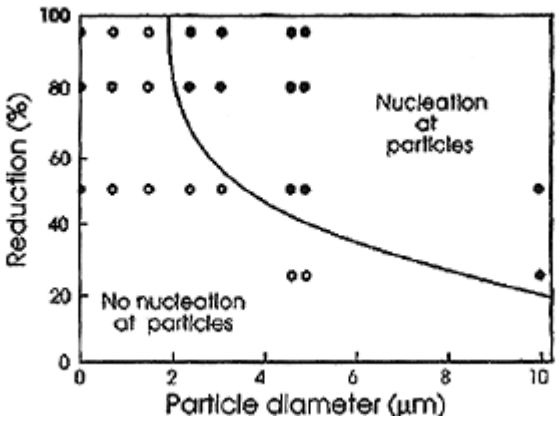

Fig.5.12: Effect of cold rolling reduction on the nucleation efficiency by PSN [Humphreys (1977)].

Humphreys and Ardakani (1994) found a mathematical equation for the evolution in misorientation across the deformation zone as a function of strain:

$$q_{max} = q_0\left(\frac{e}{1+e}\right) \qquad (5.7)$$

where q_0 =40°. If this equation is fulfilled for the present studies, the maximum misorientation across the deformation zone should be 13°, 24° and 30° for strains of 0.5, 1.5 and 3.0, respectively. This means that the subgrain growth within the deformation zone of the materials deformed to a strain of 1.5 and 3.0 would produce high angle grain boundaries (>15°) to the matrix. If this assumption is valid the growing subgrain could form close to and not necessarily at the particle surface, which often has been observed experimentally [Humphreys (1977)].

Below follows a summary of the most important aspects of the previous papers discussed above, which will be used to explain the recrystallisation texture of the LP 3103-material conditions annealed at low annealing temperatures:

- The intensity of the P-orientation increases with increasing deformation but decreases with increasing annealing temperature. The P-texture becomes stronger as the dispersoid density increases. The P-orientation has a 40°<111> rotation relationship to the Cu-orientation, which is believed to give good growth conditions during recrystallisation. The P-texture is nucleated by PSN, where P-oriented subgrains are found in the deformation zone surrounding coarse constitutive particles after large reductions. A high supersaturation of alloying elements that precipitates during annealing seems to be necessary for the nucleation of the P-texture. Mg-additions seem to have a large influence on the strength of the P-texture.
- The ND-rotated cube is as the P-texture found in case of concurrent precipitation. It becomes less rotated as the dispersoid density decreases. If the ND-rotated cube and the P-texture are present in the recrystallisation texture they almost every time appear together, but there are no consistent pattern of which of the orientations that is strongest. The ND-rotated cube orientation is less sensitive to Mg-additions. The ND-rotated cube orientation has a 40°<111> rotation relationship to the Cu-orientation.
- The appearance of the exact cube texture in case of concurrent precipitation is dependent on an initial cube texture prior to deformation. It is a necessity that some cube-oriented subgrains survive deformation, *i.e.* deformation must not be too high
- Depleted zones are found around the constitutive particles and original grain boundaries. These depleted zones results in a lower density of dispersoids upon annealing in the vicinity of these areas resulting in more effective nucleation of recrystallisation here. Diffusion of manganese occurs along the grain boundaries rather than by bulk diffusion at these temperatures.

In the following the most likely origin of the strong P- and ND-rotated cube textures observed in the present work of the LP 3103-alloy in case of concurrent precipitation will be given:

Homogenised material: Close to the constituent particles depleted zones of elements in solid solution are formed. These zones become larger as homogenisation time increases, resulting in a lower supersaturation of manganese in these zones. However, at the same time as the homogenisation

time increases (A→B→C), the matrix becomes less supersaturated and the total amount of precipitation during the subsequent processing decreases.

Deformed material: Upon deformation large rotations of the original matrix are found close to the coarse particles. It has been shown that the given orientations, *i.e.* the P- and ND-rotated cube orientations, are found in the deformation zones if the deformation is large enough.

In the present work it was observed that if the other conditions were fulfilled, *i.e.* with respect to supersaturation and annealing temperature, a reduction of ~80% was sufficient to produce a weak P-texture in combination with some ND-rotated cube. However, a strong and totally dominating P-texture was observed only after a reduction of 95%. This observation suggests that as the reduction is increased, increasing fractions of subgrains obtaining these orientations are formed within the deformation zone.

The amount of Cu-oriented deformation bands increased with increasing strain, and this orientation has a 40°<111>-orientation relationship to the actual P- and ND-rotated cube orientations, which is known to give favourable growth conditions during recrystallisation.

Subgrain growth: During the first minutes of annealing a high density of inhomogeneously distributed precipitates is formed. Within the deformation zones a lower dispersoid density is expected to be found compared to the density in the matrix. This difference in density is associated with a lower supersaturation of manganese within the deformation zones. Subgrain growth is then expected to occur easier in the deformation zone due to the lower retarding forces acting against the subgrain growth. This effect is accelerated by the fact that more subgrain boundaries are available for diffusion of solute atoms and an easier dissolution of the already formed dispersoids in the vicinity of the primary particles. As the deformation zone becomes more depleted of solute atoms subgrain growth becomes even more rapid than in the matrix. Upon annealing subgrains of the P- and ND-rotated cube orientations located within the deformation zones are allowed to grow on the expense of the deformed

substructure. At some point one or more subgrains consume the complete deformation zone.

As seen in Fig.5.4 the strength of the Cu-orientation sharpens significantly during the initial stages of annealing. This fact results in a higher possibility for a growing subgrain with a P- or ND-rotated cube orientation to grow into a Cu-oriented deformation band as the deformation zone is consumed, and thus become a successfully recrystallised grain.

Recrystallisation: The decisive step to produce a recrystallised grain by PSN is the growth out of the deformation zone. It is believed that the 40°<111> rotation relationship to the Cu-orientation results in a more effective nucleation for these orientations compared to those subgrains with no relationship between the subgrain and the matrix. With increasing deformation the number of Cu-oriented deformation bands and the total number of subgrains within the deformation zones comprising P- or ND-rotated cube orientations increases. This results, as expected, in a more effective nucleation of these orientations as the deformation increases. Other nucleation sites are more effectively pinned due to the higher density of precipitates and higher amount of elements in solid solution that effectively slow down subgrain growth. The result of this fact is that other nucleation sites do not produce recrystallised grains as frequently as by PSN. However, it should be noted that it is not only the P- and the ND-rotated cube orientations that are nucleated. From the investigations on the growth of these orientations, Fig.4.20, it was observed that only about one out of five nucleated grains belonged to one of the P- or ND-rotated cube orientations. These grains could as well be nucleated by PSN or by other nucleation mechanism like strain induced boundary migration, but these grains mainly obtained a random orientation. Since the initial texture was close to random and little cube is present in the deformed microstructure and thus nucleation from cube bands that have survived deformation can be neglected as a possible nucleation site in this study.

The P- and ND-rotated cube orientations were only found to be the dominating texture components in case of concurrent precipitation, and can thus be called precipitation texture components.

Plots showing when the P- and ND-rotated cube orientations were the dominating texture components as a function of strain and amount of manganese in solid solution are given in Fig.5.13. For the C-material the cube orientation was dominating at all temperatures. The results for the *as cast* material (0.83wt%) has been taken from a project work of a MSc-student at NTNU [Bjerkaas (2001)]. This figure indicates that for increasing strain the P- and ND-rotated cube orientations form at higher temperatures. Engler *et al.* (1996) and Vatne *et al.* (1997) have reported similar observations, but not with the same strength of these two texture components as in the present work.

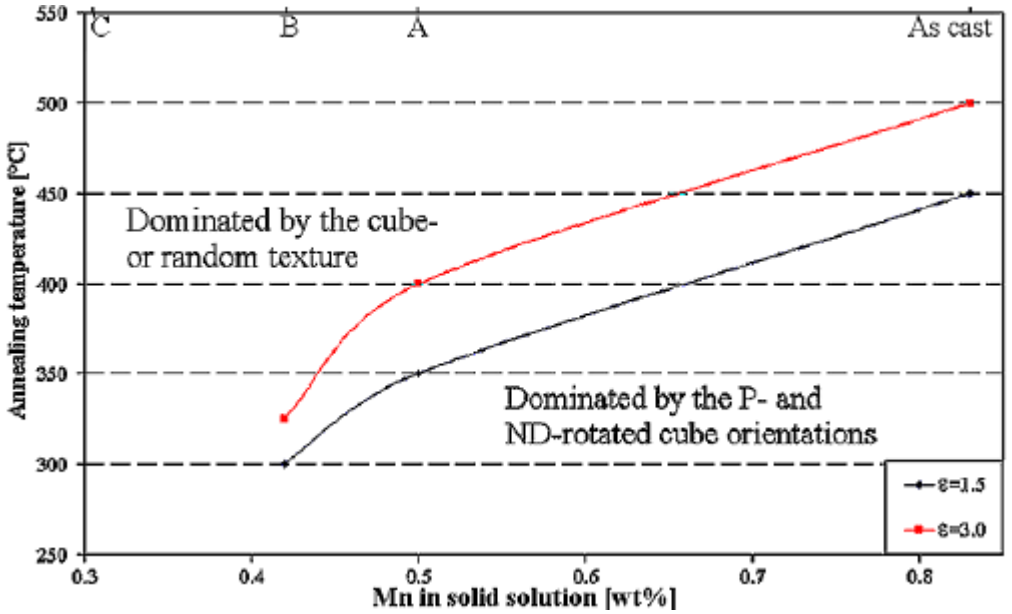

Fig.5.13: Plots of when the P- and ND-rotated cube orientations become dominating orientations of the recrystallised materials of the LP 3103-alloy.

The transition region between the areas dominated by the random/cube texture and P/ND-rotated cube texture, respectively, is not as sharp as it appears in this figure. In particular from the recrystallisation textures after a strain of 3.0 the shift is observed. For the B-material three ranges are clearly seen in Fig.4.17. For the 300°C annealing the texture consists of the P/ND-rotated cube-orientations. At 350°C a mixture of the cube orientation and *b*-fibre orientations was found, and finally at 500°C the texture consists of a combination of the cube being somewhat rotated in the ND-direction and a weak P-texture. The occurrence of these two latter combinations will be discussed in the following.

5.5.2 Recrystallisation textures unaffected by concurrent precipitation

The recrystallisation textures of the LP 3103-material conditions after a strain of 1.5 were close to randomly oriented, as seen in Fig.4.16. After a strain of 3.0 the recrystallisation textures were dominated by the cube orientation given that recrystallisation occurred prior to precipitation, Fig.4.17. To explain the presence of the cube orientations in the final texture for these conditions, it is not reasonable to think in terms of nucleation from cube-bands that have survived deformation. This mechanism is a reasonable approach if the material has been hot rolled before cold rolling, *i.e*. having an initial cube texture prior to cold rolling as for the CP 3103-alloy. To be able to explain the cube texture after a strain of 3.0 the transition bands might be important for the recrystallisation behaviour, as suggested Dillamore and Katoh (1974). They stated that the cube orientation ought to exist in the transition band separating two different stable orientations. High misorientations are found across transition bands, and their occurrence results in grain fragmentation during deformation. If transition bands are necessary to nucleate the cube orientation this should also be seen in the deformed microstructure as break-up of grains. After a strain of 1.5 very little break-up was observed, as seen in Table 5.2, while after a strain of 3.0 the number of deformation bands has more than doubled compared to the calculated value from the initial grain size. If the transition bands are important in the nucleation of recrystallised grains this suggests that cube orientation should be observed after a strain of 3.0 and not after a strain of 1.5. This difference is exactly what was observed experimentally for the LP 3103-alloy.

To explain the presence of the orientations along the b-fibre in combination with the cube it is reasonable to think in terms of strain induced boundary migration (SIBM). Here it is assumed that the stored energy of two neighbouring deformation bands is different. Upon annealing the grain boundary will bulge into the grain with the highest stored energy and eventually become a recrystallised grain.

A possible reason why a weak P-texture is found in combination with the cube texture is probably due to a similar mechanism as when the P-texture becomes the dominating one. Some subgrains within the deformation band have the right

orientation and are allowed to grow. If these are allowed to grow into a Cu-oriented grain it successfully nucleates. However, at the same time other nucleation mechanisms are active and thus the intensity of the P-orientation is suppressed.

5.5.3 Estimation of PSN-efficiency

From the recrystallised grain sizes found by EBSD-mapping it is possible to calculate the number of nucleated grains per area. For the material conditions that recrystallised above the T_c-temperature in Fig.4.12 the texture was relatively weak and the grains were fairly equiaxed. In the opposite case the grain size became large and the grain size in rolling direction was typically about twice the size in the normal direction. To calculate the volume of each grain, the size in the transverse direction has been assumed to be the same size as the size in the normal direction.

A mathematical equation of the cumulative size distribution of particles (Fig.4.7) after a strain of 3.0 for the LP 3103-material was derived:

$$f(h) = H \cdot \exp(-L h) = 1 \cdot 10^{16} \cdot \exp(-1.22h) \qquad (5.8)$$

In Table 5.3 the effectiveness of nucleation of recrystallisation is calculated. This effectiveness was calculated by only assuming nucleation by PSN. From equation (5.8) a total of about 310^{15} particles/m^3 had an over-critical size. In Table 5.3 it was assumed that only the particles larger than 1 μm could provide nuclei for recrystallisation.

Table 5.3: Nucleation efficiency at different temperatures of the LP 3103 A-condition.

Temperature [°C]	Grain size RD [μm]	Av. grain volume [μm^3]	Grains per volume [m^{-3}]	PSN-effectiveness
300	237	3.33E+6	3.0E+11	1.0E-4
350	62	59600	1.7E+13	5.7E-3
400	9.9	970	1.1E+15	0.33
500	8.8	681	1.5E+15	0.50

At high annealing temperatures of 400°C and 500°C it is seen from the table that PSN is very efficient/successful in nucleation of recrystallised grains. It should be noted that the recrystallisation textures of these materials were dominated by the cube texture. However, the intensity of the cube texture was however weak, *i.e*. PSN is still the dominating nucleation sites even though with somewhat lower effectiveness than given in the table. At low temperatures the recrystallisation textures were totally dominated by the P- and ND-rotated cube textures.

From the table it is seen that below T_c only very few particles are able to produce a nucleus. From these numbers it is easy to understand that a TEM-analysis is almost impossible to carry out to possibly confirm nucleation of these orientations. Even with SEM, it was hard to find indications of possible nucleation sites, but some OIM-maps show that PSN does play a role in the nucleation event of these orientations (Fig.4.21), although it is not proven that also other mechanisms may cause these orientations.

In Fig.5.14 the number of nucleated grains (Table 5.3), assuming only PSN, is plotted *vs*. annealing temperature. For the A-material it is seen that when annealing was carried out at temperatures below 400°C (673 K) the data points fall on a straight line in a logarithmic plot. The reason why the number of successfully nucleated grains is plotted *vs*. degree in Kelvin is that this equation is going to be used for the following modelling exercise, see Chapter 5.6. The line for the A-material is described by:

$$N_{PSN,A} = 1.1 \times 10^{-9} \times \exp(0.082 \times T) \qquad (5.9)$$

The same analysis is also included in this figure for the B3.0 material. It is seen that there is a shift in the number of PSN nucleated grains towards lower temperatures, this is due to the shift in the characteristic temperature for concurrent precipitation. It is seen that the curve for the B-material is similar to the A-material. The B-condition is described by:

$$N_{PSN,B} = 6.5 \times 10^{-11} \times \exp(0.094 \times T) \qquad (5.10)$$

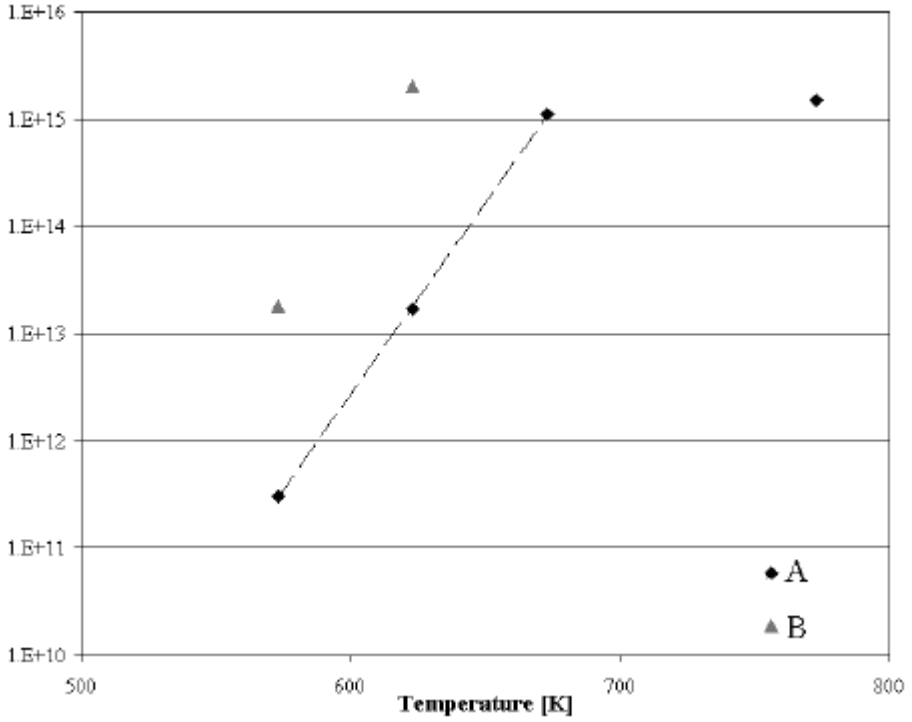

Fig.5.14: Efficiency of PSN nucleation as a function of annealing temperature.

5.5.4 Recrystallisation texture of CP 3103

The recrystallisation textures of CP 3103-alloy were measured by EBSD-mapping and the textures were found to be relatively weak at all temperatures, although a slight strengthening with increasing temperature was found. The investigated textures of the W0-condition were measured after annealing at 300°C, 325°C and 350°C. At the lowest annealing temperature concurrent precipitation occurred, and concurrent precipitation has previously been found to strengthen the cube texture [Benum and Nes (1997), Sæter *et al.* (1997)]. The alloys of these investigations, AlFeSi and AlMn, had hot rolling cube texture prior to cold rolling. These cube grains of the hot rolled material are believed to be responsible for the final cube texture after annealing, because some will survive deformation. Upon annealing the cube-subgrains reach an over-critical size before the subgrains of other orientations. During concurrent precipitation a higher subgrain size is required to nucleate a recrystallised grain, thus fewer grains will nucleate and of these successful grains an even higher fraction will be cube oriented than without precipitation. Following this, the cube texture will appear stronger in the recrystallisation texture. Even though previous

observations have shown a strengthening in case of concurrent precipitation this was not observed for the CP 3103-alloy. For the W50-condition the recrystallisation textures were also weak at all the investigated temperatures, even though the increase in conductivity indicated heavy concurrent precipitation. The texture behaviour of this material condition was similar to that of the W0-condition.

Bolingbroke *et al*. (1993) investigated the effect of cube nucleation during hot deformation of an AA3004-alloy, and it was found that the volume fraction of cube was highly dependent on the number of supercritical particles, Fig.5.15. As the number of supercritical particles increased the volume fraction of cube decreased rapidly. This effect of coarse particles can be part of the explanation of the relatively weak recrystallisation texture for the CP 3103-alloy. The high density of supercritical particles resulted in fewer successfully nucleated cube grains and/or a higher fraction of randomly oriented grains due to PSN.

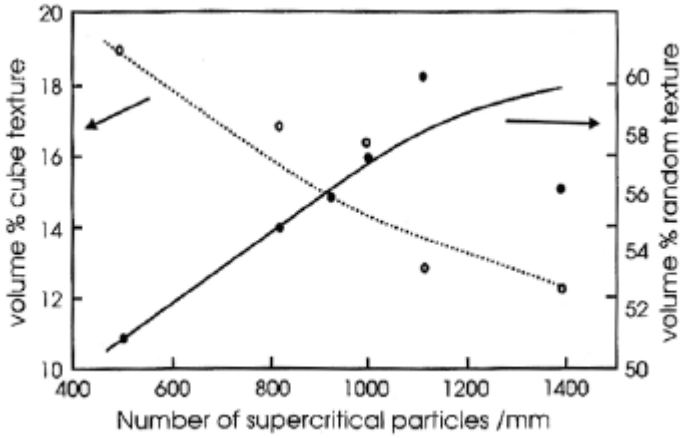

Fig.5.15: Correlation between recrystallisation texture and number of over-critical primary particles with respect to PSN [Bolingbroke *et al*. (1993)].

5.5.5 Effect of initial texture after laboratory rolling

The effect of an initial texture on the final recrystallisation texture is found when comparing the laboratory cold rolled LP 3103- (Fig.4.16 and Fig.4.17) and CP 3103-alloys (Figs 4.42 and 4.43). Both the transfer gauge (TG) and the rerolled (RR) materials had strong cube textures prior to cold rolling. With respect to the amount of Mn in solid solution, these are compared with the B and C

homogenised LP 3103-materials, respectively. The j_2=0°-section of these conditions are summarised in Fig.5.16. It is seen that the cube texture is formed at lower temperatures for the CP 3103-materials, and it is significantly stronger than for the LP 3103-materials at all temperatures. This observation is not surprising since cube oriented grains are known to nucleate from the retained cubebands [Vatne (1995)]. A weak P-texture was also found for the transfer gauge material that was annealed at 300°C, but this was significantly weaker than for the LP 3103-alloy.

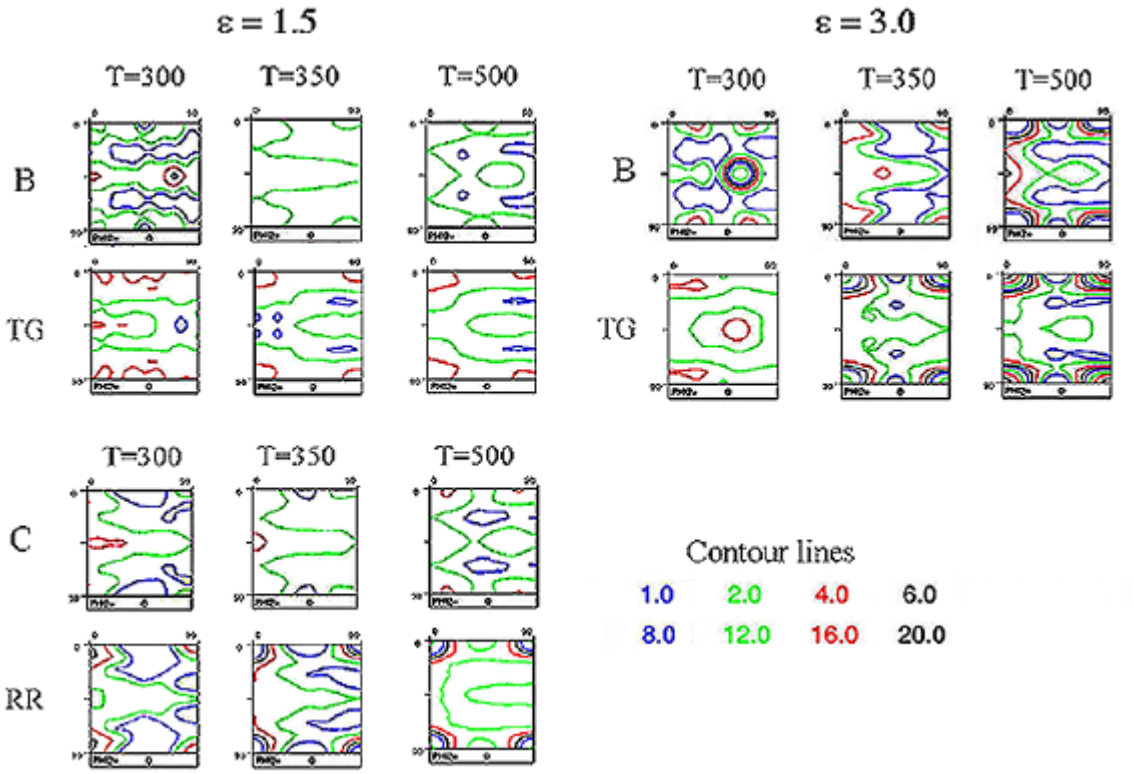

Fig.5.16: Effect of an initial texture compared to a random texture prior to cold rolling to strains of 1.5 and 3.0. The recrystallisation textures after cold rolling are compared with respect to initial amount of Mn in solid solution. The homogenised B (LP 3103) material is compared with the transfer gauge material (TG), and homogenisation C is compared with the rerolled material (RR).

Both the as homogenised (AH) CP 3103-alloy and the A-homogenised LP 3103-alloy were compared with respect to recrystallisation texture after a strain of 3.0. These materials both had random initial textures and were comparable with respect to amount of manganese in solid solution. In Fig.5.17 it is seen that the LP 3103-alloy formed a strong P-texture at low temperatures. The P-texture was only found at 300°C for the CP 3103-material but it was considerably weaker than for the LP 3103-alloy. At high annealing temperature (500°C) the recrystallisation textures were dominated by the cube texture, and the intensity was strongest for the CP 3103-material.

For the AH-material the final recrystallisation texture was dependent on the annealing temperature. At 300°C the dominating orientation in the ODF was the P-texture. This component was much weaker than the texture of the LP 3103-alloy, especially when taking into consideration the fact that the increase in conductivity during the softening annealing was higher for the AH-material (from ~22 MS/m to ~30 MS/m) than the A-homogenised LP 3103-alloy. This observation indicates that the possible nucleation position of the P-orientation strongly depends on where precipitation occurs. For the LP 3103-materials long homogenisation treatments were carried out resulting in a depletion of alloying elements close to the constituent particles. This depletion results in less precipitation during the subsequent annealing after deformation, while for the CP 3103-material the depletion was not as effective. Hence more successful nucleation by PSN is found for the LP 3103-material compared to the CP 3103-material.

At 350°C the recrystallisation texture of the CP 3103-material was dominated by the orientations along the b-fibre. From experimental investigations this material condition was found to be in a fully recrystallised state. The final recrystallisation texture thus indicated that some *in-situ* recrystallisation has occurred. At high annealing temperature the texture was dominated by the cube orientation.

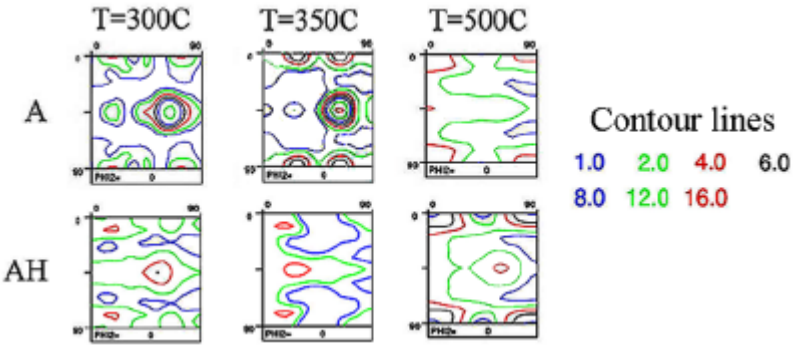

Fig.5.17: Comparison of the recrystallisation textures of the homogenised CP 3103 material (AH) with the A-homogenised LP 3103-material (A) after cold rolling strain of 3.0.

Comparison of the CP 3103- and LP 3103-material conditions given the same deformation show that the same recrystallisation texture components were present, however the intensities of these components were different. When the cube orientation was the dominating texture the CP 3103-material showed the strongest textures, while the LP 3103-material showed the strongest texture when the P-orientation dominated.

5.6 Modelling softening behaviour

The mathematical equations presented in Chapter 2.4.3 have been used to model the softening behaviour of the investigated alloys during isothermal annealing. In the following sub-chapters the modelling predictions of the different alloys will be presented. The experimentally found parameters have been included in the modelling, *i.e.* the particle size distributions, the average misorientations across the subgrain boundaries and the average subgrain sizes.

The model has been tested in detail to check for the effect of the different variable parameters and results of this testing is summarised in Appendix 7.

5.6.1 Modelling of the AA1200-alloy

First the model was tested against two different commercial pure Al-alloys, AA1050 and AA1200. Vatne (1999) has previously shown that the model is able to predict experimental results of these alloys very well. As shown below redoing the modelling of these alloys gave satisfactory results. In Fig.5.18 the results of a AA1200-alloy confirms the good agreement between experiments and modelling results previously obtained by Vatne (1999)

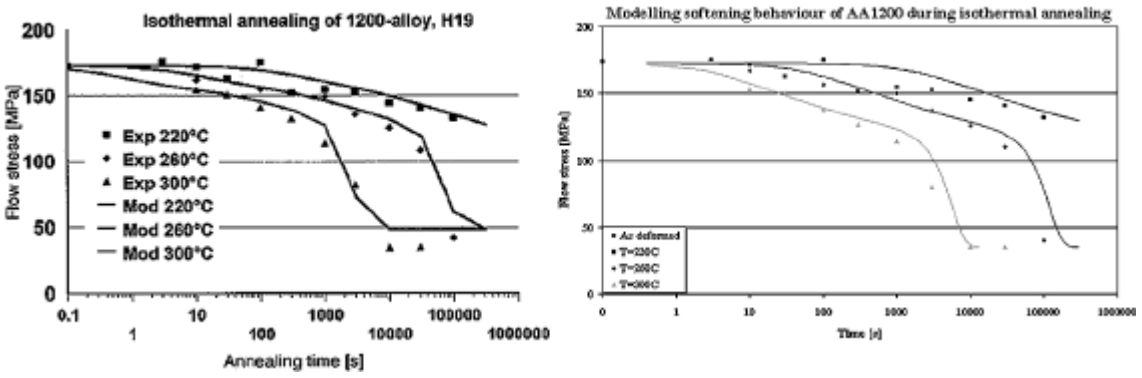

Fig.5.18: Modelling softening of an AA1200-alloy a) done by Vatne (1999) and b) reproduction of the modelling results by Vatne.

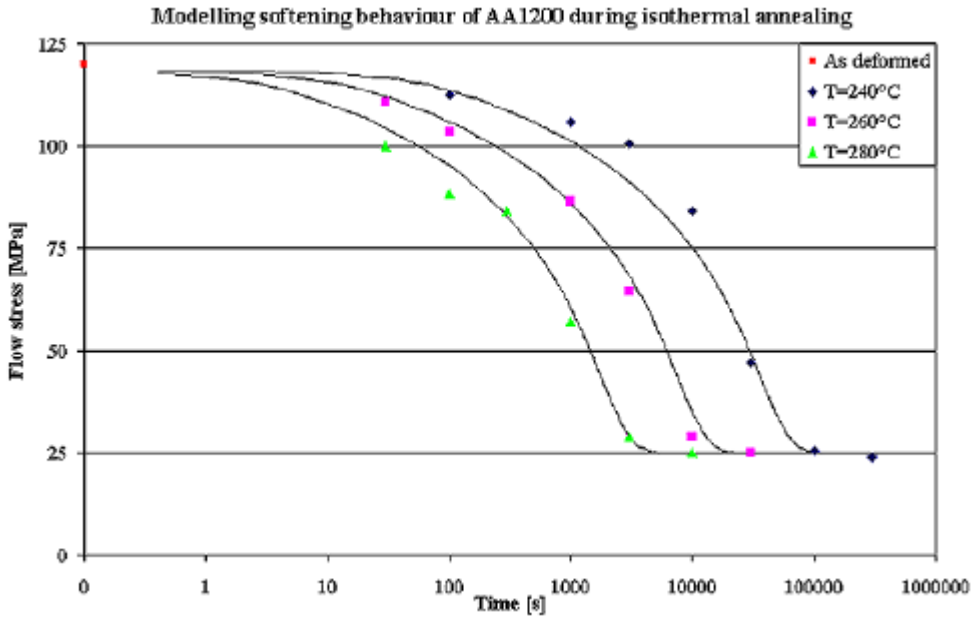

Fig.5.19: Modelling results of the softening behaviour of an AA1200-alloy. (Vir[Fab]-material produced by Alcan Int. LTD)

In Fig.5.19 the softening behaviour of the Vir[Fab] AA1200-alloy has been modelled and is compared to flow stress measurements. The time necessary to reach a fully recrystallised condition is predicted quite accurately and the shape of the softening curve is also well reproduced.

The differences between the softening curves of the AA1200 investigated by Vatne (1999) and the AA1200 investigated in this work is assumed to be due to different reductions and possibly due to different amount of elements in solid solution. Furu *et al.* (1995) investigated two commercial pure aluminium alloys containing different amounts of iron in solid solution. They found that a higher amount of iron in solid solution led to a significantly longer holding time at temperature before being transformed into a fully recrystallised condition.

5.6.2 Modelling of the LP 3103-alloy

In the following modelling of the softening behaviour of the two different AA3103-alloy (LP and CP) will be discussed. As will be shown below the modelling of these more highly alloyed materials were not unexpectedly far more complex to model than the commercial pure alloys.

For modelling of the LP 3103-alloy the hardness measurements have been converted into flow stress by the equation found valid for the CP 3103-alloy. In Table 5.4 the calculated flow stress after different reductions, by converting the Vickers hardness measurements into flow stress by equation (4.1) are given. Ryen et al. (2002) have measured the flow stress of the A-condition deformed to the different reductions, among these to true strains of 0.5, 1.5 and 3.0. The measured yield stresses after these reductions were found to be 145 MPa, 180 MPa and 230 MPa, respectively. These values are in relatively good agreement with those values calculated from the hardness measurements

Table 5.4: Calculated flow stress from Vickers hardness measurements after different cold rolling reductions.

Strain	VHN	Flow stress
0.5	53.7	158
1.5	59.3	185
3.0	69.0	231

For the first modelling attempt the softening behaviour of the presumably easiest case was chosen. This was the C-material deformed to a strain of 1.5. According to the characteristic temperature for concurrent precipitation (Fig.4.12) only annealing at 250°C should be affected by precipitation. In Fig.5.20 the results of the modelling are shown. It is seen that the softening behaviour is well predicted at temperatures above T_c, but is not able to reproduce the behaviour at 250°C.

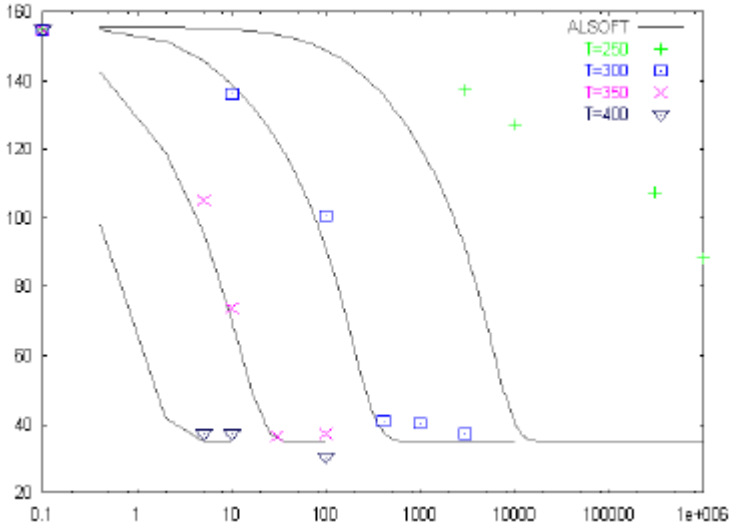

Fig.5.20: Modelling results of the C1.5-condition.

The same attempt was carried out for the B-conditions deformed to strains of 1.5 and 3.0. The modelling results for the respective strains are given in Fig.5.21 and 5.22, respectively. In a) the results without any Zener drag or differences in nucleation efficiency of PSN is shown. This was carried out to determine the activation energy of the condition, *i.e.* to fit the high temperature annealing to the experimental points.

In b) a Zener drag is included for those annealing temperatures below the characteristic temperature (T_c), which for the B-condition was found to be about 325°C. It was further assumed that only nucleation by PSN was important in these cases. From the number of successfully nucleated grains, equation (5.10), it was possible to calculate the Zener drag for nucleation. This equation has also been extrapolated to estimate the number of successfully nucleated grains at 250°C and thus the evolution at 250°C was reasonably well predicted.

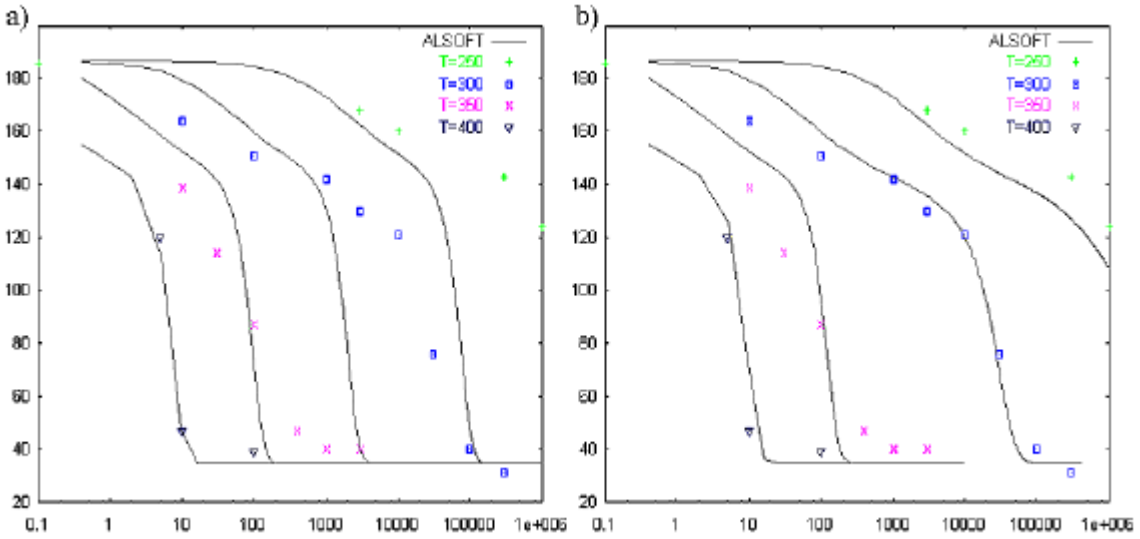

Fig.5.21: Modelling results of the B1.5-condition.

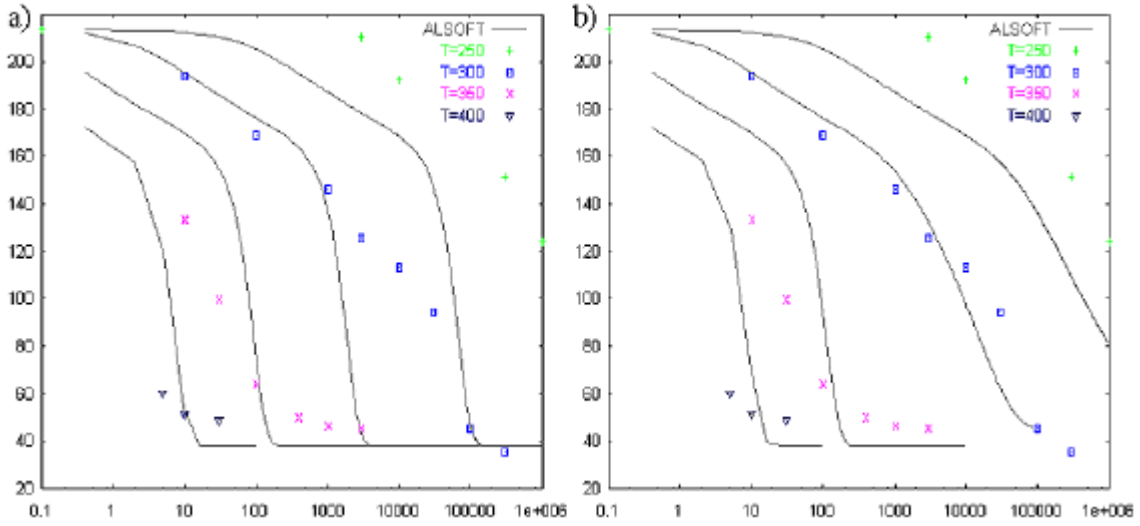

Fig.5.22: Modelling results of the B3.0-condition

However, it should be noted that two different Zener drags have been used in the model in case of concurrent precipitation. These different Zener drags are illustrated in Fig.5.23. The first is the drag that affects the nucleation frequency (P_z'), as seen in Fig.5.23a). Below T_c it has been shown that precipitation had occurred on the subgrain boundaries prior to recrystallisation, this result in a drag that retards the subgrain growth, which again results in fewer over-critical subgrains. This again lead to fewer viable nuclei for recrystallisation.

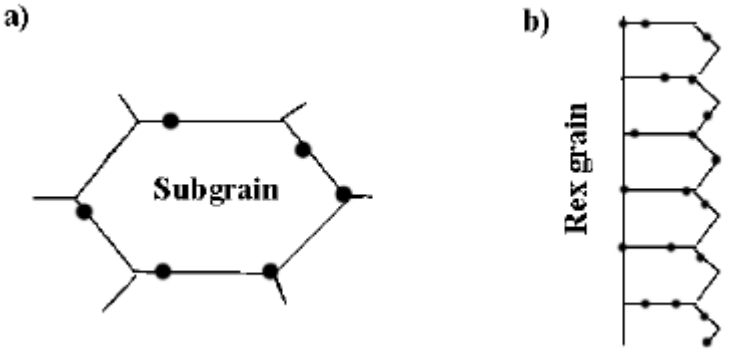

Fig.5.23: Different Zener drags acting upon recrystallisation. In a) a Zener drag which retards subgrain growth is shown, while in b) the high angle boundary interacts with a homogeneous distribution of precipitates.

In terms of the mathematical formulation of the model it is the following equations that are affected by including a Zener drag that retards nucleation:

$$N_{PSN} = C_{PSN} \int_{h_c}^{\infty} f(h)dh \qquad (5.11)$$

where C_{PSN} is a constant in order of unity (tuning parameter) and f(h) is the mathematical representation of the cumulative size distribution of particles:

$$f(h) = H \cdot \exp(-Lh) \qquad (5.12)$$

h_c is the smallest particle size that could produce a recrystallised grain, and when this size increases, fewer sites become activated. As can be seen from Equation (5.13) an increase in Zener drag for nucleation (P_z') give rise to a larger h_c, and thus fewer PSN sites (Eq. (5.11))

$$h_c = \frac{4\gamma_{GB}}{P_D - P_z'} \qquad (5.13)$$

The other Zener drag affects the growth, Fig.5.23b). This latter drag is of the classical type resulting from a spatially random distribution of dispersoids of volume fraction (f) and with a radius (r), the classical equation is given as:

$$P_z = \frac{3}{2}\frac{f\gamma_{GB}}{r} \qquad (5.14)$$

During growth of the high angle grain boundary it is believed that the boundary interact with a homogenous distribution of dispersoids as the recrystallised grain consume the deformed microstructure. This is true in the rolling direction, while in the normal direction the boundary interacts with a more inhomogeneous distribution of precipitates as they are aligned on the elongated subgrain- and old high angle grain boundaries. This is the most reasonable explanation of the difference in grain size of the fully recrystallised condition, *i.e.* the grains are longer in the rolling direction compared to the normal direction, as seen in Fig.4.15a-b).

In Fig.5.24 the modelling results of the A3.0 condition is shown. Here as well the softening curve in figure a) is calculated without a "nucleation" drag to determine the activation energy of the condition. In b) a Zener drag for nucleation is included, which has been calculated from Equation (5.9). This condition is as expected more affected by concurrent precipitation, which results in fewer nucleated grains and thus slower recrystallisation kinetics as compared to the B-condition. It is seen from the figure that this approach also predicts the softening behaviour reasonably well at all temperatures.

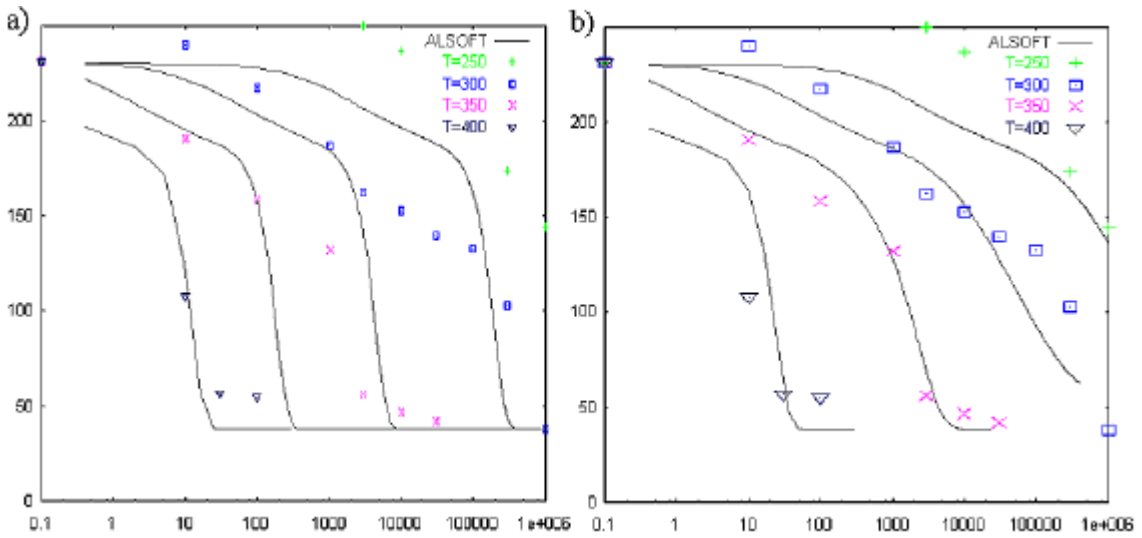

Fig.5.24: Modelling results of the A3.0-condition.

Finally the same approach have been used to model the C1.5-250°C condition. It should however be noted that no equation for the number of successfully nucleated grains has been found in this case. Here an equation for the Zener drag affecting nucleation has been tuned to the experimental point. It should be noted that the equation has a similar temperature dependence as for the other two conditions. The result of the modelling is given in Fig.5.25.

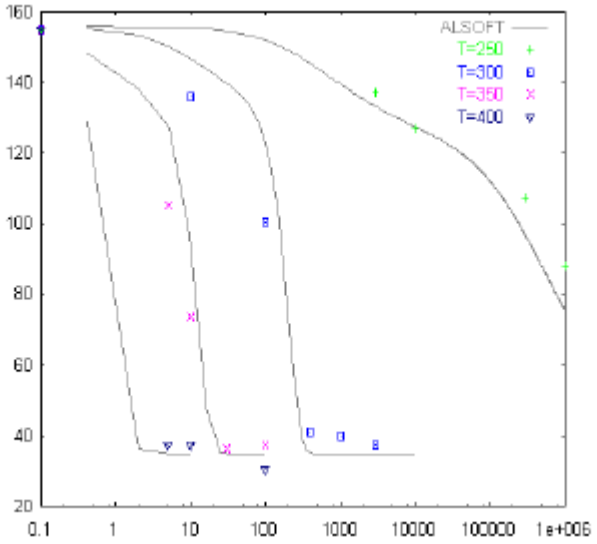

Fig.5.25: Modelling results of the C1.5-condition, including a Zener drag.

During modelling of the different condition some different values had to be used. The activation energy had to be 195 kJ, 188 kJ and 173 kJ for the A-, B- and C-conditions, respectively. The B_p and B_δ were found to be scattered around 10^5 and 10^4, respectively.

When it comes to the Zener drag for nucleation (P_z') this was set to zero above T_c, below this temperature four empirical equations have been derived:

$P_z' = -1.83 \times 10^3 \times T + 1.90 \times 10^6$, valid for the A3.0 material condition.

$P_z' = -1.83 \times 10^3 \times T + 1.73 \times 10^6$, valid for the B3.0 material condition.

$P_z' = -1.83 \times 10^3 \times T + 1.60 \times 10^6$, valid for the B1.5 material condition.

$P_z' = -1.83 \times 10^3 \times T + 1.52 \times 10^6$, valid for the C1.5 material condition.

The classical Zener drag was assumed to be independent on the supersaturation and was only valid below T_c. The retarding drag against growth of the recrystallised grains was calculated from the following equation:

$$P_z = C_{Pz}(C_{as\,def} - C_{eq}) \qquad (5.15)$$

where $C_{Pz}=5\cdot10^5$, $C_{As\ def}$ is the amount of manganese in solid solution of the as deformed condition and C_{eq} is the equilibrium concentration of manganese at the annealing temperature and is given by:

$$C_{eq} = 4.63\times10^{-20}[wt\%Mn] - 2.99\times10^{-21}\times T^{6.65} \qquad (5.16)$$

where [wt%Mn] is the original manganese concentration of the as cast material.

An increase in flow stress due to precipitation is not included in the model, the model is thus not able to predict this increase, which again results in an underprediction of the flow stress in case of concurrent precipitation.

5.6.3 Modelling of the CP 3103-alloy

The softening behaviour of the CP 3103-alloy was not well predicted. Even when including a Zener drag, reducing the total number of successfully nucleated grains, as the temperature becomes lower than T_c did not result in a good prediction as it did for the LP 3103-alloy. From the TTT-diagram, Fig.4.38, the characteristic temperature was found to be approximately 290°C. When taking a closer look on the TTT-diagram it is seen that the actual shift, *i.e.* when the time to fully recrystallised condition increases significantly is found at a temperature close to 315°C. In the following modelling of the softening behaviour this temperature has been used.

In Fig.5.26b) it is seen that the curves are shifted towards longer annealing times when including the nucleation drag, but the calculated softening behaviour is still about two orders of magnitude faster than what was observed experimentally. For this approach an activation energy of 180 kJ was used. The nucleation drag was found to follow the following empirical equation: $P_z' = -4.3\times10^3\times T + 3.0\times10^6$.

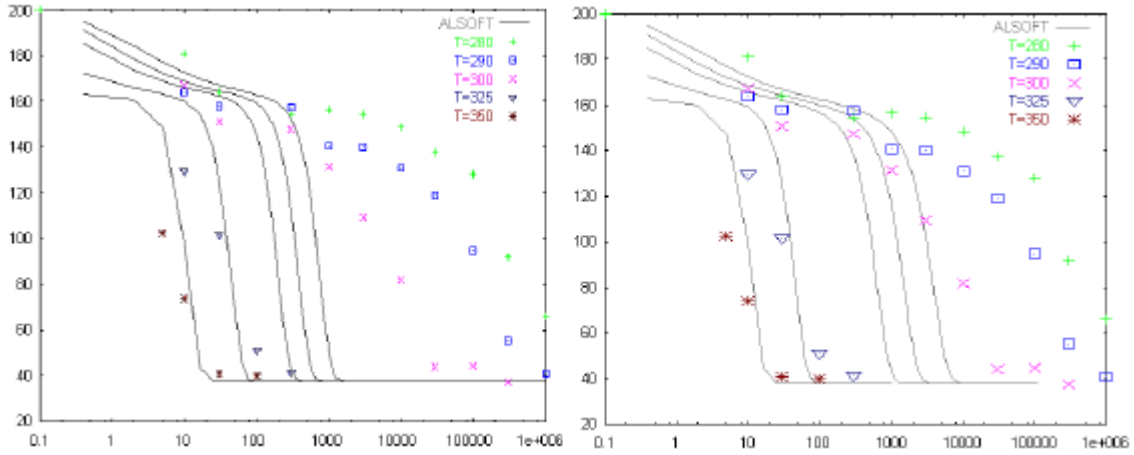

Fig.5.26: Modelling results of the CP 3103-alloy.

From these observations it can be concluded that an even more detailed model is required to predict the softening behaviour at temperatures below T_c. It might be that lots of dispersoids are formed in the early stages of annealing as the annealing is carried out below T_c. These dispersoids have to coarsen before a recrystallised grain is able to expand into the deformed matrix. This would slow down the softening, but finally a high number of grains are able to grow, resulting in a relatively small grain size. To be able to model this it is necessary to include a sub-model that predicts the precipitation behaviour and then to link this to a Zener drag. An example of such a model is the one published by Chen *et al.* (2003), the principals of this model is given in Chapter 5.3.2. However, this has not been tested within this work.

6. Conclusions

In this work the microstructural and texture evolution during cold rolling and annealing of two AlMn-alloys has been investigated. The first AlMn-alloy was laboratory processed, where the main objective was to study the effect of manganese in supersaturated solid solution on the subsequent processing after homogenisation. The other alloy was industrially processed with a focus on through process material characterisation during rolling and annealing. Finally, a commercial pure industrially cold rolled Al-alloy has been investigated, with the main focus on the softening behaviour.

The obtained results can be summarised as follows, with the conclusions of the laboratory processed AlMn-alloy given first:

Laboratory processed alloy:

1. Different homogenisation treatments resulted in different amounts of manganese in solid solution. In the present work these amounts were 0.5 wt%, 0.42 wt% and 0.31 wt% in solid solution.

2. When increasing the cold rolling reduction from a strain of 1.5 to 3.0 the misorientation increased slightly, simultaneously the subgrain size was found to decrease. As the amount of Mn in solid solution increased indications of somewhat smaller and less misoriented subgrains were found.

3. From the TTT-diagrams, produced from hardness and conductivity measurements, characteristic annealing temperatures (T_c) for the different material conditions were identified. T_c defines the annealing temperature below which precipitation interacts strongly with the recovery and recrystallisation reactions. Below T_c the recovery and recrystallisation reactions were retarded due to precipitation of high densities of very small dispersoids, while above this temperature the softening reactions were not affected by precipitation. The characteristic temperature was found to increase when the amount of manganese in supersaturated solid solution increased. When the annealing treatments to recrystallise the material conditions were carried out at temperatures above T_c fine grained and

equiaxed microstructures were found. In these cases the recrystallisation textures were random after a strain of 1.5 while they consisted of weak cube textures after a strain of 3.0. Below T_c the recrystallised grains became elongated in the rolling direction and were considerably larger and more serrated than for the high temperature annealing, *i.e.* above T_c. The recrystallisation textures differed considerably, strong P-textures in combination with weak ND-rotated cube textures were obtained when the annealing treatments were carried out below T_c.

4. The P- and ND-rotated cube orientations were found to have a growth advantage in the early stages of annealing, while in the later stages all grains seemed to grow with a constant growth rate. PSN was found to play a significant role in the nucleation event of the P- and ND-rotated cube texture components. If the deformation is large enough, subgrains with these texture components have previously been found to be present within the deformation zone surrounding the primary particles. Upon annealing at temperatures below T_c, some of these subgrains finally produce recrystallisation nuclei. These orientations were only found to dominate the recrystallisation texture in case of heavy concurrent precipitation. Previous investigations as well have found the actual orientations to dominate the recrystallisation texture in case of heavy precipitation. However, the intensity has not been reported to be as strong as in the present work. It is thus reasonable to name these texture components precipitation texture components.

5. Nucleation of the weak cube texture after a strain of 3.0 was assumed to be a result of grain fragmentation. Cube oriented subgrains are believed to be found within transitions bands that separates neighbouring volumes that have rotated towards different end positions during deformation. Since these bands are associated with a high stored energy, they are consequently favourable nucleation sites for recrystallisation during subsequent the annealing treatment.

6. When the annealing was carried out below the characteristic temperature, T_c, it was found that the precipitation reaction mainly took place on the low and high angle grain boundaries. A counting procedure of dispersoids was carried

out for one condition that had been annealed below the characteristic temperature, and for this condition a constant dispersoid density was found after a short initial nucleation and growth period.

Industrially processed alloy:

7. The amount of manganese in solid solution of the industrially produced alloy decreased throughout the hot rolling schedule as well as during the final softening annealing.

8. The textures after the different processing steps were dominated by the cube orientation, although the intensity was fairly low after the final annealing. During the final annealing, PSN, which is believed to produce random nuclei, was assumed to be the dominating mechanism in producing recrystallised grains. The remaining cube texture was believed to be a result of nucleation at old cube grains that have survived deformation. This was the operating mechanism both for the hot- and the cold deformed materials.

9. With respect to the change in the particle size distributions for the different conditions, it was found that the coarsest particles tended to break up at all the deformation steps. However, the main break-up of particles took place during hot rolling.

10. The results of the laboratory processed alloy were intended as a reference to be able to better understand the behaviour and properties of the industrially processed alloy. However, a direct comparison was not straightforward. Although the general behaviour was the same and similarities were found, the behaviour and complexity of the industrially processed material turned out to be such that limited conclusions could be drawn from direct comparisons between the two differently produced alloys.

Modelling activities:

11. Modelling of the softening behaviour of a commercial pure alloy and the laboratory processed AlMn-alloy by a physically based softening model resulted in good model predictions. However, an additional drag force affecting nucleation had to be included in the model in case of annealing

below T_c for the AlMn-alloy. The industrially processed AlMn-alloy was not well predicted even with this latter modification. It is realised through the present work that a fully adequate quantitative description of the precipitation reaction and its effects on recovery and recrystallisation is indeed a complex problem, and thus beyond the scope of this work.

7. References

Abtahi S., Sjølstad K., Marthinsen K. and Nes E: Proc. Recrystallisation and Grain Growth (ed. Gottstein and Molodov), Springer Verlag, Berlin, (2001), pp. 251.

Akef A: PhD Thesis, Ecole des Mines de St.-Etienne, France (1992).

Alexander D.T.L. and Greer A.L: Acta mater. 50 (2002), pp.2571.

Altenpohl D: Aluminium und Aluminiumlegierungen, Springer-Verlag, Berlin, (1965), pp.526.

Ashby M.F., Harper J. and Lewis J: Trans. Metall. Soc., A.I.M.E., 245 (1969), pp.413.

Ashby M.F: In "Strengthening Methods in Crystals" (ed. Kelly and Nicholson), Elsevier, Amsterdam, (1971), pp.137.

Avrami M: J. Chem. Phys., 7 (1939), pp.1103.

Bardal A., Lindseth I., Vatne H.E. and Nes E: Proc. 16th Risø Int. Symposium (ed. Hansen *et al.*), Risø National Laboratory, Roskilde, (1995), pp.261.

Barret C.S: Trans. AIME, 137 (1940), pp.128.

Benum S: PhD Thesis, The Norwegian Institute of Technology, Trondheim (1995).

Benum S and Nes E: Acta mater., 45 (1997), pp.4593.

Bjerkaas H: Project work, The Norwegian University of Sci. and Tech., Trondheim, (2001).

Bleck W. and Bunge H.J: Acta metall., 29 (1981), pp.1401.

Bolingbroke R.K., Creed E., Marshall G.J. and Ricks R.A: Proc. TMS (ed. Morris *et al.*), Warrendale, (1993), pp. 215.

Bunge H.J: Texture analysis in Material Science, Butterworth & Co, London, (1982).

Burger G., Wycliffe P., Gabryel C and Lloyd D.J: Proc. ICAA5 (ed. Driver *et al.*), Mater. Sci. Forum, vol.242 (1997), pp.101.

Burgers W.G. and Louwerse P.C: Z. Physik 61 (1931), pp.605.

Chan H.M. and Humphreys F.J: Acta Metall., 32, (1984), pp.235.

Chen S.P., Kuijpers N.C.W. and Zwaag S.v.d: Mater Sci. Eng. A, vol.341 (2003), pp.296.

Cook M. and Richards T.L: J. Inst. Met., 73 (1946), pp.1.

Crumbach M., Gottstein G., Löchte L., Piot D., Driver J., Allen C. M. and Savoie J. F: Proc. ICAA8 (ed. Gregson and Harris), Mater. Sci. Forum, vol.396-402 (2002), pp. 357-364.

Daaland O: Dr.ing thesis, The Norwegian Institute of Technology., Trondheim, (1993).

Daaland O., Dronen P.E., Vatne H.E., Næss S.E. and Nes E: Proc. Rex'92 (ed. Furentes and Sevillano), Mater. Sci. Forum, vol.113-115 (1993b), pp.115.

Daaland O. and Nes E: Acta mater. 44 (1996), pp.1413.

Dehlinger U: Metallw., 7 (1928), pp.1172.

Dillamore I.L. and Katoh H: Metal Science, 8 (1974), pp.73.

Dimitrov O., Fromageau R. and Dimitrov C: In "Recrystallization of Metallic Materials" (ed. Haeßner F) Dr. Riedrer-Verlag, Stuttgart (1978), pp.137.

Doherty R.D: Scripta met., 19 (1985), pp.927.

Doherty R.D., Hughes D.A., Humphreys F.J., Jonas J.J., Juul Jensen D., Kassner M.E., King W.E., McNelley T.R., McQueen H.J. and Rollett A.D: Mater. Sci. Eng. A, vol.A238, pp.219, 1997.

Dons A.L: Dr.ing thesis, The Norwegian University of Sci. and Tech., Trondheim, (2002).

Driver J.H: Proc. 16th Int. Risø Symposium (ed. Hansen *et al.*), Risø National Laboratory, Roskilde, (1995), pp.25.

Ekström H.E., Östensson L. and Hagström J: "Dispersoids and constituent size distribution in 2.2 mm thick hot rolled bands of AA3104", Brite-Euram Report BE96-3364, (1998).

Ekström H.E: "W-50 Sapa Tensile testing and Mn in solution", Vir[Fab]-report, Team Arena, (2002).

Engler O., Heckelmann I., Rickert T., Hirsch J. and Lücke K: Mater. Sci. Tech., 10 (1994), pp.771.

Engler O. and Yang P: Proc. 16th Int. Risø Symposium (ed. Hansen *et al.*), Risø National Laboratory, Roskilde, (1995), pp.335.

Engler O., Yang P. and Kong X.W: Acta mater., 44 (1996), pp.3349.

Engler O: Mater. Sci. Tech., 12 (1996b), pp.859.

Engler O., Kong X.W. and Yang P: Scripta Mater., 37 (1997), pp.1665.

Engler O., Kong X.W. and Lücke K: Acta mater., 49 (2001), pp.1701.

Engler O: Proc. ICOTOM13 (ed. Lee), Mater. Sci. Forum, vol.408-412 (2002), pp.1407.

Ferry M. and Humphreys F.J: Acta Mater., 44 (1996), pp.1293.

Forbord B: Dr.ing thesis, The Norwegian. University of Sci. and Tech., Trondheim, (1999).

Fricke W.G. and McShane H.B: In “Textures in Non-Ferrous Metals and Alloys” (ed. Marshant and Morris), TMS Warrendale, Detroit, (1985), pp. 31.

Friedel J: Dislocations, Addison Wesley, London (1964).

Furrer P. and Hausch G: Metal Sci., (1979), pp.155.

Furu T: Dr.ing thesis, The Norwegian Institute of Technology, Trondheim, (1992).

Furu T., Ørsund R. and Nes E: Acta Met. Mater., 43 (1995), pp.2209.

Gil Sevillano J., van Houtte P., and Aernoudt E: Prog. Mater. Sci., 25 (1980), pp.69.

Godfrey A., Juul Jensen D. and Hansen N: Acta mater., 49 (2001), pp.2429.

Haan P.C.M., Rijkom J.v. and Söntgerath J.A.H: Proc. ICAA5 (ed. Driver *et al.*), Mater. Sci. Forum, vol.217-222 (1996), pp.765.

Hagström J: “Particle Size Distribution in Alloy AA3103”, VIR[FAB]-report, WP3.task 3.4.SIMR.report.2001-002, SIMR, ISSN:1403-848/X, (2001).

Hagström J: “Microstructural Development in cold rolled Aluminium Alloy AA3103 during annealing”, Vir[Fab]-report, Team Arena, (2003)

Hamerton R: “Basic Characterisation on Materials (AA1200)”, Vir[Fab]-report, Team Arena, (2000)

Hansen N. and Bay B: Acta Metall., 29 (1981), pp.65.

Hatherly M: Proc. ICOTOM5 (ed. Gottstein and Lücke), Springer Verlag, Berlin (1978), pp.265.

Hausch G., Furrer P. and Warlimont H: Z. Metallkunde, 69 (1978), pp.174.

Hinesley C.P. and Morris J.G: Mater. Sci. Eng., 6 (1970), pp.48.

Hirsch J. and Lücke K: Acta Met., 36 (1988), pp.2883.

Hirsch J: Mater. Sci. Tech., 6 (1990), pp.1048.

Hjelen J., Ørsund R. and Nes E: Proc. “Directional Properties of Materials” (ed. Bunge), Deutsche Gesellschaft für Metallkunde, Oberursel, (1988), pp.115.

Holmedal B., Abtahi S., Marthinsen K. and Nes E: Proc. ICAA8 (ed. Gregson and Harris), Mater. Sci. Forum, vol.396-402 (2002), pp.315.

Hornbogen E. and Köstner U: In “Recrystallization of Metallic Materials” (ed. Haeßner F) Dr. Riedrer-Verlag, Stuttgart (1978), pp.159.

Houtte Pv: The MTM-FHM Software System, Version 2, Katholieke Univ. Leuven, (1994).

Hu H: Trans. Metall. Soc. A.I.M.E., 224 (1962), pp.75.

Hu H: Proc. 7^{th} Int. Risø Symposium (ed. Hansen *et al.*), Risø National Laboratory, Roskilde, (1986), pp.75.

Huang Y. and Humphreys F.J: Acta Mater., 48 (2000), pp.2017.

Hughes D.A: Proc. 16th Int. Risø Symposium (ed. Hansen *et al.*), Risø National Laboratory, Roskilde, (1995), pp.63.

Humphreys F.J: Acta Met., 25 (1977), pp.1323.

Humphreys F.J: Acta Met., 27 (1979), pp.1801.

Humphreys F.J and Kalu P.N: Acta metall. mater., 38 (1990), pp.917.

Humphreys F.J. and Ardakani M.G: Acta metall. mater., 42 (1994), pp.749.

Humphreys F.J. and Hatherly M: Recrystallisation and related annealing phenomena, Pergamon Press, Oxford, (1995).

Humphreys F.J., Huang Y., Brough I. and Harris C: J. of Microscopy, 195 (1999), pp.212.

Humphreys F.J. and Huang Y: Proc. 21th Risø Int. Symp. on Mater. Sci. (ed. Hansen *et al.*), Risø National Laboratory, Roskilde, (2000), pp.71.

Humphreys F.J: J. of Materials Sci., 36 (2001), pp.3833.

Hutchinson W.B., Oscarsson A. and Karlsson Å: Mater. Sci. Tech., 5 (1989), pp.1118.

Ito K., Lücke K. and Rixen R: Z. Metallkd., 67 (1976), pp.338.

Johnson W.A. and Mehl R.F: Trans. AIME, 135 (1939), pp.416.

Karhausen K. and Rothers F: J. Mater. Processing Tech., 123 (2002), pp.155.

Kolmogorov A.N: Izv. Akad. Nauk., USSR Ser. Matemat.,1 (1937), pp.355.

Kong X.W., Engler O. and Lücke K: Textures Microstructures, 14-18 (1991), pp.1215.

Kutner F. and Lang G: Aluminium, vol.52 (1976), pp.322.

Leffers T: Proc. 2th Int. Risø Symposium on Metallurgy and Materials (ed. Hansen *et al.*), Risø National Laboratory, Roskilde, (1981), pp.55.

Li Y. and Arnberg L: Proc. ICAA8 (ed. Gregson and Harris), Mater. Sci. Forum, vol.396-402 (2002), pp.875.

Liu C: "Production process and through process microstructure evolution of AA3103", Vir[Fab]-report, Team Arena, (2003).

Liu J. and Morris J.G: To be published in Metall. Mater. Trans. A. (2003)

Löchte L: "Solute Level of AA3103 for Through-process Modelling of Flow Stress", Vir[Fab]-report, Team Arena, (2001).

Lok Z.J: High Temperature Plastic Deformation and Related Solute Effects in Aluminium Based Alloys, The Netherlands Ins. Met. Res., Delft, (2001).

Lücke K., Pospiech J., Virnich K.H. and Jura J: Acta metall., 29 (1981), pp.169.

Lücke K: Proc. ICOTOM7 (ed. Brakman *et al.*) Netherlands Soc. of Materials Sci., (1984), pp.195.

Lücke K. and Engler O: Mater. Sci. Tech., 6 (1990), pp.1113.

Marthinsen K. and Nes E: Mater. Sci. Tech., 17 (2001), pp.376.

Martin J.W., Doherty R.D. and Cantor B: Stability of microstructure in metallic systems, Cambridge University Press, Cambridge, (1997).

Maurice C. and Driver J.H: Acta Metall. Mater., 41 (1993), pp.1653.

Milman Y.V., Galanov B.A. and Chugunova I: Acta Metall. Mater., 41 (1993), pp.2523.

Morris P.L. and Duggan B.J: Met. Sci., 12 (1978), pp.1.

Nes E. and Slevolden S: Aluminium, 55 (1979), pp.319.

Nes E., Ryum N and Hunderi O: Acta metall., 33 (1985), pp. 11.

Nes E. and Hutchinson W.B: Proc. 10th Risø Int. Symp. on Metallurgy and Materials (ed. Sørensen B *et al.*), Risø National Laboratory, Roskilde, (1989), pp.233.

Nes E: Prog. Materials Sci. 41 (1998), pp.129.

Nes E., Marthinsen K. and Rønning B: J. Mater. Tech., 117 (2001), pp.333.

Nord-Varhaug K., Forbord B., Benestad J., Pettersen T., Rønning B., Bardal A., Benum S., Marthinsen K. and Nes E: Proc. ICAA7 (ed. Starke *et al.*), Mater. Sci. Forum, vols.331-337 (2000), pp.1387.

Oscarsson A: Textures Microstructures, 14-18 (1991), pp.477.

Oscarsson A., Nicol B., Eksröm H.E., Remmelg G. and Hutchinson W.B: Proc. ICAA3 (ed. Arnberg *et al.*), Trondheim, (1992), pp.239.

Rothers F., Raabe D. and Gottstein G: Acta mater., 48 (2000), pp.4181.

Russell K.C. and Ashby M.F: Acta metall., 18 (1970), pp.891.

Ryen Ø., Holmedal B. and Nes E: Proc. ICAA8 (ed. Gregson and Harris), Mater. Sci. Forum, vol.396-402 (2002), pp.1145.

Ryu J.H. and Lee D.N: Mat. Sci. Eng. A336 (2002), pp.225.

Sachs E: Z: Ver. dt. Ing., 72 (1928), pp.734.

Samajdar I and Doherty R.D: Scr. Met., 32 (1995), pp.845.

Sandstrøm R., Lehtinen B., Hedman E., Groza I. and Karlsson S: J. Mat. Sci. 13 (1978), pp.1229.

Sjølstad K., Engler O., Tangen S., Marthinsen K. and Nes E: Proc. ICAA8 (ed. Gregson and Harris), Mater. Sci. Forum, vol.396-402 (2002), pp.463.

Sjølstad K., Engler O., Tangen S., Marthinsen K. and Nes E: Proc. ICOTOM13 (ed. Lee), Mater. Sci. Forum, vol.408-412 (2002b), pp.1471.

Smith A.W.F., Court S.A. and Humphreys F.J: Proc. Recrystallization and Grain Growth (ed. Gottstein and Molodov), Springer-Verlag, (2001), pp.1323.

Sæter J.A., Vatne H.E. Benum S. and Nes E: Proc. ReX'96 (ed. McNelley), (1997), pp.307.

Sæter J.A: Dr.ing thesis, The Norwegian University of Sci. and Tech., Trondheim, (1997).

Sæter J.A., Forbord B., Vatne H.E. and Nes E: Proc. ICAA6 (ed. Sato *et al.*) (1998), pp.113.

Tangen S., Sjølstad K., Nes E., Furu T. and Marthinsen K: Proc. ICAA8 (ed. Gregson and Harris), Mater. Sci. Forum, vol.396-402 (2002), pp.469.

Taylor G.I: J. Inst. Met., 62 (1938), pp.307.

Trømborg E., Dons A.L. and Arnberg L: Proc. ICAA3 (ed. Arnberg *et al.*), Trondheim, (1992), pp.270.

Vandermeer R.A. and McHargue C.J: Trans. AIME, 230 (1964), pp.667.

Varma S.K and Willits B.L: Met. Trans., 15A (1984), pp.1502.

Varma S.K: Mat. Sci. Eng., 82 (1986), pp.L19.

Varma S.K. and Wesstrom B.C: J. Mat. Sci. Lett., 7 (1988), pp.1092.

Vatne H.E: PhD Thesis, The Norwegian Institute of Technology, Trondheim (1995).

Vatne H.E., Furu T., Ørsund R. and Nes E: Acta Mater., 44 (1996), pp.4463.

Vatne H.E., Engler O. and Nes E: Mater. Sci. Tech., 13 (1997), pp.93.

Vatne H.E: 5th Int. Summer School on Aluminium Alloy Technology, Trondheim (1999).

Vörös G. and Kovacs I: Key Eng. Mater., vol.44-45 (1990), pp.247.

Washburn J. and Murty G: Can. J. Phys., 45(1967), pp.523.

Watanabe H., Ohori K., Takeuchi Y: Aluminium, 60 (1984), pp.373.

Weiland H: Proc. 21th Risø Int. Symp. on Materials Sci., (ed. Hansen N *et al.*), Risø National Laboratory, Denmark, (2000), pp.637.

Westengen H. and Ryum N: Mater. Sci. Eng., 34 (1978), pp.227.

Yang P., Engler O. and Klaar H.J: J. Appl. Cryst., 32 (1999), pp.1105.

Appendix 1: Measured and calculated values during homogenisation

Time [h]	**Conductivity** [MS/m]	**Mn in ss** [wt%]	**Corrected for Fe and Si in ss** [wt%]
0	17.71	0.83	0.80
6	20.31	0.63	0.60
7	20.99	0.58	0.55
8	21.25	0.57	0.54
9	21.37	0.56	0.53
10	21.70	0.54	0.51
12	21.46	0.55	0.53
14	21.75	0.54	0.51
18	22.01	0.52	0.50
23	23.18	0.46	0.44
24	23.41	0.44	0.43
25	23.26	0.45	0.43
26	23.26	0.45	0.43
27	23.22	0.45	0.44
29	23.52	0.44	0.42
31	23.49	0.44	0.42
35	23.61	0.43	0.42
41.5	24.19	0.41	0.39
42.5	24.54	0.39	0.38
43.5	24.72	0.38	0.37
44.5	24.76	0.38	0.37
45.5	24.87	0.38	0.36
47.5	24.73	0.38	0.37
49.5	25.03	0.37	0.36
53.5	25.00	0.37	0.36
57.5	25.04	0.37	0.36
61.5	25.29	0.36	0.34
65.5	25.57	0.34	0.33
68	25.47	0.35	0.34
69	25.50	0.35	0.34
70	25.43	0.35	0.34
71	25.70	0.34	0.33
72	25.50	0.35	0.34
74	25.75	0.34	0.33
76	25.84	0.33	0.32
80	25.79	0.34	0.33
84	25.72	0.34	0.33
88	26.04	0.33	0.32
92	26.07	0.32	0.31
96	26.29	0.31	0.31
100	26.26	0.32	0.31

Appendix 2: Softening and conductivity curves of LP 3103 deformed to strains of e=0.5 and e=1.5

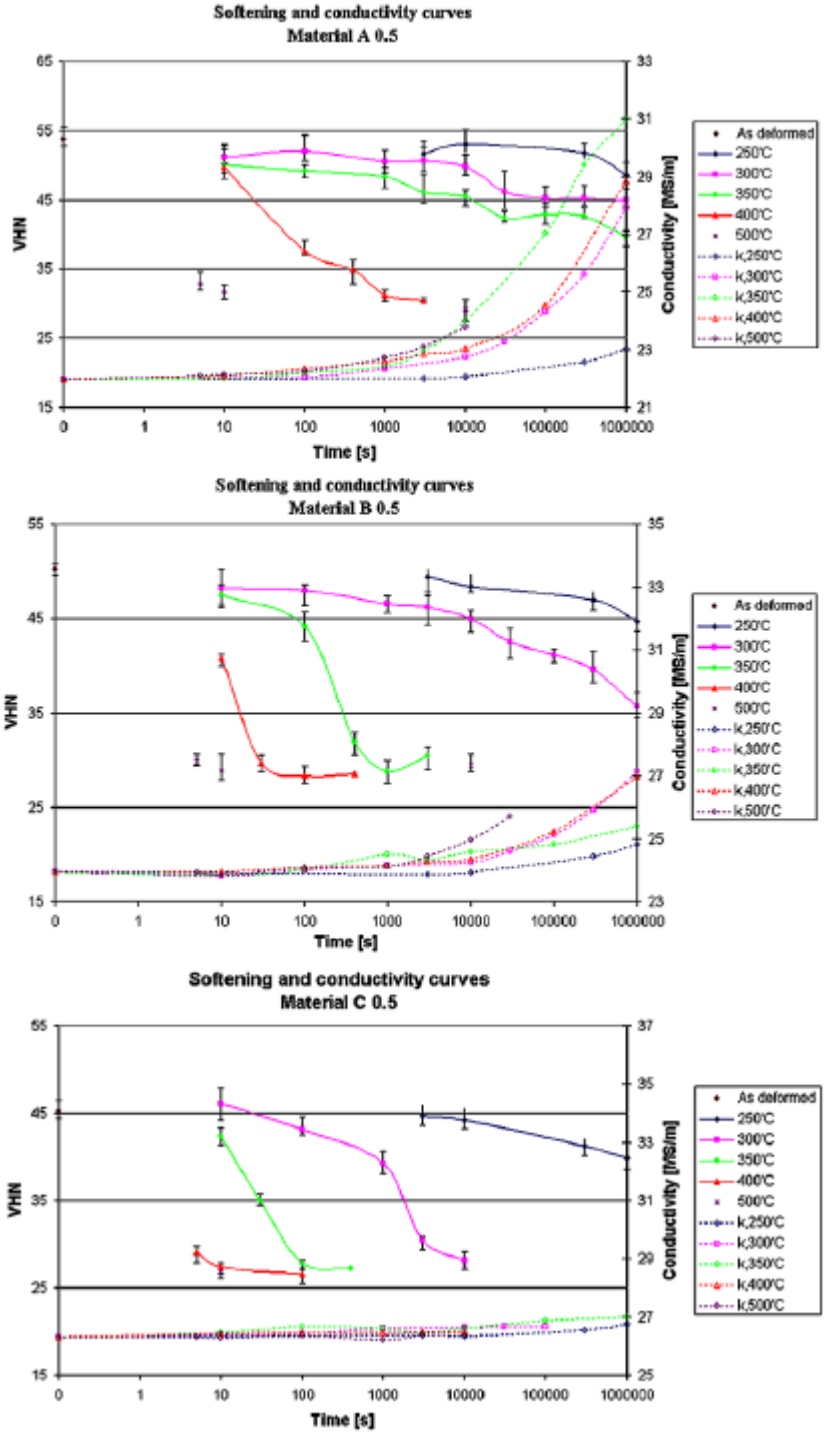

Fig.A2.1: Softening and conductivity curves of LP 3103 deformed to a strain of 0.5.

Appendix 2: Softening and precipitation curves of LP 3103

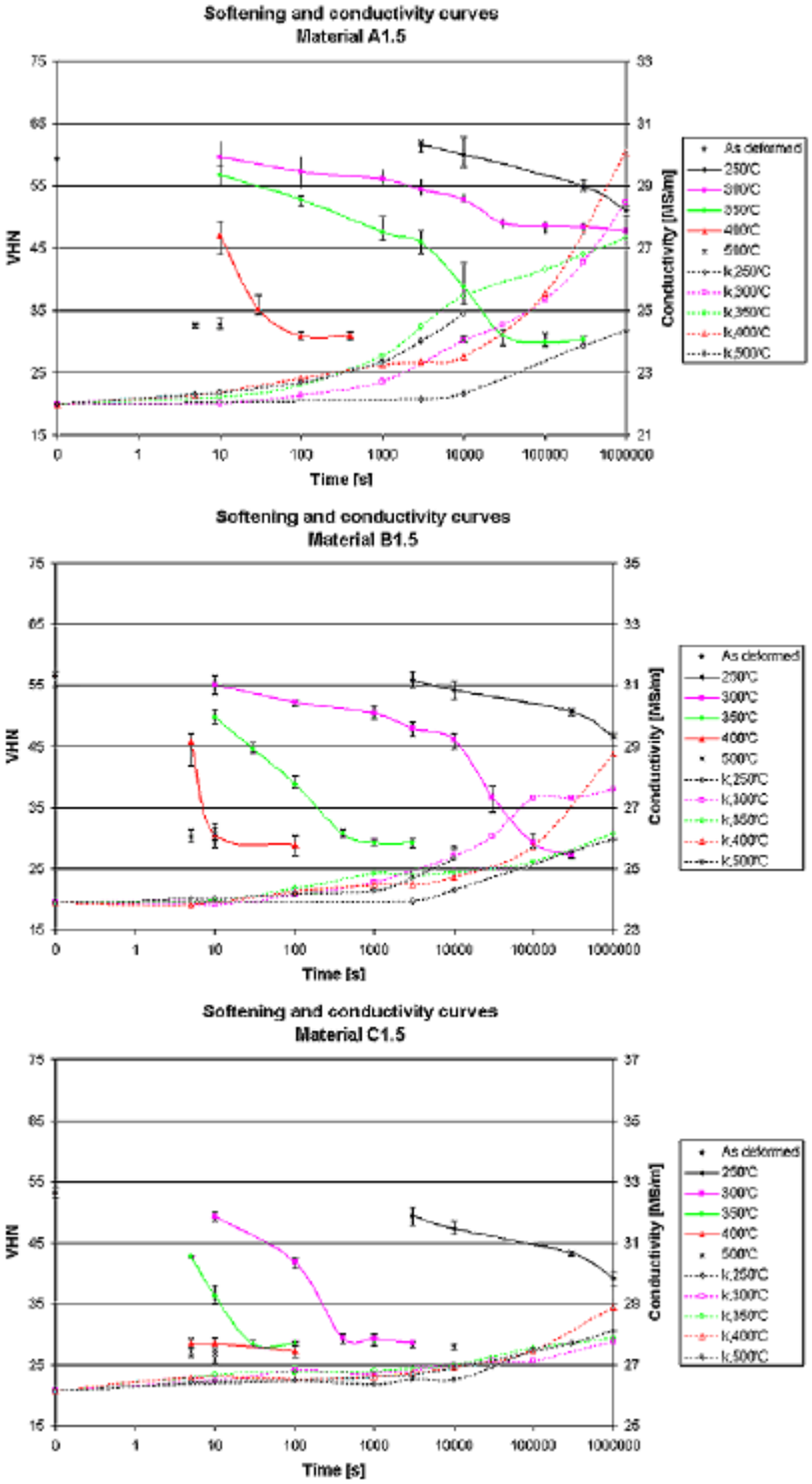

Fig.A2.2: Softening and conductivity curves of LP 3103 deformed to a strain of 1.5.

Appendix 3: Recrystallised grain size distributions of LP 3103

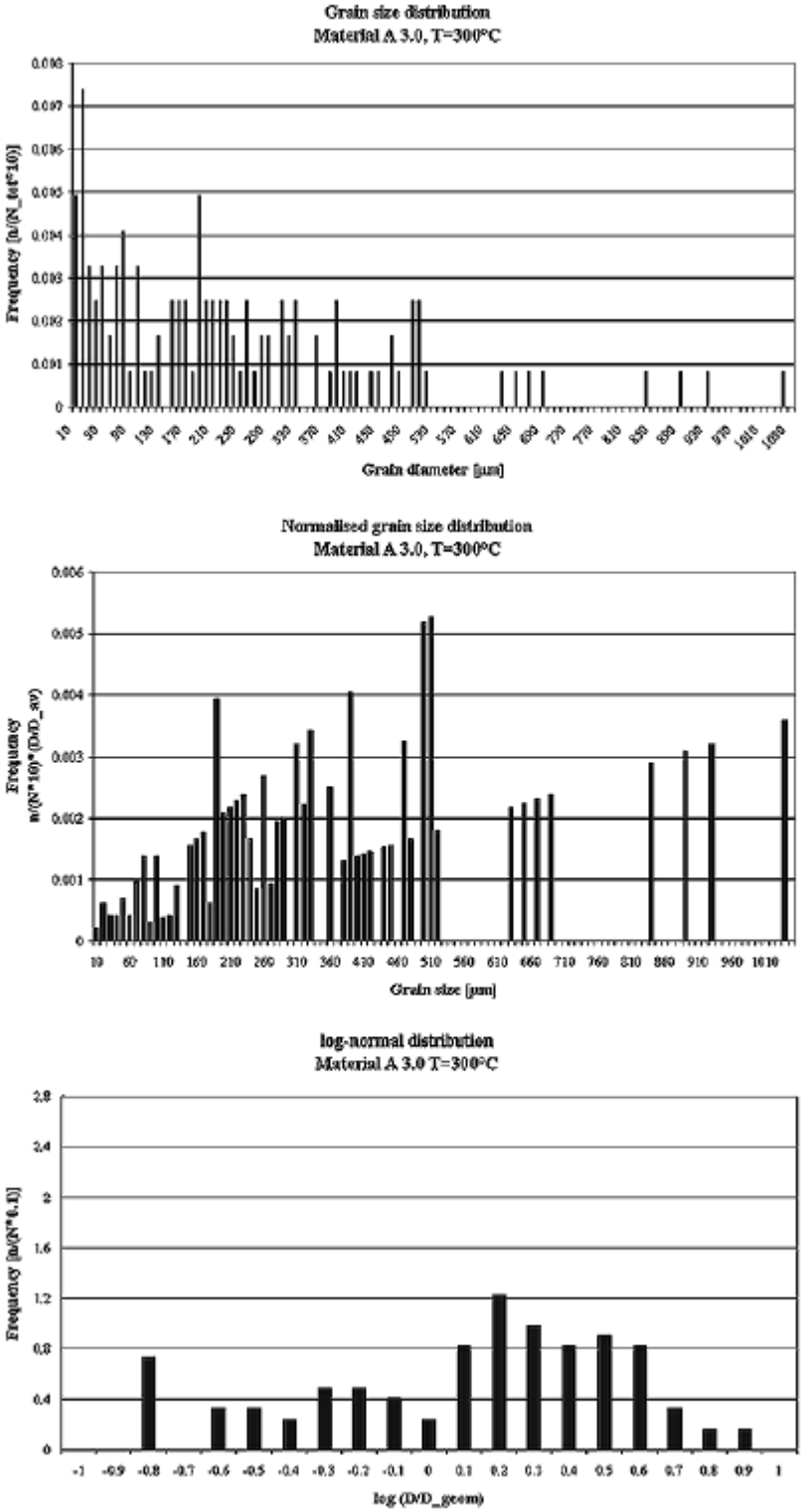

Fig.A3.1: Grain size distributions of A3.0 annealed at 300°C.

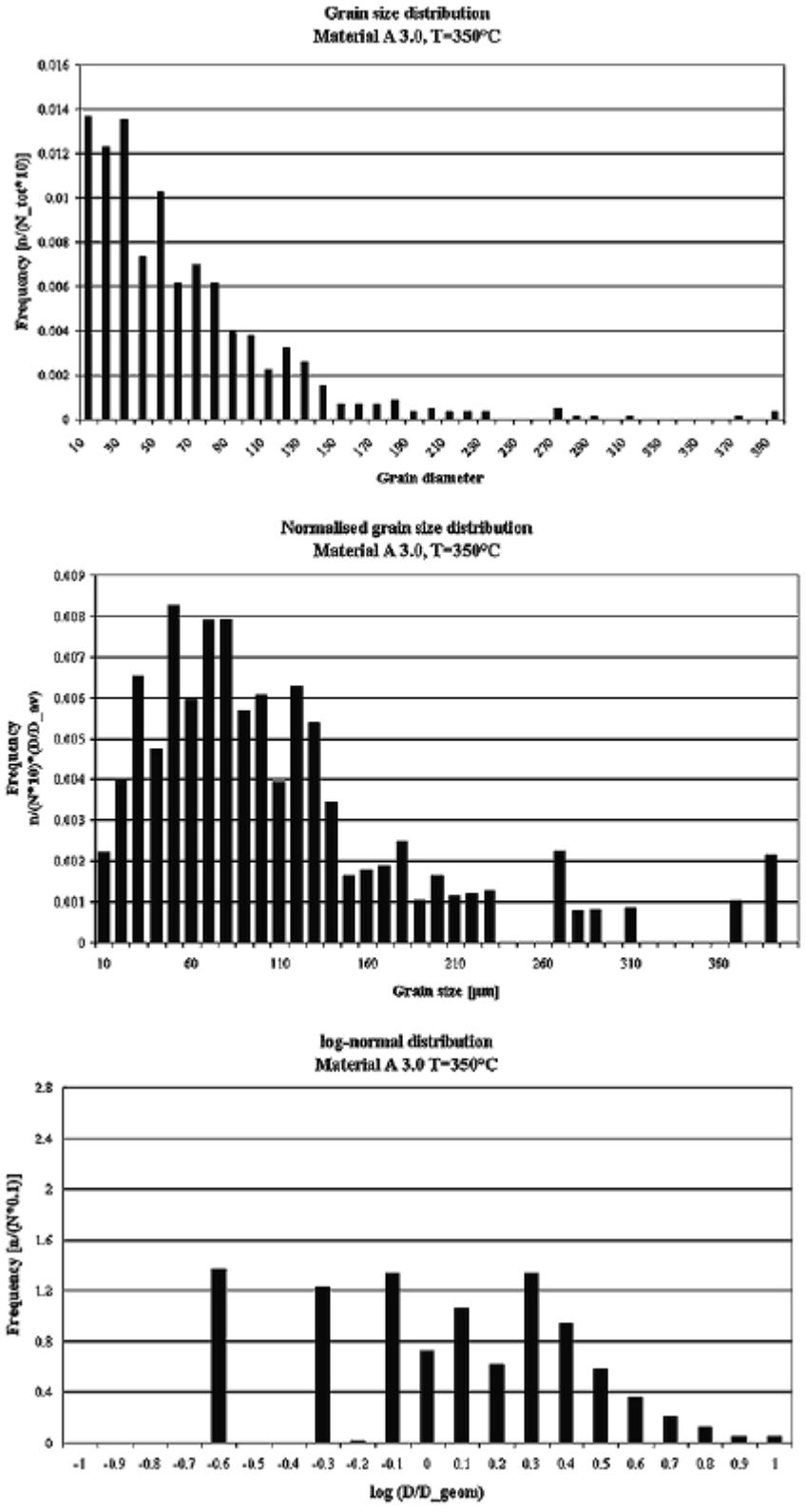

Fig.A3.2: Grain size distributions of A3.0 annealed at 350°C.

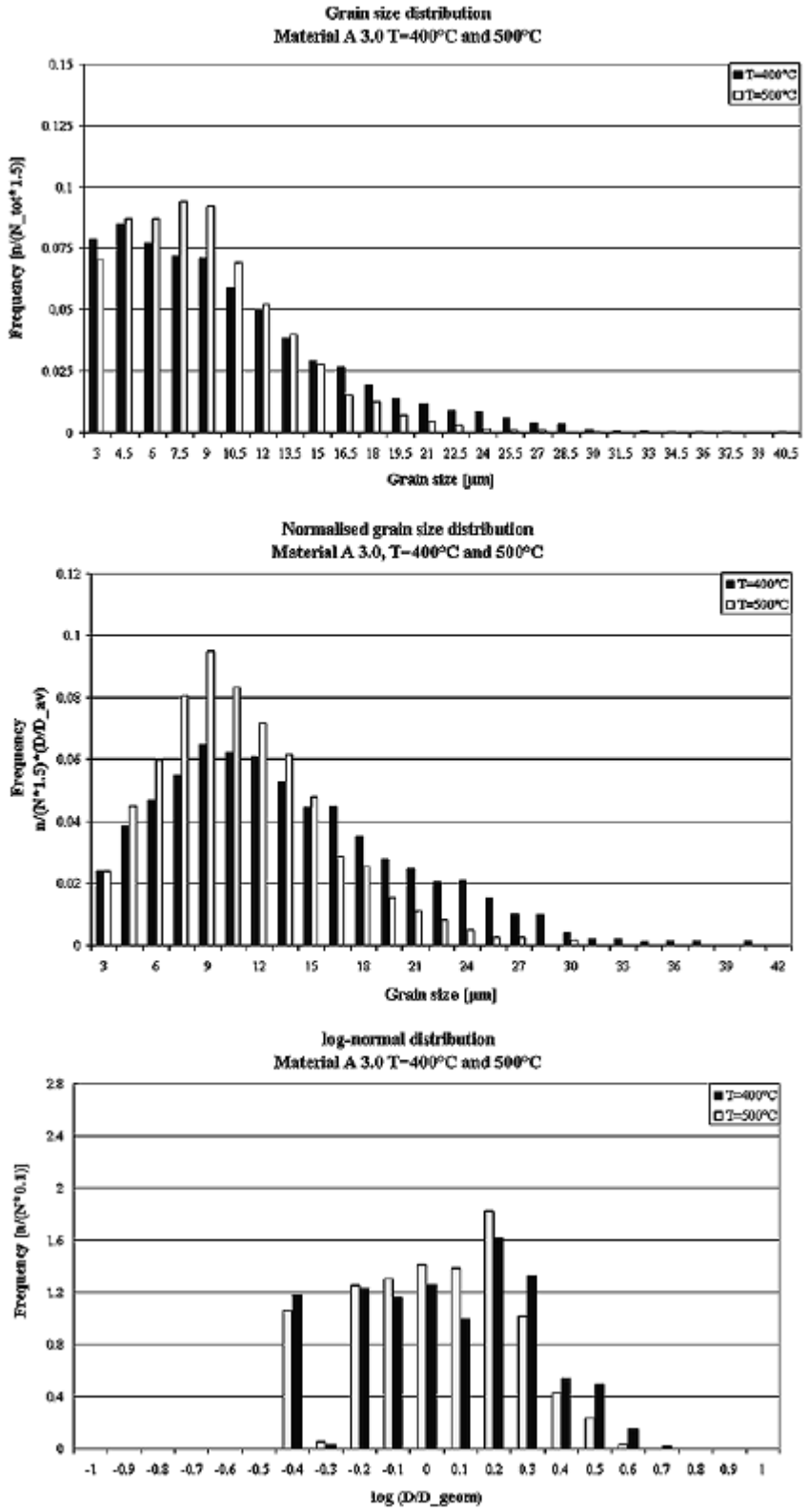

Fig.A3.3: Grain size distributions of A3.0 annealed at 400°C and 500°C.

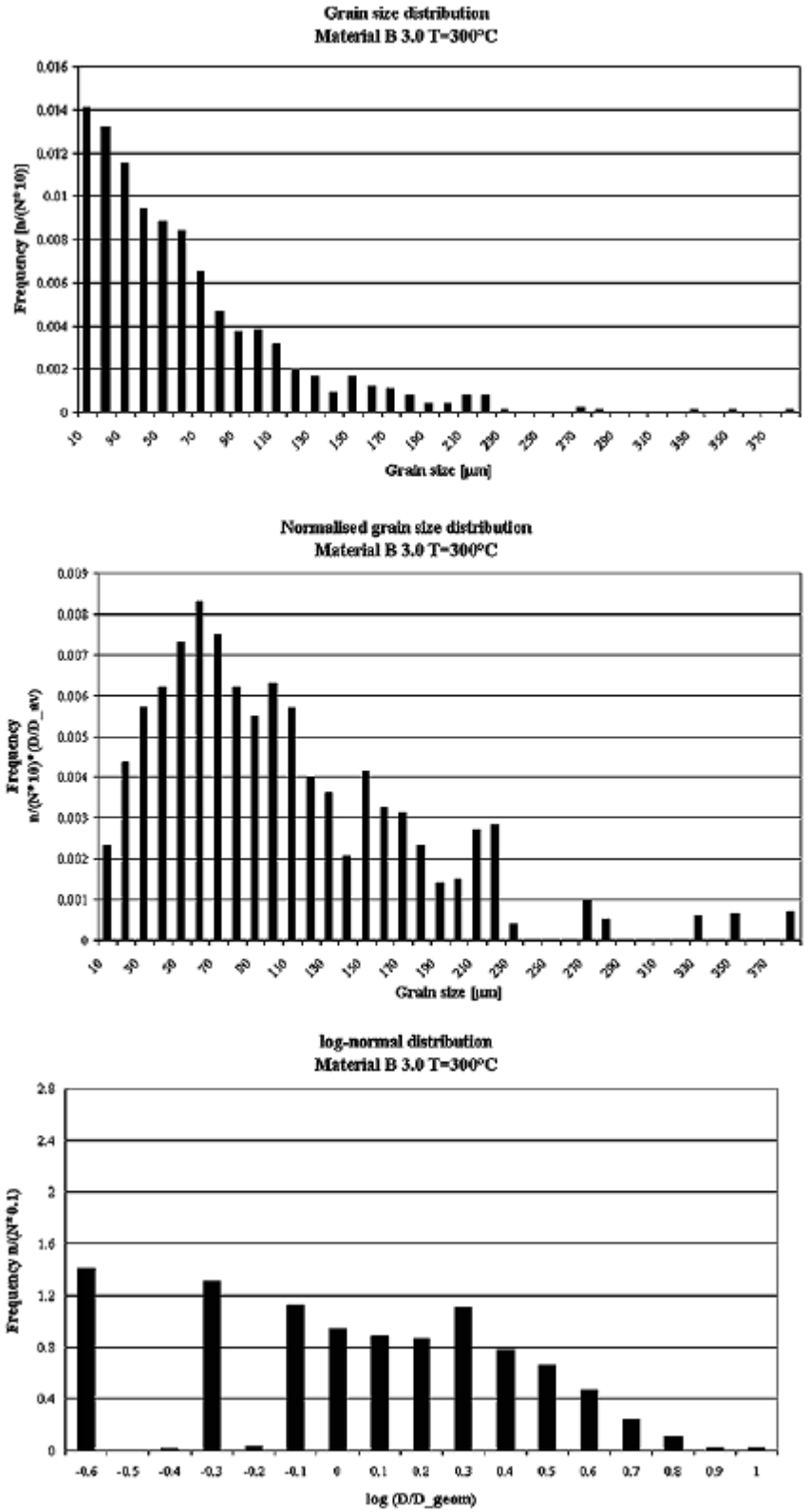

Fig.A3.4: Grain size distributions of B3.0 annealed at 300°C.

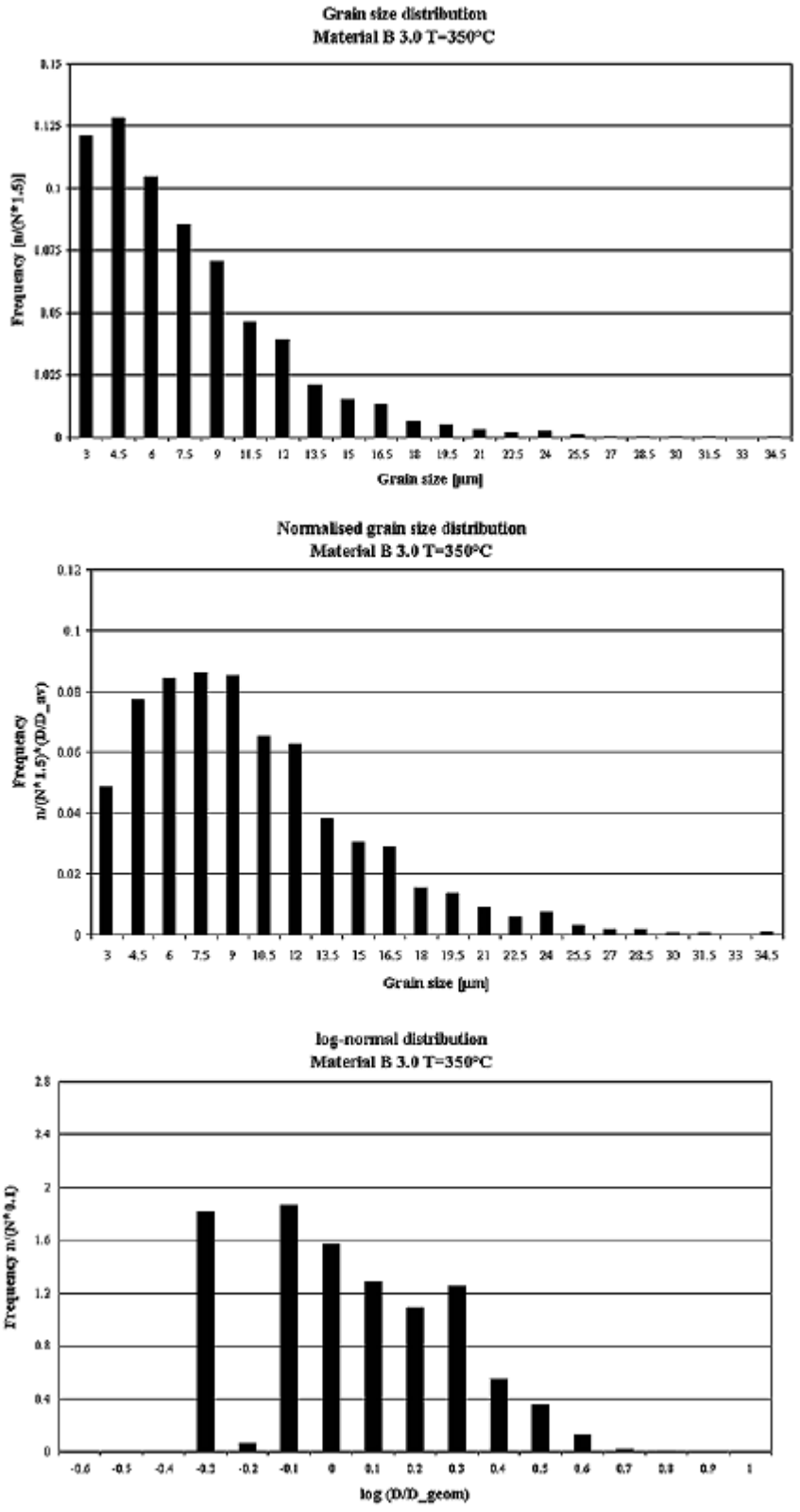

Fig.A3.5: Grain size distributions of B3.0 annealed at 350°C.

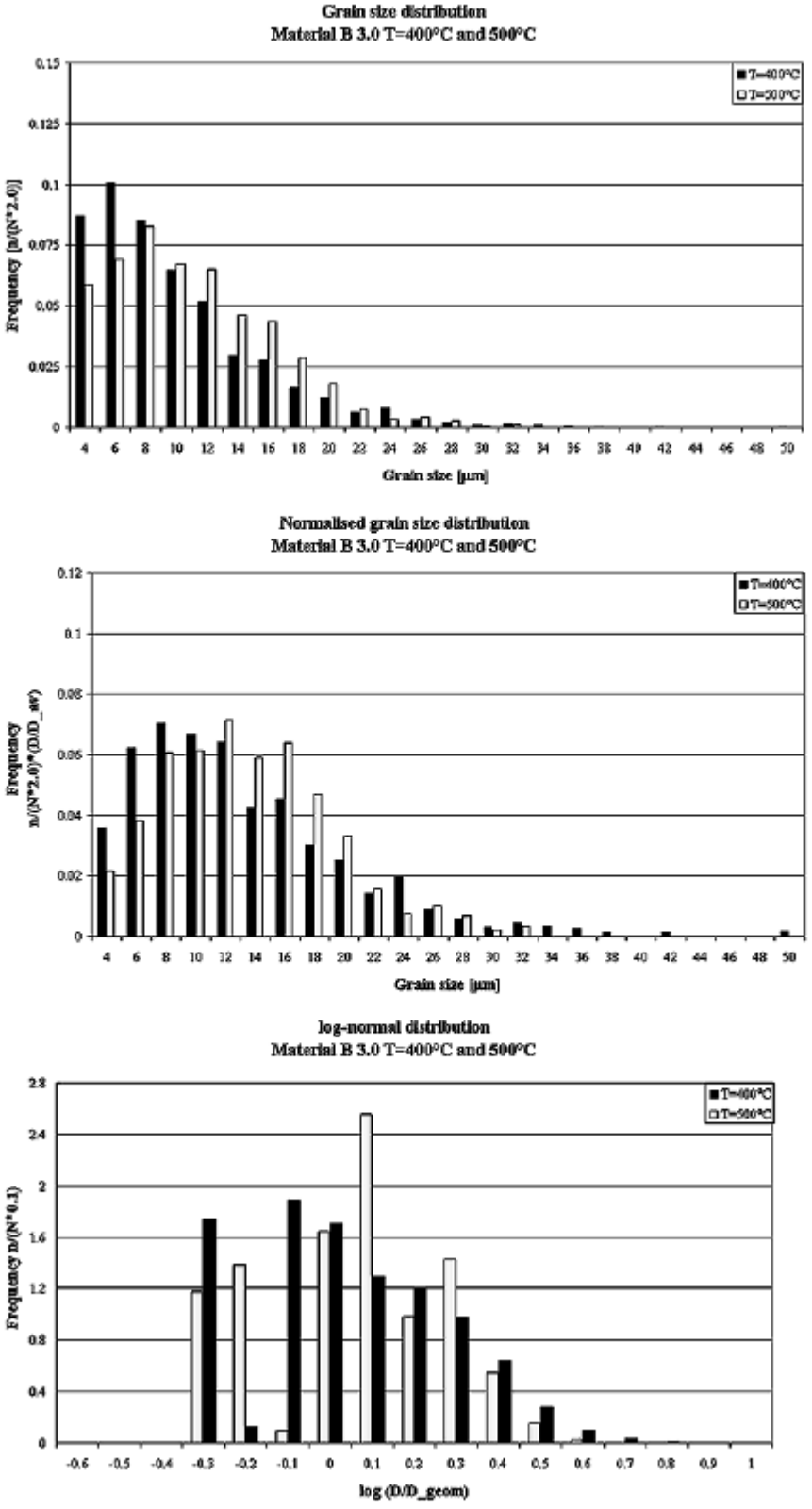

Fig.A3.6: Grain size distributions of B3.0 annealed at 400°C and 500°C.

Appendix 3: Recrystallised grain size distributions of LP 3103

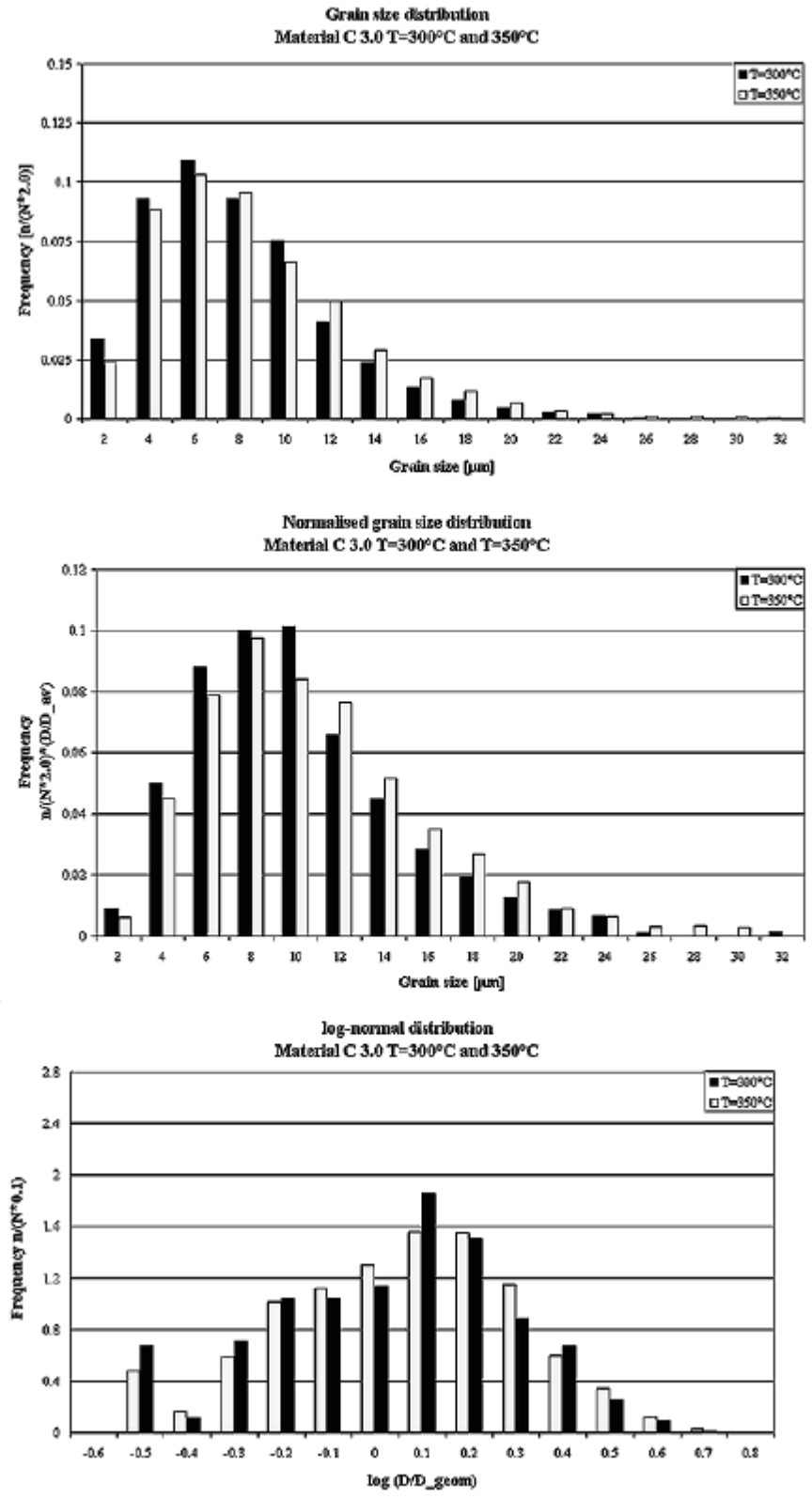

Fig.A3.7: Grain size distributions of C3.0 annealed at 300°C and 350°C.

Appendix 3: Recrystallised grain size distributions of LP 3103

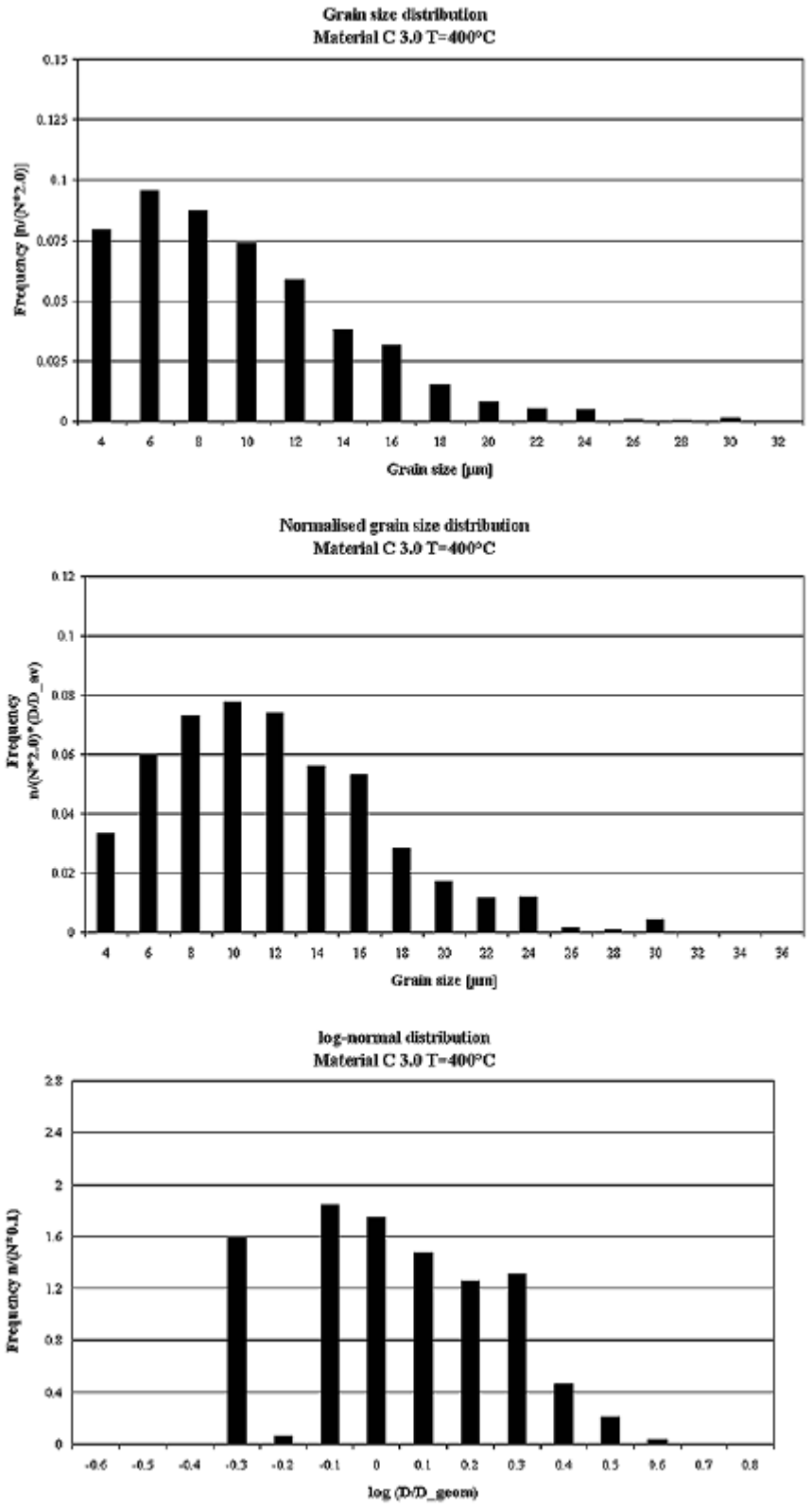

Fig.A3.8: Grain size distributions of C3.0 annealed at 400°C.

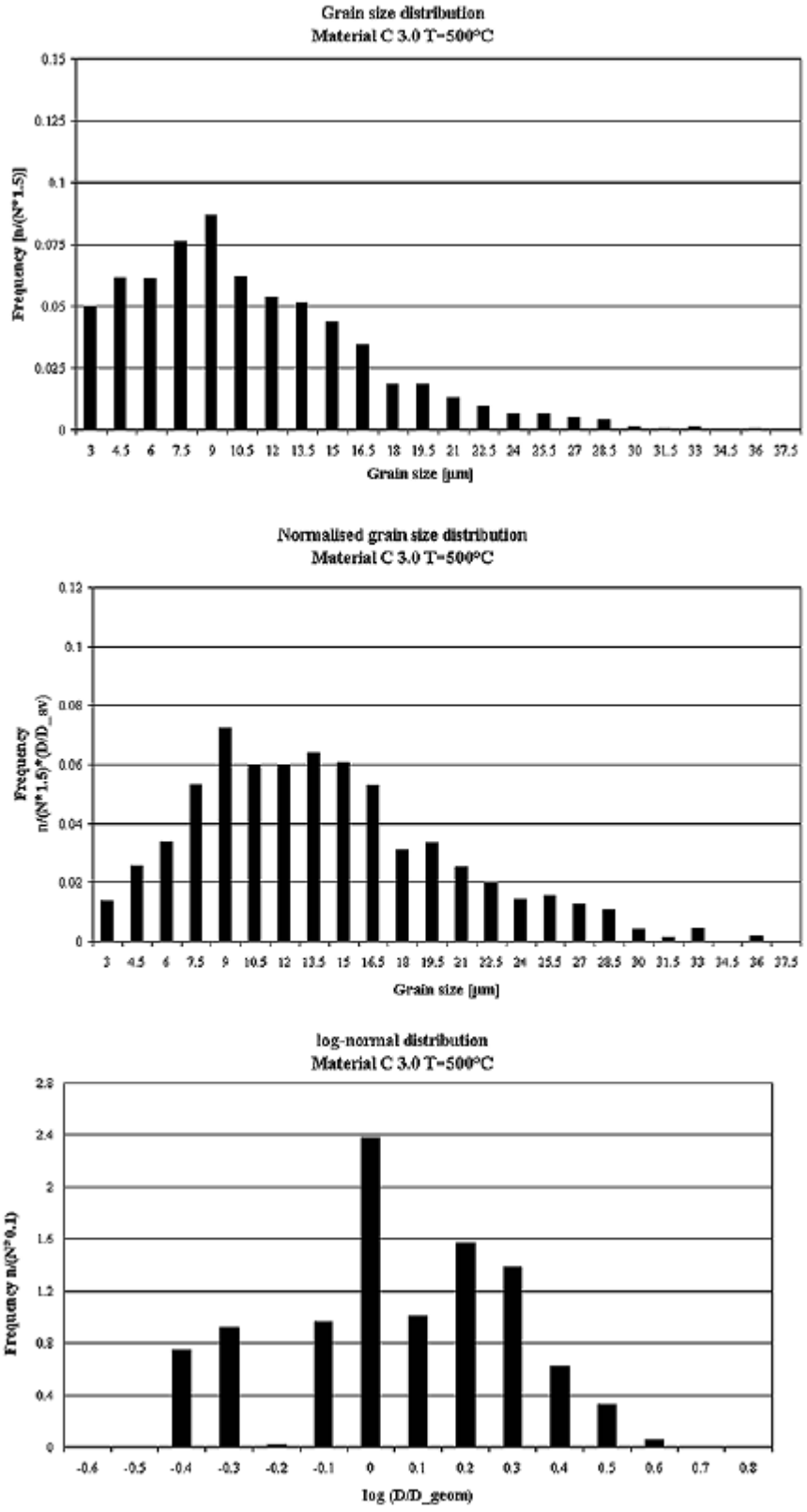

Fig.A3.9: Grain size distributions of C3.0 annealed at 500°C.

Appendix 4: Mechanical values from the tensile testing.

AA3103 produced by VAW

Table A3.1. Annealing of CP 3103-W0 at 280°C.

Time at temperature [s]	Flow stress σ_y [Mpa]	Max stress σ_m [Mpa]	Strain at fracture ε_f	Conductivity κ [MS/m]
As deformed	200	207.8	0.02	23.61
10	181	200.7	0.035	23.59
30	164	189.1	0.03	23.42
300	154.5	169.6	0.03	23.64
1,000	156.5	167.4	0.02	23.99
3,000	154.5	166.5	0.025	24.11
10,000	148.5	156.0	0.03	24.88
30,000	137.5	148.5	0.055	25.34
100,000	128	133.7	0.13	26.32
300,000	92	111.0	0.26	28.71
1,000,000	66	105.1	0.36	29.97

Table A3.2. Annealing of CP 3103-W0 at 290°C.

Time at temperature [s]	Flow stress σ_y [Mpa]	Max stress σ_m [Mpa]	Strain at fracture ε_f	Conductivity κ [MS/m]
As deformed	200	207.8	0.02	23.61
10	164	193.8	0.035	23.75
30	159	185.4	0.035	23.73
300	157.5	168.9	0.03	23.70
1,000	140.5	155.7	0.06	24.18
3,000	140	150.0	0.075	24.35
10,000	131	138.5	0.13	25.26
30,000	119	131.0	0.175	25.92
100,000	95	122.6	0.33	27.13
300,000	55.5	101.5	0.37	29.18
1,000,000	41	96.8	0.35	29.67

Table A3.3. Annealing of CP 3103-W0 at 300°C.

Time at temperature [s]	Flow stress σ_y [Mpa]	Max stress σ_m [Mpa]	Strain at fracture ε_f	Conductivity κ [MS/m]
As deformed	200	207.8	0.02	23.61
10	158.5	182.4	0.03	24.02
30	149	170.7	0.035	24.01
300	147.5	162.2	0.055	23.94
1,000	131.5	149.8	0.11	24.3
3,000	109.5	135.8	0.16	24.81
10,000	82	120.2	0.25	25.43
30,000	44	108.0	0.37	26.27
100,000	44.5	101.5	0.40	27.25
300,000	37.5	98.6	0.34	27.18

Table A3.4. Annealing of CP 3103-W0 at 325°C.

Time at temperature [s]	Flow stress σ_y [Mpa]	Max stress σ_m [Mpa]	Strain at fracture ε_f	Conductivity κ [MS/m]
As deformed	200	207.8	0.02	23.61
10	129.5	156.0	0.03	24.14
30	101.5	135.0	0.14	24.29
100	51	110.0	0.29	24.31
300	41.5	103.2	0.365	24.61

Table A3.5. Annealing of CP 3103-W0 at 350°C.

Time at temperature [s]	Flow stress σ_y [Mpa]	Max stress σ_m [Mpa]	Strain at fracture ε_f	Conductivity κ [MS/m]
As deformed	200	207.8	0.02	23.61
5	102.5	133.6	0.10	24.14
10	74	126.9	0.185	24.18
30	41	104.0	0.36	24.25
100	40	104.4	0.365	24.45

Table A3.6. Annealing of CP 3103-W50 at 290°C.

Time at temperature [s]	Flow stress σ_y [Mpa]	Max stress σ_m [Mpa]	Strain at fracture ε_f	Conductivity κ [MS/m]
As deformed	195	211.5	0.037	24.02
10	161	191.7	0.035	24.09
30	158.5	180.5	0.035	24.18
300	144.5	155.7	0.035	24.67
1,000	132.5	144.8	0.085	25.05
3,000	125	136.8	0.135	25.57
10,000	113	127.0	0.20	26.37
30,000	93	115.8	0.255	27.52
100,000	75.5	107.7	0.32	28.85
1,000,000	50	100.1	0.32	30.10

Table A3.7. Annealing of CP 3103-W50 at 300°C.

Time at temperature [s]	Flow stress σ_y [Mpa]	Max stress σ_m [Mpa]	Strain at fracture ε_f	Conductivity κ [MS/m]
As deformed	195	211.5	0.037	24.02
10	158	180.9	0.035	24.1
30	144.5	168.5	0.035	24.3
300	135	147.5	0.095	24.76
1,000	122.5	136.1	0.155	25.22
3,000	107.5	127.4	0.215	25.79
10,000	88	116.2	0.255	26.73
30,000	63	106.8	0.33	27.62
100,000	54.5	102.3	0.34	28.20
300,000	48	102.2	0.37	28.56

Table A3.8. Annealing of CP 3103-W50 at 310°C.

Time at temperature [s]	Flow stress σ_y [Mpa]	Max stress σ_m [Mpa]	Strain at fracture ε_f	Conductivity κ [MS/m]
As deformed	195	211.5	0.037	24.02
10	147	172.0	0.04	24.15
30	139	159.2	0.07	24.33
300	102.5	127.2	0.21	24.90
1,000	72.5	114.2	0.295	25.39
3,000	59.5	107.6	0.315	25.88
10,000	49	102.8	0.36	26.25
30,000	48	103.3	0.35	26.83

AA1200 produced by Alcan

Table A3.9. Annealing of AA1200 at 240°C.

Time at temperature [s]	Flow stress σ_y [Mpa]	Max stress σ_m [Mpa]	Strain at fracture ε_f	Conductivity κ [MS/m]
As deformed	120	142.0	0.05	34.77
100	112.5	127.8	0.057	34.82
1,000	106	118.6	0.063	34.97
3,000	100.5	112.7	0.096	35.08
10,000	84	98.6	0.151	35.15
30,000	47	75.5	0.295	35.35
100,000	25.5	68	0.44	35.45
300,000	24	69.3	0.45	35.53

Table A3.10. Annealing of AA1200 at 260°C.

Time at temperature [s]	Flow stress σ_y [Mpa]	Max stress σ_m [Mpa]	Strain at fracture ε_f	Conductivity κ [MS/m]
As deformed	120	142.0	0.05	34.77
30	111	130.2	0.048	34.77
100	103.5	119.3	0.051	34.79
1,000	86.5	97.7	0.117	34.95
3,000	64.5	86.6	0.21	35.12
10,000	29	70.2	0.385	35.25
30,000	25	71.2	0.43	35.24

Table A3.11. Annealing of AA1200 at 280°C.

Time at temperature [s]	Flow stress σ_y [Mpa]	Max stress σ_m [Mpa]	Strain at fracture ε_f	Conductivity κ [MS/m]
As deformed	120	142.0	0.05	34.77
30	100	122,4	0,047	34,78
100	88,5	111,6	0,06	34,79
300	84	99,7	0,13	34,87
1,000	57	82,3	0,26	35,04
3,000	29	72,2	0,38	35,16
10,000	25	70,8	0,43	35,18

Appendix 5: Recrystallised grain size distributions of CP 3103-W0

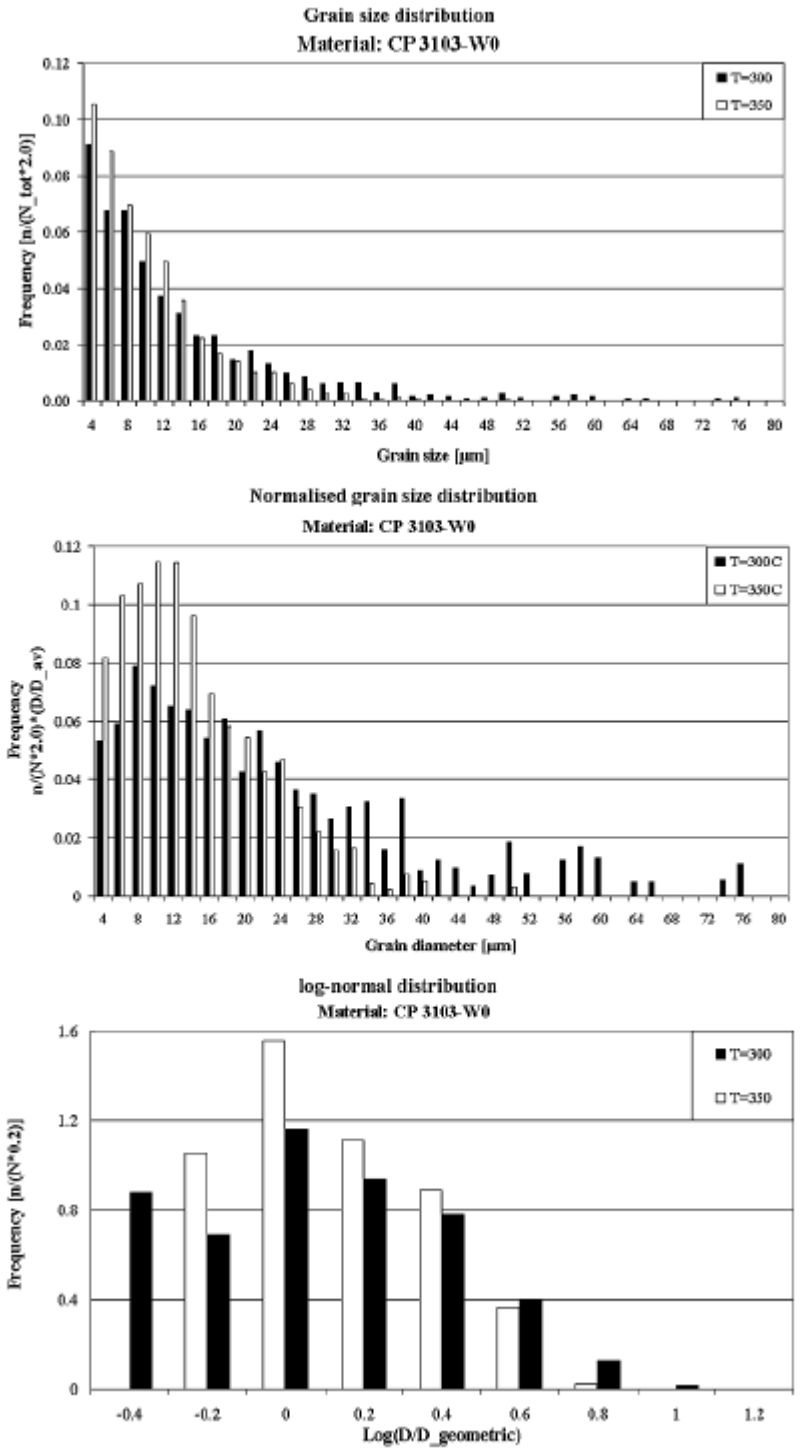

Fig.A4.1 Recrystallised grain size distribution of the CP 3103-W0 material annealed at 300°C and 350°C.

Appendix 6: Correlation between flow stress and Vickers Hardness.

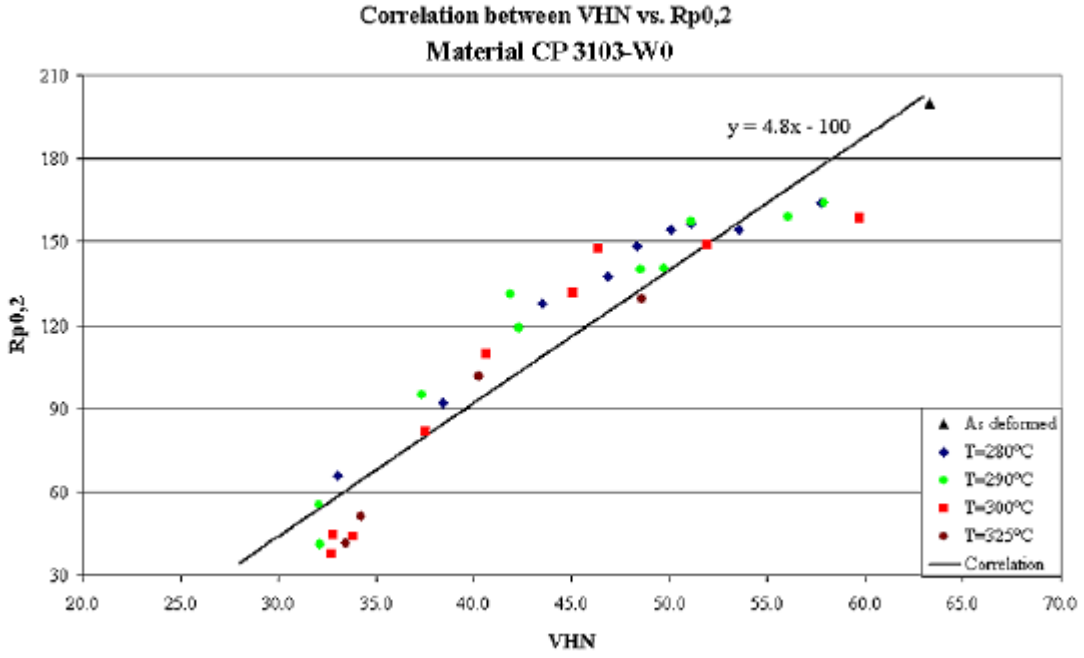

Appendix 7: Effect of the different parameters on the softening behaviour.

Table A7.1: Effect of the different variable parameters on the modelled softening curve.

Symbol	Comment or effect on the softening with increasing value
B_r	Defines when annihilation of dislocations starts. The recrystallisation knee is positioned at the same point independent on B_ρ.
$r_{i,0}$	Starting dislocation density. Increases the starting flow stress.
w_ρ	Changes shape and rate of dislocation annihilation, *i.e.* goes faster.
B_d	Defines when subgrain growth starts, *i.e.* increases the recovery rate.
$d_{i,0}$	Starting subgrain size. Increases the starting flow stress.
w_d	Changes shape and rate of subgrain growth, *i.e.* goes faster.
U_a	Decreases the amount of recovery softening prior to recrystallisation.
U_{GB}	More recovery occurs prior to recrystallisation.
c_{ss}	Calculated from the original chemical composition.
M_0	Less recovery prior to recrystallisation.
C_{PSN}	Efficiency of nucleation at the particles. Faster recrystallisation.
C_{GB}	Efficiency of nucleation at the grain boundaries. Increases rate of recrystallisation.
N_0	Less recovery prior to recrystallisation.
L	More recovery prior to recrystallisation.
D_0	Requires very small original grain size to have an effect.
j	Less recovery prior to recrystallisation.
j_c	Less recovery prior to recrystallisation.